



**HAL**  
open science

# High-performance electrochemical detection of reactive oxygen/nitrogen species inside microfluidic devices: application for monitoring oxidative stress from living cells

Yun Li

► **To cite this version:**

Yun Li. High-performance electrochemical detection of reactive oxygen/nitrogen species inside microfluidic devices: application for monitoring oxidative stress from living cells. Chemical Physics [physics.chem-ph]. Université Pierre et Marie Curie - Paris VI, 2014. English. NNT : 2014PA066367 . tel-01133304

**HAL Id: tel-01133304**

**<https://theses.hal.science/tel-01133304v1>**

Submitted on 19 Mar 2015

**HAL** is a multi-disciplinary open access archive for the deposit and dissemination of scientific research documents, whether they are published or not. The documents may come from teaching and research institutions in France or abroad, or from public or private research centers.

L'archive ouverte pluridisciplinaire **HAL**, est destinée au dépôt et à la diffusion de documents scientifiques de niveau recherche, publiés ou non, émanant des établissements d'enseignement et de recherche français ou étrangers, des laboratoires publics ou privés.

# Université Pierre et Marie Curie

Ecole doctorale de Chimie Physique et Chimie Analytique de Paris Centre

ED 388

*UMR CNRS 8640 PASTEUR, Groupe d'Electrochimie*

## **High-Performance Electrochemical Detection of Reactive Oxygen/Nitrogen Species inside Microfluidic Devices. Application for Monitoring Oxidative Stress from Living Cells.**

Par **Yun LI**

Thèse de doctorat d'Electrochimie

Présentée et soutenue publiquement le 17 septembre 2014

devant le jury composé de :

Dr. Fethi BEDIQUI (ENSCP)	Rapporteur
Pr. Pierre GROS (Université de Toulouse)	Rapporteur
Pr. Didier DEVILLIERS (UPMC)	Examineur
Pr. Bruno LE PIOUFLE (ENS Cachan)	Examineur
Dr. Laurent THOUIN (ENS)	Co-directeur de thèse
Dr. Christian AMATORE (ENS)	Directeur de thèse



## Acknowledgements

With the support of China Scholarship Council, I have undergone a great experience in pursuing my academic dreams as a PhD candidate in ENS, running like a river, small at first and then passionately past boulders and over waterfalls. During this period, many people behind the scene have made significant contributions, in one way or another, and hereby I sincerely express my heartfelt gratitude.

First and foremost, my great appreciation goes to Mr. Christian Amatore, my thesis director, for offering me such a chance to work in his electrochemistry group. Not only his intelligence or morality, but also the passion toward science, benefits me and makes me a fortunate child of favorable circumstance. Special thanks for his confidence and his effort of helping me to find a great postdoc position in Mirkin's group (CUNY, USA) to continue the study in electrochemistry.

My sincere thanks also go to Mr. Fethi Bedioui and Pierre Gros who have kindly accepted to evaluate this work and compose a relevant report to UPMC. The equivalent appreciation is own to Mr. Didier Devilliers and Bruno Lepioufle for acceding to examine this thesis.

This thesis is accomplished under supervision of Laurent Thouin. But for him, I could not have made such a progress in accumulation of knowledge. Thanks for his rigorous attitude, sense of responsibility, and degree of sophistication to view issues from different perspectives. Meanwhile, I am truly grateful to Catherine Sella for her unceasing effort to help and extreme patience during our discussion.

Many thanks go to Frédéric Lemaître and Manon Guille-Collignon for their constant concern and help in biological realm. Their brilliance as well as diligent guidance has considerably broadened my horizon, correspondingly inspiring me to extend the interest toward bioanalytical domain.

I would also like to personally thank my previous supervisors in China: Xinghua Xia and Weihua Huang. It is they who have inspired my academic voyage, leading me to a magnificent life.



Thanks to my colleagues in ENS: Cong (share joy and sorrow, be my support all the time); Wided and Pierre (many memories in the lab); Pierluca (for plenty of encouragements); Anne and Rémy (help me to become gradually familiar with microfabrication and manipulation of cells); Thomas, Ana, Xiaoqing, Guillaume, Lylian and Dali (make the scientific life very interesting and active); Feli, Margherita, Jing Zhu, etc. The colorful life will be forever embedded in my memory.

Thanks to Yong Chen and the people in his group: Megan, Xin Li, Junjun Li, Jiaji Liu, Zhitao Han, Fan Zhang, Jian Shi, Jun Liu, Jie Hu, Sisi Li, Wentao He, Zhi Li, Yu Zhang and Yadong Tang, for their help in microfluidic fabrication and company in leisure time.

Thanks to Marie-Aude and Kalthoum for the generous help in cell culture.

Thanks to Fatima, Raquel and Wei Wang for giving me a lot of perceptive advice in this work.

Great thanks to Cécile (impressively capable and hardworking), Gérardine and Eric for the smooth and orderly running of all laboratory facilities.

I shall extend my thanks to Dominique Ho Tin Noe, Anne Halloppe, Frédéric Bataille, Auguste Filippi in ENS; Soobrayen Koonavadee and Hélène Gérard in UPMC. They are always so nice to help me arrange the multifarious student affairs.

Finally, I would like to express my deepest gratitude to my family and friends. Thanks Dad, for setting up a great example of perseverance, and for his incessant encouragements in my frustrations. Thanks Mom, for not only being a tender mother, but also my best friend. Thanks to my friends Hao Chen, Cheng Qian, Yinzi Cao, Jing Li, Jun Dong, Yuan Hu, Jiazhen Zhu, Xiangxue Kong, Liang Kong, Chunjuan Sheng, Xing Jin, Lin Lin, Yi Peng, etc. They are always my courage through the exciting but sometimes arduous journey.

## Table of contents

<b>ABBREVIATIONS .....</b>	<b>1</b>
<b>RÉSUMÉ DE LA THÈSE (FRENCH ABSTRACT).....</b>	<b>7</b>
<b>GENERAL INTRODUCTION .....</b>	<b>35</b>
<b>PART A: STATE-OF-THE-ART</b>	
<b>1. OXIDATIVE STRESS AND REACTIVE OXYGEN/NITROGEN SPECIES (ROS/RNS).....</b>	<b>41</b>
1.1. <i>Natural process of oxidative stress</i> .....	41
1.2. <i>Roles of ROS/RNS in life</i> .....	46
1.2.1. Beneficial effects.....	47
1.2.2. Deleterious effects.....	49
1.3. <i>Conclusion of section 1</i> .....	50
<b>2. DETECTION METHODS FOR ROS/RNS .....</b>	<b>51</b>
2.1. <i>Some general analytical methods</i> .....	51
2.1.1. Fluorescence method.....	51
2.1.2. Chemiluminescence method .....	53
2.1.3. Electron spin resonance (ESR) spectroscopy .....	55
2.1.4. Ultraviolet-visible (UV-Vis) spectroscopy .....	56
2.1.5. Biomarkers method .....	57
2.2. <i>Electrochemical method</i> .....	58
2.2.1. Superoxide anion ( $O_2^{\bullet-}$ ) sensors .....	60
2.2.2. Hydrogen peroxide ( $H_2O_2$ ) sensors .....	61
2.2.3. Nitric oxide ( $NO^{\bullet}$ ) sensors .....	63
2.2.4. Peroxynitrite ( $ONOO^-$ ) sensors .....	66
2.2.5. Nitrite ion ( $NO_2^-$ ) sensors .....	67
2.2.6. Platinum black (Pt-black) coated electrodes .....	69
2.3. <i>Conclusion of section 2</i> .....	70

<b>3. ANALYTICAL PROGRESS IN <i>EX VIVO</i> DETECTION OF CELLULAR ELECTROACTIVE MESSAGERS.....</b>	<b>71</b>
3.1. <i>Single-cell analysis by using microelectrodes</i> .....	72
3.1.1. Microelectrodes and their advantages .....	72
3.1.2. Detection of electroactive messengers from a single living cell .....	73
3.2. <i>Microfluidic devices as functional tools for cell-based analysis</i> .....	77
3.2.1. Cell culture in microfluidic devices .....	79
3.2.2. Cell manipulation in microfluidic devices .....	82
3.2.3. Cell-based analysis on microfluidic platforms .....	84
3.3. <i>Conclusion of section 3</i> .....	89
<b>4. CONCLUSION OF STATE-OF-THE-ART AND PERSPECTIVES.....</b>	<b>89</b>

**PART B: *IN VITRO* ELECTROCHEMICAL DETECTION OF ROS/RNS AT HIGHLY SENSITIVE PT/PT-BLACK MICROBAND ELECTRODE INSIDE MICROFLUIDIC SYSTEM**

<b>1. CONVECTIVE-DIFFUSIVE MASS TRANSPORT ABOVE PT/PT-BLACK MICROCHANNEL ELECTRODE .....</b>	<b>93</b>
1.1. <i>Mass transport regimes above a single microband electrode</i> .....	93
1.2. <i>Choice of mass transport regime in our microfluidic device</i> .....	99
1.3. <i>Optimization and evaluation of Pt-black deposit</i> .....	102
1.4. <i>Conclusion of section 1</i> .....	109
<b>2. ROS/RNS <i>IN VITRO</i> DETECTION AT PT/PT-BLACK MICROBAND ELECTRODE.....</b>	<b>110</b>
2.1. <i>In vitro detection of two stable candidates: H<sub>2</sub>O<sub>2</sub> and NO<sub>2</sub><sup>-</sup></i> .....	110
2.1.1. Current responses at Pt/Pt-black electrode.....	111
2.1.2. Oxidation mechanisms of H <sub>2</sub> O <sub>2</sub> and NO <sub>2</sub> <sup>-</sup> .....	115
2.1.3. Calibration curve and electrode sensitivity .....	117
2.2. <i>In vitro detection of two unstable candidates: ONOO<sup>-</sup> and NO<sup>•</sup></i> .....	119
2.2.1. Detection of ONOO <sup>-</sup> .....	119
2.2.2. Detection of NO <sup>•</sup> .....	125
2.3. <i>In vitro detection of samples mixture</i> .....	129
2.4. <i>Conclusion of section 2</i> .....	135
<b>3. CONCLUSION OF PART B.....</b>	<b>136</b>

# **PART C: MONITORING OF CELLULAR OXIDATIVE STRESS BY PT/PT-BLACK ELECTRODES-INTEGRATED MICROSYSTEMS**

<b>1. INVESTIGATION OF OXIDATIVE STRESS IN LABORATORY .....</b>	<b>139</b>
1.1. <i>Cell models</i> .....	139
1.2. <i>Cell stimulations</i> .....	141
1.2.1. Mechanical penetration .....	141
1.2.2. Biochemical stimulation .....	143
1.3. <i>Conclusion of section 1</i> .....	146
<b>2. DETECTION OF OXIDATIVE BURSTS FROM CELLS POPULATIONS ON BASAL MICROBAND ELECTRODE .....</b>	<b>146</b>
2.1. <i>Experimental conditions</i> .....	146
2.1.1. Microdevice configuration .....	146
2.1.2. Cells viability and density .....	148
2.2. <i>Qualitative detection of ROS and RNS production</i> .....	149
2.2.1. Characteristics of amperometric responses .....	149
2.2.2. Cells variations and successive releases .....	151
2.2.3. Cells detachment and chip reuse .....	153
2.3. <i>Quantification of ROS and RNS production</i> .....	154
2.3.1. Evaluation of fluxes and quantities of ROS and RNS production .....	154
2.3.2. Evaluation of primary production of $O_2^{\bullet-}$ and $NO^{\bullet}$ .....	158
2.4. <i>Conclusion of section 2</i> .....	161
<b>3. DETECTION OF OXIDATIVE BURSTS FROM CELLS POPULATION ON DOWNSTREAM MICROBAND ELECTRODES .....</b>	<b>162</b>
3.1. <i>Experimental conditions</i> .....	162
3.1.1. Microdevice configuration .....	162
3.1.2. Cells manipulation inside microdevice .....	164
3.2. <i>Detection of ROS and RNS production</i> .....	172
3.2.1. Detection reproducibility between parallel electrodes .....	172
3.2.2. Detection reliability after biocompatible coating .....	173
3.2.3. Detection during continuous flow .....	174
3.2.4. Detection after 10-min stop flow .....	179
3.3. <i>Conclusion of section 3</i> .....	181
<b>4. CONCLUSION OF PART C .....</b>	<b>182</b>

<b>GENERAL CONCLUSION AND PERSPECTIVES.....</b>	<b>187</b>
---	------------

## **APPENDIX**

<b>APPENDIX I. ELECTROCHEMICAL PRINCIPLES AND MICROELECTRODES.....</b>	<b>191</b>
--	------------

<i>I.1. Electrochemical principles .....</i>	<i>191</i>
<i>I.2. General electrochemical techniques.....</i>	<i>196</i>
<i>I.3. Microelectrodes and their electrochemical performances .....</i>	<i>201</i>

<b>APPENDIX II. MICROFLUIDIC MATERIALS AND MICROFABRICATION.....</b>	<b>206</b>
--	------------

<i>II.1. Materials.....</i>	<i>206</i>
<i>II.2. Microfabrication techniques.....</i>	<i>209</i>

<b>APPENDIX III. EXPERIMENTAL SECTION .....</b>	<b>215</b>
---	------------

<i>III.1. Solutions preparation.....</i>	<i>215</i>
<i>III.2. Sensors preparation.....</i>	<i>217</i>
<i>III.3. Raw 264.7 macrophages preparation.....</i>	<i>230</i>
<i>III.4. Analytical measurements .....</i>	<i>233</i>

<b>REFERENCES.....</b>	<b>243</b>
------------------------	------------

## Abbreviations

**3-NT**: 3-nitrotyrosine

**A23187**: calcium ionophore (a mobile ion-carrier that forms stable complexes with divalent cations)

**AFM**: atomic force microscope

**Ag/AgCl**: silver-silver chloride reference electrode

**AuNPs**: gold nanoparticles

**BMSCs**: bone marrow stromal cells

**BSA**: bovine serum albumin

**Ca<sup>2+</sup>**: calcium ion

**CAT**: catalase

**CE**: counter electrode

**CFMDE**: carbon-fiber microdisk electrode

**cGMP**: cyclic guanosine monophosphate

**Cu**: copper

**CV**: cyclic voltammetry

**Co**: cobalt

**CO**: carbon monoxide

**CO<sub>2</sub>**: carbon dioxide

**CRMA**: carbon-ring microelectrode array

**Cys**: cysteine

**Cyt *c***: cytochrome *c*

**DAF**: diaminofluorescein

**DCFH**: 2',7'-dichlorodihydrofluorescein

**DEA-NONOate**: diethylamine nonoate (NO<sup>•</sup> donor)

**DETC**: diethyldithiocarbamate

**DHE**: dihydroethidium

**DHR 123**: dihydrorhodamine 123

**DMEM**: Dulbecco's modified eagle's medium

**DMPO**: 5,5-dimethyl-1-pyrroline-N-oxide

**DMSO:** dimethyl sulfoxide

**ECM:** extracellular matrix

**EDTA:** ethylenediaminetetraacetic acid

**ESR:** Electron spin resonance

**Ex vivo:** experimentation or measurements done in or on living tissue isolated from an intact organism with the minimum alteration of the natural conditions

**FAD:** flavin adenine dinucleotide

**FBS:** fetal bovine serum

**FcMeOH:** ferrocenemethanol

**FCS:** fetal calf serum

**Fe:** iron

**FMN:** flavin mononucleotide

**GC:** gas chromatography

**GC:** guanylate cyclase

**GelMA:** gelatin methacrylate

**GSH:** glutathione

**GSSG:** glutathione disulfide

**Hcy:** homocysteine

**HeLa:** human epithelial carcinoma cell line

**Hep G2:** human hepatocarcinoma cell line

**HO<sub>2</sub>·:** hydroperoxyl radical

**HOCl:** hypochlorous acid

**H<sub>2</sub>O<sub>2</sub>:** hydrogen peroxide

**HPLC:** high-performance liquid chromatography

**HUVECs:** human umbilical vein endothelial cells

**IL-1:** interleukin-1

**In vitro:** biological processes or reactions made to occur outside the living organism in an artificial environment to simplify study, such as in a test tube or laboratory dish

**In vivo:** a biological process or experiments occurring within a living organism

**IFM:** inverted fluorescence microscope

**IFN-γ:** interferon-γ

**IgG:** immunoglobulin G

**ITO:** indium tin oxide

**K<sub>2</sub>PtCl<sub>6</sub>:** potassium hexachloroplatinate

**LC:** lucigenin  
**LM:** luminol  
**LOD:** limit of detection  
**LPS:** lipopolysaccharide  
**LSV:** linear-sweep voltammetry  
**MAPK:** mitogen-activated protein kinase  
**MDA:** malondialdehyde  
**MEA:** microelectrode array  
**Mn:** manganese  
**MPO:** myeloperoxidase  
**MS:** mass spectrometry  
**Na<sub>2</sub>HPO<sub>4</sub>:** disodium hydrogen phosphate  
**NaH<sub>2</sub>PO<sub>4</sub>:** sodium dihydrogenphosphate  
**NADPH:** reduced nicotinamide adenine dinucleotide phosphate  
**Ni:** nickel  
**NO<sup>•</sup>:** nitric oxide  
**NO<sup>+</sup>:** nitrosonium cation  
**NO<sub>2</sub><sup>-</sup>:** nitrite ion  
**NO<sub>3</sub><sup>-</sup>:** nitrate ion  
**NO<sub>2</sub>:** nitrogen dioxide  
**NOS:** nitric oxide synthase (nNOS: neuronal isoform; iNOS: inducible isoform; eNOS: endothelial isoform; mtNOS: mitochondrial isoform)  
**N<sub>2</sub>O<sub>3</sub>:** dinitrogen trioxide  
**O<sub>2</sub>:** oxygen  
**O<sub>3</sub>:** ozone  
**O<sub>2</sub><sup>-</sup>:** superoxide ion  
**OH<sup>•</sup>:** hydroxyl radical  
**ONOO<sup>-</sup>:** peroxyxynitrite (conjugated acid ONOOH)  
**PC12:** rat pheochromocytoma cell line  
**PAAM:** polyacrylamide  
**PB:** Prussian blue  
**PBS:** phosphate buffered saline  
**PC:** polycarbonate  
**PC12:** rat pheochromocytoma cell line 12



**PDGF**: platelet-derived growth factor  
**PDMS**: polydimethylsiloxane  
**PEG**: polyethylene glycol  
**PET**: polyethylene terephthalate  
**PLGA**: *poly lactic-co-glycolic acid*  
**PLLA**: poly-L-lactic acid  
**PMA**: phorbol 12-myristate 13-acetate  
**PMMA**: polymethyl methacrylate  
**PS**: polystyrene  
**Pt**: platinum  
**PUFA**: polyunsaturated free-fatty acids  
**PVC**: polyvinylchloride  
**PVP**: polyvinylpyridine  
**REF**: reference electrode  
**RNS**: reactive nitrogen species  
**ROS**: reactive oxygen species  
**ROO<sup>•</sup>**: peroxy radicals  
**RS<sup>•</sup>**: thiyl radical  
**SAMs**: self-assembled monolayers  
**SCE**: saturated calomel electrode  
**SECM**: scanning electrochemical microscopy  
**SEM**: scanning electron microscope  
**SHE**: standard hydrogen electrode  
**SOD**: superoxide dismutase  
**SSCE**: sodium saturated calomel electrode  
**Ti**: titanium  
**TFN**: tumor necrosis factor  
**TIRFM**: total internal reflection fluorescence microscopy  
**TMCS**: trimethylchlorosilane  
**TNF- $\alpha$** : tumor necrosis factor- $\alpha$   
**UME**: ultramicroelectrode  
**UV-Vis**: ultraviolet-visible spectroscopy  
**WE**: working electrode  
**Zn**: zinc

## *Résumé de la thèse (French abstract)*

### *Sujet:*

*Détection Electrochimique à Haute Performance d'Espèces Réactives de l'Oxygène et de l'Azote à l'Intérieur de Dispositifs Microfluidiques. Application au Stress Oxydant de Cellules Vivantes.*



## Résumé de la thèse (French abstract)

### *Introduction générale*

Les études portant sur les cellules vivantes se développent sans cesse pour apporter une compréhension plus fine des phénomènes de la vie. Le stress oxydant est une des situations métaboliques importantes qui intéresse fortement la communauté en bioanalytique. Durant ce processus, des familles d'espèces réactives de l'oxygène (ROS) et réactives de l'azote (RNS) sont formées pour réguler des fonctions physiologiques et pathologiques.

D'après les propriétés électroactives de ces espèces, les microélectrodes ouvrent de nouveaux horizons et opportunités pour explorer des cellules vivantes. Cependant, en raison des variations du comportement cellulaire, les résultats statistiquement fiables au niveau de la cellule unique requièrent souvent des expériences répétitives et fastidieuses. Pour contourner ces difficultés, nous avons décidé dans ce travail de thèse de tirer bénéfice des avantages des microélectrodes et de la microfluidique pour accomplir des analyses à haut débit de RNS/ROS à partir de populations de cellules vivantes.

En premier lieu, la fabrication des microélectrodes doit être optimisée pour leur utilisation en microfluidique ainsi que leurs performances analytiques vis-à-vis des espèces considérées individuellement. Les microdispositifs seront conçus à partir de ces outils pour ensuite explorer le stress oxydant de cellules vivantes. Ainsi, le manuscrit de la thèse sera organisé de la façon suivante. Dans une première partie, nous dresserons un état de l'art du progrès des recherches actuellement menées dans ce domaine. Dans une seconde partie, nous présenterons la fabrication de microélectrodes en noir de platine et son optimisation pour atteindre des performances analytiques élevées vis-à-vis de la détection de ROS/RNS en solution. Dans la troisième et dernière partie, deux configurations de microdispositifs seront étudiées pour analyser le comportement de populations de macrophages soumis à un stress oxydant.

## ***PARTIE A: Etat de l'art***

### **1. Stress oxydant et production d'espèces ROS/RNS**

La vie dans un environnement aérobie est constamment accompagnée de la production d'espèces ROS/RNS. Lorsque le relargage excède de façon non contrôlée la capacité antioxydante, le stress oxydant prédomine tendant à engendrer des dommages au niveau cellulaire. Outre le métabolisme normal dans la chaîne respiratoire, deux familles d'enzymes spécifiques (Figure Résumé-1) sont responsables de la génération en masse d'espèces oxydantes.

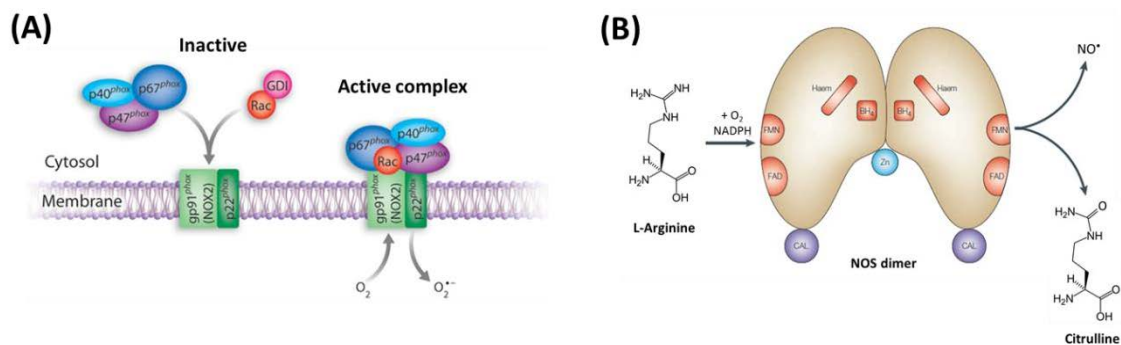


Figure Résumé-1: (A) Modèle de l'activation de NADPH oxydase. Les protéines cytosoliques *phox* et *Rac* migrent dans la membrane plasmique ou celle du phagosome, générant O<sub>2</sub><sup>-</sup> à partir des ressources en oxygène. (B) Le dimère NOS catalyse l'oxydation de la L-arginine en citrulline et NO<sup>•</sup> en présence d'oxygène et de NADPH.

Comme indiqué sur la Figure Résumé-1A, les NADPH oxydases (nicotinamide adenine dinucleotide phosphate) produisent une grande quantité d'anion superoxyde (O<sub>2</sub><sup>-</sup>) lorsqu'elles sont assemblées avec les protéines membranaires du côté cytosolique. Les synthèses de l'oxyde nitrique (NOS) sont actives par l'intermédiaire de dimères pour oxyder la L-arginine et générer l'oxyde nitrique (NO<sup>•</sup>) selon le schéma indiqué sur la Figure Résumé-1B.

Provenant de deux espèces initiales O<sub>2</sub><sup>-</sup> et NO<sup>•</sup>, diverses substances actives sont générées suivant des schémas biochimiques complexes. La chimie telle que décrite sur la Figure Résumé-2 mène à la génération de plusieurs espèces dérivées importantes.

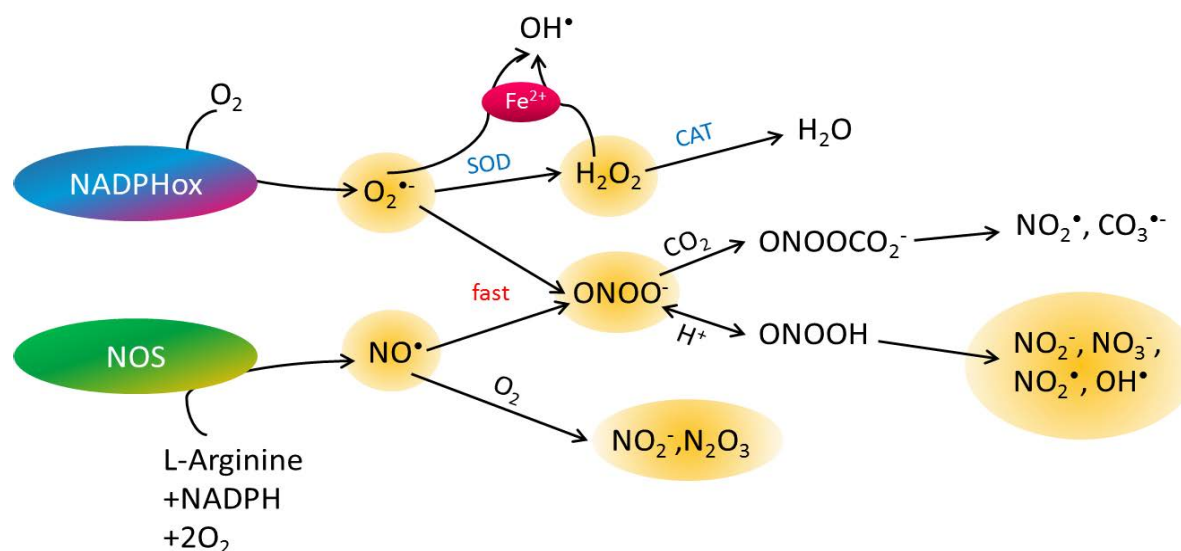


Figure Résumé-2: Schéma des principales voies de génération d'espèces ROS/RNS à partir des espèces primaires  $O_2^{\bullet-}$  et  $NO^{\bullet}$ .

Ces espèces apparaissent comme des espèces omniprésentes dans le processus global de la vie et sont imputées de rôles très ambivalents. Elles peuvent réguler des fonctions physiologiques vitales mais peuvent aussi conduire à de nombreuses affections mortelles. L'exploration approfondie des principales espèces ROS/RNS générées durant le stress oxydant permet alors une meilleure compréhension du processus métabolique.

## 2. Méthodes de détection des espèces ROS/RNS

Ces espèces étant transitoires et générées en très faible quantité, des méthodes de détection à haute performance (fluorescence, chimiluminescence, etc.) sont requises. Nombre d'entre elles sont actuellement à l'étude. Parmi celles-ci, on trouve l'électrochimie qui offre une approche directe, sans marquage, car fondée sur les propriétés électroactives de ces espèces.

Des modifications post fonctionnelles de la surface d'électrode ont été développées afin d'améliorer les performances de la détection. Parmi les dépôts possibles, il y a le noir de platine (noir-Pt) qui a été reporté comme le dépôt offrant une sensibilité et sélectivité optimales vis-à-vis de la détection de quatre espèces oxydantes ( $H_2O_2$ ,  $NO^{\bullet}$ ,  $ONOO^-$ , et  $NO_2^-$ ).

En effet, ces quatre composés sont considérés comme les espèces clés du stress oxydant puisque les autres qui sont impliquées sont soit de trop courte durée de vie (e.g.,  $\text{OH}^\bullet$ ) ou encore non électroactives (e.g.,  $\text{NO}_3^-$ ) dans les conditions expérimentales données. En effet, avant de pouvoir être détecté,  $\text{O}_2^-$  par exemple est majoritairement éliminé par la réaction rapide d'antidismutation. Une alternative consiste alors à détecter le principal produit de la réaction ( $\text{H}_2\text{O}_2$ ) pour sa quantification.

### **3. Progrès analytiques dans la détection *ex vivo* de messagers cellulaires électroactifs**

Les propriétés connues des microélectrodes ouvrent de nouveaux horizons et de nouvelles opportunités pour explorer les cellules vivantes en raison des caractéristiques suivantes: (i) réponse rapide; (ii) rapport signal sur bruit élevé et (iii) résolution spatiale. Une configuration importante est celle de la synapse artificielle (Figure Résumé-3A). En approchant une microélectrode à la surface émettrice d'une cellule isolée, les messagers électroactifs sont détectés avec haute efficacité et haute résolution temporelle. Suivant cette configuration, notre groupe a exploré de façon intensive le stress oxydant au niveau de la cellule unique. D'autres développements dans l'instrumentation et les méthodologies permettent des études intracellulaires (Figure Résumé-3B) et la détection simultanée de multiples espèces (Figure Résumé-3C). Cependant, en raison des variations importantes observées au niveau du comportement des cellules, des résultats statistiquement fiables nécessitent la répétition d'expériences souvent fastidieuses à réaliser.

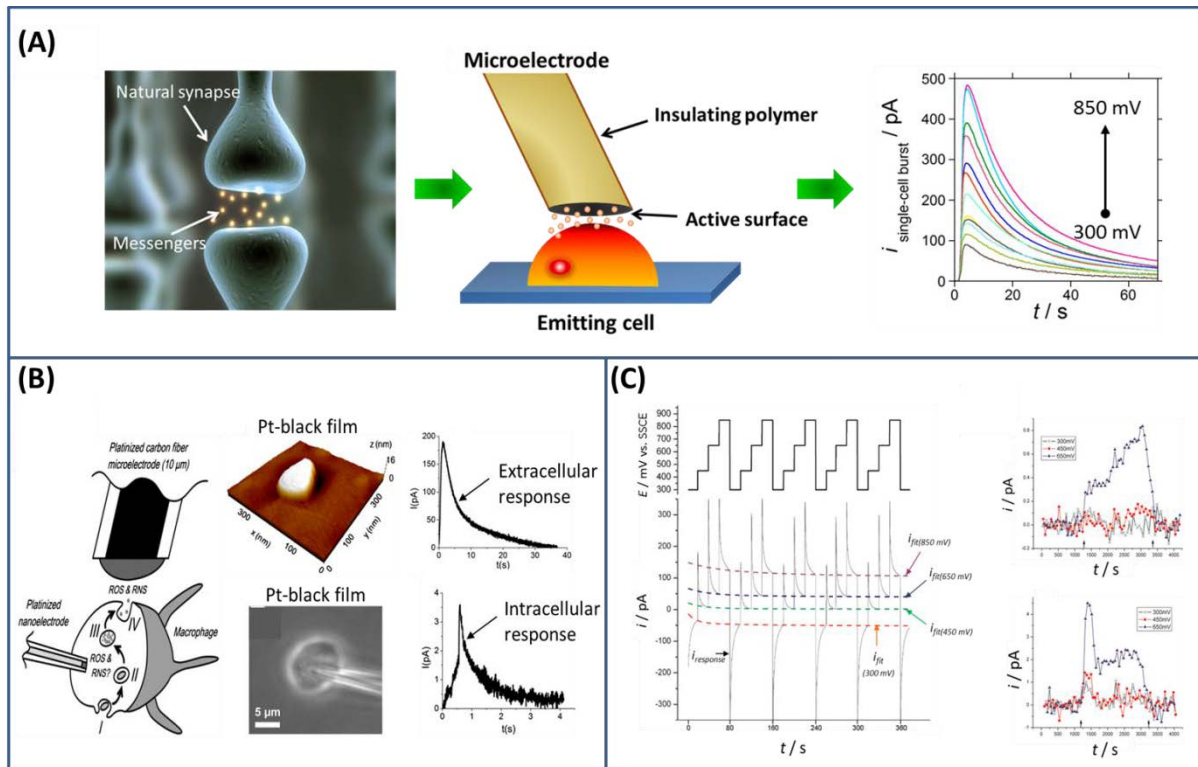


Figure Résumé-3: (A) Illustrations d'une vraie synapse (à gauche) et d'une synapse artificielle pour un assemblage cellule vivante unique/microélectrode (au milieu), puis le suivi ampérométrique résultant de l'émission d'espèces par la cellule unique. (B) Suivi de la production intracellulaire de ROS/RNS durant le stress oxydant (à gauche). Une nanoélectrode après dépôt de noir-Pt (rayon de 80 nm) est insérée à l'intérieur d'un macrophage (au milieu). Des exemples de mesures de courant pour des détections extracellulaires et intracellulaires sont également reportés (à droite). (C) Courants mesurés (en bas à gauche, ligne continue) lors d'une séquence de sauts de potentiel (à gauche en haut) appliquée à une électrode fibre de carbone platinisée. Les quatre lignes en tiret sont les meilleurs ajustements du courant moyen à la fin de chaque saut. Les potentiels imposés sont successivement 0.30, 0.45, 0.65 et 0.85 V vs. ECSS, pendant une durée de 20 s. Chaque figure du côté droit montre des chronoampérogrammes à 0.30 (croix noires), 0.45 (carrés rouges) et 0.65 V (triangles bleus) vs. ECSS à partir d'un seul macrophage. Des mesures sont reportées pour deux cellules différentes.

En raison de la biocompatibilité des matériaux tels que le PDMS, une des voies prometteuses consiste à intégrer ce type d'expérience à l'intérieur d'un système microfluidique. Les technologies de microfabrication avancées ainsi que les caractéristiques fluidiques font que toutes les étapes de culture cellulaire (Figure Résumé-4A), de manipulation (Figure Résumé-4B) et de détection (Figure Résumé-4C) peuvent être réalisées dans un dispositif « tout en un ». A l'opposé de la détection sur cellule unique (suivant une configuration de type synapse artificielle), la détection sur une plateforme microfluidique permet des analyses simples et simultanées de groupes de cellules durant une courte durée d'expérience. En élaborant différentes configurations, la détection peut être réalisée pour satisfaire les exigences et les besoins de l'expérience.



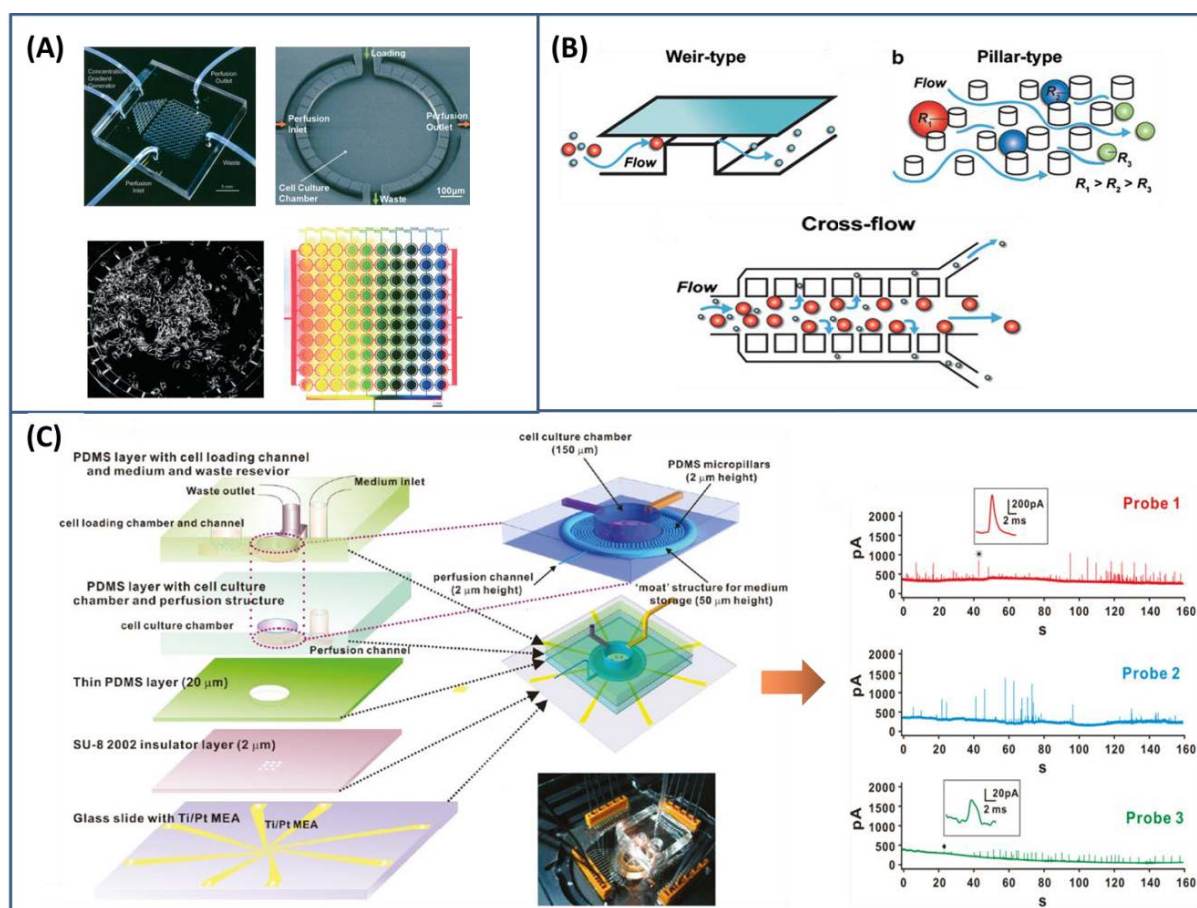


Figure Résumé-4: (A) Réseau de perfusion microfluidique à haut débit pour des cultures cellulaires de longue durée. Le dispositif complet est de 2×2 cm en taille, et chaque chambre de culture possède quatre voies d'accès et plusieurs canaux de perfusion aux alentours. Des cellules Hela sont cultivées sous perfusion pendant 6 jours. Le profil du gradient de concentration est mis en évidence par un colorant rouge perfusé de gauche à droite, et des colorants bleu et jaune sont introduits en haut du générateur de gradient. (B) Manipulations de cellules par solution circulante en microfluidique. Suivant les tailles caractéristiques, les cellules peuvent être séparées en passant simplement à travers différentes microstructures. (C) Réseau de microélectrodes intégré dans un bloc de PDMS pour la détection de cellules uniques. La structure du dispositif multicouche est montrée à gauche. La dopamine émise à partir de trois cellules individuelles PC12 est collectée par le réseau d'électrodes.

#### 4. Conclusion et perspectives

D'après l'état de l'art qui a été dressé, des microdispositifs PDMS-verre intégrant des microélectrodes devraient déboucher sur la réalisation d'excellentes plateformes pour mener à bien des détections à haut débit d'espèces ROS/RNS à partir de cellules vivantes. Des dispositifs hautement sophistiqués peuvent être élaborés pour effectuer des cultures cellulaires, des stimulations et des détections simultanées d'espèces. Cependant, pour le développement de tels microdispositifs, certaines études préliminaires demeurent nécessaires comme par exemple l'optimisation du dépôt de noir de platine pour satisfaire les conditions d'utilisation requises en microfluidique.

Ainsi, dans ce contexte et afin d'atteindre un couplage optimal entre la microfluidique et une détection ampérométrique, nous nous intéresserons principalement (i) à l'optimisation des électrodes microbandes Pt/noir-Pt et à la validation de leurs performances analytiques vis-à-vis des espèces individuelles ROS/RNS à l'intérieur de canaux microfluidiques et (ii) au suivi simultané de ces espèces émises à partir de cellules vivantes. Différentes configurations de dispositifs pourront alors être envisagées afin d'accéder à une compréhension fine du comportement de cellules, à la fois au cours d'études cinétiques et de détections quantitatives.

## ***PARTIE B: Détection électrochimique in vitro d'espèces ROS/RNS à l'intérieur de microcanaux à partir d'électrodes microbande en Pt/noir-Pt***

Dans cette partie, le dépôt de noir de platine sur des électrodes microbandes en platine a été optimisé pour une utilisation à l'intérieur de microcanaux. Les performances analytiques vis-à-vis de solutions synthétiques de  $\text{H}_2\text{O}_2$ ,  $\text{NO}^\bullet$ ,  $\text{ONOO}^-$ , et  $\text{NO}_2^-$  ont été évaluées en comparant les résultats expérimentaux avec les régimes théoriques du transport de masse par diffusion-convection.

### **1. Electrode microbande en Pt/noir-Pt**

Comme décrit sur la Figure Résumé-5, une approximation à deux dimensions de la géométrie d'un canal rectangulaire peut être appliquée pour évaluer plus simplement les réponses en courant des électrodes en fonction des paramètres géométriques et hydrodynamiques.

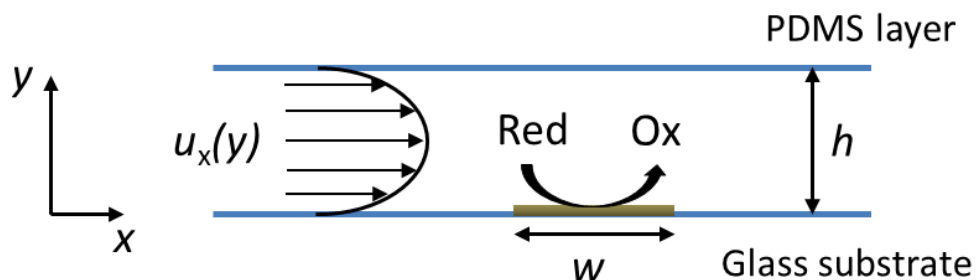


Figure Résumé-5: Schéma 2D de la configuration utilisée pour les simulations numériques avec le profil parabolique du flux à l'intérieur du microcanal.

En effet, deux paramètres  $W$  ( $w/h$ ) et  $Pe$  ( $u_{av}h/D$ ) contrôlent le régime du transport de masse au voisinage des électrodes avec des effets opposés. Lorsque  $W/Pe > 1.2$  (zone I), le transport de masse est contrôlé par la diffusion. A l'opposé, lorsque  $W/Pe < 0.04$  (zone III), l'épaisseur de la solution sondée par les électrodes est principalement fixée par la convection. Un comportement intermédiaire prend place lorsque  $0.04 < W/Pe < 1.2$ . Une valeur seuil de  $W/Pe \approx 0.56$  permet finalement de distinguer la prédominance de la convection ou de la diffusion sur le régime.

Dans le cas de notre dispositif microfluidique, (Figure Résumé-6A: hauteur de canal = 20  $\mu\text{m}$ , largeur de canal = 200  $\mu\text{m}$ , largeur d'électrode de travail = 197  $\mu\text{m}$ ), la vitesse d'écoulement a été choisie pour assurer un régime stationnaire de type convectif. La vitesse ne doit pas être trop élevée pour des raisons pratiques d'expérience et pas trop basse pour maintenir un rapport signal sur bruit élevé. Un bon compromis (zone rouge dans la Figure Résumé-6B) a été fixé pour établir un régime du transport de masse répondant au critère  $0.02 < W/Pe < 0.1$ .

En tenant compte de la géométrie de notre dispositif, une valeur de 2  $\mu\text{L min}^{-1}$  a été fixée expérimentalement. Cette vitesse d'écoulement permet, d'une part, d'assurer une stabilité de l'écoulement sans problème de fuites au niveau du dispositif et d'autre part, d'assurer la manipulation de cellules à l'intérieur du système sans les endommager ou engendrer une perte de leur adhésion.

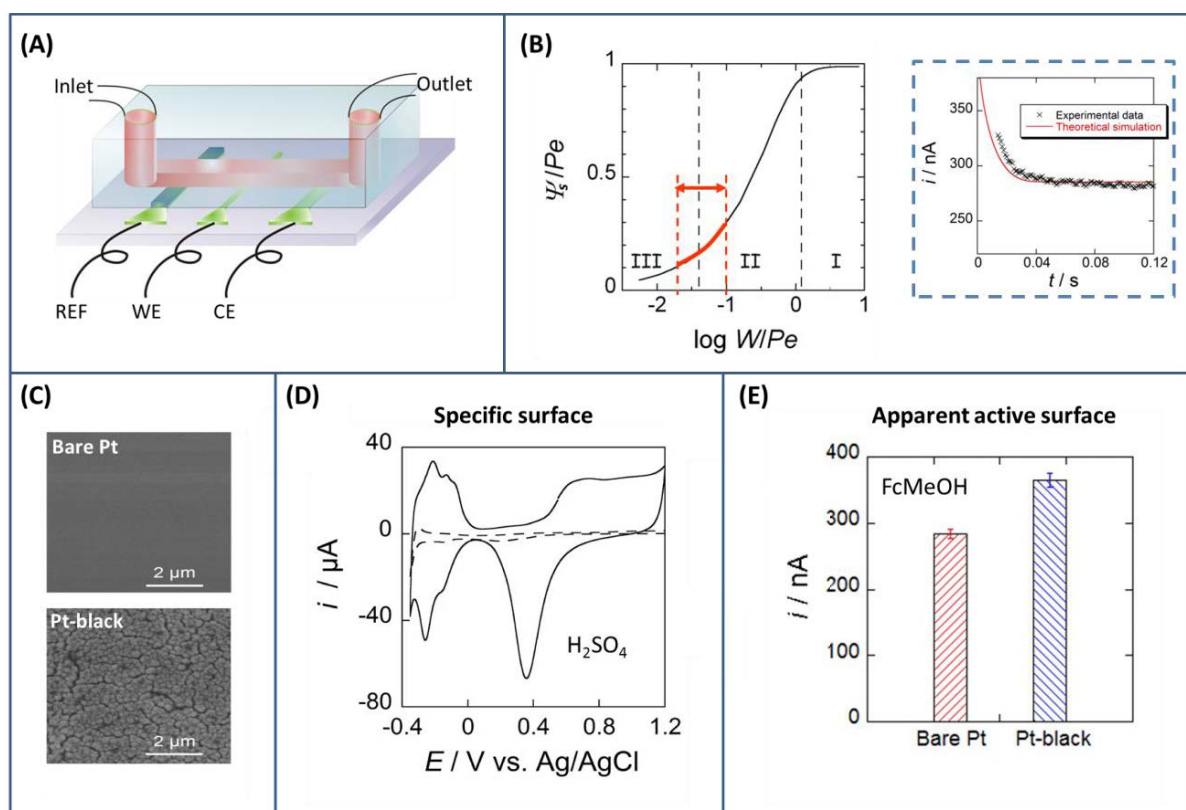


Figure Résumé-6: (A) Vue schématique de dispositif microfluidique montrant les positions relatives de l'électrode de référence (REF), électrode de travail (WE) et contre électrode (CE) à l'intérieur du microcanal. (B) Simulations numériques montrant la prédominance des régimes de diffusion – convection suivant le rapport  $\log W/Pe$ ; la zone en rouge représente les conditions utilisées dans nos expériences avec  $0.02 < W/Pe < 0.1$ . L'insert de la figure montre la comparaison entre les données expérimentales (après soustraction du courant résiduel, croix noires) et la simulation théorique (ligne rouge) durant l'établissement de l'état stationnaire en ampérométrie. (C) Images SEM de la surface nue d'une électrode de Pt et d'une électrode Pt/noir-Pt.  $J = -8 \text{ mA cm}^{-2}$  et  $Q = -240 \text{ mC cm}^{-2}$  ont été appliqués pour le dépôt de noir de Pt. (D) Voltammogrammes cycliques enregistrés à  $100 \text{ mV s}^{-1}$  dans une solution  $0.1 \text{ M H}_2\text{SO}_4$  pour une électrode nue de Pt (courbe en tiret) et une électrode Pt/noir-Pt avec un facteur de rugosité de 36.8 (courbe en trait plein). (E) Courants à l'état stationnaire pour une solution  $0.5 \text{ mM FcMeOH}$  sur électrode nue de Pt et Pt/noir-Pt sous conditions d'écoulement similaires. 5 dispositifs ont été utilisés pour effectuer ces comparaisons.

Un bon accord a été obtenu entre les résultats théoriques et expérimentaux (Figure Résumé-6B) avec utilisation de FcMeOH comme médiateur rédox. Cependant, pour améliorer la sensibilité et la stabilité à long terme des électrodes lors de la détection d'espèces ROS/RNS, du noir de platine a été déposé sur des électrodes microbande de platine. Ce dépôt limite en effet la passivation des électrodes et facilite le transfert d'électron. Après l'optimisation de la procédure, des dépôts uniformes avec des épaisseurs compatibles (Figure Résumé-6C) ont été obtenus pour conduire un rapport signal sur bruit élevé. Les caractéristiques du régime convectif ont pu être vérifiées expérimentalement à partir de ces électrodes. Un facteur de 1.3 a été évalué pour la surface active apparente (Figure Résumé-6E) alors qu'une valeur bien plus grande de 36.8 a été estimée pour la surface spécifique (Figure

Résumé-6D). Ainsi, les performances analytiques vis-à-vis des espèces individuelles ROS/RNS ont pu être évaluées sous régime stationnaire convectif à l'intérieur de microcanaux.

## 2. Détection *in vitro* de deux espèces stables : le peroxyde d'hydrogène et les nitrites

$\text{H}_2\text{O}_2$  et  $\text{NO}_2^-$  ont été choisis en premier lieu pour vérifier les performances analytiques atteintes pour les électrodes Pt/noir-Pt et pour plusieurs raisons. Ce sont les espèces les plus stables chimiquement dans ces conditions physiologiques. Leurs potentiels d'oxydation couvrent toute la gamme de potentiels des espèces RNS/ROS intéressantes à étudier. De plus, ces deux espèces ont une forte tendance à passiver les électrodes.

La Figure Résumé-7A, -7B montre les voltamogrammes à l'état stationnaire obtenus pour une vitesse d'écoulement de  $2 \mu\text{L min}^{-1}$  et des solutions de  $0.1 \text{ mM H}_2\text{O}_2$  et  $0.1 \text{ mM NO}_2^-$ . L'activation électrochimique par sauts de potentiels alternés conduit à des résultats hautement reproductibles. Cependant, en comparaison avec des électrodes nues de platine, les avantages résultants de dépôts de noir de platine sont non seulement visibles à partir de l'amplification du courant mais aussi sur l'allure des voltamogrammes. Les courants de plateau suggèrent un régime stationnaire alors que les montées rapides en courant montrent un transfert d'électron rapide. A l'inverse, des pics de courants ont été observés aux électrodes nues en Pt pour les deux espèces étudiées, indiquant une plus faible activité de ces électrodes à plus hauts potentiels.

En réalisant plusieurs injections successives à potentiel constant, les électrodes Pt/noir-Pt ont montré une stabilité des mesures remarquables (Figure Résumé-7C) alors que les courants sur électrodes nues en Pt diminuent lors d'une injection et chutent de façon significative d'une injection à l'autre (Figure Résumé-7D).

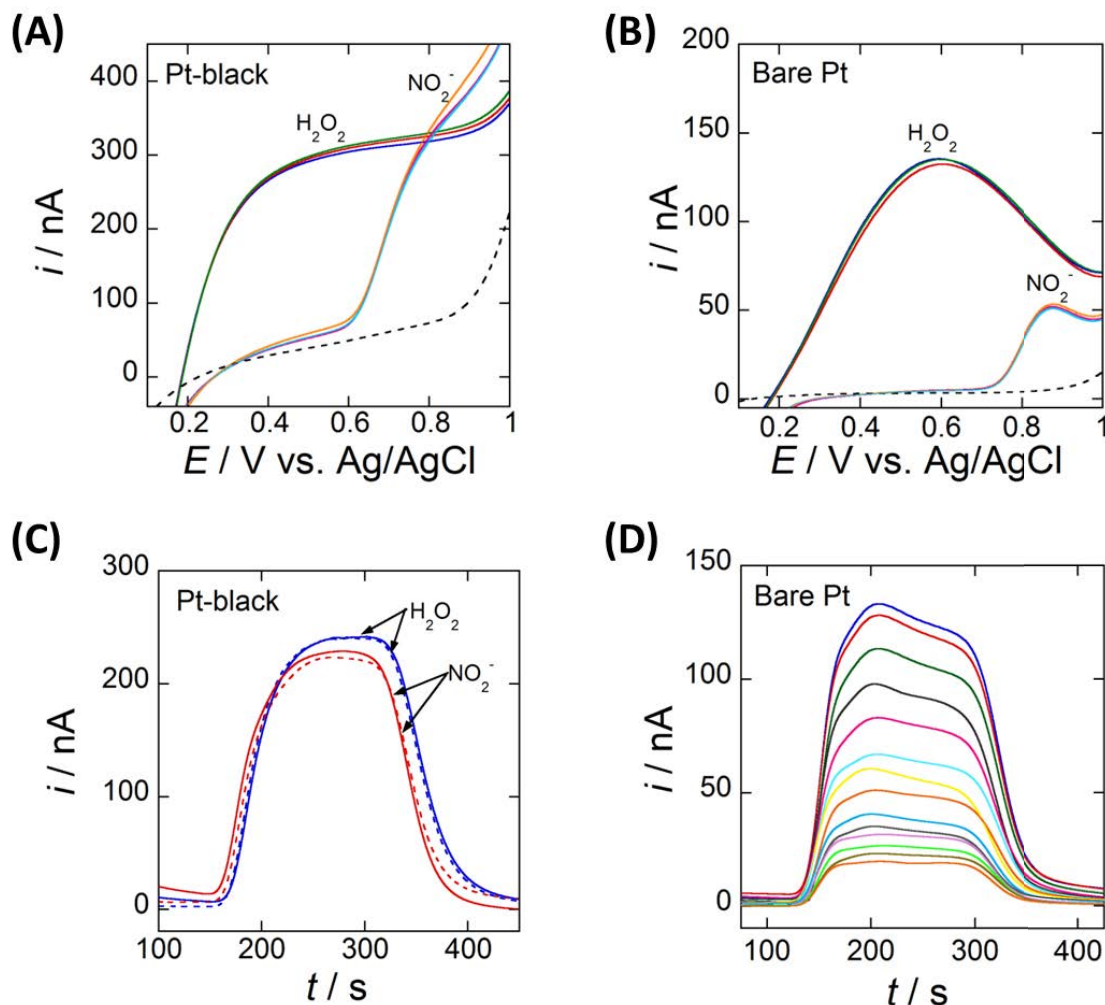


Figure Résumé-7: Voltammogrammes à l'état stationnaire à  $10 \text{ mV s}^{-1}$  dans un flux continu de  $0.1 \text{ mM H}_2\text{O}_2$  et  $0.1 \text{ mM NO}_2^-$  pour des électrodes (A) noir-Pt et (B) en Pt avec les courants résiduels du PBS (courbe en tiret). Chaque courbe en trait plein représente un voltammogramme d'une électrode microbande soit pour une électrode Pt/noir-Pt ou en Pt. (C) Réponses en courant de microinjections de  $5 \mu\text{L}$  de  $0.1 \text{ mM H}_2\text{O}_2$  ( $E = 0.45 \text{ V/REF}$ , courbes bleues) et  $0.1 \text{ mM NO}_2^-$  ( $E = 0.85 \text{ V/REF}$ , courbes rouges) à une électrode Pt/noir-Pt. Dans chaque cas, les courants sont représentés pour la première (courbe en trait plein) et la cinquième injection (courbe en tiret). (D) Variation de la réponse en courant après des injections répétitives de  $5 \mu\text{L}$  de  $0.1 \text{ mM H}_2\text{O}_2$  ( $E = 0.60 \text{ V/REF}$ ) à une électrode en Pt, de la première (en haut) à la quatorzième (en bas) injection.

Afin de mieux évaluer le transport de masse aux électrodes Pt/noir-Pt, les courants limites pour les deux espèces ont été tracés en fonction de la vitesse d'écoulement et ont été comparés aux prévisions issues de régimes convectifs stationnaires théoriques. (Figure Résumé-8).



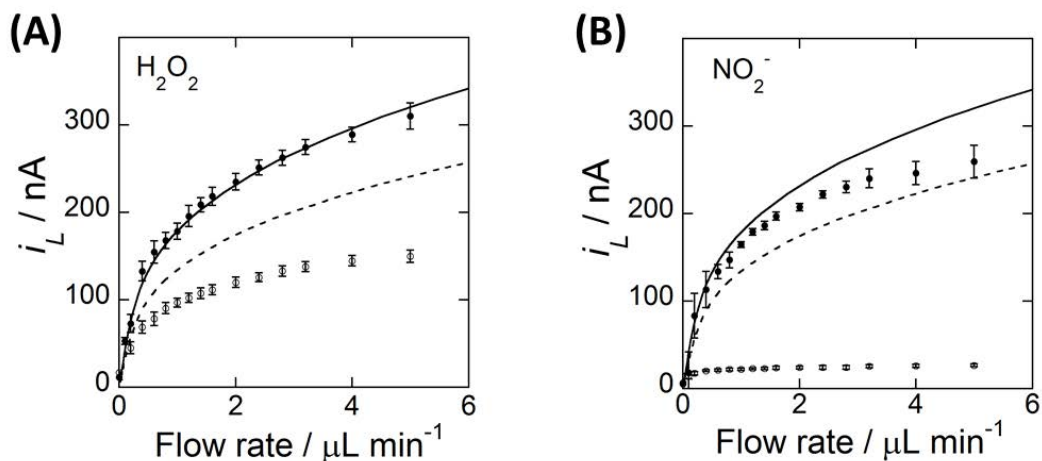


Figure Résumé-8: Comparaison entre courants limites théoriques et expérimentaux en fonction de la vitesse d'écoulement. (A) Détection de 0.1 mM  $\text{H}_2\text{O}_2$  sur électrodes Pt/noir-Pt ( $E = 0.45 \text{ V/REF}$ ) et électrodes en Pt ( $E = 0.6 \text{ V/REF}$ ). (B) Détection de 0.1 mM  $\text{NO}_2^-$  sur électrodes de noir-Pt ( $E = 0.85 \text{ V/REF}$ ) et électrodes en Pt ( $E = 0.9 \text{ V/REF}$ ). Dans (A, B), les courants expérimentaux sur électrodes Pt/noir-Pt (●) et électrodes en Pt (○) sont comparés avec les valeurs théoriques simulées avec  $D_{\text{H}_2\text{O}_2} = D_{\text{NO}_2^-} = 1.5 \times 10^{-5} \text{ cm}^2 \text{ s}^{-1}$ . (courbe en trait plein pour Pt/noir-Pt avec un facteur de surface active apparente de 1.3, courbe en tiret pour électrodes en Pt)

Il convient de noter que  $\text{H}_2\text{O}_2$  est oxydé par le biais de sites actifs  $\text{Pt}(\text{OH})_2$  générés électrochimiquement. Ce processus en lui-même est très rapide mais la vitesse de la réaction globale est inhibée par de l'adsorption compétitive ou oxydation ultérieure de sites actifs. Dans le cas de  $\text{NO}_2^-$ , une oxydation globale a lieu à travers une réaction de d'antidismutation du dioxyde d'azote. La vitesse du transfert d'électron diminue avec la formation de couches d'oxydes à la surface de platine.

Bien que les mécanismes soient fondamentalement différents, l'oxydation des deux espèces sur électrodes Pt/noir-Pt est contrôlée par les régimes du transport de masse. Ceci démontre qu'un nombre plus large de sites actifs à l'échelle nanométrique peut effectivement empêcher les effets d'inhibition/passivation et faciliter le transfert d'électron. Ainsi, l'adsorption passive d'espèces et la formation de sites de platine inactifs ne masquent pas l'activité globale de l'électrode sur la surface active apparente.

### 3. Détection *in vitro* de deux espèces instables : le peroxydinitrite et l'oxyde nitrique

#### Détection du peroxydinitrite

La décomposition rapide du peroxydinitrite à travers sa forme acide (ONOOH, pKa 6.8) rend sa détection extrêmement difficile dans les conditions physiologiques, mais la forme anionique est suffisamment stable en milieux alcalins (conformation *cis*). Les études en voltamétrie de solutions 0.1 mM ONOO<sup>-</sup> (Figure Résumé-9A) ont donc été réalisées à pH 11.1 pour évaluer la performance des électrodes sans changement significatif de la concentration durant les mesures électrochimiques.

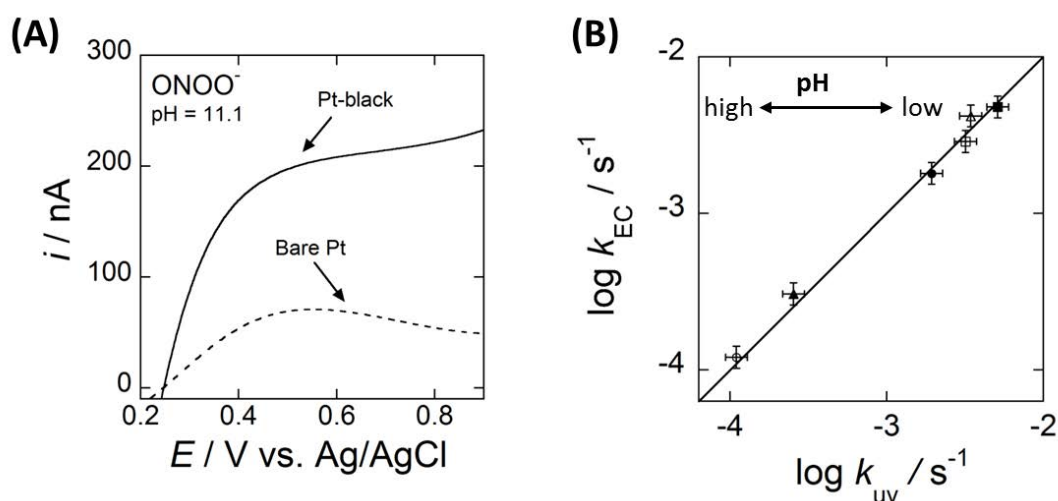


Figure Résumé-9: (A) Voltammogrammes obtenus pour des solutions circulantes de 0.1 mM ONOO<sup>-</sup> à des électrodes Pt/noir-Pt (courbe en trait plein) et électrodes en Pt (courbes en tiret) à pH 11.1 PBS. Vitesse de balayage 10 mV s<sup>-1</sup>. (B) Comparaison entre constantes cinétiques évaluées par détection électrochimique ( $k_{EC}$ ) et par analyses de spectres UV-Vis ( $k_{UV}$ ) à des temps n'excédant pas 200 s après la préparation de la solution. Dans (B), pH = 11.1 (○), 10.8 (▲), 10.2 (●), 9.4 (□), 8.9 (△) et 8.4 (■).

De façon similaire aux cas de H<sub>2</sub>O<sub>2</sub> et NO<sub>2</sub><sup>-</sup>, un régime stationnaire du transport de masse a été atteint pour des électrodes Pt/noir-Pt alors que des voltammogrammes sous forme de pics ont été observés à des électrodes nues en Pt avec des courants deux fois plus petits. La détection d'ONOO<sup>-</sup> a été de loin la plus performante avec des électrodes Pt/noir-Pt.

La cinétique de décomposition de ONOO<sup>-</sup> à des pH plus faibles a été alors évaluée à la fois par des mesures électrochimiques et par des spectres UV-Vis. Les résultats ont été consistants (Figure Résumé-9B) et ont de nouveau démontré la faisabilité et la fiabilité de la détection d'ONOO<sup>-</sup> sur noir de platine.



## Détection de l'oxyde nitrique

La performance de la détection de  $\text{NO}^{\bullet}$  a été évaluée par la génération dynamique de  $\text{NO}^{\bullet}$  à travers la décomposition de solutions de DEA-NONOate. Cependant, la concentration de  $\text{NO}^{\bullet}$  ne résulte pas seulement de la décomposition du donneur ( $k_1$ ) mais aussi d'une réaction compétitive entre  $\text{NO}^{\bullet}$  et l'oxygène ( $k_2$ ).

L'extraction du courant d'oxydation de  $\text{NO}^{\bullet}$  nécessite une correction par le courant résiduel. Une vague a été obtenue avec un maximum à  $E = 0.62$  V/REF (Figure Résumé-10A) contrairement à un plateau prévu sous régime stationnaire. Ce comportement peut être relié à la génération progressive d'espèces interférentes (dus principalement aux anions nitrites) durant le balayage de potentiel. Néanmoins, en comparaison avec les électrodes nues en Pt, les voltamogrammes corrigés ont montré une amplitude de courant 350 fois plus importante avec les dépôts en noir de platine.

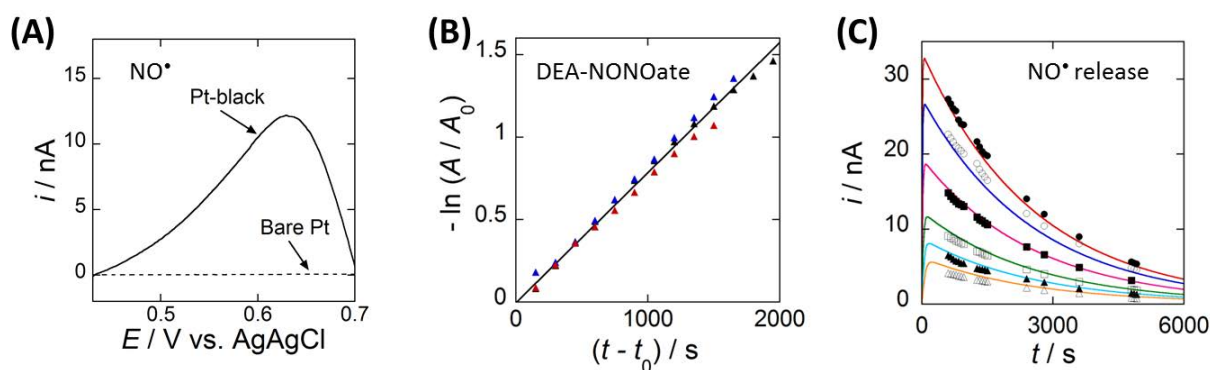


Figure Résumé-10: (A) Voltamogrammes corrigés du courant résiduel à des électrodes Pt/noir-Pt (courbe en trait plein) et nues en Pt (courbe en tiret) avec des mesures initiales effectuées 270 s après la préparation de la solution. (B) Analyses des intensités de pic UV-Vis pour trois séries de mesures dans des solutions de 0.1 mM DEA-NONOate à  $\text{pH} = 7.4$ .  $\lambda = 250$  nm,  $t_0 = 40$  s représente le point de départ des mesures après la préparation des solutions. Droite ajustée avec une pente égale à  $k_1 = 7.8 \times 10^{-4} \text{ s}^{-1}$ . (C) Courants en chronoampérométrie théoriques (courbes en trait plein) et expérimentaux (symboles) à des électrodes Pt/noir-Pt pour des concentrations variées de solutions circulantes de DEA-NONOate. De haut en bas : 1.5 (●), 1 (○), 0.5 (■), 0.2 (□), 0.1 (▲) et 0.05 mM (Δ). Ajustement de courbes avec  $k_1 = 7.8 \times 10^{-4} \text{ s}^{-1}$ ,  $k_2[\text{O}_2] = 5.5 \times 10^2 \text{ M}^{-1} \text{ s}^{-1}$  et  $i/[\text{NO}^{\bullet}] = 1.13 \times 10^3 \text{ A M}^{-1}$ .

En réalisant des séries de spectres UV-Vis, la vitesse de décomposition de DEA-NONOate a été suivie (Figure Résumé-10B) à travers la diminution de l'absorbance. Une valeur moyenne de  $k_1$  a été déterminée avec  $(7.8 \pm 0.5) \times 10^{-4} \text{ s}^{-1}$ . En introduisant cette valeur dans la cinétique de génération et de décomposition de  $\text{NO}^{\bullet}$ , la constante  $k_2$  a été évaluée à partir du meilleur ajustement d'une série de courbes chronoampérométriques enregistrées à 0.62 V/REF à plusieurs concentrations de solutions de DEA-NONOate (Figure Résumé-10C).

Il convient de souligner que le contrôle du transport de masse par convection de  $\text{NO}^\bullet$  à des électrodes Pt/noir-Pt a été une hypothèse de départ durant l'ajustement. Le fait que la valeur trouvée de  $k_2 = (2.2 \pm 0.4) \times 10^6 \text{ M}^{-2} \text{ s}^{-1}$  corresponde à celles de la littérature confirme notre hypothèse.

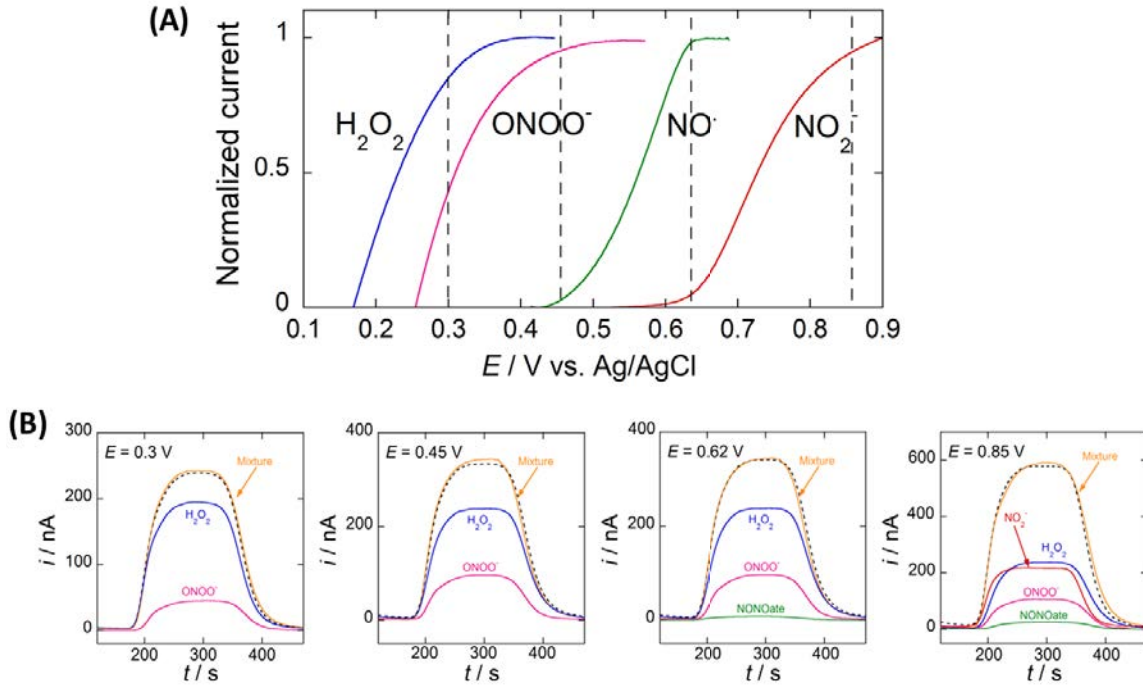
Ainsi, nos résultats ont montré que les microbandes optimisées de Pt/noir-Pt, offrent une meilleure sensibilité et fiabilité des réponses électrochimiques vis-à-vis des espèces ROS/RNS les plus intéressantes. Le détail des performances analytiques sont listées dans le tableau Table Résumé-1.

*Table Résumé-1: Performances analytiques de la détection des quatre espèces ROS/RNS sur électrodes microbandes de Pt/noir-Pt ( $w = 197 \mu\text{m}$ ) à l'intérieur de microcanaux ( $L = 200 \mu\text{m}$ ,  $h = 20 \mu\text{m}$ ) sous transport de masse contrôlé par la convection (vitesse d'écoulement =  $2 \mu\text{L min}^{-1}$ ).*

	Potentiel d'oxydation (V vs. Ag/AgCl)		Sensibilité ( $\text{A M}^{-1}\text{cm}^{-2}$ )	LOD (nM)	Linéarité
$\text{H}_2\text{O}_2$	0.45	0.3 (85%)	6.02	7	10 nM – 2.5 mM
$\text{ONOO}^-$		0.3 (43%)	2.64	40	50 nM – 5.0 mM
$\text{NO}^\bullet$	0.62		2.87	30	50 nM – 22 $\mu\text{M}$
$\text{NO}_2^-$	0.85		5.54	12	20 nM – 3.0 mM

#### 4. Détection de mélanges

Les courbes voltamétriques de  $\text{H}_2\text{O}_2$ ,  $\text{ONOO}^-$ ,  $\text{NO}^\bullet$  et  $\text{NO}_2^-$  ont été reportées et comparées sur la Figure Résumé-11A. Comme il peut être observé, l'oxydation de  $\text{H}_2\text{O}_2$  se superpose fortement avec celle de  $\text{ONOO}^-$  tandis que celles de  $\text{NO}^\bullet$  et de  $\text{NO}_2^-$  sont bien séparées des autres. Ainsi, quatre potentiels optimaux de détection ont été définis comme le montrent les lignes verticales en tiret. Ainsi, en réalisant à ces potentiels des séries de microinjections de mélanges (Figure Résumé-11B), un bon accord a été obtenu par additivité des courants sans qu'aucune réaction annexe ne soit observée.



Sur la base de ces résultats nous avons:

$$i_{0.30V} = 0.85i_{H_2O_2} + 0.43i_{ONOO^-} \quad (\text{Resume.1})$$

$$i_{0.45V} = i_{H_2O_2} + i_{ONOO^-} \quad (\text{Resume.2})$$

$$i_{0.62V} = i_{H_2O_2} + i_{ONOO^-} + i_{NO^\cdot} \quad (\text{Resume.3})$$

$$i_{0.85V} = i_{H_2O_2} + i_{ONOO^-} + i_{NO^\cdot} + i_{NO_2^-} \quad (\text{Resume.4})$$

Ceci démontre la possibilité d'évaluer les contributions des quatre espèces et par conséquent de détecter, caractériser et quantifier un mélange d'espèces ROS/RNS provenant de cellules vivantes.

## 5. Conclusion de la Partie B

Contrairement aux électrodes de platine nues, les électrodes en noir de platine permettent d'améliorer les performances analytiques de détections électrochimiques avec une stabilité sur de longues durées d'expérience pour les quatre espèces ROS/RNS (i.e.,  $\text{H}_2\text{O}_2$ ,  $\text{ONOO}^-$ ,  $\text{NO}^\bullet$ , et  $\text{NO}_2^-$ ). Ces avantages sont dus à un plus grand nombre de sites actifs sur la surface de l'électrode qui facilite le transfert d'électrons et empêche les effets de passivation ou d'inhibition d'électrode. Le processus de platinisation a été optimisé afin d'atteindre le rapport signal sur bruit le plus élevé tout en préservant la compatibilité des épaisseurs de dépôt avec les dispositifs microfluidiques. Parallèlement, l'activation des électrodes donne des résultats reproductibles, rendant ces électrodes facilement réutilisables.

Le transport de masse par convection à l'état stationnaire à l'intérieur de microcanaux nous a permis d'étudier les mécanismes d'oxydation ( $\text{H}_2\text{O}_2$  et  $\text{NO}_2^-$ ) et de décomposition ( $\text{ONOO}^-$  et  $\text{NO}^\bullet$ ). De plus, les détections ont été réalisées de façon satisfaisante dans le cas du mélange des quatre espèces. La composition des échantillons a pu être évaluée aux potentiels de détection sélectionnés. Ces résultats valident la possibilité d'effectuer des détections électrochimiques simultanées de ROS et RNS dans des dispositifs microfluidiques en utilisant des électrodes en noir de platine.

## *PARTIE C: Suivi du stress oxydant de cellules avec des électrodes Pt/noir-Pt intégrées dans des microsystèmes*

Dans cette partie, des dispositifs intégrant des électrodes Pt/noir-Pt ont été étudiés pour suivre l'émission d'espèces ROS/RNS à partir de cellules vivantes. En raison de la flexibilité des procédures de microfabrication, les espèces oxydantes issues d'une population de cellules ont été caractérisées à la fois par détection basale ou en aval d'une chambre de culture cellulaire.

### 1. Modèle cellulaire et méthode de stimulation

Les macrophages de type Murine Raw 264.7 constituent des modèles de laboratoires idéaux pour étudier le stress oxydant de cellules parce qu'ils sont robustes et présentent des

quantités abondantes d'enzymes permettant de générer des espèces ROS/RNS. Ils ont été choisis dans notre laboratoire pour effectuer des études antérieures sur cellules uniques. Pour faciliter les comparaisons, ils ont été utilisés dans nos expériences.

Dans cette étude, les macrophages ont été stimulés par du calcium ionophore A23187 parce que cet activateur permet d'effectuer de réelles stimulations de façon reproductible, en contournant les manipulations répétitives (dans le cas de pénétration mécanique) ou le long processus de transcription et reconnaissance (dans le cas d'immunostimulation).

## 2. Détection d'émission d'espèces oxydatives à partir de populations de cellules par détection basale

Inspiré par la configuration de synapse artificielle pour la détection de cellules uniques, nous avons développé ci-après un microdispositif PDMS-verre à l'intérieur duquel des électrodes microbandes en Pt/noir-Pt ont été placées juste en dessous de cellules émettrices (Figure Résumé-12). Les macrophages ont été confinés dans des chambres à proximité des électrodes de travail avec un nombre moyen de 1200 cellules adhérentes. Après stimulation, des mesures ampérométriques ont été faites simultanément à 0.30, 0.45, 0.62 et 0.85 V vs. Ag/AgCl à chaque électrode dans chacune des quatre chambres.

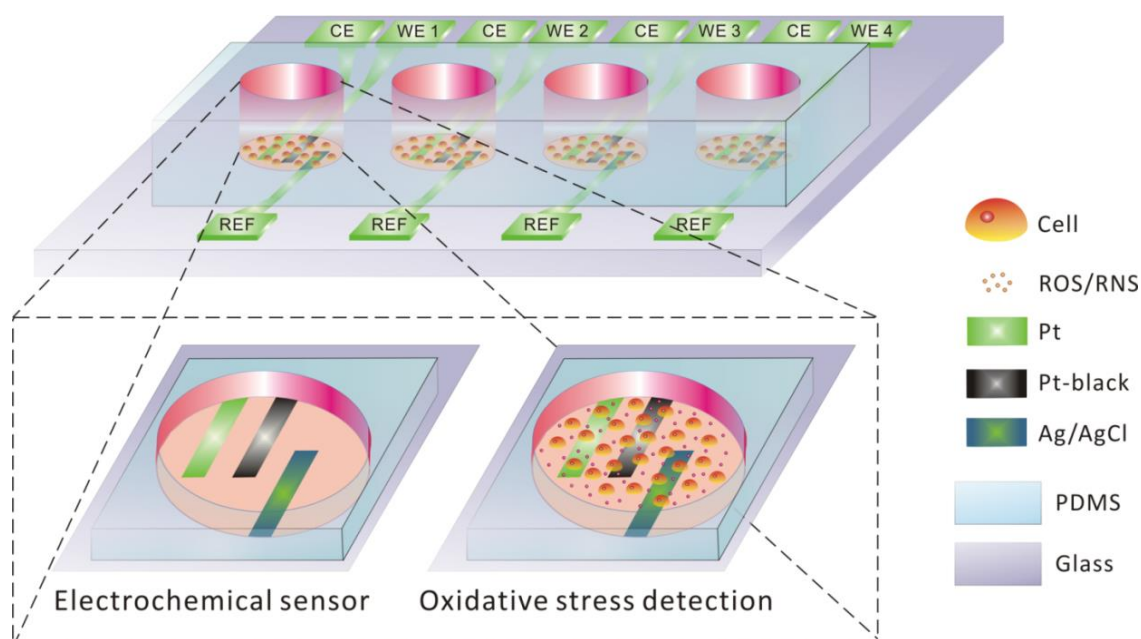


Figure Résumé-12: Illustration schématique des 4 chambres du microdispositif en PDMS-verre (figure du haut); et vues agrandies des électrodes microbandes CE, WE et REF à l'intérieur de chacune des chambres, avant (figure en bas à gauche) et durant la détection basale (figure en bas à droite).

L'amplitude des courants résultante augmente de façon significative avec le potentiel (Figure Résumé-13A), démontrant que plus d'espèces électroactives sont détectées à plus hauts potentiels. Cependant, la cinétique de relargage (réponse chronoampérométrique) est similaire dans chaque condition. Une augmentation immédiate après stimulation indique une activation rapide des enzymes, le maximum de l'intensité de courant étant atteint 5 minutes après stimulation avec une durée de relargage de 10 minutes environ. Des caractéristiques similaires ont été observées lors de la détection de cellules uniques dans une configuration de synapse artificielle, ce qui justifie a posteriori la configuration présente avec une détection basale sur des électrodes de Pt/noir-Pt.

Suivant la combinaison linéaire des courants détectés, des résultats ont pu être déduits à la fois sur la cinétique (flux temporels d'espèces) et sur les quantités d'espèces (quantité totale). Le relargage moyen par cellule évalué suivant une détection basale a été comparé avec les données de mesures effectuées sur cellules uniques (Figure Résumé-13B). La production des deux espèces stables  $\text{H}_2\text{O}_2$  et  $\text{NO}_2^-$  est similaire alors que celles de  $\text{NO}^\bullet$  et  $\text{ONOO}^-$  sont légèrement plus faibles. Cette différence peut provenir de possibles interactions entre cellules en raison de leur proximité, ou du mode de détection basale qui peut conduire à une plus faible efficacité de collecte à l'apex des cellules.

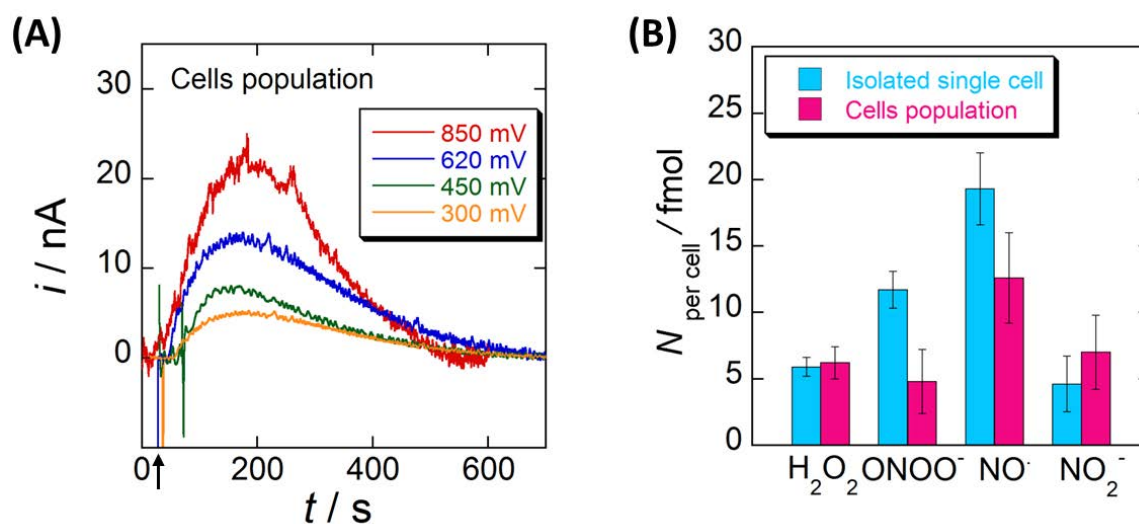


Figure Résumé-13: (A) Réponses ampérométriques simultanées de populations de cellules (c.a. 1200 cellules) après une stimulation par 10  $\mu\text{M}$  A23187. Quatre courbes sont enregistrées respectivement à 0.30, 0.45, 0.62 et 0.85 V vs. Ag/AgCl. La flèche noire sur l'axe x indique le temps lorsque A23187 est injecté pour initier le stress oxydant. (B) Comparaison du relargage de  $\text{H}_2\text{O}_2$ ,  $\text{ONOO}^-$ ,  $\text{NO}^\bullet$  et  $\text{NO}_2^-$  par cellule à partir de détections sur cellule unique (colonnes bleues) et à partir de populations de cellules avec détection basale (colonnes roses) après stimulation par 10  $\mu\text{M}$  A23187. Les données pour la détection sur cellule unique ont été obtenues après la réalisation de 20 – 30 expériences à chaque potentiel ( $n > 100$  expériences en tout); alors que seulement 5 mesures simultanées ont été faites à partir de populations de cellules.

Cependant, les résultats à partir de cellules uniques n'ont été fiables statistiquement qu'après avoir réalisé plus de 100 expériences individuelles (20 – 30 tests à chaque potentiel de détection) alors que les résultats correspondants pour une population de cellules ont été obtenus seulement après la combinaison de 5 expériences. Ce résultat montre que la détection basale doit être privilégiée pour des études biologiques élaborées mettant en jeu un grand nombre de conditions expérimentales et de paramètres.

En outre, la longue durée du signal enregistré et la détection simultanée de  $\text{H}_2\text{O}_2$ ,  $\text{ONOO}^-$  et  $\text{NO}^\bullet$  observées au cours de nos expériences montrent une activation simultanée de deux systèmes enzymatiques, c'est-à-dire des sites de NOS adjacents qui produisent  $\text{NO}^\bullet$ , et NADPH oxydase transmembranaire qui génère  $\text{O}_2^-$ . Après analyses des réponses, la production initiale de  $\text{O}_2^-$  et de  $\text{NO}^\bullet$  a été quantifiée respectivement aux alentours de 25 fmol et 27 fmol par macrophage lors d'une détection basale. Des quantités similaires et des cinétiques de production comparables ont été trouvées pour les deux espèces, ce qui suggère que les deux types de systèmes enzymatiques opèrent en tandem, en étant probablement couplés pour fournir une composition définie et stable de ROS/RNS durant le relargage.

### **3. Détection en aval de bouffées oxydantes à partir d'une population de cellules**

Afin de contourner les perturbations qui pourraient résulter d'un contact direct des cellules avec les électrodes de travail, nous avons conçu une autre configuration de dispositif PDMS-verre qui permet de séparer la zone de culture cellulaire de la zone de détection électrochimique. Comme décrit sur la Figure Résumé-14, les cellules sont immobilisées dans une chambre en amont. Les produits oxydants sont entraînés dans quatre canaux puis détectés séparément sur une électrode de travail. Chaque électrode est polarisée à un potentiel sélectionné (i.e., 0.30, 0.45, 0.62 ou 0.85 V vs. Ag/AgCl). Il faut souligner qu'à l'interface entre la microchambre et les microcanaux, un réseau de micropiliers a été incorporé ( $d = 50 \mu\text{m}$ , avec distance inter piliers  $10 \mu\text{m}$ ) pour empêcher les cellules de se déplacer de la chambre vers les microcanaux.



De la fibronectine a été prédéposée sur le substrat de verre pour faciliter l'adhésion des cellules et leur perfusion sur de longues durées. Une étude électrochimique a été réalisée après 12 à 24 h de culture cellulaire lorsque la population de cellules devient homogène en distribution avec une densité acceptable. Un calcul théorique montre qu'un nombre de cellules de  $3.5 \times 10^4$  est nécessaire dans la microchambre pour générer des espèces ROS/RNS en quantité suffisante après stimulation par de l'A23187.

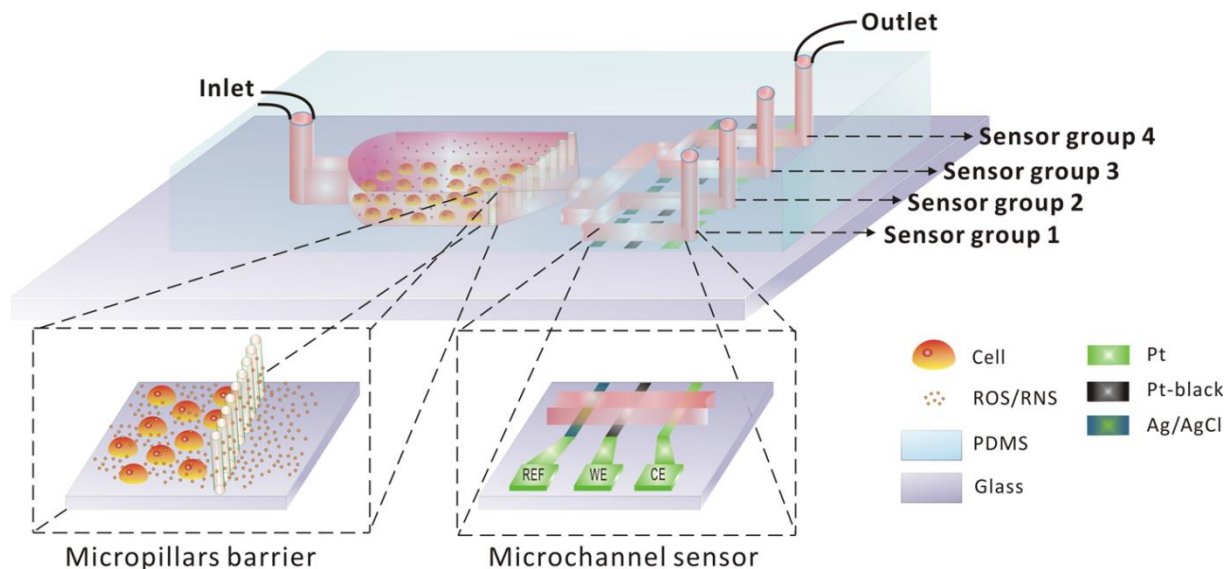


Figure Résumé-14: Illustration schématique de microdispositif PDMS-verre intégrant 4 canaux pour la détection en aval de bouffées oxydantes émises par une population de cellules. (figure du haut). Vues agrandies décrivant la barrière de micropiliers qui sépare les cellules de la zone de détection. (figure en bas à gauche), et le groupe d'électrodes REF, WE et CE insérées dans chacun des canaux (figure en bas à droite).

### Détection sous flux continu

Sous flux continu, les espèces ROS/RNS émises sont immédiatement transférées vers les électrodes situées en aval (en moins de 1 s, du bout de la chambre jusqu'aux électrodes). Les réponses enregistrées dans les 4 microcanaux sont reportées sur la Figure Résumé-15A. Les signaux présentent des formes similaires à celles obtenues avec une configuration de synapse ou encore avec une détection basale.

Les espèces ROS/RNS ont été évaluées à partir de la combinaison des courants mesurés dans chaque canal. Cependant, afin de réaliser cette opération, les courants ont été convertis en concentrations locales d'espèces en tenant compte du régime du transport de masse par convection. Ce calcul a été réalisé en utilisant les courbes de calibration reportées dans la partie B. Ainsi, la quantité moyenne d'espèces émise par cellule a été intégrée sur la



durée des signaux (Figure Résumé-15B). Dans cette configuration, les quantités de  $\text{ONOO}^-$  et  $\text{NO}^\bullet$  sont plus faibles en comparaison des valeurs obtenues sur cellule unique dans la configuration de synapse. Cependant, contrairement au mode de détection basale, ce résultat est probablement dû au délai de temps nécessaire aux espèces pour transiter des cellules vers les électrodes situées en aval. Malgré cet écart, la production de ROS/RNS (20 – 30 fmol par cellule) est suffisamment importante pour caractériser et quantifier les bouffées oxydantes à partir des populations de cellules. Les résultats traduisant le comportement moyen de c.a.  $3.5 \times 10^4$  cellules ont été obtenus durant une seule expérience. Les barres d'erreur indiquées sur la Figure Résumé-15B (sur les colonnes roses) décrivent les variations sur cinq groupes de cellules.

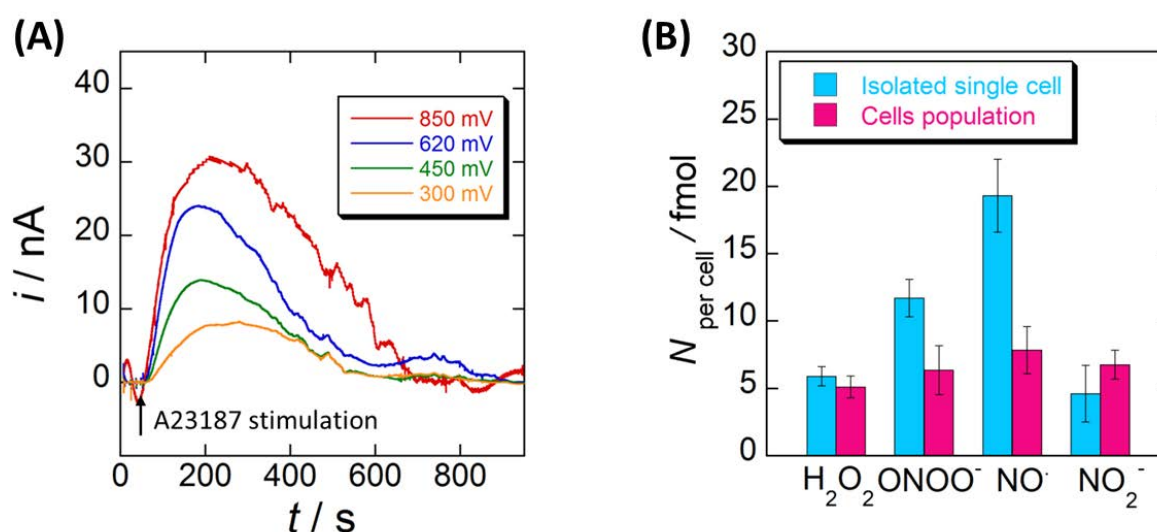


Figure Résumé-15: (A) Réponses ampérométriques simultanées à partir d'une population de cellules ( $3.5 \times 10^4$  cellules) après stimulation par  $10 \mu\text{M}$  A23187. Les quatre courbes sont respectivement enregistrées à 0.30, 0.45, 0.62 et 0.85 V vs. Ag/AgCl. La flèche noire sur l'axe x indique le moment où la solution A23187 est pompée à travers la chambre et les espèces transférées de la chambre vers les électrodes en aval. Vitesse d'écoulement =  $2 \mu\text{L min}^{-1}$  dans chaque canal. (B) Comparaison des quantités moyennes de  $\text{H}_2\text{O}_2$ ,  $\text{ONOO}^-$ ,  $\text{NO}^\bullet$  et  $\text{NO}_2^-$  relarguées par cellule à partir de détections sur cellule unique (colonnes bleues) et à partir de population de cellules (colonnes roses). Les données pour cellule unique ont été obtenues après la réalisation de 20 – 30 expériences à chaque potentiel ( $n > 100$  expériences au total alors que 5 expériences ont été seulement menées pour les populations de cellules).

Des stimulations successives ont été aussi réalisées avec le présent dispositif. Comme il est montré sur la Figure Résumé-16, des réponses hautement reproductibles sur trois stimulations successives ont montré le bénéfice de cette configuration. Aucune perturbation du comportement cellulaire n'a été observée, ni même une altération des réponses des électrodes.

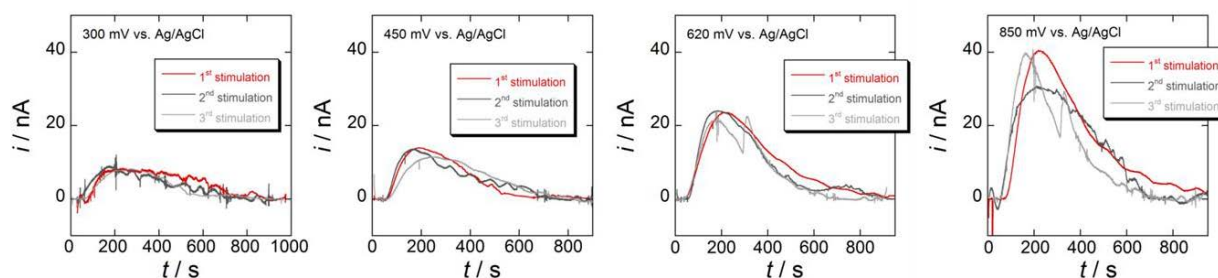


Figure Résumé-16: Stimulation successive par  $10 \mu\text{M}$  A23187 à partir d'une même population de c.a.  $3.5 \times 10^4$  macrophages immobilisés dans la microchambre. Les réponses ampérométriques ont été enregistrées aux potentiels de 0.30, 0.45, 0.62 et 0.85 V vs. Ag/AgCl dans les microcanaux. Entre chaque stimulation, un intervalle de 10 minutes a été fixé pour restaurer l'activité des cellules.

### Détection par arrêt de l'écoulement

La détection en aval des populations de cellules a également été menée par arrêt de l'écoulement (mode stop flow) 10 min pendant la phase de stimulation. La production d'espèces oxydantes a été ainsi accumulée dans la microchambre pendant cette durée puis transférée rapidement vers les microcanaux en aval pour y être détectée.

Un résultat typique est montré sur la Figure Résumé-17A. Des courants faradiques bien plus élevés ont été mesurés sur une courte période en comparaison des mesures effectuées en flux continu. Cette observation a confirmé la concentration plus élevée des espèces due à leur confinement et suite à l'arrêt de l'écoulement durant la phase de stimulation. Une autre différence notable est la diminution drastique des réponses observées après plusieurs stimulations répétées (Figure Résumé-17B). Une influence sur l'activité des cellules par les espèces ROS/RNS accumulées localement est probablement à l'origine de ce phénomène.

L'évaluation sur les réponses des contributions de chaque espèce est donnée Figure Résumé-17C. Les détections de  $\text{ONOO}^-$  et  $\text{NO}^\bullet$  n'ont pas été possibles car le délai de temps est trop long par rapport à leur très faible durée de vie (quelques secondes). Ces deux espèces hautement réactives ont dû être converties en  $\text{NO}_2^-$ , ce qui explique notamment la réponse plus élevée du signal de  $\text{NO}_2^-$  par rapport aux mesures réalisées en flux continu. A ce niveau, on ne peut donc pas mesurer les quantités de  $\text{ONOO}^-$  et  $\text{NO}^\bullet$  émises. Cependant, une quantification à partir des deux espèces les plus stables (e.g.,  $\text{H}_2\text{O}_2$  et  $\text{NO}_2^-$ ) est toujours possible en tenant compte de leur décomposition sur la période de temps considérée.

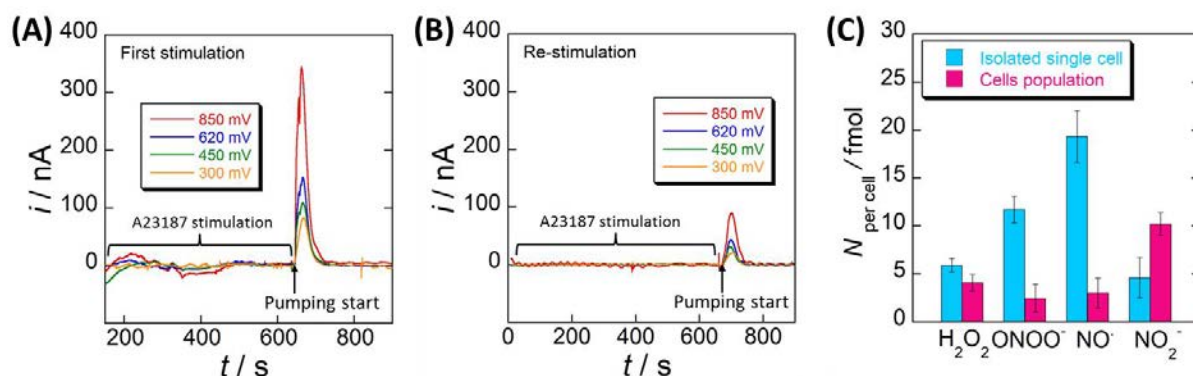


Figure Résumé-17: Réponses ampérométriques enregistrées après stimulation par une solution de  $10 \mu M$  A23187 d'une population de c.a.  $3.5 \times 10^4$  cellules avec une accumulation dans la microchambre pendant 10 min. Les réponses représentatives sont données en (A) après la première stimulation et en (B) après la seconde stimulation. Les électrodes ont été polarisées respectivement à 0.30, 0.45, 0.62 et 0.85 V vs. Ag/AgCl. La flèche noire sur l'axe des x indique le moment où la solution est transférée de la chambre vers les microcanaux. Vitesse d'écoulement =  $8 \mu L \min^{-1}$  à l'entrée du dispositif. (C) Relargage moyen par cellule de  $H_2O_2$ ,  $ONOO^-$ ,  $NO^0$  et  $NO_2^-$  durant la stimulation de la population de cellules (colonnes roses). Les données sur cellule unique (colonnes bleues) ont été obtenues après avoir réalisé 20 – 30 expériences à chaque potentiel ( $n > 100$  expériences en tout) alors que 5 expériences ont été menées pour la population de cellules.

Ainsi, cette dernière configuration devrait permettre de réaliser une plateforme microfluidique avec des détections performantes menées en parallèle pour des études biologiques complexes, à la fois sous flux continu ou avec arrêt d'écoulement suivant le type d'application envisagé.

#### 4. Conclusion de la Partie C

En bénéficiant des performances analytiques des électrodes Pt/noir-Pt dans un environnement microfluidique, des dispositifs incorporant ces électrodes ont été conçus pour étudier le stress oxydant à partir de populations de macrophages. Le mode de détection basale a procuré des résultats reproductibles tant au niveau des quantités d'espèces ROS/RNS relarguées qu'au niveau des flux émis. Cependant, ce mode de détection semble présenter deux inconvénients majeurs qui sont d'une part une perte de collecte des espèces émises à l'apex des cellules et d'autre part une perturbation de l'activité des cellules par leur contact direct avec les électrodes polarisées. La séparation de la zone où se situent les cellules de celle de la détection semble la meilleure solution pour contourner ces effets. Cependant, cela conduit inévitablement à un temps de transport plus long entre le point où sont émises les espèces et celui où sont situées les électrodes. Une sous-estimation des quantités des deux

espèces les plus réactives (i.e.,  $\text{ONOO}^-$  et  $\text{NO}^*$ ) est observée en comparaison de détections sur cellule unique. Toutefois, il faut noter que ces résultats s'avèrent dans ces conditions hautement reproductibles et par conséquent incontournables s'il s'agit de comprendre le comportement d'une population de cellules à différentes étapes clés de l'émission.

Un point important qui doit être souligné ici est qu'un microsystème n'est performant que pour étudier des événements sous des conditions spécifiques, i.e., résolution temporelle, évaluation des quantités détectées, caractérisation des espèces à l'origine des événements initiés. Dans ce cadre, la configuration de synapse artificielle offre le meilleur choix pour les performances analytiques atteintes. Cependant, d'autres performances peuvent être requises dans le contexte d'études biologiques de grand intérêt comme l'évaluation des effets de principes actifs sous différentes conditions mettant en jeu de nombreux paramètres. C'est pourquoi, le dispositif qui sépare une population de cellules de la zone de détection présente certains avantages.

## ***Conclusion générale et perspectives***

L'objectif de ce travail a été de développer des dispositifs microfluidiques pour détecter de multiples espèces oxydantes émises par des cellules vivantes. L'idée principale était de contourner les expériences répétitives et fastidieuses de détections habituellement menées sur cellules uniques avec une configuration de synapse artificielle. En utilisant des dispositifs microfluidiques permettant la culture de cellules et leur manipulation, la détection simultanée des espèces peut être réalisée suivant des procédures menées en parallèle et automatisées. Les technologies standards de microfabrication ont été utilisées pour élaborer plusieurs dispositifs correspondant à différentes finalités. Avec l'intégration d'électrodes microbandes, des détections à la fois *in vitro* de solutions synthétiques et *ex vivo* de bouffées oxydantes émises par des cellules vivantes ont été réalisées.

Les performances analytiques d'électrodes Pt/noir-Pt vis à vis de quatre espèces clés (i.e.,  $\text{H}_2\text{O}_2$ ,  $\text{ONOO}^-$ ,  $\text{NO}^\bullet$ , et  $\text{NO}_2^-$ ) ont été étudiées et optimisées en premier lieu. En raison d'un grand nombre de sites actifs de platine à l'échelle nanométrique, l'efficacité et la stabilité à long terme des réponses électrochimiques ont été obtenues à l'intérieur de microcanaux. Les mécanismes d'oxydation incluant les cinétiques de décomposition ont été étudiés sur la base de prédictions théoriques. De larges gammes de concentration et des sensibilités élevées ont été évaluées. La sélectivité des détections a été atteinte en fixant précisément les potentiels de détection. Dans une dernière partie, les électrodes ont été intégrées dans des microdispositifs élaborés pour suivre l'émission de bouffées oxydantes de macrophages. Les microélectrodes ont été placées pour effectuer une détection basale ou encore une détection en aval des cellules. Les électrodes situées en dessous des cellules procurent une résolution temporelle élevée alors que les électrodes situées en aval permettent un suivi sans perturbation du comportement cellulaire. Malgré une plus faible efficacité de collecte dans le cas des espèces hautement réactives, les quantités globales détectées ont toutefois été comparables à la configuration utilisée pour une détection sur cellule unique. Des résultats reproductibles et statistiquement viables ont été obtenus en seulement quelques expériences.

En conclusion, le couplage dans ce domaine d'étude de la microfluidique avec une détection électrochimique est très prometteur. En élaborant plusieurs configurations, des détections multiples d'espèces peuvent être réalisées à partir de populations de cellules en quelques expériences seulement. En perspective, des dispositifs plus sophistiqués seront certainement élaborés intégrant des procédés totalement automatisés pour la réalisation de mesures à haut débit.

## *General introduction*



## General introduction

Life science is more and more solicited by modern societal demands. This is why investigations on living cells and subcellular messengers develop increasingly to give a deep understanding of complex life phenomena. Among metabolic situations of interest, oxidative stress is one that appears ubiquitous in the whole life process. It can be initiated by radiation, air pollution, smoking, virus or bacteria. During oxidative stress, a family of reactive oxygen species (ROS) and reactive nitrogen species (RNS) are formed under complex imbrication pathways. They work together to regulate vital physiological functions. However, they can also be potent mediators that trigger cellular damages when the release exceeds antioxidant capability.

Due to the subtle generation and transient existence of these active candidates, high-performance detection methods are required. Among these methods, electrochemistry offers a direct and label-free approach owing to the intrinsic electroactive properties of some ROS and RNS. In this context, microelectrodes provide new scope and opportunities to explore living cells *ex/in vivo* according to their well-known properties: (i) fast responses; (ii) high signal-to-noise ratio and (iii) high spatial resolution. By approaching a microelectrode to the emitting surface of an isolated living cell, excellent temporal resolution, sensitivity and collection efficiency are achieved due to the confined space and high concentration of species released locally. Based on this artificial synaptic configuration, our group has previously studied extensively the oxidative stress from single cells. Four key oxidative compounds (i.e.,  $\text{H}_2\text{O}_2$ ,  $\text{NO}^\bullet$ ,  $\text{ONOO}^-$ , and  $\text{NO}_2^-$ ) were identified, and their releases were analyzed dynamically. However, due to some differences in cells behaviors at the single-cell level, statistically reliable results often require fastidious and repetitive experiments (long time duration of measurements, complications in experimental part, intense human labors, etc.).

To overcome these difficulties, we wanted hereafter to take benefit of microfluidics to ease and optimize the analysis of RNS/ROS released from populations of cells. Indeed, microfluidics offers new opportunities in biological studies to grow, manipulate and monitor living cells. Dimensions of microfluidics components match well with biological scales.



Advanced and standard microfabrication technologies, such as photolithography, enable flexible designs of microdevices with the use of biocompatible materials such as PDMS (polydimethylsiloxane). Furthermore, fluidic features inside microchips allow also to automatize the entire bioanalytical experiment. Therefore, after the versatile implementation of ultrasensitive microelectrodes into these “all-in-one” devices, high-throughput analysis of ROS and RNS are expected with high performances and low consumptions of materials.

However, before the development of such highly-effective microdevices, preliminary studies are required to optimize the electrode performances within microfluidic channels. This is the context in which the present work takes place. In order to enhance the sensitivity of the electrochemical detection, deposition of Pt-black films onto microbands will be investigated. Pt-black deposits are expected to prevent electrode inhibitions and to improve the stability of the measurements. Under such configurations, performances of the Pt/Pt-black microband electrodes towards  $\text{H}_2\text{O}_2$ ,  $\text{NO}^\bullet$ ,  $\text{ONOO}^-$ , and  $\text{NO}_2^-$  will benefit also from convective mass transport above the electrodes.

Therefore, to achieve our goal, we will mainly focus on: (i) the optimized fabrication of Pt/Pt-black microelectrodes and assessment of their analytical performances towards interested ROS/RNS *in vitro*, and (ii) the simultaneous monitoring of these oxidative species from living cells in more elaborated devices. The manuscript is then organized in the following way:

In **Part A**, we report the state-of-the-art of research advances in this domain. The generation of ROS/RNS cocktails and their ambivalent roles in life process are first recalled. Detection methods and their analytical performances are then summarized and discussed. Particular attention is paid on existing electrochemical methods. Methodologies for detecting single-cell events or population of cells are summarized. Details about cell culture, manipulation and monitoring in microfluidic system are also described.

In **Part B**, the fabrication of Pt-black deposits onto Pt microband electrodes is optimized for subsequent integration within microfluidic device by considering various electrodeposition conditions. The analytical performances towards individual *in vitro* solutions of  $\text{H}_2\text{O}_2$ ,  $\text{NO}^\bullet$ ,  $\text{ONOO}^-$ , and  $\text{NO}_2^-$  are evaluated by comparing experimental results with theoretical mass transport regimes. The electrochemical performances are then studied over a wide range of applied potentials and compared to data obtained from bare Pt electrodes. Steady-state currents are also investigated to confirm the mechanisms and evaluate the

kinetics. Finally the mixtures of four synthetic solutions are studied for performing simultaneous detections.

In the last **Part C**, two configurations of microelectrodes-integrated devices are considered to perform simultaneous *ex vivo* detections of oxidative products released by cells population. Parallel Pt/Pt-black microband electrodes are localized either directly beneath living cells within culture chamber, or at the downstream channels to avoid any disturbance between sensors and cells. Experimental results from both configurations are discussed kinetically and quantitatively. They are compared with the ones obtained from the synaptic configuration with single cells. Devices biocompatibility, reproducibility and long-term reuse are also investigated. Finally, the statistical results are compared with data reported in literature to assess the analytical performances towards these species.



*PART A: State-of-the-art*



## **PART A: State-of-the-art**

### **1. Oxidative stress and reactive oxygen/nitrogen species (ROS/RNS)**

#### **1.1. Natural process of oxidative stress**

Aerobic organisms require oxygen ( $O_2$ ) during energy supplementation. Paradoxically,  $O_2$  is meanwhile a permanent threat since it allows continuous production of highly reactive radicals that might jeopardize physiological functions.

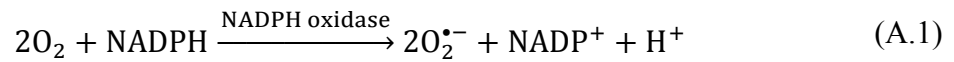
The general oxidative stress family in terms of reactive oxygen species (ROS) and reactive nitrogen species (RNS) comprises a variety of hazardous substances, including hydrogen peroxide ( $H_2O_2$ ), hydroxyl radical ( $OH^\bullet$ ), hydroperoxyl radical ( $HO_2^\bullet$ ), peroxy radical ( $ROO^\bullet$ ), peroxyxynitrite ( $ONOO^-$ ), nitrite ( $NO_2^-$ ), nitrogen dioxide ( $NO_2^\bullet$ ), dinitrogen trioxide ( $N_2O_3$ ), nitrosonium cation ( $NO^+$ ), etc. [1]. Nevertheless, these secondary species are mainly from two precursors, namely superoxide ion ( $O_2^{\bullet-}$ ) and nitric oxide ( $NO^\bullet$ ).

ROS/RNS generation may be initiated by radiation, air pollution, smoking, or even by invading virus or bacteria. Moderate produce is usually suppressed by protection complexes (e.g., catalase, glutathione peroxidase, superoxide dismutase, and vitamin C). However, when the release uncontrolledly exceeds antioxidant capability, critical oxidative stress prevails, tending to irreversibly convert neighboring biological components and amplify cell damages.

Two specific enzyme families, beside the normal metabolism in respiratory chain, are responsible for mass generation of oxidative bursts.

Nicotinamide adenine dinucleotide phosphate (reduced form: NADPH) oxidases and superoxide anion

During oxidative stress, larger quantities of  $O_2^{\bullet-}$  are produced with membrane-bound enzymatic complexes: NADPH oxidases:



As shown in Figure A-1, activation of classical NADPH oxidase (NOX2) needs assembly of cytosolic and integral membrane proteins to form a multi-subunit complex (i.e., gp91<sup>phox</sup> and p22<sup>phox</sup> accompanied with translocation of p40<sup>phox</sup>, p47<sup>phox</sup>, p67<sup>phox</sup> and a small GTPase-Rac2) [2]. Defects in any cofactor will lead to an inactivate NADPH oxidase, and no mass production of  $O_2^{\bullet-}$  will be observed.

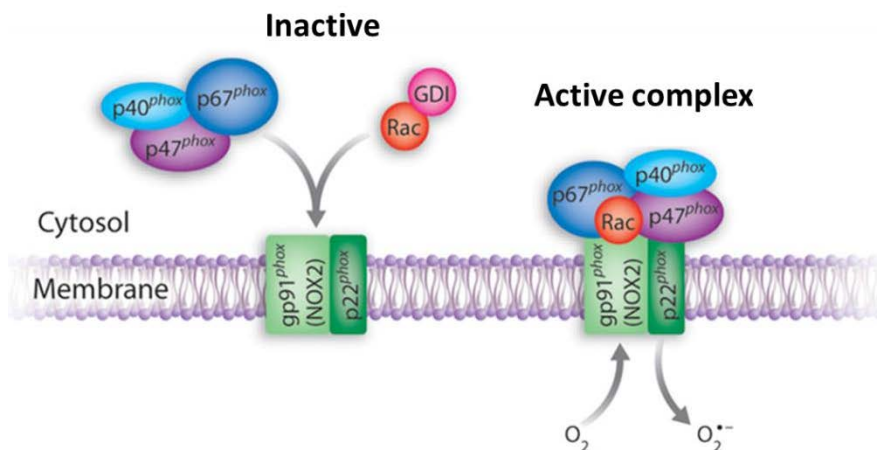


Figure A-1: Model of NADPH oxidase activation [2]. Cytosolic phox proteins and Rac translocate to the phagosomal or plasma membrane, generating active  $O_2^{\bullet-}$  from oxygen resources.

This classical NADPH oxidase was first described in phagocytes such as neutrophils and macrophages, originally thought only for host defense. However, studies over the past two decades indicate that several homologs (NOX1, NOX3–5, and DUOX1–2) are also present in a wide range of non-phagocytic cells. More recently, the resources of  $O_2^{\bullet-}$  further extend to intracellular mitochondria and endoplasmic reticulum.

## Nitric oxide synthases (NOS) and nitric oxide

The other precursor ( $\text{NO}^{\bullet}$ ) is synthesized from L-arginine in a reaction catalyzed by NOS. NADPH and oxygen are also involved during this process [3].

These enzymes are active only as dimers (Figure A-2), with essential cofactors tetrahydrobiopterin ( $\text{BH}_4$ ), haem, flavin mononucleotide (FMN) and flavin adenine dinucleotide (FAD). Electron transfers from reductase-domain flavins to oxygenase-domain haem to complete reaction, and the bound calmodulin is thought to further enhance this transfer rate.

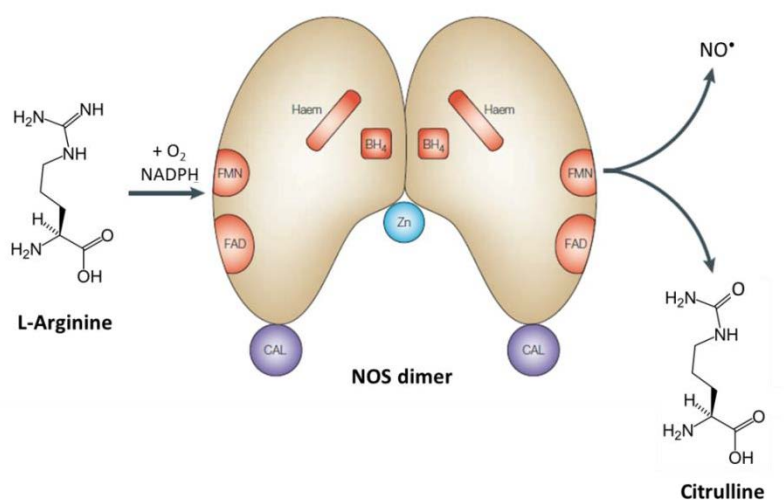


Figure A-2: The NOS dimer catalyzes oxidation of L-arginine to citrulline and  $\text{NO}^{\bullet}$  in presence of oxygen and NADPH [3].

Different NOS isoforms have been identified according to cell type or conditions in which they were first described [4]:

- Neuronal NOS (nNOS or NOS1) is the first nitric oxide synthase to be cloned from peripheral nerves. It has the most complex genomic organization in humans with multiple splice variants being produced. Its activity is controlled by intracellular calcium changes.
- Inducible NOS (iNOS or NOS2) from macrophages is tightly bound to calmodulin. Unlike nNOS, it is strongly induced by proinflammatory stimuli rather than changes of calcium concentration. However, this enzyme produces  $\text{NO}^{\bullet}$  at a less substantial rate as compared to the other isoforms.

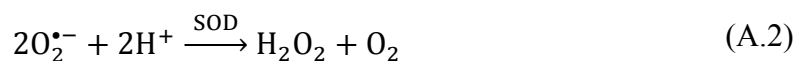


- Endothelial NOS (eNOS or NOS3) is later cloned from cardiovascular system and is a constitutive isoform located to the plasma membranes. It is strongly activated by entry of calcium and is also regulated by phosphorylation.
- Mitochondrial NOS (mtNOS) is recently described to play an important role in modulating mitochondrial respiration of cells from liver, brain and kidney. It is also responsive to calcium concentration in the matrix.

### Derived family of ROS and RNS

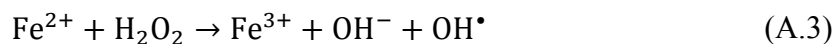
From the two primary species:  $O_2^{\bullet-}$  and  $NO^{\bullet}$ , diverse active substances are generated afterwards.

Under physiological conditions, the  $O_2^{\bullet-}$  is readily scavenged through the natural disproportionation into hydrogen peroxide and oxygen ( $k = 2 \times 10^5 \text{ M}^{-1} \text{ s}^{-1}$  at  $25^\circ\text{C}$ ); nevertheless, in mammalian aerobic cells, this process is even accelerated by superoxide dismutase (SOD,  $k = 2.5 \times 10^9 \text{ M}^{-1} \text{ s}^{-1}$  at  $25^\circ\text{C}$ ) [5]:



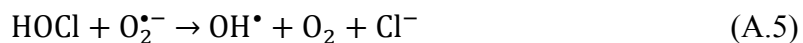
There are two main types of SOD, present respectively in mitochondria (manganese type: Mn SOD); or in cytoplasm and membranes (copper and zinc type: Cu/Zn SOD). Therefore,  $H_2O_2$  can be synthesized almost everywhere in and out of the living cells.  $H_2O_2$  is not a free radical but is considered a more potent cytotoxic chemical since the long lifetime allows its diffusion to any cellular compartment.

Moreover,  $H_2O_2$  contributes to generation of very toxic hydroxyl radical ( $OH^{\bullet}$ ) at the presence of ferrous ion (via the last step of Fenton reaction) [6]:

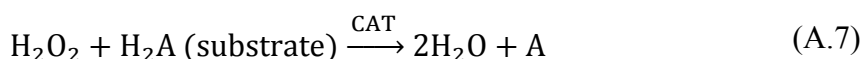


$OH^{\bullet}$  can only diffuse less than the diameter of a typical protein; however, it is the best hydrogen atom acceptor that reacts with almost every biological molecule. Another  $OH^{\bullet}$  generation pathway (at the presence of myeloperoxidase (MPO) and chloride), is even more harmful, because one of the strongest oxidant hypochlorous acid (HOCl) is formed as an intermediate [7]:



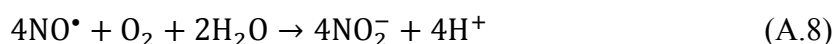


To prevent extensive generation of these lethal products, some antioxidant molecules thus play the protective roles. For instance, catalase (CAT), exists in every cell, can convert  $\text{H}_2\text{O}_2$  into water (Equation (A.6)) or use  $\text{H}_2\text{O}_2$  to detoxify other substances (Equation (A.7)) [6]:



These processes are essential for limiting oxidative damages,  $\text{H}_2\text{O}_2$  concentration is then maintained at nanomolar levels.

$\text{NO}^{\bullet}$  is an omnipresent and hydrophobic messenger that travels freely across cell membranes.  $\text{NO}^{\bullet}$  itself is a weak oxidant which is expected to react with oxygen ( $k = 2 \times 10^6 \text{ M}^{-1} \text{ s}^{-1}$ ) to form  $\text{NO}_2^-$  [5]:

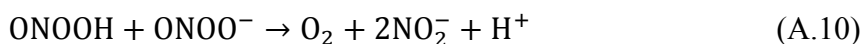


However, once it collides with  $\text{O}_2^{\bullet-}$  in the vicinity (a few cell diameters), they couple extremely fast (at diffusion-limited rate:  $k = 2 \times 10^{10} \text{ M}^{-1} \text{ s}^{-1}$ ) to form a powerful oxidant peroxyntirite ( $\text{ONOO}^-$ ):

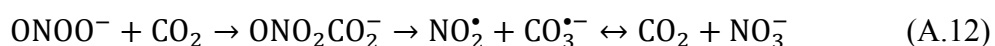


In contrast to  $\text{OH}^{\bullet}$ , peroxyntirite can diffuse quite far on a cellular scale. Accordingly, it possesses a better selectivity towards target components (nucleic acids, lipids and thiol groups) and has more subtle actions on cells.

At physiological pH, peroxyntirite is unstable and decomposes through its conjugated acid  $\text{ONOOH}$  into ions  $\text{NO}_2^-$  and  $\text{NO}_3^-$  [8]:



On the other side, reaction between  $\text{ONOO}^-$  and  $\text{CO}_2$  ( $k = 3 - 6 \times 10^4 \text{ M}^{-1} \text{ s}^{-1}$ ) may compete the main decomposition route, especially in blood since  $\text{CO}_2$  concentration is considerably high there (12 – 30 mM). This process gives short-lived intermediate species nitrosoperoxycarbonate ( $\text{ONO}_2\text{CO}_2^-$ ), ending up into potent nitrating radical  $\text{NO}_2^{\bullet}$  and carboxylating radical  $\text{CO}_3^{\bullet-}$  [9]:



Nitrogen and oxygen can exist in various redox states and lead to perplexing biochemical pathways. The very intricate chemistry originated from  $O_2^{\bullet-}$  and  $NO^{\bullet}$  is depicted in Figure A-3, marked with several important derivatives.

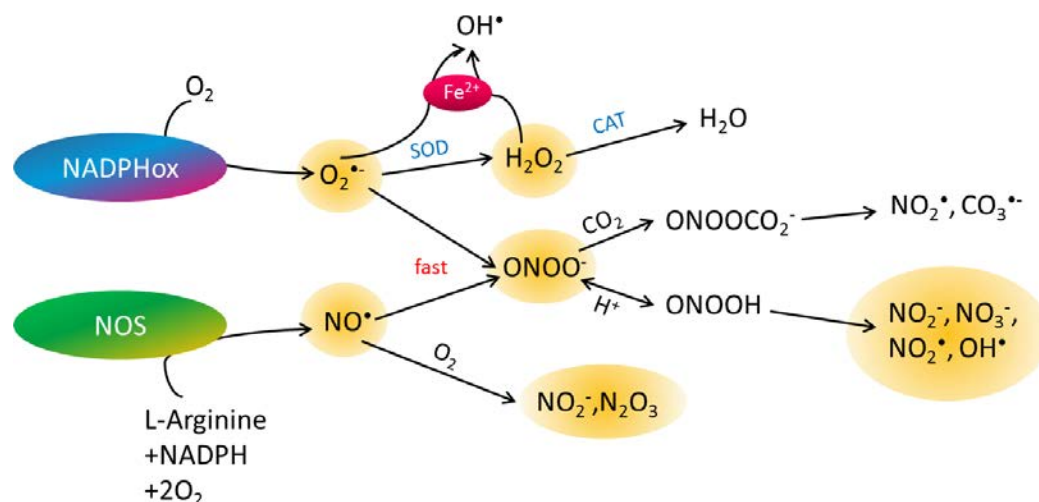


Figure A-3: Scheme of the main routes of ROS/RNS generation from primary superoxide ion and nitric oxide.

## 1.2. Roles of ROS/RNS in life

The imbrication of ROS/RNS metabolism appears ubiquitous in the whole life process. Indeed, their roles in biological activities are quite complex and ambivalent. They can regulate metabolic signaling; whereas can also be potent mediators that trigger cellular damages.

These contrasting effects may come from collaboration of several ROS and RNS; or only from one species as a function of its concentration and local condition. For instance, endogenous  $NO^{\bullet}$  can promote (low concentrations) or inhibit (high concentrations) apoptosis, kill tumors or increase metastasis, relieve or enhance damages after stroke [3]. The controversial role of ROS/RNS is one of the most popular topics in physiological and pathological community; and the following content shows some essential affects in living systems.

### 1.2.1. Beneficial effects

#### Host immunity

The primary function of phagocyte ROS is the defense against invading microorganisms, such as microbes, viruses, and even foreign antigens. During phagocytosis (Figure A-4A), NADPH oxidase are activated to generate microbicidal ROS. Rather than pure  $O_2^-$ , some secondarily derived metabolites such as  $H_2O_2$ ,  $OH^\bullet$  and  $HOCl$  probably contribute more in the host immunity [10]. Efficiency of phagocytosis and ROS production is further augmented if microbes are opsonized with host serum proteins (e.g., antibody or complement). If some defects lead to inactivated NADPH oxidase, accumulation of phagocytes unable to kill ingested pathogens is likely to provoke inflammations.

#### Regulation of vasodilatation

Maintenance of blood pressure is of a great importance since the deviations from normal level could be life-threatening.  $NO^\bullet$  is well recognized as one key relaxation factor synthesized by endothelial cells on the interior wall of blood vessels. Benefited from its fast diffusing and the free permeability to membranes,  $NO^\bullet$  then activates guanylate cyclase (GC) in surrounding smooth muscle cells to generate increased level of cyclic guanosine monophosphate (cGMP), and consequently dilates blood vessel (Figure A-4B) [11-13]. This self-regulation mechanism ensures adequate blood flow and tissue perfusion to maintain organs within the normal physiological ranges.

It is currently thought that vasodilatation is also modulated by vascular ROS (generated in fibroblasts, endothelial cells, smooth muscle cells) [14]. As mentioned before,  $NO^\bullet$  would be consumed anytime it encounters  $O_2^-$ , so its bioavailability is actually regulated by the balance with  $O_2^-$ . Excessive ROS will upset the balance and accordingly cause endothelial dysfunction, vasoconstriction and hypertension.

#### Cell signaling

The high reactivity and rapid diffusion of ROS/RNS facilitate surrounding cells to generate appropriate physiological signaling. One example is temporal integration of local neuronal activity with  $NO^\bullet$  signaling. The convoluted trails and life span make  $NO^\bullet$  an ideal messenger to surrounding synapses [15], offering retrograde signaling pathway from

postsynaptic cells to presynaptic terminals and consequently maintaining long-lasting synaptic transmission (Figure A-4C) [16,17].  $\text{ONOO}^-$  behaves as a potent modulator of various signal-transduction pathways. At low concentrations (10 – 200  $\mu\text{M}$ ), it was observed to promote phosphotyrosine signaling in different cells [9]; however, higher concentrations of  $\text{ONOO}^-$  can impair downstream signaling through nitrotyrosine formation.  $\text{H}_2\text{O}_2$  and other ROS also play important roles in cellular signaling. Among which, the activation of nuclear transcription factors in the mitogen-activated protein kinase (MAPK) pathways perhaps is the most significant one [18]. These factors are able to control expression of protective genes that repair damaged DNA, power the immune system, and arrest the proliferation of damaged cells [19].

### Redox regulation

The redox environment of a cell is critical determinant for the trigger of apoptosis. ROS/RNS can lead to a temporary redox regulation and modify intracellular homeostasis.

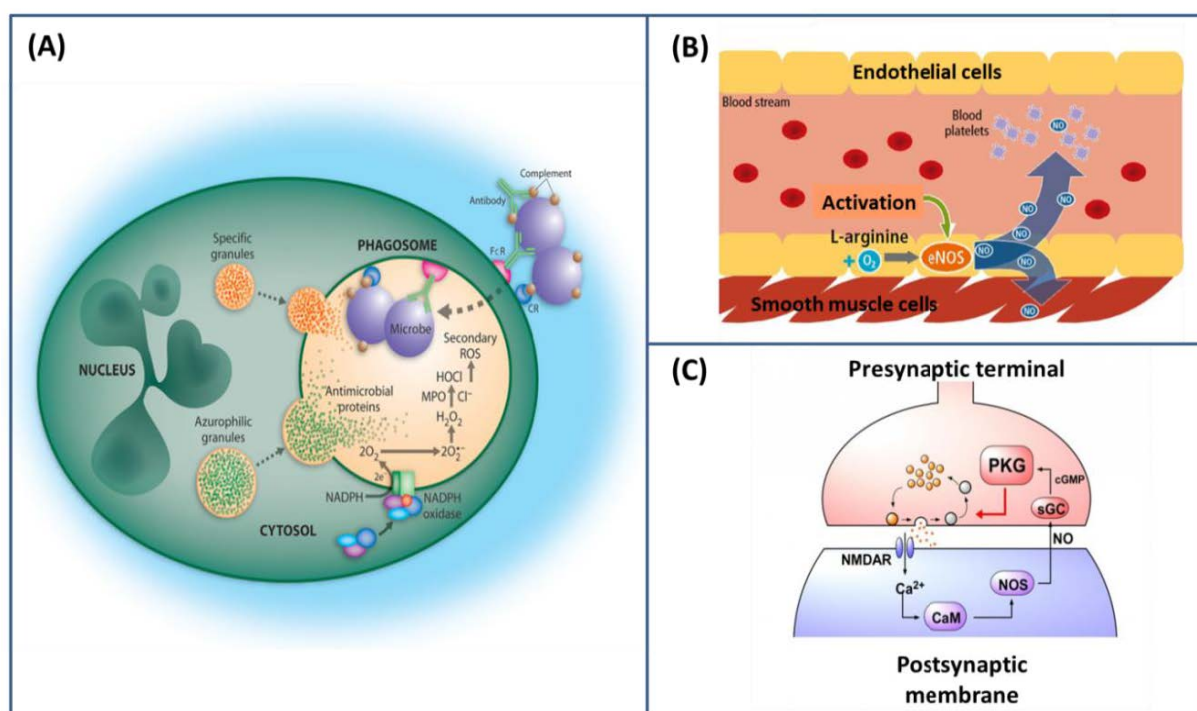


Figure A-4: Examples of ROS/RNS regulating physiological processes. (A) Activation of NADPH oxidase and microbicidal systems during phagocytosis [2]. (B)  $\text{NO}^{\cdot}$  generation from endothelial cells elicits vasodilatation process [20]. (C) Retrograde regulation of synaptic functions by  $\text{NO}^{\cdot}$ . Vesicle endocytosis is accelerated through  $\text{NO}^{\cdot}$  activating soluble guanylate cyclase (sGC) and protein kinase (PKG) [16].

### 1.2.2. Deleterious effects

Despite those physiological regulations, overwhelming generation of ROS/RNS can irreversibly damage cellular compounds. This will lead to many life-threatening diseases, including cardiovascular disease, cancer, neurological disorders, diabetes and ageing [21,22].

#### Lipid peroxidation

Oxidative bursts can initiate a chain reaction of lipid peroxidation (in membranes, liposomes, and lipoproteins), by abstracting a hydrogen atom from polyunsaturated free-fatty acids (PUFA) [23]. This reaction produces some secondary hydroperoxy radicals (e.g., ROO<sup>•</sup> and LOO<sup>•</sup>) that continue attack neighboring PUFAs and ultimately result in degeneration of membrane lipids (Figure A-5A). Lipid peroxidation changes membrane fluidity, permeability, and the capacity to maintain equilibrated concentration gradient [24]. Consequently, cells will suffer from loss of intracellular liquids, enzymes, and other important biological elements.

#### Protein alteration

ROS/RNS such as OH<sup>•</sup>, O<sub>2</sub><sup>•-</sup>, and ONOO<sup>-</sup> have large potential to oxidize amino acids in the peptide chain, altering protein structures and functions. The most prevalent reaction is that with cysteine (Figure A-5B), leading to formation of disulfides (RSSR) from two thiols [25]. This oxidation inactivates many enzymes involved in cellular energetic processes. Besides, thiols may also be oxidized into thiyl radicals (RS<sup>•</sup>) to further promote oxidative stress. Other protein modifications include oxidation of transition metal centers-containing proteins (e.g., hemoglobin, myoglobin, and cytochrome *c*) [26], cytotoxic tyrosine nitration in nervous system [27], and proteins degradation (through alteration of lysosomal systems and proteasomes) [28].

#### DNA lesion

Another important damaging effect of ROS/RNS is their capability to attack almost every part of DNA (e.g., purine, pyrimidine, and deoxyribose backbone) [29], and then cause DNA strand breaks (Figure A-5C). The *in vivo* repair system is also affected, not totally inhibited, but its capacity and repair procedures can be impaired. This permanent DNA lesion represents the first step in mutagenesis and carcinogenesis.

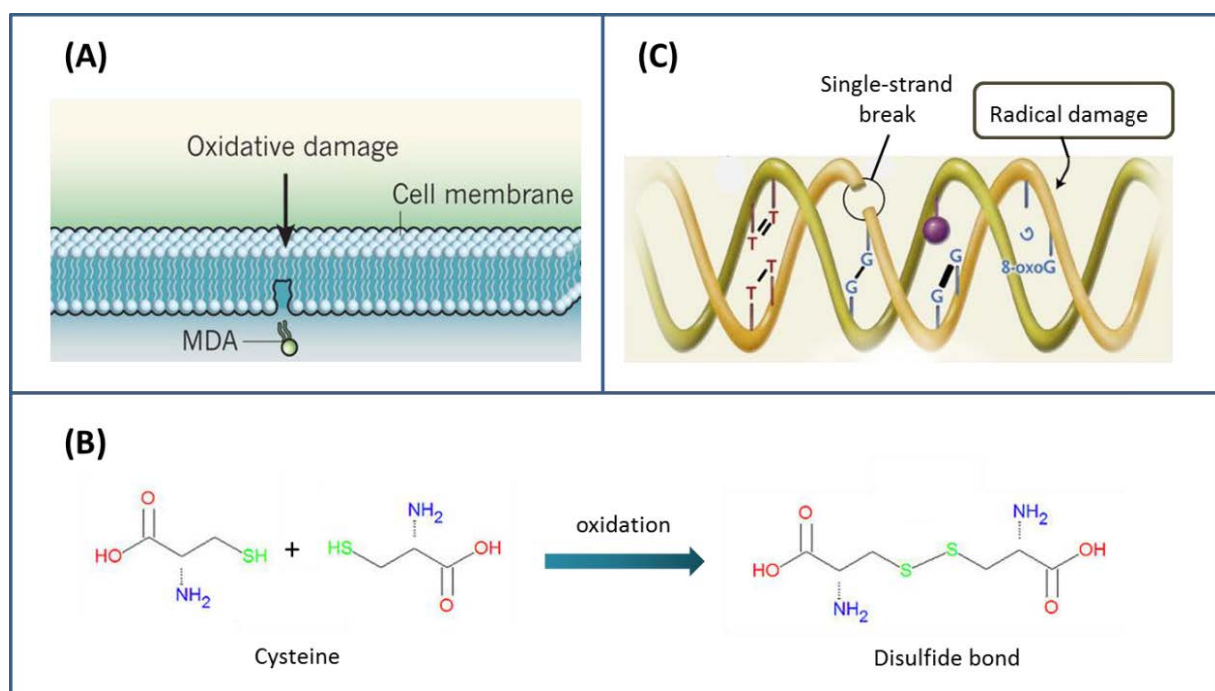


Figure A-5: Examples of oxidative damages in vivo. (A) Bi-lipids membrane degeneration via peroxidation of PUFA (with typical product of malondialdehyde MDA) [23]. (B) Oxidation of amino acid cysteine [25]. (C) DNA lesion with broken strand [29].

### 1.3. Conclusion of section 1

Life in an aerobic environment is constantly accompanied by **ROS/RNS** generation. Originated from two primary species ( $O_2^-$  and  $NO^*$ ), a cocktail of derived candidates work together to regulate vital physiological functions. When the ROS/RNS release uncontrolledly exceeds antioxidant capability, via activation of **NADPH** and **NOS** enzymatic pools, critical **oxidative stress** prevails.

Indeed, physiological and pathological processes are to a large extent due to the collective regulating and damaging effects mentioned above. Therefore, the in-depth exploration of main ROS/RNS candidates should allow a better understanding towards metabolic process.

## 2. Detection methods for ROS/RNS

Due to the apparent ubiquity and importance of ROS and RNS, it is of great interest to monitor their production during oxidative stress. Indeed, rather than the long-term observation of patients' metabolites, direct measurements are much preferred in deciphering the intricate mechanisms at different oxidative stress stages. Despite the difficulties of subtle generation and transient existence of those active species, highly-sensitive and selective analytical methods have undergone great progress and some of which are introduced in the following context.

### 2.1. Some general analytical methods

#### 2.1.1. Fluorescence method

Two types of fluorescent probes are commonly adapted in this domain, namely “oxidant-sensitive” or “non-redox” indicators [30]. The former dyes comprise aromatic compounds which can be oxidized by free radicals and then generate fluorescent end products (Figure A-6A). The other probes release masked fluorophores after oxidants' attack on the blocking groups (Figure A-6B).

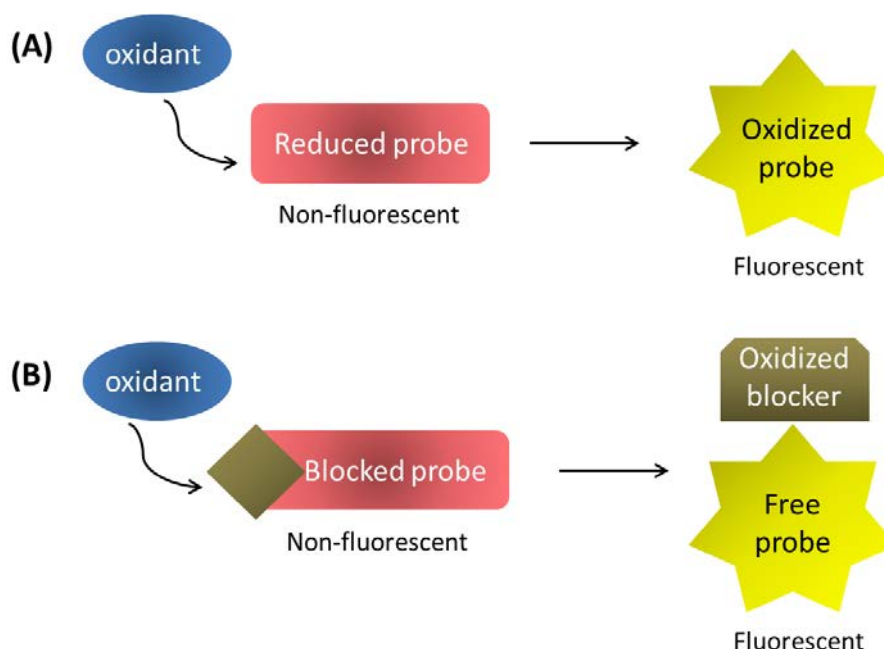


Figure A-6: Principles of oxidants fluorescence detection by using (A) “oxidant-sensitive” dyes, or (B) “non-redox” probes.



The “oxidant-sensitive” dyes can detect samples at very low concentration (several to tens of nanomolar [31-33]) but react simultaneously with various oxidants, providing the global cellular redox activity rather than specifically for one analyte. In addition, misinterpreted signals usually result from unstable intermediates, side production, and autofluorescence. Famous fluorescent probes of this type include 2',7'-dichlorodihydrofluorescein (DCFH, Figure A-7), dihydrorhodamine 123 (DHR 123, targets to  $\text{H}_2\text{O}_2$ , HOCl and  $\text{ONOO}^-$ ), dihydroethidium (DHE, targets to  $\text{O}_2^{\bullet-}$ ) and diaminofluorescein (DAF, targets to  $\text{NO}^{\bullet}$  [33-35]).

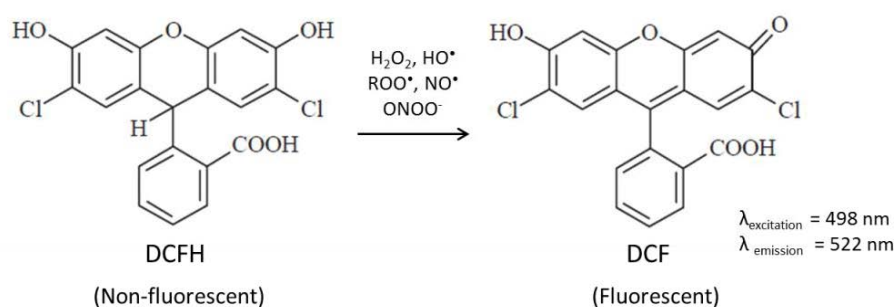


Figure A-7: Mechanism of 2,7-dichlorodihydrofluorescein (DCFH) oxidation to form fluorescent 2,7-dichlorofluorescein (DCF) by several ROS and RNS [33].

As an alternative, the “non-redox” probes (e.g., boronate, benzene sulfonyl, and benzyl based compounds [33]) release fluorophores from protecting groups (Figure A-8) instead of being directly involved in radical-intermediate reactions, and accordingly avoid some potential complications. However, these probes tend to be selective (towards a particular group of reactive species) rather than specific (towards only one target species); and their low reactivity (boronate probes react with  $\text{H}_2\text{O}_2$  at  $k \approx 1 \text{ M}^{-1} \text{ s}^{-1}$ ) usually raises questions.

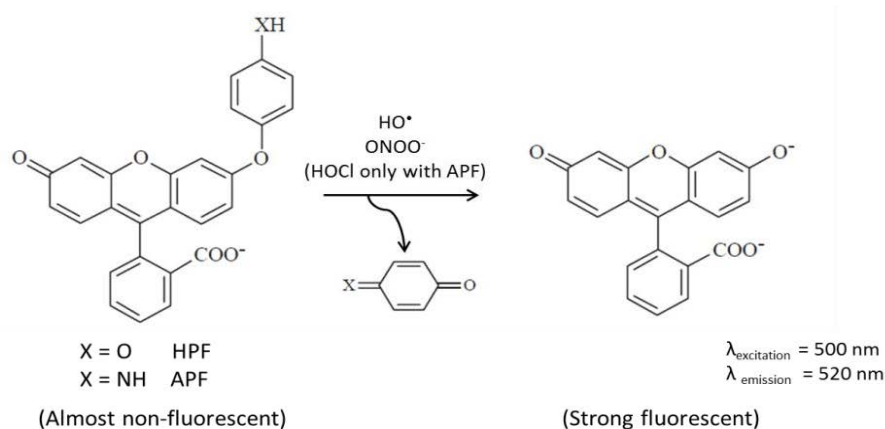


Figure A-8: Mechanism of 2-[6-(4'-hydroxy)phenoxy-3H-xanthen-3-on-9-yl]benzoic acid (HPF) and 2-[6-(4'-amino)phenoxy-3H-xanthen-3-on-9-yl]benzoic acid (APF) O-dearylation induced by highly reactive ROS and RNS [36].

Beyond those two main types, one new group called genetically encoded proteins (e.g., reduction-oxidation sensitive green fluorescent protein (roGFP) [37]) can react rapidly and selectively with oxidants (detection limit down to 0.1 nM). Moreover, they can be targeted to different sites in the cell to monitor local oxidant production. But their functions are likely to be affected by cellular reductases and enzymatic peroxide metabolism.

Yet, the fluorescence-based assays provide primary investigation of a variety of oxidative species. But the lack of specificity and multi-step reactions still trigger problems in interpreting the absolute identification or quantification. Some additional techniques (e.g., high-performance liquid chromatography (HPLC), mass spectrometry (MS) and gas chromatography (GC)) are thus needed to accomplish the whole analysis.

### 2.1.2. Chemiluminescence method

Chemiluminescence detection consists in a probe or an enhancer that provokes light emitting during oxidant reaction (Figure A-9). It is highly sensitive but has the same limitations as fluorescence method issued from the specificity and multi-step radical mechanisms.

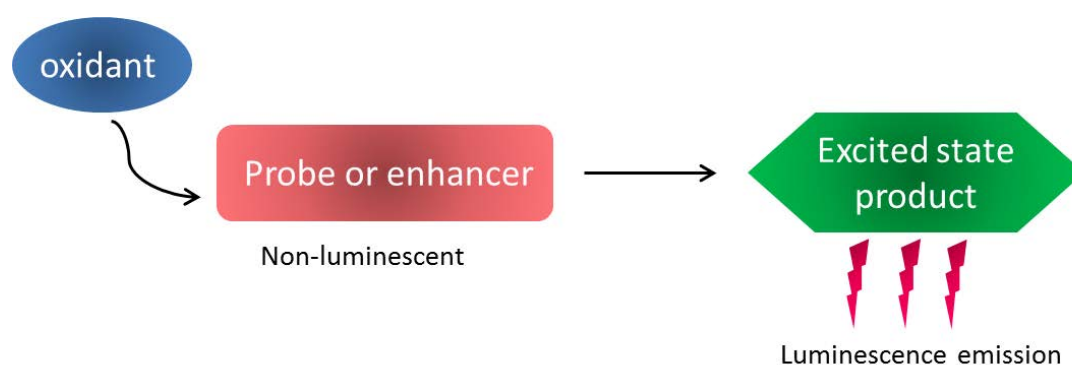


Figure A-9: Principle of oxidant chemiluminescence detection with probe or enhancer.

Luminol (LM) is the most famous chemiluminescent probe which has been reported to selectively detect ROS/RNS in activated phagocytes (detection limit down to the range of femtomolar) [31]. But it cannot identify the oxidants or provide mechanistic information since a host of active species (e.g.,  $\text{OH}^\bullet$ ,  $\text{O}_2^\bullet$ ,  $\text{ONOO}^-$  or  $\text{H}_2\text{O}_2$  plus peroxidase) can similarly initiate oxidation step and offer luminescence signals (Figure A-10). At the same time, luminol

radicals can reduce  $O_2$  into  $O_2^{\bullet-}$ , acting both the source and detector of  $O_2^{\bullet-}$  and thus inevitably leading to artifactual results.

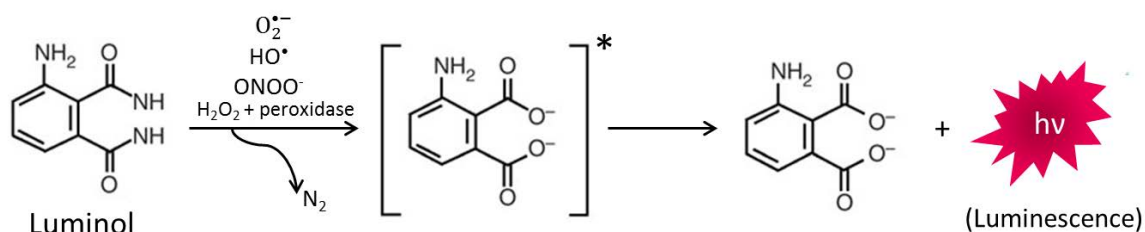


Figure A-10: Mechanism of luminol oxidation by ROS and RNS to emit luminescence [38].

Lucigenin (LC) is often thought more specific for  $O_2^{\bullet-}$  [39], but neither react directly with  $O_2^{\bullet-}$ . It must be first reduced to cation radical ( $LC^{+\bullet}$ ) which then initiate reaction to generate luminescence. Some more promise and specific probes such as coelenterazine and analogues of LM and LC [40] still remain the same issues of specificity and interference, since no matter in which case, an initial oxidation step and subsequent radical reactions are involved.

$NO^{\bullet}$  is measured by chemiluminescence using reaction with ozone ( $O_3$ ) to form nitrogen dioxide in its excited state ( $NO_2^{*\bullet}$ ). The subsequent emission from  $NO_2^{*\bullet}$  (600 – 875 nm) gives signal proportional to the concentration of  $NO^{\bullet}$  [41]:



To prevent underestimation of  $NO^{\bullet}$ , its side oxidation must be minimized by introducing inert gas (nitrogen or argon). Nevertheless, other species that may react with  $O_3$  (e.g., ethylenes, carbonyls or sulfur compounds) also skew the results. Finally, despite the good sensitivity (1 nM), neither oxygen-free environment nor the presence of  $O_3$  (highly toxic) seems suitable for investigation of living cells.

### 2.1.3. Electron spin resonance (ESR) spectroscopy

ESR spectroscopy is used for measuring paramagnetic species through their transition of spin states under magnetic field (Figure A-11). For the detection of oxidative species, specific complexes “spin traps” [42] are needed to convert radicals to long-lived spin-adducts. Characteristic and quantitative information is then acquired from spectra of those stable adducts.

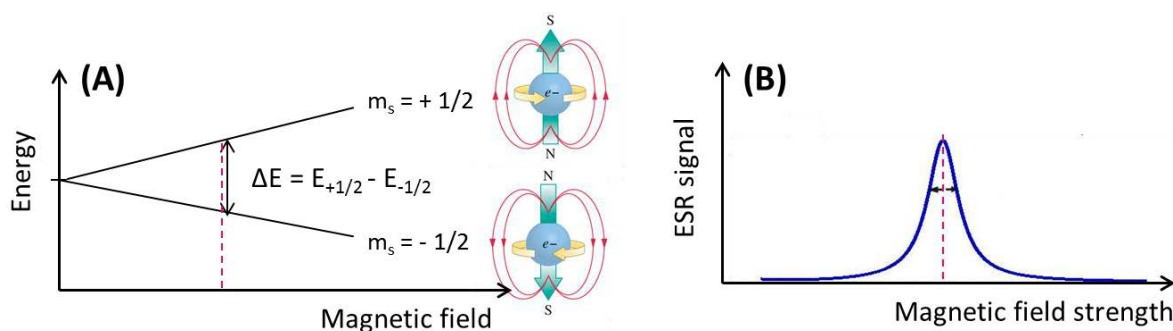


Figure A-11: Illustration of electron spin resonance method [43]. (A) Principle of energy levels splitting directly proportional to the magnetic field's strength. An unpaired electron can only move between magnetic moment  $m_s = +1/2$  and  $m_s = -1/2$ . (B) One example of resulting ESR spectrum.

The most frequently used spin traps include pyrroline-based cyclic nitrones (e.g., 5,5-dimethyl-1-pyrroline-N-oxide (DMPO) [44]) which react with  $\text{OH}^\bullet$  and  $\text{O}_2^\bullet$  to generate  $-\text{OH}$  and  $-\text{OOH}$  adducts; and colloid iron (II) diethyldithiocarbamate ( $\text{Fe}^{2+}$ -DETC) [45] which is specific for bioactive  $\text{NO}^\bullet$ .

ESR spin trapping offers higher selectivity compared with previous optical methods. From the adduct spectrum, identification, concentration, and even the relevant reaction kinetics of free radicals could be obtained. However, it is not directly available for the oxidants without unpaired electrons (e.g.,  $\text{H}_2\text{O}_2$  and  $\text{ONOO}^-$ ). Some additional limitations also hamper its application in living cells, such as adverse alteration of conjugates (by endogenous metabolites), long recording times, expensive and cumbersome setup, as well as low-temperature usually required during measurement.

### 2.1.4. Ultraviolet-visible (UV-Vis) spectroscopy

UV-Vis spectroscopy provides a direct detection method of  $\text{ONOO}^-$ . Unlike fluorescence or chemiluminescence detection, it does not need a probe compound; neither like SER, there is no requirement of the presence of unpaired electron).  $\text{ONOO}^-$  can be easily quantified by measuring absorbance intensity at 302 nm ( $\epsilon = 1705 \text{ M}^{-1} \text{ cm}^{-1}$ ) [46,47]. However, experiments are usually performed in basic solution since adequate species stability is guaranteed in such environment.

Indeed, for most oxidants, special techniques are needed to circumvent their transient nature and to induce light absorbing property. One famous assay is the detection of  $\text{NO}^\bullet$  from its oxidation product  $\text{NO}_2^-$  [48].

As demonstrated in Figure A-12,  $\text{NO}_2^-$  reacts with the Griess reagents (sulfanilamide and *N*-1-naphthylethylenediamine) to form a red-pink color azo dye which is then monitored spectroscopically at 540 nm. These series of chemical reactions and indirect nature of detection forbid real-time analysis of  $\text{NO}^\bullet$  generation, despite the low price and simple execution. In addition, precaution should be taken in the quantitative analysis since  $\text{NO}_2^-$  from other resources can lead to the overestimation of  $\text{NO}^\bullet$ . Sensitivity of this method is highly dependent on solution composition. In ultrapure deionized distilled water, detection limit for commercially available Griess reagent kits is roughly 2.5  $\mu\text{M}$ .

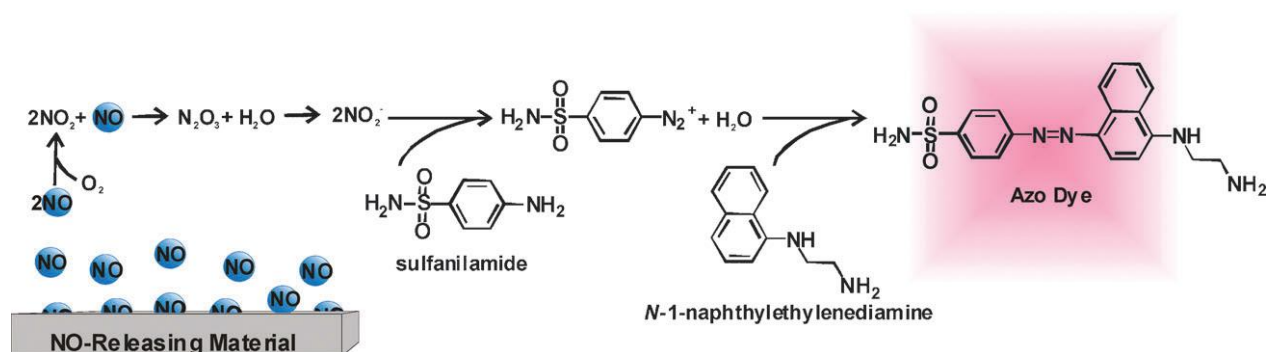


Figure A-12: The reaction of  $\text{NO}_2^-$  with Griess assay reagents forms an azo dye that is easily detected spectrophotometrically to extrapolate  $\text{NO}^\bullet$  concentration [48].

### 2.1.5. Biomarkers method

In living cells, oxidative species are ascribed to regulating some biomarkers, including glutathione (GSH), glutathione disulfide (GSSG), 3-nitrotyrosine (3-NT), homocysteine (Hcy), and cysteine (Cys) [49]. These biomarkers can be accurately determined by advanced instrumental assays like UV-Vis and fluorescence. Accordingly, they act as signaling media that offer a new chance to investigate oxidative stress.

To conduct biomarker analysis, a small, functional and simply-operated carrier is needed. For example, a sensitive and quantitative assay of ROS/RNS ( $\text{H}_2\text{O}_2$ ,  $\text{OH}^\bullet$ ,  $\text{HOCl}$ ,  $\text{NO}^\bullet$ , and  $\text{O}_2^\bullet$ ) has been accomplished by using glutathione-modified gold nanoparticles (GSH-AuNPs) [50]. The GSHs on the AuNP surface can be readily detached via the formation of glutathione disulfides (GSSGs) upon reaction with ROS/RNS. These destabilized particles subsequently aggregated into plasmonic couplings and triggered the red shift in UV-Vis spectrum (Figure A-13). The change of solution color was directly observed by naked eyes. This method works smoothly for highly reactive radicals; but for non-radical species such as  $\text{H}_2\text{O}_2$ , it is necessary to improve detection efficiency by converting  $\text{H}_2\text{O}_2$  to the radical from  $\text{OH}^\bullet$ , via the  $\text{FeCl}_2$ -catalyzed decomposition. By using this analysis, cancerous cells with higher oxidative stress level were distinguished rapidly from the normal ones. However, identification of specific analyte is still problematic.

Nitration of phenolic probes (e.g., tyrosine) has been utilized as a more specific modification induced by  $\text{NO}^\bullet$ -derived oxidants [51]. The product 3-nitrotyrosine is stable and can be directly assessed spectrophotometrically (350 – 450 nm region). This method was previously used to detect  $\text{ONOO}^-$  but more recently for the collective detection of potential nitrating species. This detection is strongly pH-dependent, giving detection limit around 1  $\mu\text{M}$  and might being subjected to interference from other compounds that may absorb in the same region. Therefore, it is suitable for relatively concentrated and pure samples. To achieve more sensitive and specific detection, HPLC, MS, GC, or electrochemical techniques are often required.

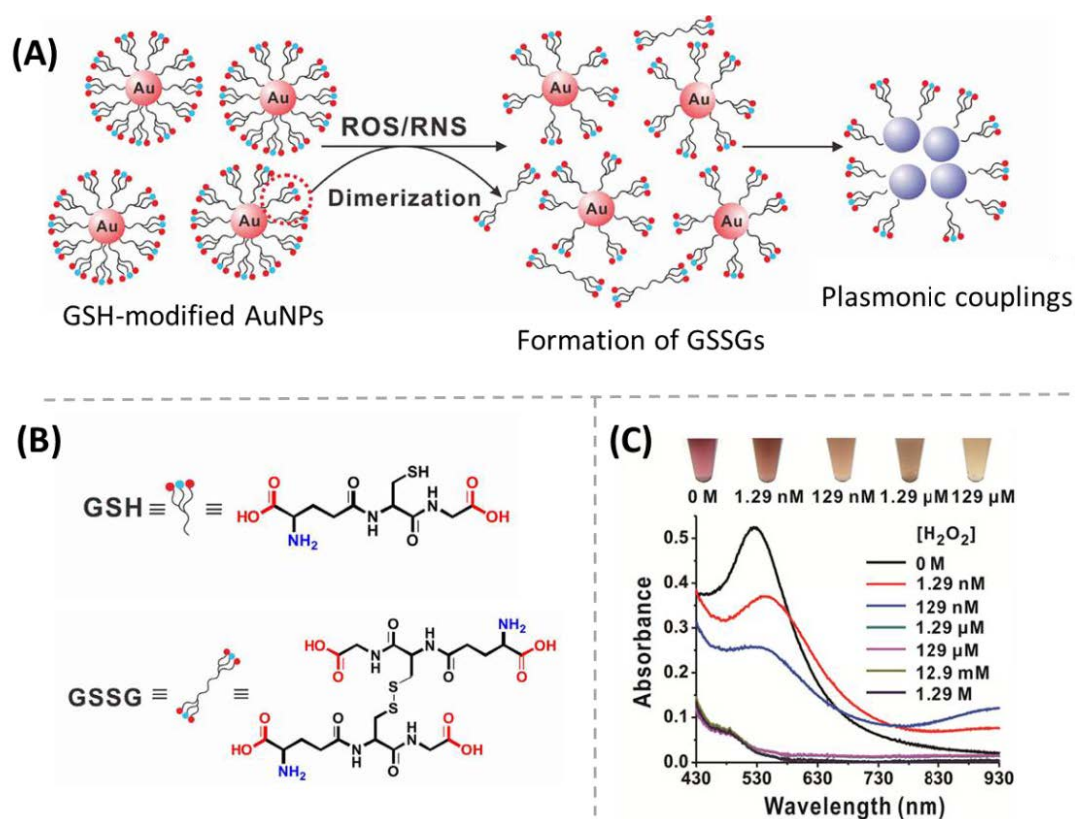


Figure A-13: (A) Reaction between GSH-AuNPs and ROS/RNS to form plasmonic couplings. (B) Structures illustration of GSH and GSSG. (C) The plasmonic couplings-based colorimetric and spectroscopic detection [50].

## 2.2. Electrochemical method

Electrochemistry has been identified since centuries and is widely accepted as a scientific branch to investigate the processes of electron-transfer-involved chemical reactions (the fundamental electrochemical principles and techniques are introduced in Appendix I.1 and I.2). Electrochemical methods solve many constraints described with previous approaches owing to the intrinsic electroactive properties of several important oxidative species. Therefore, a direct and label free investigation is allowed to study oxidative stress at its very origin.



Detection of ROS/RNS is carried out via either reduction or oxidation at the working electrode. Electro-reduction is promising but inevitably suffers from interference of oxygen in aerobic environments. Electro-oxidation is preferred in general; however, high overpotential usually precludes the accurate detection since a global signal from all feasible species is measured rather than from one particular analyte. Moreover, the traditional bare electrodes (e.g., carbon, platinum and gold) are quite easily passivated in biological medium, resulting in unstable results.

To improve the selectivity and sensitivity, functional materials were developed to modify electrode surface (Figure A-14) [5,52-54]. Immobilization of specific biomolecules on electrode surface is commonly used; specificity of this sensor is linked to reaction between analyte and those biological substances. The permselective membranes prevent diffusion of undesired molecules, by size or charge exclusion (e.g., Nafion®), to electrode surface. Thin layer of metal-containing catalytic complexes are tunably electrodeposited to increase electron-transfer kinetics and negatively shift the detection potential. More recently, metal nanoparticles attract great interest because of their favored chemical, physical and electronic properties than usual bulk materials. Improved electrons transfer as well as better surface stability is often observed at metal-particles deposited electrodes. Multiple modification layers are sometimes incorporated to minimize diverse interference; but usually at the expense of decreasing sensitivity and prolonging respond time.

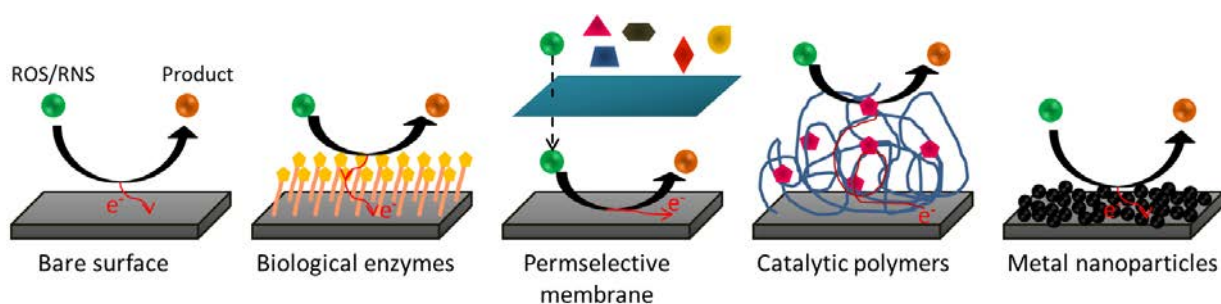


Figure A-14: Illustration of different surface modifications on bare electrode surface for ROS/RNS measurements.

In the following context, some widely used electrochemical sensors are introduced, with special attention paid to the two primary radicals ( $O_2^{\bullet -}$  and  $NO^{\bullet}$ ) and the three main electroactive derivatives ( $H_2O_2$ ,  $ONOO^-$  and  $NO_2^-$ ).



### 2.2.1. Superoxide anion ( $O_2^{\cdot-}$ ) sensors

$O_2^{\cdot-}$  is an “easily-detected” target due to the low oxidation potential at ordinary electrode surface; whereas better performances can be achieved by coating biomolecules such as cytochrome *c* (cyt *c*) or, more elegantly, its natural scavenger superoxide dismutase (SOD) [52,55,56].

As shown in Figure A-15A, Fe(III)-cyt *c* can be immobilized on gold or platinum surface, reduced by  $O_2^{\cdot-}$  ( $k = 2 \times 10^6 \text{ M}^{-1} \text{ s}^{-1}$ ) and then immediately re-oxidized at electrode surface at a quite low potential (15 – 25 mV vs. Ag/AgCl (silver-silver chloride reference electrode)). The oxidation current of cyt *c* constitutes analytical response for continuous  $O_2^{\cdot-}$  in bulk solution. On the other side, SOD-based biosensor works through converting  $O_2^{\cdot-}$  to  $H_2O_2$  and then oxidizing this stable product (Figure A-15B). Nevertheless, this sensor may encounter the difficulty in distinguishing the previously existed  $H_2O_2$  (by natural disproportionation process).

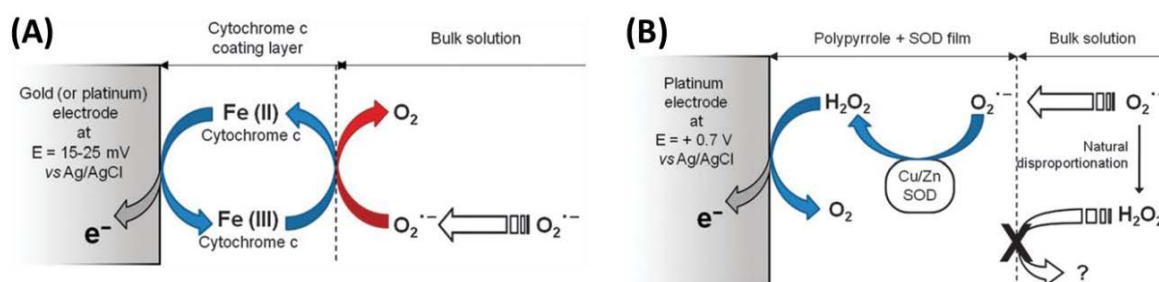


Figure A-15: Illustration of reaction processes for (A) cyt *c*-based  $O_2^{\cdot-}$  biosensor or (B) SOD-based  $O_2^{\cdot-}$  biosensor [52].

Different examples of  $O_2^{\cdot-}$  sensor and their analytical performances are listed in Table A-1.

Table A-1: Constitutions and performances of several  $O_2^{\cdot-}$  electrochemical sensors.

Electrode	Modification	Characteristics and performances
Carbon fiber [57]		+0.10 V vs. SCE (saturated calomel electrode) <ul style="list-style-type: none"> <li>✿ Surface passivation and protein fouling</li> </ul>
Glassy carbon [58]	Benzylidenephényl nitrone	Detection limit: 25 $\mu\text{M}$ Linear range: 0.03 – 1.0 mM <ul style="list-style-type: none"> <li>✿ Interference comes from free radicals such as <math>\text{OH}^{\cdot}</math></li> <li>✿ Poor sensitivity impedes biological use</li> </ul>

Pyrolytic graphite [59]	Immunoglobulin G (IgG)	+0.05 V vs. Ag/AgCl <ul style="list-style-type: none"> <li>✿ Cells absorbed and activated by IgG, exhibiting very low current (a few pA)</li> </ul>
Gold [60,61]; Platinum [62]	Cytochrome <i>c</i>	+0.02 V vs. Ag/AgCl Sensitivity: 0.5 pA pM <sup>-1</sup> <ul style="list-style-type: none"> <li>✿ Improved selectivity against NO<sup>•</sup></li> </ul>
Platinum	SOD-containing polypyrrole [56,63]	+0.70 V vs. SCE Detection limit: 15 nM Response time: ~ 5 s <ul style="list-style-type: none"> <li>✿ Temperature-stability at physiological pH</li> <li>✿ No clear discrimination of external H<sub>2</sub>O<sub>2</sub></li> </ul>
	SOD-containing gel/Teflon [64]	+0.60 V vs. Ag/AgCl <ul style="list-style-type: none"> <li>✿ Capable to discriminate external H<sub>2</sub>O<sub>2</sub></li> </ul>

Although O<sub>2</sub><sup>•-</sup> is primarily related to oxidative stress, its electrochemical responses usually present quite low local concentrations (nanomolar) during oxidative bursts. This may result from either trace production, or more likely, from the fact that larger level of production is scavenged by the rapid disproportionation (Equation (A.2)) before being detected. Based on the reaction kinetics (~10<sup>9</sup> M<sup>-1</sup> s<sup>-1</sup> when SOD exists), 50% O<sub>2</sub><sup>•-</sup> decomposes into H<sub>2</sub>O<sub>2</sub> after diffusing over a distance of 0.1 μm from the emitting point (half life time less than 10 μs) [65].

Therefore, detection of its main products H<sub>2</sub>O<sub>2</sub> is relevant for quantitative evaluation of oxidative stress as well as for a better understanding of the derivation process since SOD enzymes are abundant in living cells.

### 2.2.2. Hydrogen peroxide (H<sub>2</sub>O<sub>2</sub>) sensors

H<sub>2</sub>O<sub>2</sub> is the most stable member among ROS family, but it has a poor sensing performance on bare carbon surface. The kinetics on metal electrode is comparatively higher; however, the activity is gradually downgraded by formation of oxide layer plus passive adsorption. Thus, current researches mainly focus on surface modification that allows electrocatalytic detection of H<sub>2</sub>O<sub>2</sub> [66]. Utilization of heme proteins, Prussian blue (PB), and transition metals or metal oxides have been reported.

Some constructions and characteristics of H<sub>2</sub>O<sub>2</sub> sensors are listed in Table A-2.

Table A-2: Constitutions and performances of H<sub>2</sub>O<sub>2</sub> electrochemical sensors.

Electrode	Modification	Characteristics and performances
Glassy carbon [67]; Graphite [68]; Gold [69]; Titanium dioxide [70]	Horseradish peroxidase [70]; Catalase [71]; Cyt <i>c</i> [69];	-0.2 V vs. SCE Detection limit: ~ 1 μM * Heme proteins allow less exposure to interfering reactions
Carbon [72]; Gold [73]	PB nanoparticles	-0.05 V vs. Ag/AgCl Detection limit: 25 nM Sensitivity: 1.3 μA μM <sup>-1</sup> cm <sup>-2</sup> * Immune to large molecules such as ascorbic acid, uric acid, and para-acetyl-amino-phenol * Lack of stability in neutral and alkaline solutions
Gold [74]	Nafion-polypyrrole /multi-walled carbon nanotubes	+0.7 V vs. SCE Detection limit: 1 μM Linear range: 5 – 30 mM Sensitivity: 1.47 μA μM <sup>-1</sup> cm <sup>-2</sup> Respond time: ~ 80 s * Capable to perform detection in deionized water, without need of supporting electrolytes
Carbon fiber ( <i>d</i> = 15 μm) [75-79]; Gold [80]; Platinum [81]	Platinum black particles	+0.30 to +0.45 V vs. SSCE (sodium saturated calomel electrode) Detection limit: 10 nM Linear range: 100 nM – 1 mM Sensitivity: 4.08 A M <sup>-1</sup> cm <sup>-2</sup> Response time: < 0.5 s * 17000 times more sensitive than the bare carbon fiber counterpart toward 1 mM H <sub>2</sub> O <sub>2</sub> * Kinetic profiles of oxidative bursts from single fibroblasts give clue of enzymatic activity

### 2.2.3. Nitric oxide (NO<sup>•</sup>) sensors

NO<sup>•</sup> is oxidizable at a higher potential on ordinary bare electrodes; and may encompass large interferences from other electroactive species in real samples (NO<sub>2</sub><sup>-</sup>, H<sub>2</sub>O<sub>2</sub>, ascorbic acid, etc.). Among which, NO<sub>2</sub><sup>-</sup> is considered the most significant interference since it prevails *in vivo*, and has a similar size and oxidation potential as NO<sup>•</sup>.

The primitive NO<sup>•</sup> sensors are dependent on permselective membranes (size- or charge-repulsive). A better performance is obtained by further incorporating catalytic redox mediators. Typical catalysts include porphyrins or phthalocyanines (with metal centers of nickel (Ni), copper (Cu), iron (Fe), cobalt (Co) or manganese (Mn)). Decreased oxidation potential (~ 0.1 V less) and enhanced sensing sensitivity (detection limit down to a few nanomolars) were evidenced [52]. The Ni-porphyrin/Nafion sensor (multiple-coating) is expected to achieve highly sensitive NO<sup>•</sup> detection with immunity to NO<sub>2</sub><sup>-</sup>, because of the impermeability of Nafion to anions. Other blocking membranes (e.g., polycarbazole, polyphenol, polymethylcellulose) have also been developed to fulfil different requirements. The permeability or catalytic effect is adjustable by the film morphology and thickness. Thicker coating enables great selectivity, but often leads to a poor sensitivity and low temporal resolution.

On the other side, the instrumentation of NO<sup>•</sup> sensors has undergone great progress as well, evolving from electrolyte-filled glass pipette sealed with a gas-permeable rubber film (Shibuki-style electrode) into miniaturized and whole-solid assembly (Figure A-16) [54,82].

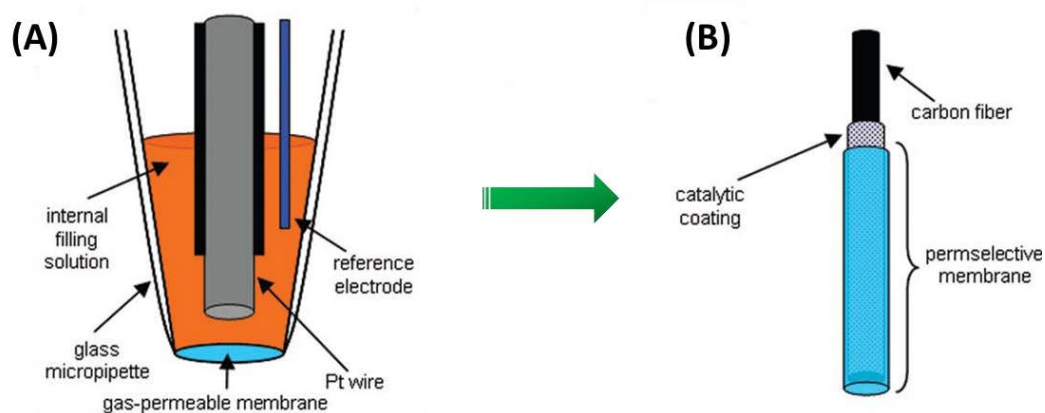


Figure A-16: Schematic diagrams of (A) Shibuki-style NO<sup>•</sup> sensor, and (B) whole-solid catalytic NO<sup>•</sup> sensor [54].

Many remarkable NO<sup>•</sup> sensors are characterized in terms of sensitivity, selectivity, dynamic range, response time and applications as reported in the following Table A-3.

Table A-3: Constitutions and performances of NO<sup>•</sup> electrochemical sensors.

Electrode	Modification	Characteristics and performances
Carbon fiber [83]		+0.95 V vs. Ag/AgCl Detection limit: a few $\mu\text{M}$ Sensitivity: 250 – 500 pA $\mu\text{M}^{-1}$ * Decreased sensitivity in biological samples
<b>Permselective membranes (<math>\sim +0.9</math> V vs. Ag/AgCl)</b>		
Platinum wire [84] (Shibuki-style electrode)	Chloroprene rubber film ( <i>gas permeable</i> )	Sensitivity: 2.5 – 106 pA $\mu\text{M}^{-1}$ Response time: $\sim 1$ s * Immune to $\text{O}_2^-$ and $\text{NO}_2^-$ * Poor reproducibility
Carbon fiber [85]; Gold [86]; Platinum [87,88]	Nafion; Polycarbazole [87]; Polystyrene [88]; ( <i>charge exclusion</i> )	Detection limit: 50 nM Linear range: 0.1 – 100 $\mu\text{M}$ * Immune to $\text{NO}_2^-$ and ascorbic acid
	Cellulose [89] ( <i>size exclusion</i> )	* Immune to large biological molecules such as proteins
	Nafion/ <i>o</i> -phenylenediamine [85,90] ( <i>charge/size exclusion</i> )	Detection limit: 35 nM Sensitivity: 1 nA $\mu\text{M}^{-1}$ * Immune to ascorbic acid, $\text{NO}_2^-$ , dopamine * Stable for lasting detection in intact brains
<b>Catalytic metal-containing polymer complexes (<math>\sim +0.75</math> V vs. Ag/AgCl)</b>		
Carbon fiber [91,92]; Gold [93,94]	Metalloporphyrins or metallophthalocyanines (center ions: Ni, Zn, Mn, Co, or Fe)	Detection limit: 10 nM Linear range: 0.1 – 40 $\mu\text{M}$ Sensitivity: 11 pA $\mu\text{M}^{-1}$ Respond time: $\sim 0.5$ s * Currents enhance 2 – 3 times than bare surface * Resist surface degradation during detection

<b>Multi-layered coatings</b> ( $\sim +0.75$ V vs. Ag/AgCl)		
Carbon fiber ( $d = 0.5 \mu\text{m}$ ) [95]; Platinum [96,97]	Metalloporphyrins or metallophthalocyanines /Nafion	Detection limit: 10 nM Linear range: 0.1 – 300 $\mu\text{M}$ Sensitivity: 8 pA $\mu\text{M}^{-1}$ <ul style="list-style-type: none"> <li>✳ Immune to <math>\text{NO}_2^-</math>, dopamine, ascorbic acid</li> <li>✳ Good efficiency to detect real-time release from single endothelial cells [98] or in the brain of a freely moving animal [99]</li> </ul>
	Ni-porphyrins/hydrogel [100]	<ul style="list-style-type: none"> <li>✳ <math>\text{NO}^*</math> freely diffuses inside hydrogel</li> <li>✳ Improved biocompatibility of adherently growing cells</li> </ul>
<b>Nanoparticle deposits</b> (+0.65 to +0.75 V vs. Ag/AgCl)		
Platinum [101]	Pt-Fe(III) nanoparticle composites	+0.75 V vs. Ag/AgCl <ul style="list-style-type: none"> <li>✳ Improved sensitivity</li> <li>✳ Selective against carbon monoxide (CO)</li> <li>✳ Only 5% sensitivity decrease after 2.5 h continuous use</li> </ul>
Carbon fiber ( $d = 10 \mu\text{m}$ ) [11]	Platinum black particles	+0.65 V vs. SSCE Detection limit: < 50 nM Linear range: 50 nM – 1 mM Response time: $\sim 0.3$ s <ul style="list-style-type: none"> <li>✳ High sensitivity and stability</li> <li>✳ Immune to coexistent <math>\text{NO}_2^-</math></li> <li>✳ Direct examine the nature of <math>\text{NO}^*</math> release by neurons in an acute rat brain slice</li> </ul>

### 2.2.4. Peroxynitrite (ONOO<sup>-</sup>) sensors

ONOO<sup>-</sup>, generated from coupling of O<sub>2</sub><sup>-</sup> and NO<sup>•</sup>, is a crucial intermediate to quantify and interpret oxidative stress. However, its fast decomposition (through acid conjugates ONOOH) in physiological condition (pH = 7.4) considerably hampers the accurate quantification. Indeed, very few reports are directly dedicated to ONOO<sup>-</sup> despite its electrochemically feasible redox potential. Beside normal bare metal surface, catalytic metal-polymer complexes and metal nanoparticles are also coated on electrode surface to facilitate ONOO<sup>-</sup> detection.

Table A-4 recapitulates significant examples reported in the literature.

Table A-4: Constitutions and performances of ONOO<sup>-</sup> electrochemical sensors.

Electrode	Modification	Characteristics and performances
Gold [47]		-0.1 V vs. SCE * Immune to NO <sup>•</sup> , NO <sub>2</sub> <sup>-</sup> , H <sub>2</sub> O <sub>2</sub> , and dopamine
Palladium [102]		+0.9 V vs. Ag/AgCl Detection limit: 2.4 μM Linear range: 3 – 100 μM
Mercury film [103]		-0.1 V vs. Ag/AgCl Detection limit: 12 μM Linear range: 10 – 200 μM Sensitivity: 41 mA M <sup>-1</sup> * Suffers from oxygen interference
Carbon fiber [104,105]; Platinum [106,107]	<b>Conducting polymer-manganese ion complexes</b>	
	Tetraaminophthalocyanine manganese (Mn(TAPc)) /polyvinylpyridine (PVP) [104] [106]	0 V vs. Ag/AgCl Detection limit: 18 nM Linear range: 0.02 – 80 μM * Immune to dopamine, ascorbic acid, and uric acid and large proteins
	Manganese-[poly-2,5-di-(2-thienyl)-1H-pyrrole-1-(p-benzoic acid)](Mn-pDPB)/polyethyleneimine (PEI) [107]	+0.2 V vs. Ag/AgCl (reduction process) Detection limit: 1.9 nM Linear range: 0.02 – 50 μM Response time: 15 s

Glassy carbon [108]	Poly(cyanocobalamin)	Detection limit: 100 nM Linear range: 2 – 300 $\mu$ M
Carbon fiber ( $d = 10 \mu\text{m}$ ) [79,109]	Platinum black particles	+0.5 V vs. SSCE Detection limit: a few nM Response time: $\sim 0.1$ s * The first time of unmediated characterizing ONOO <sup>-</sup> in oxidative bursts emitted by human fibroblasts

### 2.2.5. Nitrite ion (NO<sub>2</sub><sup>-</sup>) sensors

NO<sub>2</sub><sup>-</sup> is essentially the end products of NO<sup>•</sup> metabolism. It is very stable though the main trouble arises from the poor behaviors at most ordinary electrode substrates under relatively high detection potential. A variety of substrates have been investigated, including carbon, pyrolytic graphite, indium tin oxide (ITO) and transition metal electrodes. Among which, transition metal nanoparticles and bimetallic alloy nanoparticles are prevalently used due to their excellent electrocatalytic activity and stability.

More detailed examples of NO<sub>2</sub><sup>-</sup> sensors are demonstrated in Table A-5.

Table A-5: Constitutions and performances of NO<sub>2</sub><sup>-</sup> electrochemical sensors.

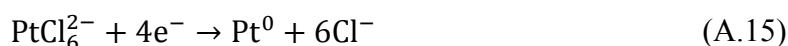
Electrode	Modification	Characteristics and performances
Glassy carbon [110]		+1.0 V vs. SCE Detection limit: 400 nM Linear range: 2.5 – 10 $\mu$ M Sensitivity: 36 mA M <sup>-1</sup>
Ion-selective electrodes [111]	Rh(III)-porphyrins or salophen ligands /carboxylated polyvinylchloride (PVC)	Detection limit: 5 $\mu$ M Response time: 3 – 4 min * Enhanced potentiometric selectivity with interfering anions: ClO <sub>4</sub> <sup>-</sup> , SCN <sup>-</sup> , NO <sub>3</sub> <sup>-</sup> , Br <sup>-</sup> , Cl <sup>-</sup> * Slow response time due to intrinsic reaction kinetics



Glassy carbon [112]; ITO [113]; Gold [114]	Fe(III)-porphyrins or Cu-phthalocyanine	+0.8 V vs. SCE Detection limit: 36 nM Linear range: 0.12 – 12.2 $\mu\text{M}$ Sensitivity: 0.83 $\mu\text{A } \mu\text{M}^{-1}$ * Good reproducibility
Glassy carbon [115]	Graphene/polypyrrole /chitosan nanocomposites	+0.9 V vs. SCE Detection limit: 0.1 $\mu\text{M}$ Linear range: 0.5 – 722 $\mu\text{M}$ * Retains 85% initial activity after one month
Glassy carbon [116]	Au-Fe(III) nanoparticles	+0.73 V vs. SCE Detection limit: 0.1 $\mu\text{M}$ Linear range: 0.2 – 150 $\mu\text{M}$ Sensitivity: 0.13 $\mu\text{A } \mu\text{M}^{-1}$ * Good reproducibility and stability
Carbon fiber [79,117,118]	Platinum black particles	+0.85 V vs. SSCE Detection limit: a few nM * High sensitivity and stability * Real-time detection of secreted species fluxes from single fibroblast or macrophage

### 2.2.6. Platinum black (Pt-black) coated electrodes

Since the nineties, our group has focused on monitoring of four key oxidative species ( $\text{H}_2\text{O}_2$ ,  $\text{ONOO}^-$ ,  $\text{NO}^\bullet$ , and  $\text{NO}_2^-$ ) by Pt-black coated carbon-fiber microelectrodes (Figure A-17A) [5,75,76,79,109,117-119]. Black platinum is electrodeposited from a Pt(IV) solution following a  $4e^-$  reduction into Pt(0) on a microelectrode surface:



By controlling plating process, the deposit thickness and surface morphology are adjustable. The especial synergetic effect between nanotechnology and electrochemical determination is highlighted since superior sensing performances towards ROS/RNS over the conventional bulk materials are frequently observed.

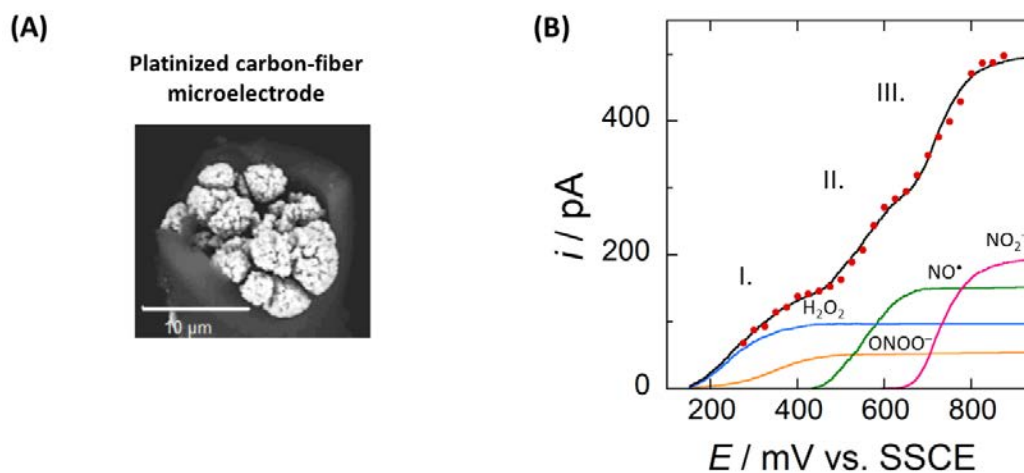


Figure A-17: (A) Scanning electron microscope (SEM) image of the carbon-fiber microelectrode after Pt-black plating. (B) Solid curves refer to independent *in vitro* steady-state voltammograms of  $1.4 \mu\text{M}$   $\text{H}_2\text{O}_2$  (blue curve),  $1.7 \mu\text{M}$   $\text{ONOO}^-$  (yellow curve),  $19 \mu\text{M}$   $\text{NO}^\bullet$  (green curve) and  $4 \mu\text{M}$   $\text{NO}_2^-$  (purple curve) obtained at this platinized microelectrode. Black solid curve is the arithmetic addition of these individual voltammograms, which neatly match the constructed voltammogram (red points) derived from amperometric responses (25 mV interval) during cellular oxidative stress [79,117].

According to the *in vitro* voltammetric study at this platinized carbon-fiber microelectrode (Figure A-17B) [79,117], selectivity of the four analytes is provided through precise control of microelectrode potential. The oxidation waves of  $\text{NO}^\bullet$  and  $\text{NO}_2^-$  are well separated from each other and from the waves of the other two compounds. The electrochemical waves of  $\text{H}_2\text{O}_2$  and  $\text{ONOO}^-$  overlap, however, possessing different features ( $\text{H}_2\text{O}_2$ :  $E_{1/2} = 0.250 \pm 0.005$  V vs. SSCE; and  $\text{ONOO}^-$ :  $E_{1/2} = 0.35 \pm 0.02$  V vs. SSCE) [109,118]. As a consequence, the constructed voltammogram from cells oxidative bursts (red points in Figure A-17B) can be neatly broken down into arithmetic addition of independent

voltammograms derived from the four suspicious compounds ( $\text{H}_2\text{O}_2$ ,  $\text{ONOO}^-$ ,  $\text{NO}^\bullet$ , and  $\text{NO}_2^-$ ); and chemical nature of oxidative content in this experimental condition could be finely deciphered.

Owing to the excellent analytical property, platinum black remains popular in ROS/RNS investigations. In addition, the easy regeneration of active surface, flexible deposition onto conductive surfaces of any shape or dimension, further promotes its incorporation as coating film in a wide range of biochemical sensors.

### 2.3. Conclusion of section 2

As compared to most spectroscopic methods (fluorescence, chemiluminescence, etc.), **electrochemistry** allows a more direct approach to unravel the complex biological roles of ROS/RNS and their intricate derivate pathways.

Thanks to the excellent analytical properties of **Pt-black coating films**, several oxidative species ( $\text{H}_2\text{O}_2$ ,  $\text{ONOO}^-$ ,  $\text{NO}^\bullet$ , and  $\text{NO}_2^-$ ) have been sensitively and selectively detected by controlling the electrode working potential. Indeed, these four compounds are considered as the key species of interest since the others are either too short-lived (e.g.,  $\text{OH}^\bullet$ ) or not electroactive (e.g.,  $\text{NO}_3^-$ ) to be treated as significant components of amperometric response.  $\text{O}_2^\bullet$  is neither considered since the majority of this production is scavenged by the rapid disproportionation before its detection could occur. Alternatively, detection of its main products  $\text{H}_2\text{O}_2$  makes great importance for quantitative characterization.

Since our interests evolve from *in vitro* to the *ex vivo* world, living cells will become in the following the objects of studies. The recent progress of cell-based analysis is discussed. Although our main objective will focus on electrochemical detection of ROS/RNS during oxidative stress, some investigations of other electroactive messengers are included so as to give a general overview about experimental designs and analytical performances achieved till now.

### 3. Analytical progress in *ex vivo* detection of cellular electroactive messengers

Cells, usually called as “building blocks of life”, are fundamental units with elaborate machinery. Although varying a lot in size, shape and biological attribute, cells are quite similar in structure and composition (illustration of an animal cell in Figure A-18) [120]. To be specific, one cell has: a phospholipid bilayer membrane, as an envelope to separate interior from surrounding environment, regulating passage of molecules or ions through specific proteins and maintaining electric potential of the cell; salty cytoplasm which takes up most of the cell

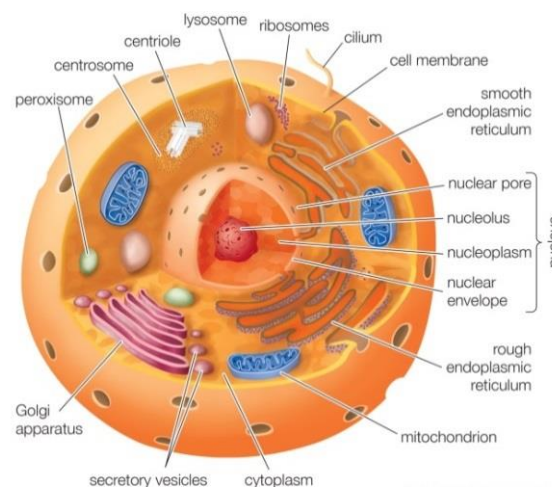


*Figure A-18: Illustration of a typical animal cell [120].*

volume, acting as a house to anchor organelles in place, organizing and sustaining cell's shape and activity; and some typical subcellular components with vital functions such as nucleus (solitary in each cell), mitochondria, ribosomes, peroxisomes, lysosomes and secretory vesicles (numerous in each cell).

Cellular communication takes place through the release of specific chemical/biochemical messengers (e.g., release of neurotransmitters, hormones, and peptides during vesicular exocytosis; and the ROS/RNS generation during oxidative bursts as we mentioned above). Indeed, almost all the cellular activities (life cycle regulation, proliferation, signaling, apoptosis, etc.) are accompanied with directional and orderly transfer of charged or electroactive components, making a living cell essentially an electrochemical dynamic system [121]. In this case, electrochemistry offers an excellent medium that well suits biological systems, and gives a direct chance to understand metabolic stages, pathological processes and some other complex life phenomena.

### 3.1. Single-cell analysis by using microelectrodes

Detection of secreted species from a living cell is principally constrained by the infinitely minute number of molecules (zepto- to attomoles) released during a fairly short time period. In this section, the progresses of instrumentations and methodologies in electrochemistry towards single-cell analysis are first demonstrated.

#### 3.1.1. Microelectrodes and their advantages

Nowadays, the field of microelectrodes in cellular biology has outpaced a topical curiosity among community of electrochemistry. They are sufficiently small (micro- or nanometers at least in one dimension) to be used for instance for the detection of living cells. The high sophistication of fabrication [122-124] offers new scope and opportunities to tackle the most difficult problems of cellular events with several relevant properties: (i) high spatial resolution; (ii) fast time response; (iii) high signal-to-noise ratio; (iv) improved selectivity after surface modification; (v) non-destructive detection; and (vi) inexpensive and simple instrumentation favored in clinical use.

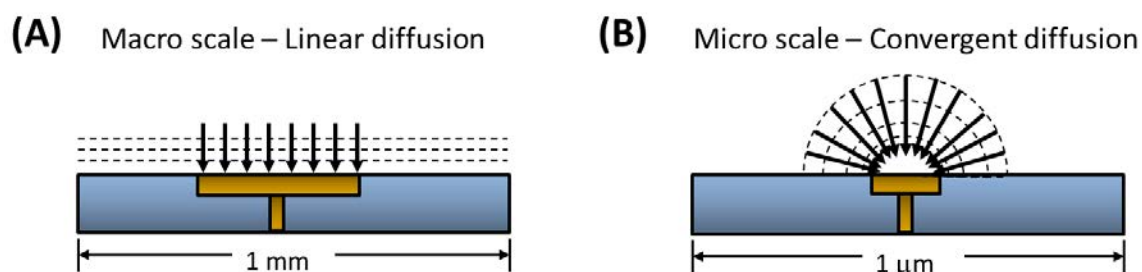


Figure A-19: Schematic illustrations of (A) linear diffusion above macro scale planar electrode; and (B) convergent radial diffusion above micro scale electrode which offers the fast-established steady state.

As compared to the macroscopic counterpart, convergent diffusion above microelectrode exhibits drastic advantages (Figure A-19). The planar diffusion is only a transition step before reaching steady state when diffusion layer ( $\delta$ ) grows to the order of microelectrode critical dimension ( $\sim r_0$  for microdisk). Correspondingly, the mass transport at microelectrodes is very fast due to radial diffusion that leads to high spatial resolution and well defined steady-state regimes. Timescale of this process varies with electrode size and shapes. Generally, the smaller the electrode, the shorter time it needs to reach steady state.

More details about the regimes and electrochemical behaviors of several commonly used microelectrodes can be found in Appendix I.3.

Beside the spatial resolution and fast mass transport, all the other advantages are related to their small dimension: the time constant of the electrochemical response ( $RC_d \propto r$ ) which decreases with the size, as well as the charging current ( $i_c \propto e^{-t/RC_d}$ ) which becomes less predominant versus the faradaic current. The Ohmic drop distortion ( $iR$ ) is also minimal in less conductive media since the current detected is usually in nA or pA level. Therefore, microelectrodes provide favorable tools in many sophisticated investigations of cellular events [125-127].

### 3.1.2. Detection of electroactive messengers from a single living cell

Using a configuration similar to that of synapse in nervous system (Figure A-20A, left), one can image an assembly where one microelectrode approaching the emitting surface of isolated cell is collecting the cellular messengers immediately after their production. This configuration, termed as “artificial synapse” (Figure A-20A, middle), offers excellent sensitivity and efficiency since the small distance ensures an adequate local concentration (micro- to millimolar) even for extremely minute release by one cell (atto- to femtomoles), leading to measurable and reliable electrochemical responses from an analytical point of view.

Based on this synaptic assembly, our group has explored extensively the oxidative stress at single-cell level. In the series of experiments [5,75,76,79,109,117-119], the platinized carbon-fiber microelectrode was designed to nearly match cells dimension ( $d \approx 10 \mu\text{m}$ ) and only the tip surface was left conductive while the other area of whole fiber shaft was insulated. Thus the faradaic signals were sufficiently collected while the electrical noise from overall conducting surface decreased significantly. A maximum signal-to-noise ratio and an effective collection in real time are expected. The current variations after intense initiation of oxidative stress were recorded at several different constant potentials (Figure A-20A, right), and the exact quantity and kinetics of generated ROS/RNS from activated single cells (fibroblasts, macrophages, etc.) were obtained after performing statistically enough measurements.

Similarly, microelectrodes with tip size close to that of a mammalian cell have been reported to monitor dopamine release (Figure A-20B) [128]. Series of current spikes were recorded amperometrically, with each spike corresponding to one vesicle event, indicating many complex features (release frequency, time length, individual and average quantity and kinetics). Higher spatial resolution was achieved by further decreasing tip diameter (100 nm) to match the size of a vesicle. In this case, a single spike was detected meaning only one vesicular event just beneath the electrode during this time period. This shrinking size also gives chance to map different release sites on cell membrane or probe molecular mechanism at any desired part of the cell network (Figure A-20C) [129].

Another important progress is the possibility of harmless penetration of nanoscale electrode into a living cell, in order to investigate more precisely the central contribution of intracellular events. One example is the detection of ROS/RNS inside macrophage (Figure A-20D, left) [130]. The Pt-black deposit was deposited inside an etched nanocavity ( $r \approx 80$  nm, see Figure A-20D, middle), while the overall electrode with glass insulator was less than 1  $\mu\text{m}$  in diameter. A tight seal around nanoelectrode shaft was evidenced through the drastic attenuation of  $\text{Ru}(\text{NH}_3)_6^{3+}$  reduction signal after penetrating the electrode into a cell (cells were bathed in PBS containing 1 mM  $\text{Ru}(\text{NH}_3)_6\text{Cl}_3$ ). Cell remained alive for the entire experiment period (more than ten min) with a nanoelectrode inside it. A weak and very short release was detected intracellular as striking comparison to the intense and longer-time lasting response detected outside (Figure A-20D, right). This indicates that macrophage can rapidly reduce ROS/RNS concentration inside its cytoplasm and thus avoiding serious damage.

In some researches, more elaborate techniques are incorporated to obtain additional information during single-cell electrochemical detection. For example, the scanning electrochemical microscopy-carbon-fiber microdisk electrode (SECM-CFMDE) system has been developed to obtain 3D images of Human umbilical vein endothelial cells (HUVECs) during  $\text{NO}^\bullet$  release (Figure A-20E) [131]. This regulation of cell morphological changes provided a new perspective for further understanding of physiological and pathological effects of  $\text{NO}^\bullet$  release in vascular relaxation.



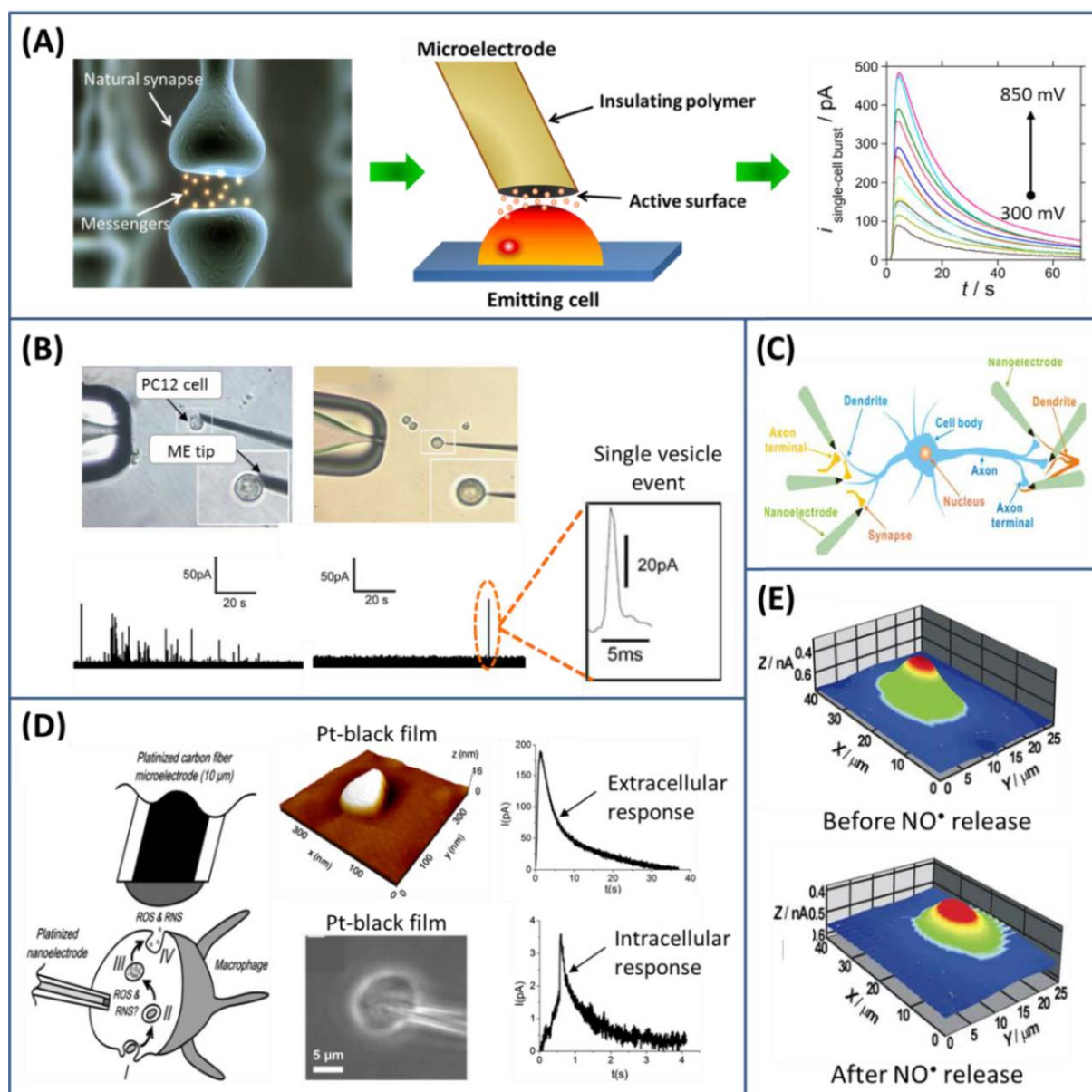


Figure A-20: (A) Schematic illustrations of natural synapses (left) [132], artificial synaptic assembly of living cell/microelectrode (middle), and the ensuing amperometric monitoring of single-cell oxidative release by this synaptic microelectrode [117]. (B) SEM images and amperometric recordings of dopamine release from PC12 single cells (rat pheochromocytoma cells) by electrodes respective with 5  $\mu\text{m}$  (left) and 100 nm diameter (right) [128]. (C) Schematic diagram shows possible monitoring position by microelectrode during cellular communications [129]. (D) Monitoring of intracellular ROS/RNS production during oxidative stress (left). An etched Pt nanoelectrode after Pt-black deposition (radius of 80 nm) and its insertion into a single macrophage are shown (middle). And corresponded current traces for extracellular and intracellular detections are presented (right) [130]. (E) Images obtained from SECM-CFMDE system to illustrate morphological changes of HUVECs before and after  $\text{NO}^*$  secretion [131].



Beside the experiments mentioned above, a domain that concerns high-throughput detection of multiple analytes is presently under rapid progress. One example is given by a methodological extension of the synaptic assembly. Simultaneous monitoring of multiple ROS/RNS at one platinized carbon-fiber microelectrode was achieved by triple potential-step chronoamperometry [133]. The successive potential step-sequence is demonstrated in Figure A-21A (at 0.30, 0.45, 0.65, and 0.85 V vs. SSCE), and only the currents near the end of each step (duration of 20 s for each step) were analyzed to minimize capacitive contribution. This method enabled three individual amperograms to be recorded simultaneously at corresponded potentials (0.85 V was excluded due to the greater dispersion of background currents and the significant gain in temporal resolution) for each single cell (Figure A-21B). Thus a direct comparison of the oxidative response was obtained without concerning of any cellular variability or changes of electrode's reactivity.

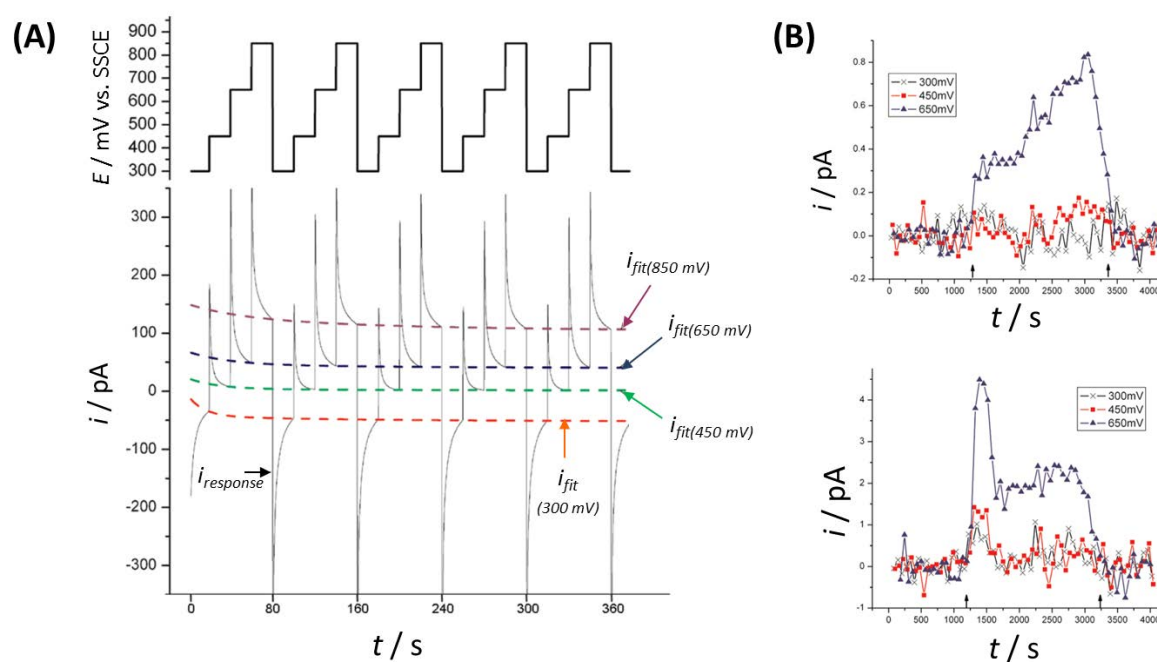


Figure A-21: (A) Measured current (left bottom, solid line) resulting from a successive sequence of potential steps (left top) applied to a platinized carbon-fiber microelectrode [133]. The four dashed lines are the best fits of the mean current near the end of each step. Potentials imposed respectively at 0.30, 0.45, 0.65, and 0.85 V vs. SSCE, with 20 s duration of each step. Each figure at the right side shows amperograms at 0.30 (black crosses), 0.45 (red squares), and 0.65 V (blue triangles) vs. SSCE obtained from one single macrophage. Measurements of two different single cells are reported here as example. The black arrows at x-axis indicate the time at which the microelectrode is positioned near and then removed away from the surface of the cell.

Another exploration is based on miniaturized electrodes array. Ewing's group fabricated a carbon-ring microelectrode array (CRMA,  $r = 2.5 \mu\text{m}$ ; total electrode tips less than  $50 \mu\text{m}$ ) through pulling multiple quartz capillaries together (Figure A-22A) [134]. Both microelectrodes number and tip size were independently tunable. Simultaneous detection with subcellular temporal heterogeneities can be obtained from a single PC12 cell during one experiment (Figure A-22B).

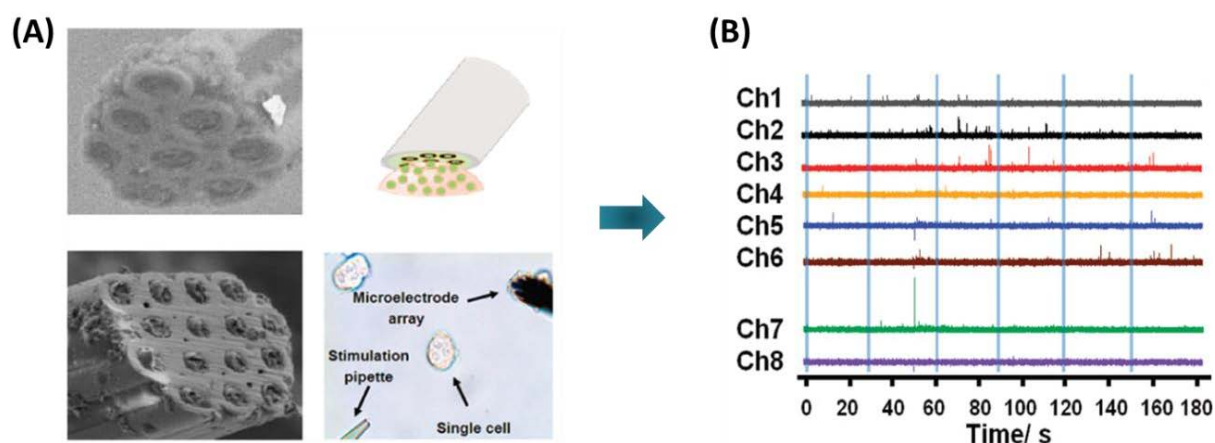


Figure A-22: (A) CRMAs contains eight microring electrodes for electrochemical monitoring of dopamine release from single PC12 cells. (B) Representative amperometric traces indicating subcellular temporal heterogeneities of exocytosis [134].

Following the single-cell detection by using synaptic microelectrode, the very nature of electroactive messengers are detected with significant temporal and spatial resolution. Despite the excellent precision and accuracy of such measurements, to allow for statistically meaningful results, it is inevitable to conduct a large number of repetitive and fastidious measurements due to the cellular variability. When a few different experimental conditions are incorporated, the high intense of human labors and considerably long working time are required.

### 3.2. Microfluidic devices as functional tools for cell-based analysis

One future trend is to integrate the overall experiment into a microfluidic system where multiple microelectrodes can be flexibly patterned and manipulated in an autonomous “all-in-one” device [97,135-138]. By designing particular configuration, simultaneous detection either at single-cell stage or towards cells population is readily carried out in high

throughput. The investigation of cells in microfluidic system is so widespread, and here we strive to cultivate a general opinion by highlighting recent advances in cell culture, manipulation and electrochemical monitoring of biological messengers.

The advent of microfluidics stems back to early 1950s when efforts were made to dispense small amount of liquids [139] and propel fluid within microchannels for GC [140] or HPLC [141]. Later at the beginning of 21<sup>st</sup> century, also regarded as an unprecedented progressive period of microfluidics, structural variety and functional integration burgeoned

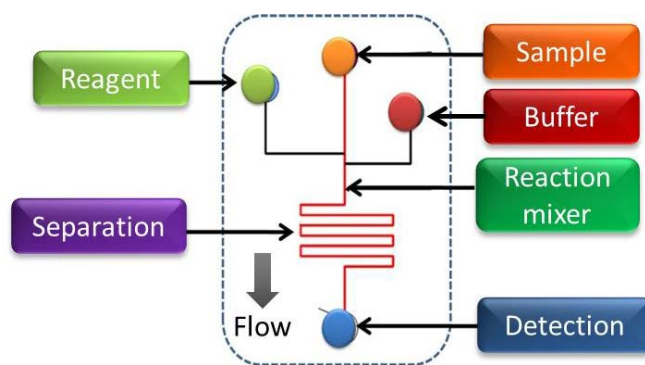


Figure A-23: Concept of integrated microfluidic system with channel network.

through polydimethylsiloxane (PDMS) soft lithography [142] along with implementation of functional units [143]. Nowadays, microfluidic system, also called as “lab-on-a-chip” [144], comprises a massive multitude of microchannel networks, integrating sample injection, reaction, separation, detection, and some other operations into a small chip (a few square centimeters in size), acting similarly as a macro-laboratory with various chemical and biological functions (Figure A-23). Owing to controllable fluids, low reagent consumption, fast analysis, high sensitivity, effective cost and portability, microfluidic system becomes gradually intriguing in interdisciplinary fields [145,146], and is generally described as one new technology that “changes everything”.

Although microfluidic devices initially dominated in chemistry and physics, the application in biology (such as the realm of biosensor [147,148], drug screening [149-151], tissue engineering [152,153], point-of-care diagnosis [154,155], etc.) has recently grown as a major focus within scientific community.

Beside the advantages mentioned above, there are still some particular merits for bioanalysis:

- The dimension of microfluidic unit (typically several tens of micrometers) parallels size of cells [156], giving access to establishing realistic environment for living cells.
- High integration of pumps, valves, and other smart microstructures design [157], enabling precise control of microenvironments.

- Certain microfluidic materials (e.g., PDMS) are biocompatible and permeable to O<sub>2</sub> and CO<sub>2</sub> that are vital for cell maintenance.
- Compatibility with ultrasensitive detection methods for detecting cells and subcellular molecules in an eligible, efficient and less risky manner.

The minute regulation in local environment such as matrix composition, flow rate, pH and temperature, even structural dimension, is of first-rate importance to cell mechanical and biochemical functionalities [156]. To appropriately design a microfluidic platform capable of cell loading, cell culture, signal delivery and final measuring, one need to acquire enough accumulation of knowledge in multiple academic domains, including physicochemical properties of microenvironment, cell culture techniques, analytical monitoring methodologies, and practical experience on device fabrication.

### 3.2.1. Cell culture in microfluidic devices

As a regenerative and simplified alternative to the whole organism or animal tests, cell culture is the technique to grow cells *ex vivo*, acquiring extensive use for diagnosis and therapeutic purpose [158-160]. To maintain a constant cell culture, an artificial physiological environment is needed to provide suitable temperature (36 – 37°C ), pH value (around 7.4), sterility, nutrition, atmospheric O<sub>2</sub> and CO<sub>2</sub> concentrations. As compared to traditional culture tools (flask, petri dish, microtiter plate, etc.), microfluidic platform shows great potential to achieve a low consuming and inexpensive cell culture in an automated approach.

#### Cell adhesion

On different substrates, cell attachment could be facilitated by coating intermediate proteins or peptides, such as fibronectin [161], collagen [162], laminin [163], elastin [164] or the extracellular matrix [165], (ECM comprises various proteins, Figure A-24A). In contrast, at undesired region, resistance of cell adhesion could be accomplished after pretreatment with protective compounds including polyethylene glycol (PEG) and polyacrylamide (PAAM) [166]. Some groups [167,168] have demonstrated cellular patterns on microfluidic platform (Figure A-24B) through modifying surface properties.

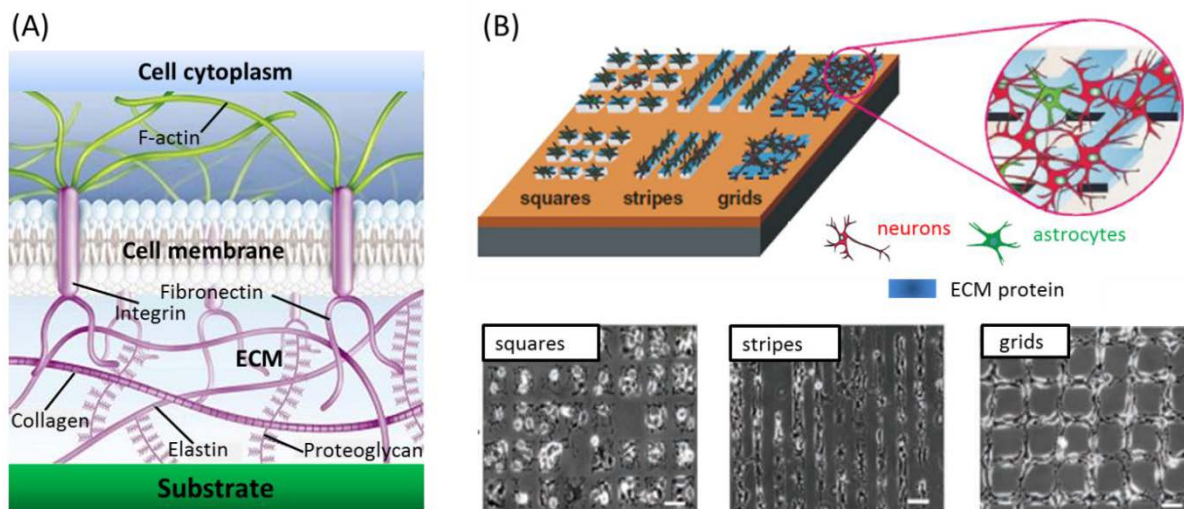


Figure A-24: Cell adhesion on modified surface. (A) Simplified scheme of ECM proteins bonding a cell via surface receptors (integrins) [169]. (B) Illustration of neural stem cells differentiating into either neurons (red) or astrocytes (green) on protein patterns with square, stripe and grid shapes. Phase contrast images show cell attachment and growth on patterned substrates after 2 days of seeding. Scale bar is  $50\mu\text{m}$  in each image [168].

Firm and fast attachment is a crucial prerequisite for cell study in microfluidic system [170], since only limited time left for cell adhesion under static conditions before nutrients and oxygen must be replenished through media perfusion.

Although most microfluidic systems adopt two-dimensional (2D) bottom monolayer cell culture, the idea of 3D cell culture is looming recently in order to better mimic *in vivo* organs (liver, lung, kidney and adipose tissue) [171]. In 3D configuration, cells are typically confined into ECM-coated scaffolds (e.g., PDMS [172], PLGA (poly lactic-co-glycolic acid) [173] and PLLA (poly-L-lactic acid) [174]); or immobilized in micro-patterned hydrogels [175] to achieve tissue-like connectivity (Figure A-25). By using polymers, cells are able to be trapped during gelling process, resulting in more uniform distribution; further with incorporation of laminar flow, concentration gradients could also be realized.

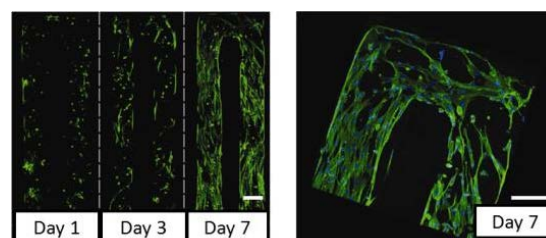


Figure A-25: Bone marrow stromal cells spreading within GelMA hydrogel patterns to form 3D network. Scale bars:  $250\mu\text{m}$  [175].



### Long-term perfusion culture

The microenvironment gives greater physiological relevance for cell growth. However, as indicated in Figure A-26A, the small culture volume (in range of micro-, nano-, or even picoliter) results in faster depletion of nutrients and more local accumulation of secreted metabolites (might be toxic at high concentrations). Therefore, to accomplish long-term cell culture in microfluidic system, techniques that allow frequent replacement of culture media are needed. For adherent cells, perfusion culture (continuous flow) is an appropriate choice to realize constant nutrition replenishment and wastes removal. And meanwhile, it accurately mimics the *in vivo* mass transport within microvascular network [170], thus providing more biologically meaningful data for cell-based assays. For instance, with perfusion culture, human hepatocarcinoma cell line (Hep G2) has undergone attachment, spreading and growth inside two-layer PDMS chip [176]. Blood vessel cells have also been successfully cultured on the inner surface of microchannels to generate vasculature system in-situ [177].

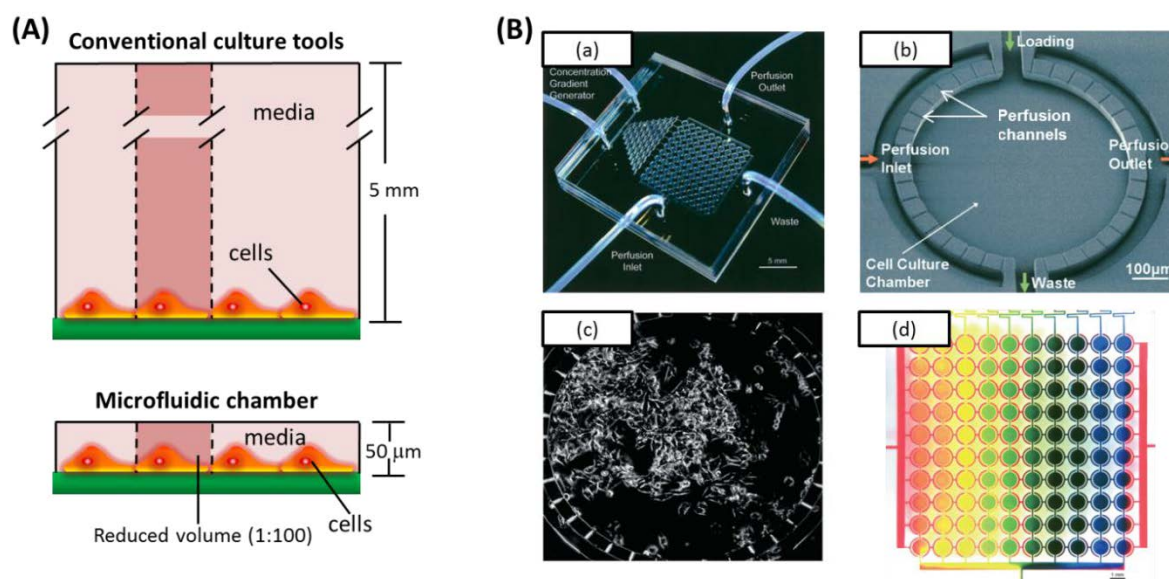


Figure A-26: Cell culture in microfluidic system. (A) Illustration of “small-volume effects” in microfluidic devices. (B) High-throughput microfluidic perfusion array for long-term cell culture [178]: (a) Photograph of  $2 \times 2$  cm device. (b) SEM image of a single culture chamber with four fluidic access paths and several surrounding perfusion channels. (c) Phase contrast image of Hela cells growing under perfusion culture for 6 days. (d) Concentration gradient profile demonstrated by red dye perfused from left to right, blue and yellow dyes loaded from top of gradient generator.

Taking the advantages of microfluidic units such as channels, valves and gradient generators, parallel perfusion is easily conducted to create multiple microenvironments without manual intervention. Hung et al. [178] presented a single self-contained microfluidic system (Figure A-26B) which assembled 100 individually controllable cell culture units

(10×10 array) for high-throughput assays. Each single unit comprised a circular chamber surrounded by several narrow perfusion channels and four fluidic access ports. Continuous perfusion of medium and reagents enabled long-term growth (14 days), passage, and real-time fluorescence monitoring of HeLa cells. Stable gradient of concentrations (unique microenvironment in each chamber) could be easily accomplished by using two fluidic inlets, making it quite suitable for parallel assays, and accordingly exhibiting large applicable potential in drug screening, bioinformatics and quantitative cell biology.

Generally for microfluidic 2D bottom culture, cells experience continuous laminar flow of medium driven by gravity, external syringe pumps or on-chip peristaltic pumps [170]. This robust perfusion culture allows cell growing under stable condition for several weeks until confluence is reached [179]. In most situations, perfusion rates are balanced between sufficient mass transport and safe shear stress. Low shear stress from microfluid leads to nearly no injury to the normal activities of cells, and that is particularly meaningful to the following cell-based research. Shear stress may have detrimental effects at high levels; however the levels can be reduced by many ways such as decreasing flow rate, increasing height of culture chamber, and incorporating micropillars or microwells. Medium perfusion as well as fluid velocities varies greatly depending on cell type. For certain highly environment-sensitive cells (e.g., neuron cells [180]), culture is even maintained in static or half-perfusion (molecule diffusion with persistent nutrients supply) microenvironments.

### **3.2.2. Cell manipulation in microfluidic devices**

In microfluidic system, various manipulation techniques [181] have been developed to realize accurate control of cell trajectory. Typical manipulations, categorized by externally applied forces, including:

- **Optical manipulation:** From differences between pulling force and repulsive force exerted by a highly focused laser beam, target cells can be simultaneously measured and separated according to their sizes or intrinsic optical attributes. Although it may induce photodamage, due to the high sensitivity and contactless manipulation, this method is still applied onto a wide range of biological molecules or whole cells (Figure A-27A), especially in blood-disease-related and cell deformability-based diagnosis [182,183].

- **Magnetic manipulation:** Magnetic forces come from either intrinsic such as iron-containing hemoglobin in erythrocytes, or extrinsic like cells labeled with magnetic nanoparticles through specific surface proteins [184,185]. Effective recognition and localization could be achieved under certain magnetic field (Figure A-27B).

- **Electrical manipulation:** Target cells are driven to move by a non-uniform electric field (Figure A-27C) [186]. The motion is determined based on their dielectric properties such as magnitude and polarity of particles' electrical charge. Viable and nonviable cells could be separated in this way.

- **Mechanical manipulation:** Hydrodynamic cell manipulation such as sheath fluid [187] to align cells into a single line, or narrow microstructures selectively permit cells passage according to their sizes [188]. This method utilizes the intrinsic merit of laminar flow, achieving cell manipulation simply by adjusting flow rate or microstructural components (Figure A-27D).

- **Other methods:** Cell control is operated through droplet-based encapsulating with controlled microenvironment (Figure A-27E) [189]; through acoustophoresis initiated by radiation force [190]; or through affinity between cell surface receptors and a surface of pre-coated microstructures (Figure A-27F) [191].

All these technologies permit predicable separating, sorting, trapping, focusing and alignment of target cells from heterogeneous solution, offering new tools to study cell biology more accurately and pertinently, making microfluidic system more eligible for both fundamental and clinical applications.



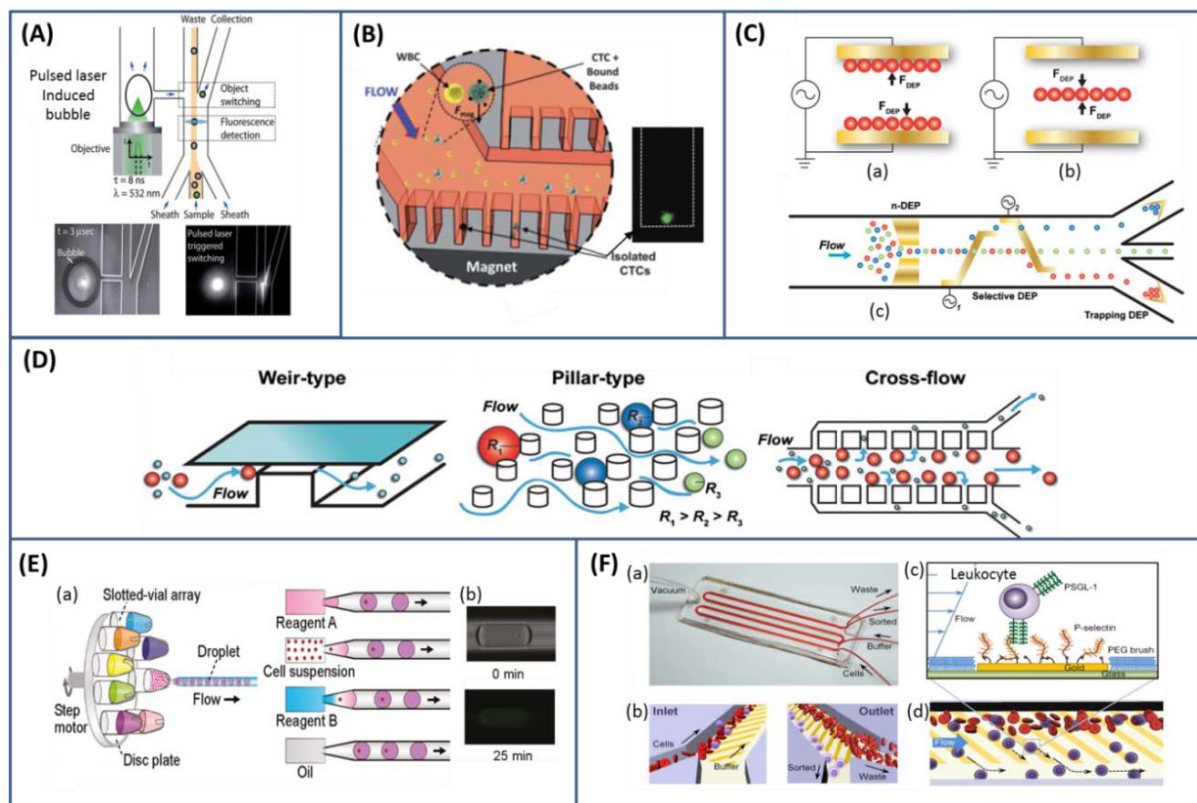


Figure A-27: Main cell manipulation techniques in microfluidics. (A) Schematic of pulsed laser triggered fluorescence cells sorter, the target cell detected upstream and deflected towards collection channel by a cavitation bubble from focused pulsed laser beam [182]. (B) Magnetic bead-bound circulating tumor cells isolated from whole blood inside a microfluidic-micromagnetic separation device [185]. (C) Dielectrophoretic manipulation can be (a) positive or (b) negative to (c) affect where cells are positioned [186]. (D) According to sizes, cells can be separated simply through passing different microstructures [186]. (E) High-efficiency single-cell encapsulation with sequential reagents addition in droplet-based microfluidic system [189]. (a) Schematics of the system. (b) Enzymatic reaction on single cell is initiated inside droplet. (F) Affinity-based cell separation [191]. (a) Photograph of device. (b to d) A mixture of cells from blood sample can get a fast segregation after interaction with inclined molecular patterns.

### 3.2.3. Cell-based analysis on microfluidic platforms

Microdevices of diverse materials (see the context in Appendix II.1) have been developed for specific assays. Among which PDMS-glass hybrid microchip, owing to its elasticity, biocompatibility, and optical transparency, has become the standard base for cells analysis. The entire biological study can be compacted in one portable device. After integration of ultrasensitive analytical instruments, myriad meaningful biological information such as intracellular contents, cellular responses to chemical stimulus, and even cell-cell interactions are obtainable with a high throughput and low consumption.

Based on microfluidic system, thousands of innate immune responses of fibroblasts to inflammatory cytokine tumor necrosis factor (TNF- $\alpha$ ) have been recorded during a single optical experiment [192]; and massive data of T-cell dynamic secretion [193], stem cell differentiation [194], cell migration [195], G-protein-coupled signaling [196] have also been extracted in a high parallelized fashion.

Besides the highly-pervasive optical sensing method, electrochemical detection gains extraordinary popularity due to high selectivity, sensitivity, fast response, ease of miniaturization and minimum instrumentation. Nowadays, advanced microfabrication technologies (photolithography, lift-off, etc.; see Appendix II.2) further accelerate the sophistication of electrodes-incorporated microdevice. Electroactive compounds released by living cells have been effectively detected.

The most frequently used design to detect emitted electroactive species is to place planar microelectrode beneath activated cells [197-200]. Cui et al. [201] fabricated microelectrode array (MEA) of planar Au microdisks with a diameter of 30  $\mu\text{m}$  in an attempt to conduct drug-screening research on a group of PC12 cells (Figure A-28A). Real-time amperometric spectra of released dopamine were obtained in a rapid and high-throughput manner.

More recently, simultaneous detection of multiple messengers was accomplished in the group of Bedioui [202]. By establishing individually sets of gold microdisk (50  $\mu\text{m}$  in diameter) arrays, two biologically-relevant molecules  $\text{NO}^{\bullet}$  and  $\text{ONOO}^{-}$  were detected simultaneously (Figure A-28B). Great sensitivity and selectivity were obtained on the electrode network through surface modification and potential optimization (-0.1V vs. Ag/AgCl at pristine gold surface for  $\text{ONOOH}$  reduction; +0.8 V vs. Ag/AgCl at polyeugenol and polyphenol bilayer coated gold surface for  $\text{NO}^{\bullet}$  oxidation). Neither obvious interfering response nor cross-talk between individual sensors was observed. This work gives promising opportunity to screen  $\text{NO}^{\bullet}$  and  $\text{ONOO}^{-}$  production from living cells.

In some cases, optical techniques are incorporated during electrochemical detection to give complementary information. One example is shown in Figure A-28C, this previous work in our group [203] reported the monitoring of active neurotransmitter serotonin from BC21 cells by collaboration of transparent ITO electrodes and total internal reflection fluorescence microscopy (TIRFM). Thanks to the electrode's transparency, simultaneous electrochemical

and optical results were obtained during the same release process, enabling elucidation of secretory mechanism and active zone at the single-vesicle level.

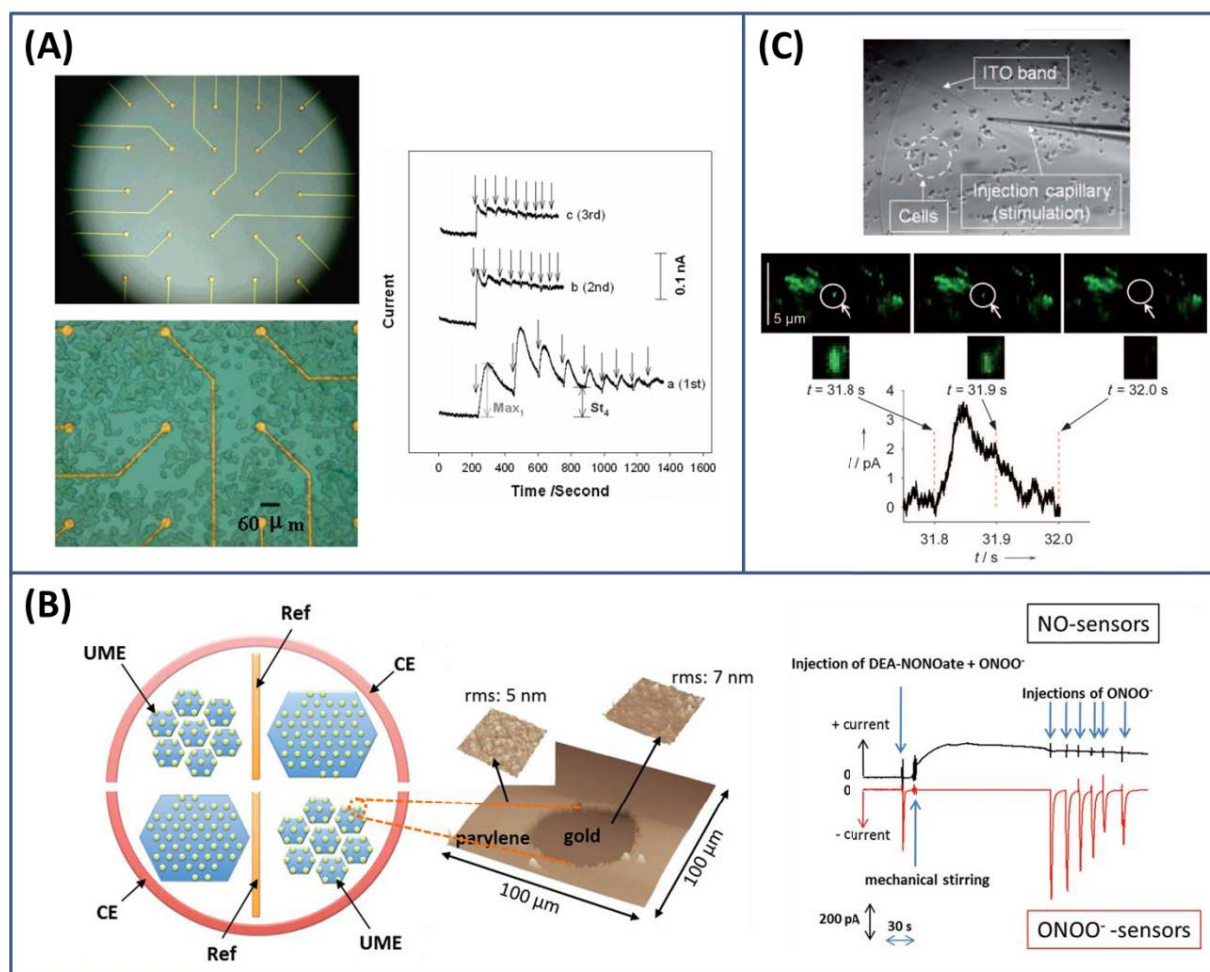


Figure A-28: Electrochemical detection of cellular messengers inside microfluidic system. (A) Gold microdisks-integrated biochip for dopamine detection from a group of PC12 cells, showing statistical information of drug effects [201]. (B) Electrochemical sensor arrays that allow simultaneous amperometric detection of NO<sup>•</sup> and ONOO<sup>-</sup> on individual sets of microelectrodes [202]. (C) Coupled TIRFM-amperometry real-time measurement of secretory neurotransmitter from adherent BC21 cells on ITO microband electrodes [203].

Recently, Huang et al. [204] have developed a MEAs-integrated multi-layer PDMS microchip (structure shown in Figure A-29A) to realize automated long-term cell culture and to amperometrically monitor cellular trace release during their propagation process. In their work, cells were continuously cultured inside a microchamber in a “circular-center” and “bottom-up” perfusion model; while underlying Ti/Pt MEAs (each with radius of 12.5 μm) real-time collected the trace release of dopamine from PC12 cells (Figure A-29B).

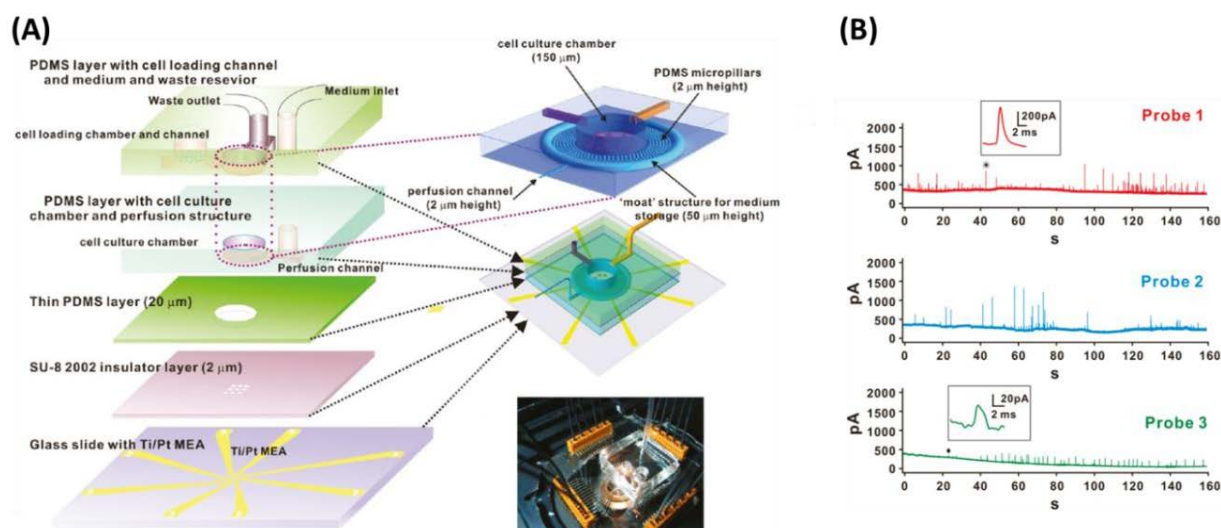


Figure A-29: MEAs-integrated PDMS-glass microchip for living cells detection [204]. (A) Structure of multi-layer microdevice. (B) Dopamine released from three individual PC12 cells collected by MEAs.

On the other side, taking the advantage of fluidic manipulation inside microsystem, not only the perfusion culture of living cells is guaranteed but also facilitates a precise spatial and temporal delivery of drugs and ensuing secretion. The common fluid network renders relatively simple design of the versatile platform [205]. Devices with well-designed structures and instruments would be established according to specific experimental requirements.

Goto et al. [206] established one highly-integrated microchip which successfully detected NO<sup>•</sup> released from population of macrophage-like cells (Figure A-30A). Cell culture, chemical/enzymatic reaction, and detection were integrated in separate zones; with the overall process connected by flowing solution. As compared to the repetitive detection of isolated single cell, monitoring of a global population of cells presently gains its popularity [207,208]. These assays provide statistical relevance to exclude rare events, allowing direct access to the insightful cognition of cells average behaviors.

By incorporating delicate microfluidic trapping array (microwells, microjails or valve-based structures), single cells could be individually localized at desired place when loaded by driven flow [209-211] (Figure A-30B). Thus the statistic data as well as cells variations can be simultaneously investigated. However, extraordinarily sensitive monitor is indispensable for each data collection.

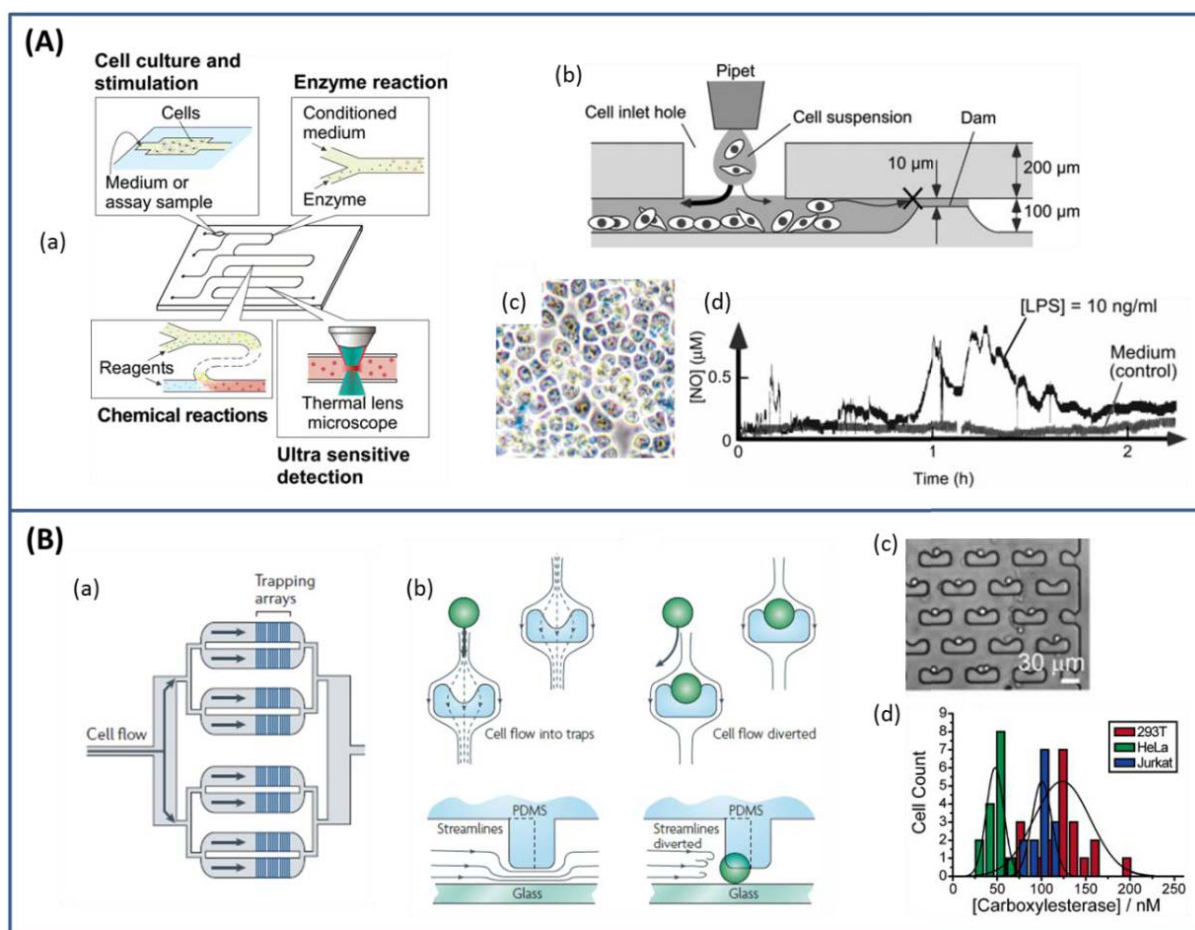


Figure A-30: Integrated bioassay systems for cell monitoring. (A)  $\text{NO}^*$  released from macrophage-like cell populations monitored within a glass microchip [206]. (a) Concept of this flow-based system including cell culture, stimulation, enzyme/chemical reactions and downstream detection. (b) Cross section of culture chamber, with cell suspension dropped from inlet hole and held back by the dam structure. (c) Micrograph of J774.1 cells in microchamber for 2 days under continuous flow. (d) Typical time course of  $\text{NO}^*$  release from J774.1 cells stimulated by lipopolysaccharide. (B) Single-cell analysis using high-density trapping arrays [211]. (a) A sketch of overall microchip. (b) Top and side view of schemes that describe cell isolation mechanism. The cup-shaped PDMS site can trap one cell while fluid flow diverting succeeding cells pass by. (c) A phase contrast image of an array of single trapped cells with scale bar of 30  $\mu\text{m}$ . (d) Histogram of intracellular carboxylesterase concentrations for 293T, HeLa, and Jurkat cells detected on this platform.

The feasibility of fluidic manipulation within microdevice ought to be highlighted particularly for electrochemical detection [212]. Owing to the flowing solution and the forced convection above sensing electrodes, mass transport of electroactive analyte should drastically increase and lead to higher signal-to-noise ratio. Thus by combining elaborately-designed microstructures, ultrasensitive sensors, and controllable flow, microfluidic devices can offer versatile and effective platforms for cellular and subcellular monitoring.



### 3.3. Conclusion of section 3

Investigation of living cells gives a direct chance to understand complex life phenomena. The advent of **microelectrode**, with its compatible dimension, high signal-to-noise ratio, fast response, offers new scope and opportunities to reveal the most difficult mechanisms of cell-related behaviors. By approaching a micro- or nano-scale electrode near isolated single cell, diverse electroactive messengers (including ROS/RNS products during oxidative stress) can be detected in efficiency and accuracy. However, an insightful and reliable understanding of cells statistical behaviors usually needs fastidious repetition of series of experiments.

Recent **microfluidic devices** have become more sophisticated in an effort to provide powerful platform for biological analysis. This system integrates cell culture, reaction, and detection into a portable device. With the unique benefit of laminar flow, the on-chip bioanalytical experiments are conducted in an automated and high-throughput approach. Multiple microelectrodes (no matter in band, disk, square, or circle shapes) can be flexibly patterned at the device substrate and the parallel detection of multiple analytes is thus feasible. In contrast to the traditional synaptic detection which offers each time one result from one single cell, the detection in microfluidic platform allows convenient and simultaneous analysis of a collective group of living cells during a short experimental period. Further miniaturizing and multiplexing are also feasible without compromising device functionalities, making this portable electrochemical sensor really a viable approach in bioanalytical domain.

## 4. Conclusion of state-of-the-art and perspectives

In exploring the in-depth origins of oxidative stress, electrochemistry, with ongoing refinements in instrumentation and methodology, gains enormous popularity to decipher the bursts contents from living cells. Surface modification of microelectrode such as Pt-black deposit promotes the detection sensitivity and selectivity of several key oxidative compounds (i.e.,  $\text{H}_2\text{O}_2$ ,  $\text{ONOO}^-$ ,  $\text{NO}^*$ , and  $\text{NO}_2^-$ ). Besides, microfluidic device, with the unique benefits of

advanced microfabrication technologies and laminar flow, offers a way to manipulate and detect living cells in an automated and high-throughput manner. Thin-layer microelectrodes can be easily patterned onto microfluidic substrate and enhanced faradaic currents can be expected under the convective mass transport formed by flowing solution. Therefore, **microelectrodes-integrated microdevices** should offer excellent and flexible platforms to perform high-performance detection of electroactive **ROS/RNS** from **living cells** during cellular activities.

PDMS-glass hybrid microchips are well adapted to bioanalytical experiments due to the optical transparency, biocompatibility, and stable chemical/mechanical properties of assemblies. PDMS upper layers contain microstructures while microband electrodes are usually patterned on glass substrate. Very elaborated devices can be envisaged to achieve cell culture, stimulation, and simultaneous detection of multiple ROS/RNS under different experimental configurations.

In this context, coupling of microfluidics with electrochemical detections is thus very promising. Ensuing results should allow a fine and rapid understanding of cells behaviors, for quantitative and kinetic investigations.

*PART B: In vitro electrochemical detection  
of ROS/RNS at highly sensitive Pt/Pt-black  
microband electrode inside microfluidic  
system*





## **PART B: *In vitro* electrochemical detection of ROS/RNS at highly sensitive Pt/Pt-black microband electrode inside microfluidic system**

As preliminary steps for developing highly effective microelectrodes-integrated microdevices, the fabrication of Pt-black deposits onto thin-layer microbands need to be optimized before use in microfluidics. According to the convective mass transport under laminar flow inside microchannel, analytical performances of the integrated Pt/Pt-black electrodes can be evaluated by comparing the electrochemical responses from synthetic solutions with steady-state predictions. In this context, theoretical regimes at microchannel electrodes will be first presented. Then the optimization of Pt-black deposition and the measurements towards  $\text{H}_2\text{O}_2$ ,  $\text{ONOO}^-$ ,  $\text{NO}^\bullet$ , and  $\text{NO}_2^-$  solutions will be sequentially investigated.

### **1. Convective-diffusive mass transport above Pt/Pt-black microchannel electrode**

#### **1.1. Mass transport regimes above a single microband electrode**

##### Principle

By considering an embedded microband electrode (width  $w$ ) within a microchannel (width  $L$  and height  $h$ ), the convective-diffusive mass transport regimes can be identified as a function of these geometrical parameters in association with the hydrodynamic parameters. Taking into account a wide rectangular microchannel ( $L \gg h$ ), a simplified 2D approximation

can be applied (Figure B-1) to evaluate the current responses by neglecting the influence of lateral walls onto the flow velocity profile [213].

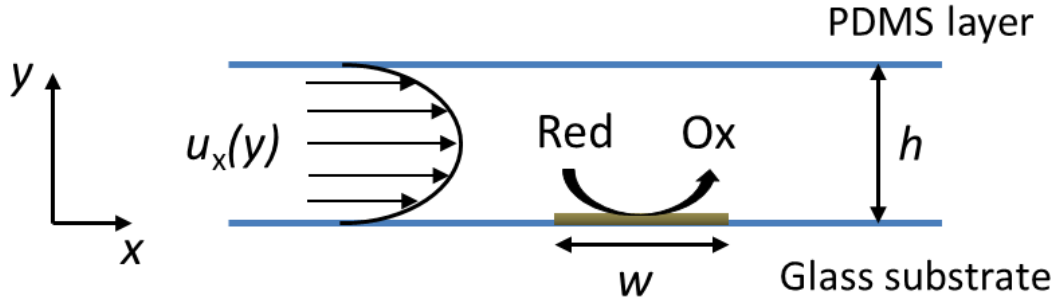


Figure B-1 : 2D-scheme of device used for numerical simulations when a parabolic flow propagates across the microchannel [213].

Under this assumption, problems can be solved by numerical simulations. Some previous results from our group are presented below giving a general overview of regimes achieved under such conditions [214,215]. Diffusion and convection are governed by the following mass transport equation:

$$\frac{\partial c}{\partial t} = D \left( \frac{\partial^2 c}{\partial x^2} + \frac{\partial^2 c}{\partial y^2} \right) - u_x(y) \frac{\partial c}{\partial x} \quad (\text{B.1})$$

where  $D$  is diffusion coefficient and  $c$  is redox species concentration.  $u_x(y)$  is the flow velocity whose profile is assumed to be parabolic across microchannel section:

$$u_x(y) = 6u_{av} \frac{y}{h} \left( 1 - \frac{y}{h} \right) \quad (\text{B.2})$$

where  $u_{av}$  is the average flow velocity over this section.

$Pe$  is the Péclet number matching the time scales of convective and diffusional transport:

$$Pe = \frac{u_{av} h}{D} \quad (\text{B.3})$$

Several dimensionless parameters are introduced to simplify the resolution, including geometries normalized by the channel height  $h$ :  $X = x/h$ ,  $Y = y/h$ ,  $W = w/h$ ; and concentrations normalized by the bulk concentration  $c^*$ :  $C = c/c^*$ .

Time scale is given by:

$$\tau = \frac{Dt}{h^2} \quad (\text{B.4})$$

And the flow velocity is:

$$V_x(Y) = \frac{u_x(Y)h}{D} \quad (\text{B.5})$$

Equation (B.1) becomes:

$$\frac{\partial C}{\partial \tau} = D \left( \frac{\partial^2 C}{\partial X^2} + \frac{\partial^2 C}{\partial Y^2} \right) - V_x(Y) \frac{\partial C}{\partial X} \quad (\text{B.6})$$

Simulation of the diffusion-convection process is performed by solving numerically the new Equation (B.6) under the following boundary conditions:

$$\tau < 0, C = 1 \text{ in the microchannel} \quad (\text{B.7})$$

$$\tau \geq 0, C = 0 \text{ at the electrode surface} \quad (\text{B.8})$$

$$\tau \geq 0, C = 1 \text{ at the solution upstream far away from electrode} \quad (\text{B.9})$$

$$\partial C / \partial Y = 0 \text{ at insulating surface} \quad (\text{B.10})$$

Accordingly, the dimensionless current is calculated by:

$$\Psi_{(\tau)} = \frac{i_{(\tau)}}{nFDLc^*} = \int_0^W \left( \frac{\partial C_{(\tau)}}{\partial Y} \right)_{Y=0} dX \quad (\text{B.11})$$

And the value for steady-state current is:

$$\Psi_s = \frac{i_s}{nFDLc^*} = \int_0^W \left( \frac{\partial C}{\partial Y} \right)_{Y=0} dX \quad (\text{B.12})$$

### Theoretical convective-diffusive regimes

Concentration profiles simulated with time for several conditions ( $W$ ,  $Pe$ ) are shown in Figure B-2A.  $W$  and  $Pe$  have opposite-mirror effects on controlling the physical nature of diffusion-convection transport. Depending on the ratio  $W/Pe$ , three main steady-state regimes may be achieved under flow conditions. When  $W/Pe > 1.2$ , a thin layer regime is set (zone I); diffusion-convection layer thickness is the highest and limited by channel height. In contrast,

when  $W/Pe < 0.04$  (zone III), a Levich regime is quickly established and the layer thickness is mainly controlled by convection. When  $0.04 < W/Pe < 1.2$  (zone II), the behavior is intermediate between the two previous situations.

A zone diagram which describes all the contributions that govern mass transport at a single band electrode is represented in Figure B-2B. Obviously, zone II is prevalent. A threshold value of  $W/Pe \approx 0.56$  (dashed line in this figure) distinguishes the predominant role of convection from diffusion. More specifically, when  $W/Pe > 0.56$ , regime tends to behave according to a thin-layer behavior; whereas when  $W/Pe < 0.56$ , situation turns more like Levich-type condition. Beside three main domains, two additional zones (IVa and IVb) are also presented in the diagram, but they only account for deviations at very low  $W$  and/or  $Pe$  value.

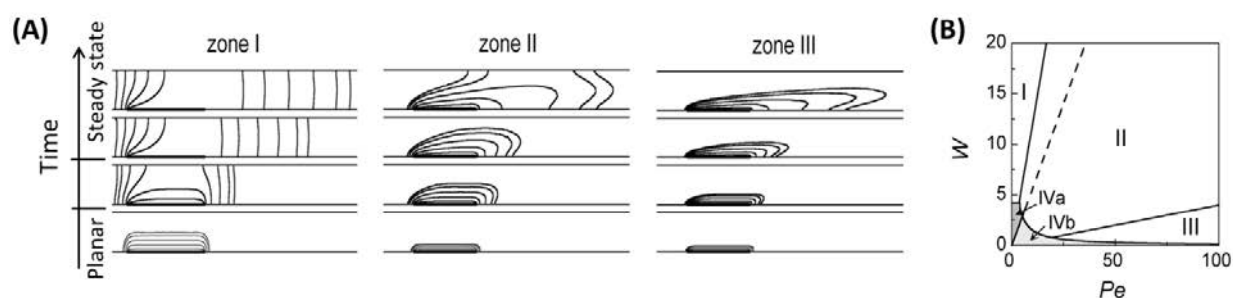


Figure B-2: (A) Simulated concentration profiles for three principal regimes of convective-diffusive mass transport, from transient states (bottom) to steady states (top) [215]. (B) Zone diagram shows location of zone I, II, III, IVa and IVb according to  $(W, Pe)$ . Dashed line represents  $W/Pe \approx 0.56$  where contributions of diffusion and convection are equivalent [214].

### Validation and prediction

Validity of these numerical simulations was tested experimentally by monitoring steady-state current  $\Psi_s$  with redox mediators for various values of  $Pe$  and  $W$  (Figure B-3A). A good agreement between theoretical predictions and experimental data was found, especially for conditions under prevalence of convection (solid symbols at zone II and III in Figure B-3B).

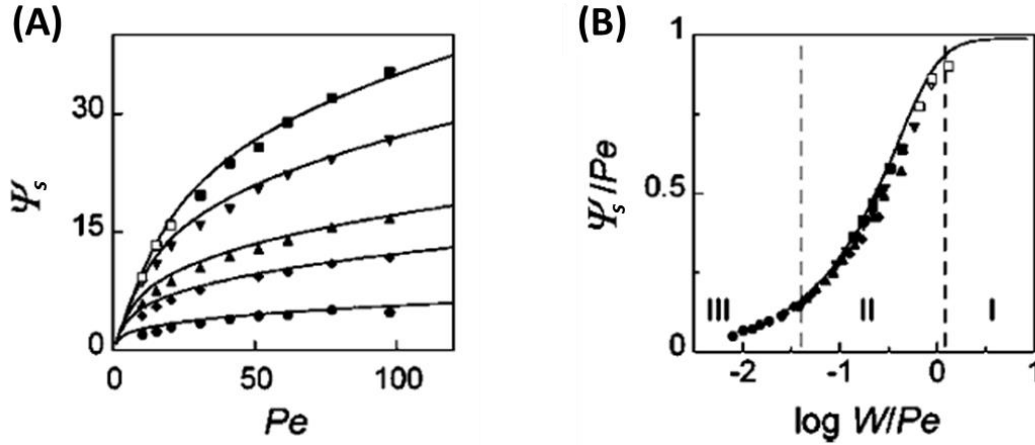


Figure B-3: (A) Experimental (symbols) and simulated (lines) steady-state current  $\Psi_s$  as a function of  $Pe$  for various  $W$ : (●,○) 0.8; (◆,◇) 2.6; (▲,△) 4.4; (▼,▽) 8.9; (■,□) 13.5. (B) Variation of  $\Psi_s/Pe$  versus  $\log W/Pe$ . Empty symbols correspond to conditions when diffusion is dominant ( $W/Pe > 0.56$ ) and solid symbols when convection prevails ( $W/Pe < 0.56$ ). In all cases,  $WPe > 15$  [214].

For each condition under laminar flow, a steady state is reached. The average thickness of diffusion-convection layer ( $H_s$ ) developed over the microband is estimated graphically by analyzing the streamline layers deduced from concentration profiles (Figure B-4A). These streamlines describe species trails and determine the solution volume probed by the electrode. Equivalent diffusion layer thickness  $\delta_s$  is given into the dimensionless form:

$$H_s = \frac{\delta_s}{h} \quad (\text{B.13})$$

A numerical evaluation of  $H_s$  has been performed in each zone investigated above, and these values are shown as a function of  $\log W/Pe$  in Figure B-4B. Note when mass transport is mainly controlled by convection (for zone III and part of zone II), a simple relation between current and layer thickness is obtained on the basis of Nernst concept:

$$i_s = \frac{nFLwDc^*}{\delta_s} \quad (\text{B.14})$$

With the use of present dimensionless parameters, Equation (B.13) can be rewritten as:

$$H_s = \frac{W}{\Psi_s} \quad (\text{B.15})$$

Comparison between  $H_s$  (simulated  $H_s$  and  $H_s$  determined from experimental current) as function of  $W/Pe$  shows a good agreement as long as convection predominates. Under other conditions, equivalent concept of the Nernst layer does not strictly apply.

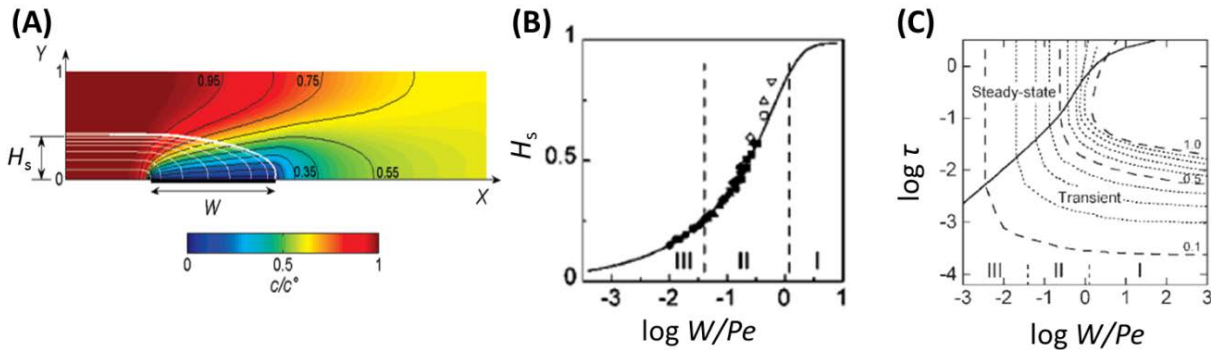


Figure B-4: (A) Simulated concentration profiles and related streamlines (white curves) across the microchannel when performing detection in zone II where convection is dominant. In this case, average thickness of the diffusion-convection layer:  $H_s = 0.42$  for  $W = 3$  and  $Pe = 20$ . (B) Values of  $H_s$  estimated from experimental currents as comparison with numerical simulation curve (same symbols as in Figure B-3B). (C) Transition time  $\tau_s$  in three zones (solid line), and  $H$  values (10 isolines plotted from  $H = 0.1$  to 1) as function of  $\tau$  and  $W/Pe$ . The results were based on setting a relative threshold on variation of steady-state current in 5% [215].

The dimensionless time  $\tau_s$  required for the current to attain its steady-state value increases with the ratio  $W/Pe$ . Its variation in three principal zones is shown in Figure B-4C (solid line). Clearly, this transition time from planar diffusion to steady state is quite short when convection prevails on diffusion. For conditions  $W/Pe < 0.1$  (zone III and part of zone II) it obeys a simple relationship:

$$\tau_s = 0.23 \left( \frac{W}{Pe} \right)^{2/3} \quad (\text{B.16})$$

When  $W/Pe > 0.1$ , this equation is no longer valid but  $\tau_s$  still depends on  $W/Pe$ .

All these theoretical simulations and experimental validations help to establish a fundamental overview about diffusive-conductive mass transport taking place at a single microband electrode embedded within a linear microchannel. Under assumption of a parabolic flow profile in laminar flow, different limiting and intermediate regimes could be delineated according to device geometry and flow velocity. Moreover, current responses, diffusive-convective layer thickness, as well as transition time could also be deduced. This gives clues to predict and optimize electrode behaviors inside microdevice for particular analysis.

## 1.2. Choice of mass transport regime in our microfluidic device

In order to monitor minute amount of ROS/RNS in a short time, a microfluidic system with small channel dimensions, moderate electrode size and sufficiently high flow rate is required. This device is supposed to deliver a steady-state current proportional to concentration, with a high signal-to-noise ratio due to convective mass transport. For that purpose, the convective regimes described above (zone III and zone II for  $W/Pe < 0.56$ ) are more suitable for monitoring concentrations of reactive species inside microchannel. According to channel dimensions usually used in microfluidics and microfabrication procedures, the characteristics of the microchip and flow velocity were chosen as detailed below.

### Microchannel dimensions

Scheme of our integrated device is illustrated in Figure B-5A.

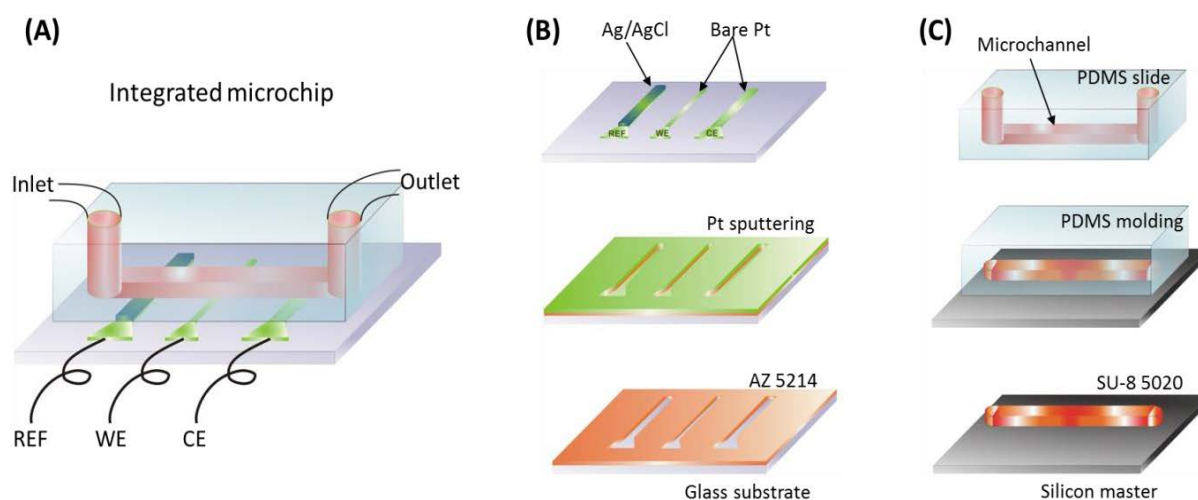


Figure B-5: (A) Schematic view of microfluidic device, showing the relative positions of reference electrode (REF), working electrode (WE) and counter electrode (CE) inside microchannel. (B) Illustration of fabrication process of microband electrodes (from bottom to top), and (C) the molding process of PDMS replica (from bottom to top).

It consisted of two components: a glass substrate patterned with microband electrodes sequentially through photolithography and lift-off technologies (Figure B-5B); and a microchannel-comprised PDMS slide molded from a prefabricated silicon master (Figure B-5C). Then, the microchannels were assembled perpendicular to the parallel microband electrodes after plasma treatment. The home-made Ag/AgCl reference electrode (REF,  $w = 500 \mu\text{m}$ ; made by immersing Ti/Pt/Ag microband in 5 mM  $\text{FeCl}_3$  for 30 s) was located



upstream of Pt working electrode (WE,  $w = 197 \mu\text{m}$ ; Ti/Pt microband), and the Pt counter electrode (CE,  $w = 500 \mu\text{m}$ ; Ti/Pt microband) was located downstream. In this part of work, all the potentials described as “/REF” were supported versus Ag/AgCl. The details of fabrication are presented in Appendix III.2 of “Microsensor for *in vitro* detection”. The effective electrode lengths were limited by microchannel width ( $L = 200 \mu\text{m}$ ) and the volume of solution above these microbands was restricted by microchannel height ( $h = 20 \mu\text{m}$ ). The real microdevice consisted of three independent microchannels and several parallel WEs for the sake of use; however, during each experiment, only one WE was connected and only one channel was filled with solution, the others remaining empty.

### Flow velocity

As mentioned previously, the flow velocity was chosen to ensure a convective regime at the microband electrodes. However, flow velocity cannot be too fast for practical reasons and ease of experiments and not too slow to maintain a good signal-to-noise ratio. A good compromise was thus to set the mass transport regime in zones III and II with:

$$0.02 < \frac{W}{Pe} < 0.1 \quad (\text{B.17})$$

The corresponding conditions are reported on the diagram below (red zone in Figure B-6):

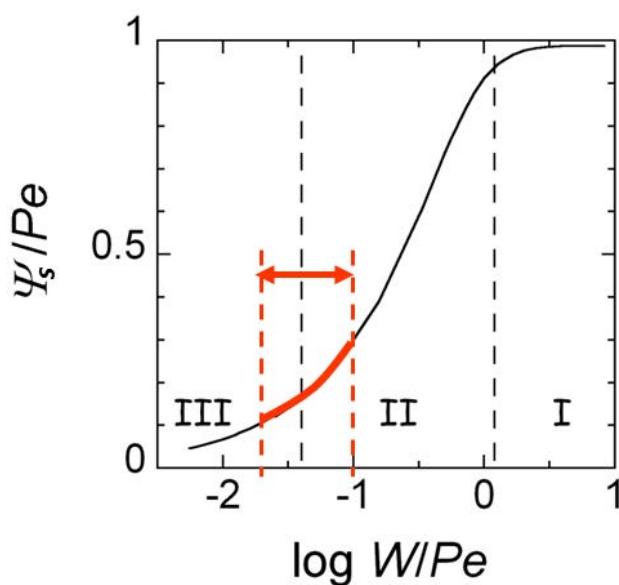


Figure B-6: Numerical simulation of  $\Psi_s/Pe$  vs.  $\log W/Pe$ ; red zone refers to conditions when  $0.02 < W/Pe < 0.1$ .

According to the microchannel height and electrode width used ( $h = 20 \mu\text{m}$  and  $w = 197 \mu\text{m}$ ),  $Pe$  is between:

$$100 < Pe < 500 \quad (\text{B.18})$$

A moderate value of  $2 \mu\text{L min}^{-1}$  (i.e.,  $u_{\text{av}} = 0.83 \text{ cm s}^{-1}$  inside the microchannel) was experimentally set as a good choice. Firstly it is because this flow rate allows analytes with diffusion coefficient from  $0.3$  to  $1.7 \cdot 10^{-5} \text{ cm}^2 \text{ s}^{-1}$  (for most aqueous molecules) to be analyzed within the  $Pe$  range indicated above. Moreover, no leakage or flow instability is usually observed under this velocity. This value should not induce also any cell damages for future applications with living cells.

### Experimental validation of the mass transport regime

Analytical performance under flow rate of  $2 \mu\text{L min}^{-1}$  was tested and compared to theoretical predictions at bare Pt electrodes using ferrocenemethanol (FcMeOH:  $D = (7.6 \pm 0.4) \times 10^{-6} \text{ cm}^2 \text{ s}^{-1}$ ;  $n = 1$ ;  $c^* = 0.5 \text{ mM}$ ) as redox mediator.

Here the Peclet number was given:

$$Pe = 218 \quad (\text{B.19})$$

And the corresponding steady-state current ( $i_s$ ), convective-diffusion layer thickness ( $\delta_s$ ) and time to reach the steady-state regime ( $t_s$ ) were respectively:

$$i_s = \Psi_s F D L c^* = 280 \text{ nA} \quad (\text{B.20})$$

$$\delta_s = H_s h = 5 \mu\text{m} \quad (\text{B.21})$$

$$t_s = \frac{\tau_s h^2}{D} = 0.02 \text{ s} \quad (\text{B.22})$$

Experimentally, our first results showed a good agreement between predictions and experimental results as observed in Figure B-7. The average steady-state current (more than 10 devices were investigated) was equal to the theoretical value within 3% error. And the quite fast establishment of steady state (plateau feature of voltammogram in Figure B-7A as well as the immediately reached limiting current during amperometrical recording in Figure B-7B) was also verified in our microfluidic device.

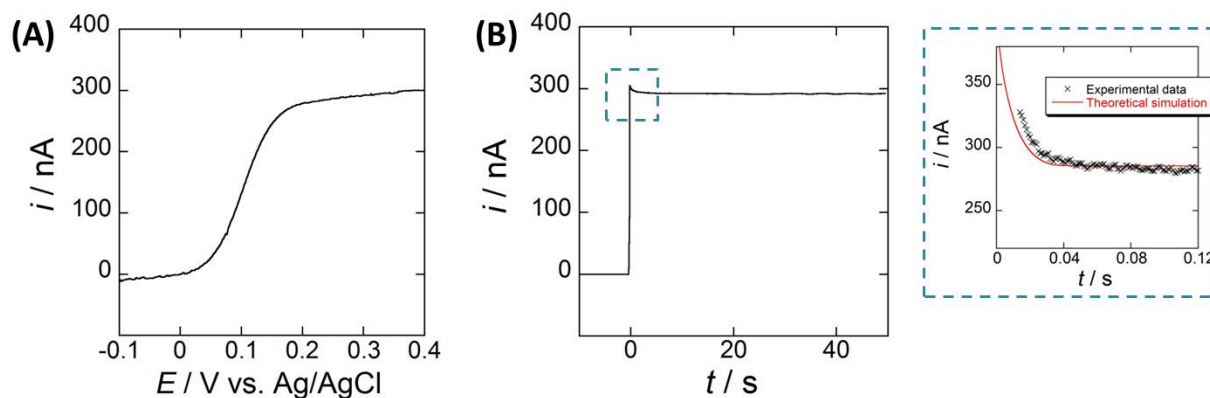


Figure B-7: Electrochemical measurements of 0.5 mM FcMeOH (dissolved in 10 mM PBS) flowing solution at Pt microband electrode. (A) Voltammogram at scan rate of  $10 \text{ mV s}^{-1}$ . (B) Chronoamperometry curve at  $0.4 \text{ V/REF}$ ; potential imposed at  $t = 0$ . The inset graph (within blue pane) demonstrates the comparison between experimental data (black crosses, after subtracting PBS background current) and theoretical simulation (red line) during the establishment of steady state in amperometry.

Therefore, beside low samples and reagent consumptions, the present microdevice allows fast and effective electrochemical detections under well-defined steady states. Measurements are performed in a reliable and predictable manner. In this case, samples with minute quantities are expected to be detected accurately.

### 1.3. Optimization and evaluation of Pt-black deposit

The present microfluidic device promotes advanced analytical methods for performing rapid analysis with high sensitivity. However, the detection of cellular messengers on metallic electrode still involves considerable challenges that need to be addressed. As mentioned in the introduction (Part A 2.2.), bare electrode suffers greatly from low electron transfer kinetics and surface fouling, often resulting in diminished activity, poor reproducibility, and even failure of detection. Indeed, analytical measurements must necessarily display satisfying sensitivity as well as long-term stability, and electrodes must enable their electrochemical activities constantly at a high level.

For this purpose, platinum-black coated platinum electrodes (Pt/Pt-black electrodes) were used in this work [216]. This surface coating is well known for a high surface area with a large number of active sites to prevent electrode against surface passivation [217-219].

Effective detections of important ROS/RNS from living cells have been successfully achieved on platinized carbon-fiber microelectrode [11,75,109,117,133,220], indicating that Pt-black deposit is an attractive modification strategy to guarantee high analytical performances even in a complex physiological environment.

In the following, Pt-black films are deposited onto microband electrodes and integrated into microfluidic device to establish a new generation of high-performance electrochemical device. Platinization and evaluation of Pt/Pt-black microband electrodes are achieved. The optimal conditions are investigated as a function of thickness, morphology and electrochemical responses.

#### Pt-black plating process

Pt-black was platinized upon Pt(IV) reduction from hydrogen hexachloroplatinate(IV) solution ( $\text{H}_2\text{PtCl}_6$ ). Lead(II) acetate trihydrate was also involved in this solution as an impurity to initiate and control the Pt-black growth during electrodeposition. This composition should result in highly porous surface of the deposits [221].

Electrochemical fabrication and characterization of the Pt deposits were carried out in static open solutions (i.e., without microchannel on top of electrodes) at room temperature. In order to determine suitable platinizing conditions, a cyclic voltammetry of deposition solution was performed beforehand at bare Pt microelectrode (Figure B-8A). A gradually-increased current density from +0.2 to -0.6 V vs. Ag/AgCl was ascribed to Pt(IV) reduced into Pt(0); while a sharp increase observed at more negative potentials resulted from the secondary reaction of hydrogen formation. Therefore, Pt-black platinization was performed within the former zone. In a first approach, deposits fabricated by means of constant potential and constant current were both investigated (Figure B-8B). We observed that constant-current mode gave dense Pt-black deposits without serious cracks or defects as compared to the operations under constant-potential mode.

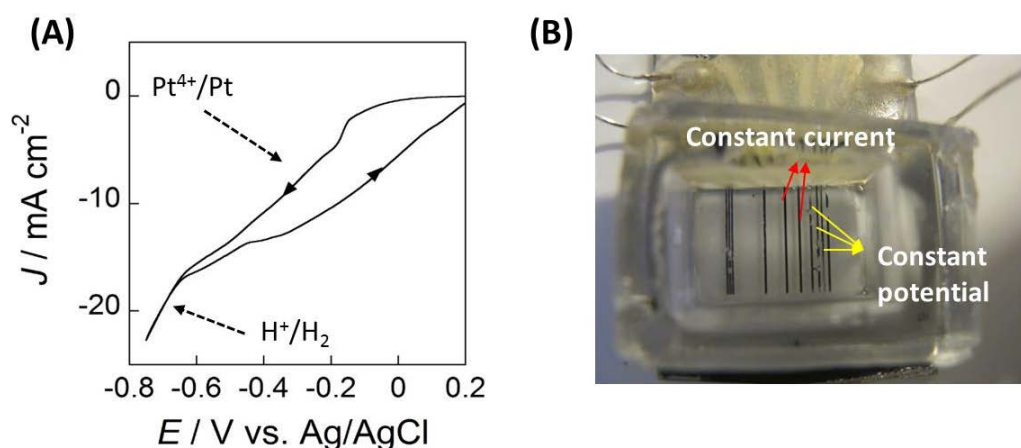


Figure B-8: Platinization conditions and methods. (A) Cyclic voltammogram in 1%  $\text{H}_2\text{PtCl}_6$  at  $5 \text{ mV s}^{-1}$  on bare Pt microband electrode (solution preparation see Appendix III.I). (B) Photo of Pt/Pt-black microband electrodes after plating by constant current ( $-9 \text{ mA cm}^{-2}$ ) or constant potential ( $-0.25 \text{ V/REF}$ ).

Therefore, in the following, depositions of Pt-black on bare Pt microbands were carried out in a constant-current mode. Optimization of current density and charge density applied during the electroplating procedure were performed.

### Optimal electroplating conditions

Figure B-9 and B-10 show the influence of current density  $J$  and charge density  $Q$  on the thickness and vertical profiles of Pt-black deposits.

Under the range of conditions investigated, the thickness of platinum deposits did not exceed 700 nm. Beyond 300 nm, the thickness profiles displayed very high roughness and sharp peaks located on the electrode edges (Figure B-9). These phenomena are associated to the inhomogeneous distribution of current during plating which follows well-known characteristics of mass transport at micrometric electrodes. Indeed, higher current densities prevail on the edges leading locally to higher deposition rates.

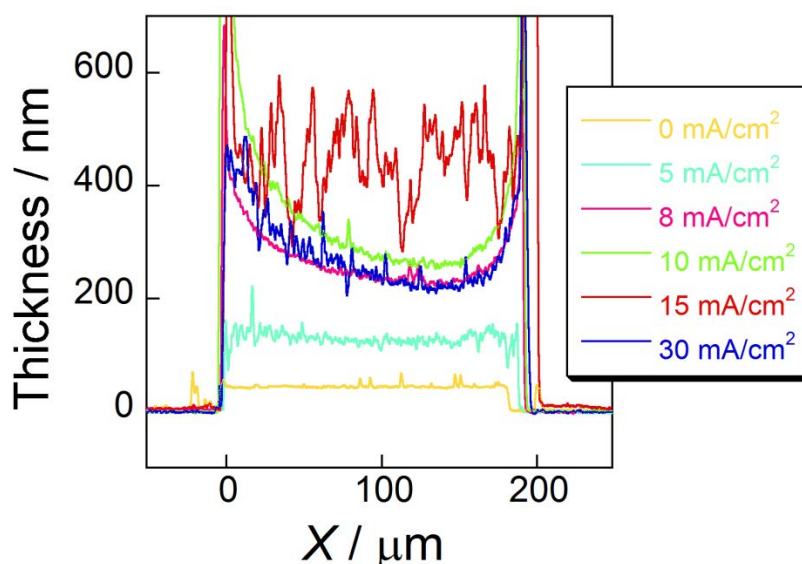


Figure B-9: Thickness profiles of Pt-black coated electrodes as a function of applied current density  $|J|$  with charge density  $|Q|$  fixed at  $200 \text{ mC cm}^{-2}$ .  $|J| = 0 \text{ mA cm}^{-2}$  corresponds to bare Pt electrode (Ti/Pt: 8/25 nm).

Besides, the average thickness of deposits depended also strongly on  $J$  as shown in Figure B-9, B-10A. As an example, for a same charge density  $|Q| = 200 \text{ mC cm}^{-2}$ , the thickness increased with  $|J|$  till  $|J| = 15 \text{ mA cm}^{-2}$  and then dropped in magnitude (Figure B-10A). This threshold value of  $J$  corresponded almost to the limiting current density observed in cyclic voltammetry upon Pt(IV) reduction (Figure B-8A). For higher  $|J|$ , protons reduction took place leading locally to the formation of hydrogen. This process probably altered the deposition of Pt-black resulting in thinner deposits. At lower  $|J|$ , plating was more efficient as the average thicknesses of deposits remained proportional either to  $|J|$  (Figure B-10A) or  $|Q|$  (Figure B-10B).

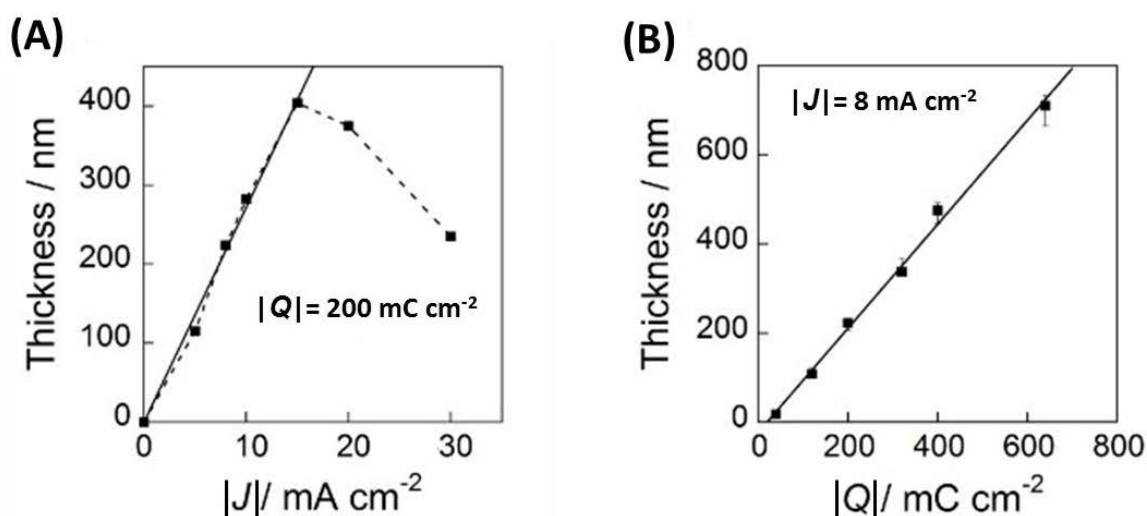


Figure B-10: (A) Average thickness of Pt-black deposits as a function of the applied current density. (B) Average thickness of Pt-black deposits as a function of the charge density.

Current values of corresponding electrodes in 0.1 mM  $H_2O_2$  solution (a stable and representative ROS) are first reported to evaluate the electrochemical performances (Figure B-11).

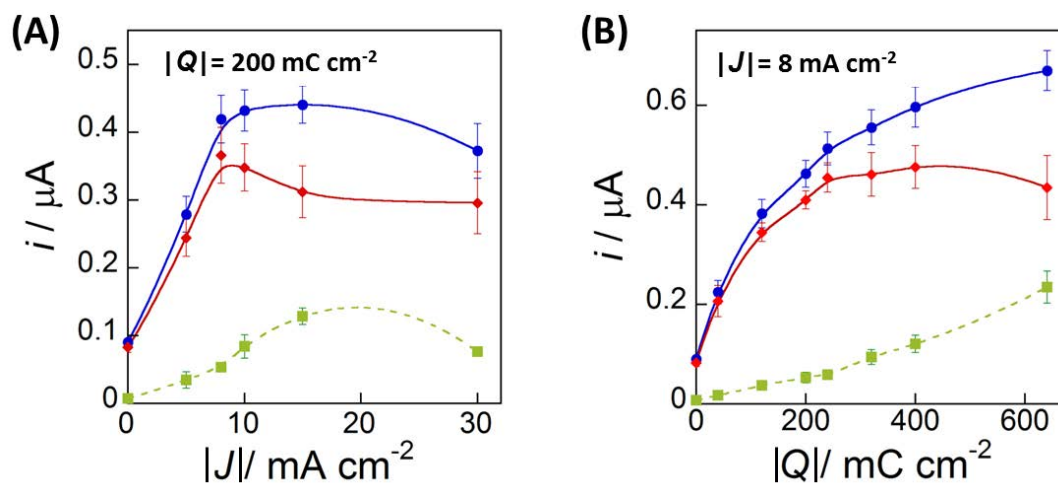


Figure B-11: Anodic currents at Pt/Pt-black electrodes in 0.1 mM  $H_2O_2$  (prepared in 10 mM PBS) as a function of (A) the current density, and (B) the charge density. In both cases, the symbols correspond to background currents in PBS ( $\blacksquare$ ), currents in 0.1 mM  $H_2O_2$  diluted in PBS ( $\bullet$ ), and PBS background-subtracted faradaic currents ( $\blacklozenge$ ), fitted lines showing current responses trends.  $E = 0.45\ V/REF$  and  $t = 140\ s$  after amperometric recording.

For plating conditions corresponded to fixed  $|Q|$  and increasing  $|J|$ , the faradaic currents (Figure B-11A) displayed almost the same variation as thickness observed in Figure B-10A. Indeed, the highest faradaic currents were achieved for electrodes plated with  $J = -8\ mA\ cm^{-2}$ . The correlation between faradaic currents and thickness confirmed that a large number of active sites improving the catalytic activity of Pt microelectrodes were formed with thicker deposits.

In addition, faradaic current increased significantly with  $|Q|$  up to  $240\ mC\ cm^{-2}$  (Figure B-11B). However, beyond this value, a limiting behavior was progressively reached. According to Figure B-10B, this situation corresponded to deposits thicker than 300 nm. This intrinsic property of Pt/Pt-black electrodes can be associated to the roughness of Pt-black deposits. Indeed, beyond a given  $Q$ , the apparent active surface area available for diffusing species increases much less than the specific surface area that includes the formation and the development of hindered pores [222]. Accordingly, the faradaic current remained almost constant whereas the background current still increased with  $|Q|$  (Figure B-11B).

Considering the efficiency and signal-to-noise ratio, optimal conditions for Pt-black platinization required a current density of  $J = -8\ mA\ cm^{-2}$  and a charge density of  $Q = -240\ mC\ cm^{-2}$ . Under these conditions, Pt-black deposits were uniform with a thickness of about

300 nm. These characteristics in height make them fully compatible for implementation of these modified electrodes in micrometric devices.

### Surface roughness and morphology of Pt-black deposit

The roughness factor (i.e., specific surface area over geometric surface area) of optimal deposit was evaluated from voltammetric peaks recorded in 0.1 M sulfuric acid solution ( $H_2SO_4$ ), using hydrogen adsorption/desorption process (Figure B-12A) [223]. The background-subtracted currents were integrated during the hydrogen adsorption domain from -0.35 to +0.1 V vs. Ag/AgCl. Assuming that a monolayer of hydrogen corresponded to a hydrogen adsorption of  $210 \mu C cm^{-2}$  [81], a roughness factor of 36.8 was evaluated for this deposit. In comparison, a roughness factor of only 1.57 was estimated for bare Pt electrode. These values confirmed the drastic enhancement of the specific surface area produced by the Pt-black coating. They are in full agreement with other data reported in the literature [224,225] although they still remain in the lower range. One must underline here that the signal-to-noise ratio and microdimension compatibility was considered for delineating the optimal plating conditions. This discriminating parameter prohibits the use of thicker deposits with higher roughness.

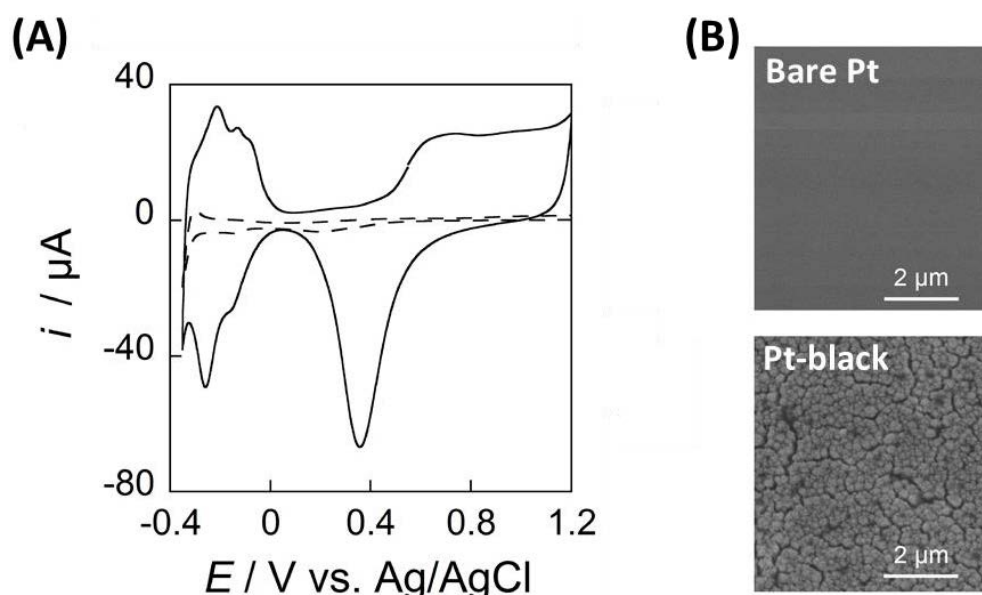


Figure B-12: Characterization of optimized Pt/Pt-black electrode. (A) Cyclic voltammograms recorded at  $100 mV s^{-1}$  in 0.1 M  $H_2SO_4$  solution for bare Pt electrode (dashed curve) and Pt/Pt-black electrode with a roughness factor  $RF = 36.8$  (solid curve). (B) SEM images of a bare Pt electrode surface and Pt/Pt-black electrode surface.  $J = -8 mA cm^{-2}$  and  $Q = -240 mC cm^{-2}$  were applied for Pt-black plating.



On the other hand, SEM images of the electrode surfaces are shown in Figure B-12B, giving a direct view about differences between bare Pt and Pt-black surface morphology. It can be clearly seen that for Pt-black, small particles of tens of nanometers in diameter were distributed randomly on the surface, establishing a rather uniform network, though several spots clustered together forming netting lines on the whole surface.

#### Performances of Pt/Pt-black microband electrode inside microchannel

Afterwards, the deposited Pt/Pt-black microband electrodes were integrated into the microdevice (Figure B-13A) and the following experiments were performed inside microchannels under the same hydrodynamic condition ( $2 \mu\text{L min}^{-1}$  in channel).

Current responses of 0.5 mM FcMeOH during voltammetry and amperometry were recorded (Figure B-13B, -13C). Convective steady-state characteristics were observed similarly as on the bare Pt microband (Figure B-7), despite the slight larger contribution of charging current was observed at Pt-black due to the highly-increased conductive surface. An average factor of 1.3 was obtained corresponding to the enhanced limiting currents after Pt-black deposition (Figure B-13D). This was directly related with apparent active surface area available for diffusing, although no obvious increase in geometrical width was observed as compared to bare Pt electrode (Figure B-9).

One must note that this factor of apparent active surface (i.e., 1.3) is much lower than the roughness factor previously evaluated (i.e., 36.8) since the latter is related to the specific surface area which is necessarily larger. With the presence of numerous Pt sites on electrode surface, passive adsorptions of species and formation of inactive sites should not hinder the electrode overall activity. The electrochemical reaction is thus supposed to be controlled by convective mass transport on the apparent active surface area of Pt-black deposits.

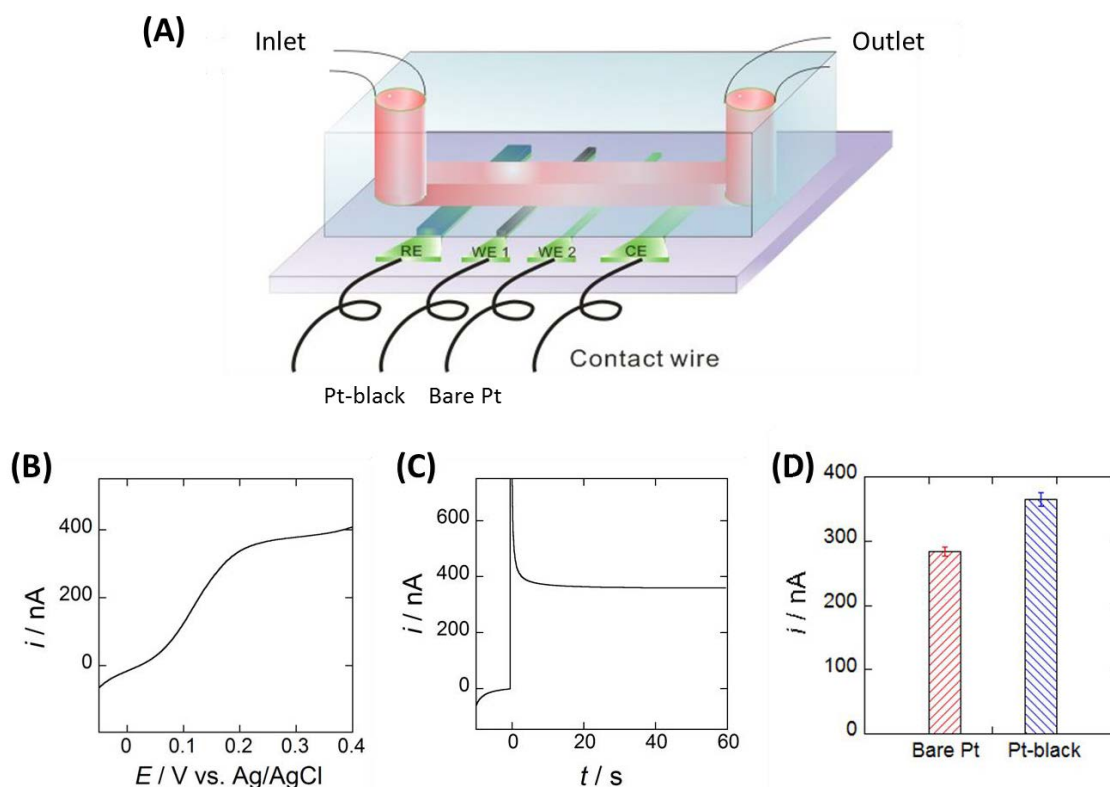


Figure B-13: (A) Schematic view of integrated microfluidic device. Pt-black and bare Pt electrodes were embedded in the same channel for future comparison. (B, C) Electrochemical measurements of  $0.5 \text{ mM}$  FcMeOH at Pt-black microband electrode inside the microdevice. Voltammogram at scan rate of  $10 \text{ mV s}^{-1}$ ; chronoamperometry curve at potential of  $0.4 \text{ V/REF}$  imposed at  $t = 0$ . (D) Steady-state currents on bare Pt and Pt-black microbands obtained under similar convection regime. 5 devices were taken into parallel comparison here.

#### 1.4. Conclusion of section 1

In this section, fabrication of **Pt-black** on bare Pt microband electrodes was optimized from various electrodeposition conditions. A constant-current plating process (current density of  $J = -8 \text{ mA cm}^{-2}$  and a charge density of  $Q = -240 \text{ mC cm}^{-2}$ ) was found to offer the optimal Pt-black deposit with compatible thickness (300 nm) for subsequent integration within microchannel.

As compared to bare Pt, a factor of **1.3** was obtained referring to the apparent active surface area of Pt-black deposit; whereas a much higher value of **36.8** was estimated for the specific surface area of porous structure. Much enhanced activity towards  $\text{H}_2\text{O}_2$  as representative oxidative compound was observed at this Pt-black deposit since a large number of active sites at nanometric scale were generated to prevent electrode passivation. As a result,

Pt/Pt-black electrodes-integrated microchip is expected to provide a viable biosensor for the detection of oxidative species with high analytical performances and long-term reliability.

## **2. ROS/RNS *in vitro* detection at Pt/Pt-black microband electrode**

### ***2.1. In vitro* detection of two stable candidates: H<sub>2</sub>O<sub>2</sub> and NO<sub>2</sub><sup>-</sup>**

In the previous section, we showed that mass transport can be enhanced drastically under convection regimes. We demonstrated also that Pt-black nanoparticles improve the electrodes activities. In the following, NO<sub>2</sub><sup>-</sup> and H<sub>2</sub>O<sub>2</sub> were chosen as two stable representative species of oxidative bursts to check the analytical performances of the detection at Pt/Pt-black electrodes.

H<sub>2</sub>O<sub>2</sub> is an essential indicator of primary oxidative species O<sub>2</sub><sup>•-</sup> and is commonly involved in a wide range of “redox chemistry” biological process. NO<sub>2</sub><sup>-</sup> is the end product of most RNS. Both species are involved in various fields due to their potential cytotoxicity. Compared to other highly reactive and short-lived species (e.g., O<sub>2</sub><sup>•-</sup>, NO<sup>•</sup>, OH<sup>•</sup> and ONOO<sup>-</sup>), H<sub>2</sub>O<sub>2</sub> and NO<sub>2</sub><sup>-</sup> are the most stable in physiochemical environment and their oxidation potentials mainly encompass the whole interested RNS/ROS [5,226]. Finally, from an electrochemical point of view, they are the most difficult to detect because of their tendency to passivate most metallic electrodes. Measurements based on H<sub>2</sub>O<sub>2</sub> and NO<sub>2</sub><sup>-</sup> solutions at Pt-black deposits are undoubtedly a reliable assessment of the analytical performances reached by our device.

Measurements were performed together at bare Pt microbands for comparison purpose. Oxidation mechanisms for both species were investigated based on theoretical predictions of steady-state regimes under convective mass transport.

### 2.1.1. Current responses at Pt/Pt-black electrode

#### Steady-state voltammograms

Figure B-14A shows some steady-state voltammograms obtained under continuous flow of 0.1 mM  $\text{H}_2\text{O}_2$  and 0.1 mM  $\text{NO}_2^-$  solutions (prepared in PBS, pH = 7.4). Oxidation waves of  $\text{H}_2\text{O}_2$  and  $\text{NO}_2^-$  started respectively at 0.2 and 0.65 V/REF. In comparison to bare Pt electrodes (Figure B-14B), the current was magnified about 3 times in case of  $\text{H}_2\text{O}_2$  and 6 times for  $\text{NO}_2^-$ .

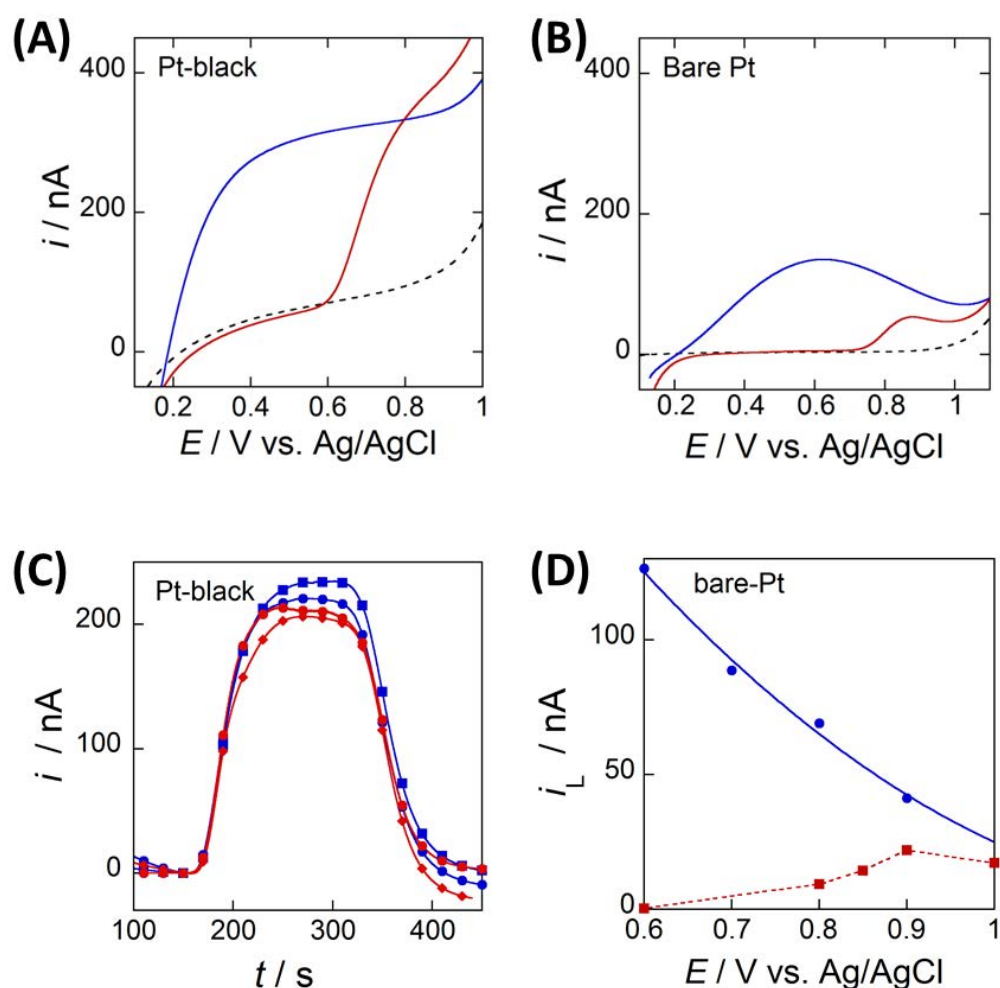


Figure B-14: Current responses on microchannel electrodes. (A, B) steady-state voltammograms at  $10 \text{ mV s}^{-1}$  in a continuous flow of 0.1 mM  $\text{H}_2\text{O}_2$  (blue curve) and 0.1 mM  $\text{NO}_2^-$  (red curve) at (A) Pt/Pt-black and (B) bare Pt electrodes, with PBS background currents (dashed curve). (C, D) Current responses for 5  $\mu\text{L}$  injections of 0.1 mM  $\text{H}_2\text{O}_2$  (blue curve) and 0.1 mM  $\text{NO}_2^-$  (red curve) by using sample loop. (C) Chronoamperometric currents recorded at different potentials at Pt-black electrodes,  $E = 0.45 \text{ V}$  (squares),  $0.85 \text{ V}$  (circles) and  $1.0 \text{ V/REF}$  (diamonds) during separate injections. (D) Limiting current for  $\text{H}_2\text{O}_2$  (●) or  $\text{NO}_2^-$  (■) detection at bare Pt electrode as a function of potential in chronoamperometry.

Advantages resulting from Pt-black deposits were not only visible on the current amplification but also on the shapes of voltammograms. Indeed, current plateaus were observed with Pt/Pt-black electrodes whereas peaks, which were not supposed to show up in fast-established steady-state regime [214], were monitored at bare Pt electrodes for both species. These results were confirmed by performing several injections of  $\text{H}_2\text{O}_2$  and  $\text{NO}_2^-$  solutions and monitoring the amperometric currents as a function of the detection potential at Pt/Pt-black microband (Figure B-14C) or at bare Pt microband (Figure B-14D).

In addition, the steepness of the waves in Figure B-14A, -14B suggested a faster rate of electron transfer with Pt/Pt-black electrodes than that with bare Pt electrodes (especially in the case of  $\text{H}_2\text{O}_2$  where plateau potential was 0.45 V/REF on Pt-black electrodes versus 0.6 V/REF on bare Pt counterparts). This evidenced that at bare Pt surface  $\text{H}_2\text{O}_2$  and  $\text{NO}_2^-$  oxidations are controlled by kinetic, diffusion and competitive poisoning (more explanations in the following mechanism investigation). Responses of Pt electrodes strongly depend on their surface states and therefore surface activation is usually required [227,228].

#### Electrodes activity, reproducibility and stability

Since electrodes may be passivated during experiments, we applied an activation procedure that consisted of performing systematically a series of alternating potential pulses (+0.2 V/REF, 1 s and -0.5 V/REF, 1 s; 30 cycles) in buffer solution before measurements. The electrochemical responses after activation are compared in Figure B-15 for both Pt/Pt-black and bare Pt electrodes in flowing solutions of  $\text{H}_2\text{O}_2$  and  $\text{NO}_2^-$ .

At bare Pt electrodes, activation resulted in a drastic increase of the faradaic currents (Figure B-15B) in comparison to electrodes without any treatment. The currents were amplified by 4 times, either for the oxidation of  $\text{H}_2\text{O}_2$  or  $\text{NO}_2^-$ . No shift of waves in potential indicating higher electron transfer rates or hypothetical catalytic effects was observed.

The same trend was noticed in case of Pt/Pt-black electrodes but led to a moderate increase of currents after activation showing great intrinsic activity of Pt-black deposits (Figure B-15A). Current at Pt/Pt-black electrodes still remained higher than at bare Pt electrodes, either before or after activation.

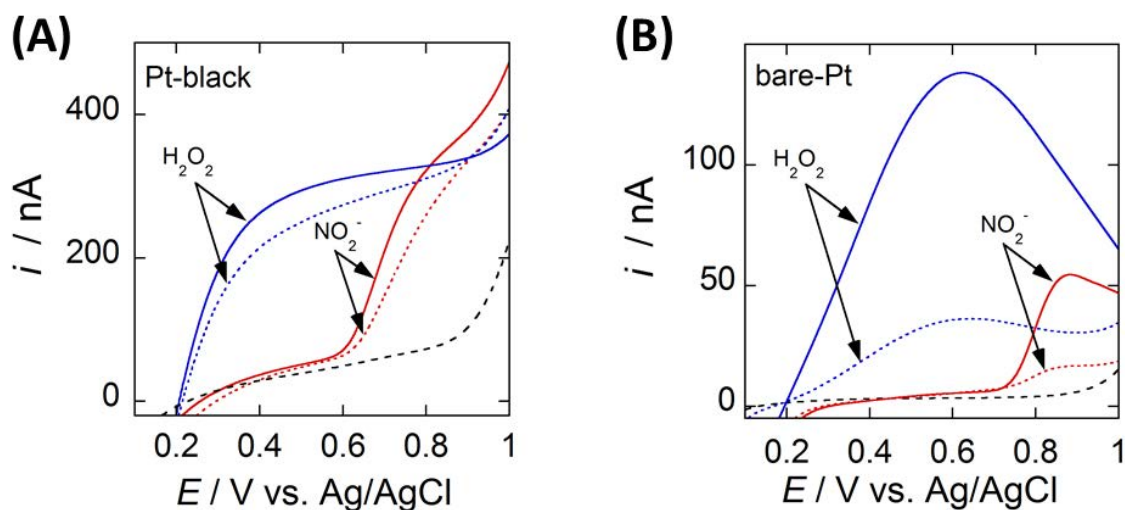


Figure B-15: Steady-state voltammograms before (dotted curve) and after activation (solid curve) shown with background currents (dashed curve), with continuous flow of  $0.1 \text{ mM H}_2\text{O}_2$  and  $0.1 \text{ mM NO}_2^-$  at (A) Pt-black or (B) bare Pt electrodes. Scan rate is  $10 \text{ mV s}^{-1}$ .

In all cases, the shapes of voltammograms were kept displaying plateaus at Pt-black electrodes and peaks at bare Pt electrodes.

Besides the signal enhancement, activation procedure also led to high reproducible results from individual electrodes, no matter for Pt-black or bare Pt surface. Reproducible voltammograms of both species were observed on different electrodes (Figure B-16).

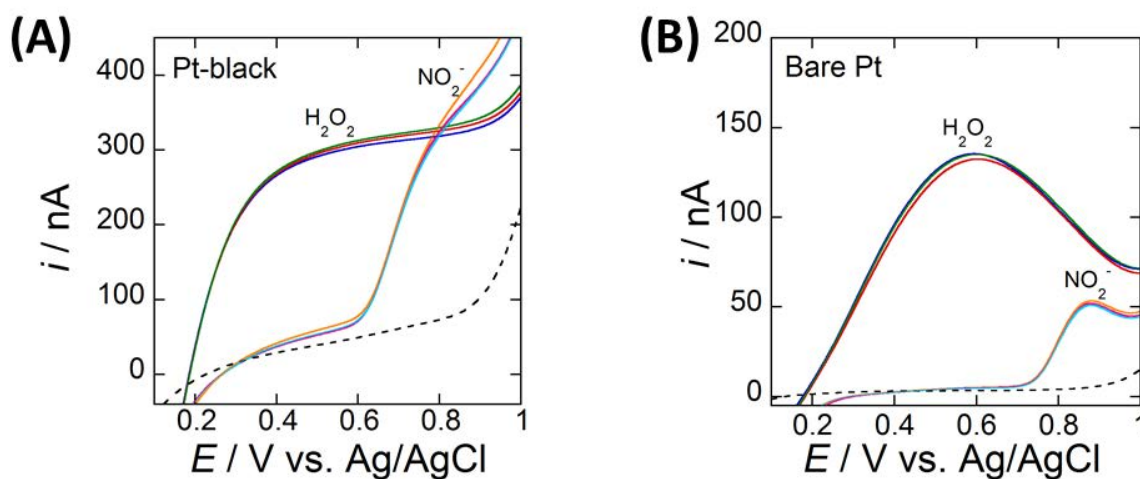


Figure B-16: Current responses of  $0.1 \text{ mM H}_2\text{O}_2$  and  $0.1 \text{ mM NO}_2^-$  at a set of (A) Pt-black and (B) bare Pt electrodes. Each solid curve refers to voltammogram after electrochemical activation, either for Pt-black or bare Pt. Dashed curves show background currents in PBS; scan rate is  $10 \text{ mV s}^{-1}$ .

The stability of electrodes has also to be considered since they tend to lose their sensitivity with time, which necessarily degrades the long-term performances. By performing several repetitive injections after activation, responses at Pt/Pt-black electrode were remarkably stable for both  $\text{H}_2\text{O}_2$  and  $\text{NO}_2^-$  (Figure B-17A). In contrast, currents at bare Pt electrode decreased during the detection of one injection and dropped significantly from one to the others till reaching values recorded before activating treatment (Figure B-17B).

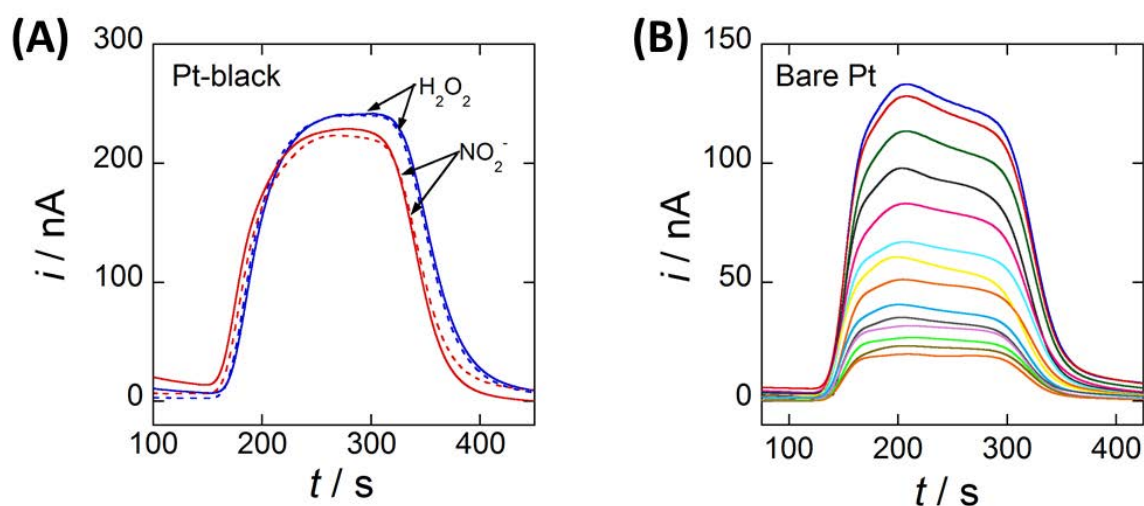


Figure B-17: (A) Current responses of  $5 \mu\text{L}$  microinjections of  $0.1 \text{ mM H}_2\text{O}_2$  ( $E = 0.45 \text{ V/REF}$ , blue curve) and  $0.1 \text{ mM NO}_2^-$  ( $E = 0.85 \text{ V/REF}$ , red curve) at Pt-black electrode. In each case, the currents are shown for the first (solid curve) and fifth injections (dashed curve). (B) Variation of the current responses after repetitive  $5 \mu\text{L}$  injections of  $0.1 \text{ mM H}_2\text{O}_2$  ( $E = 0.60 \text{ V/REF}$ ) at bare Pt electrode, from the first (top) to the fourteenth (bottom) injections.

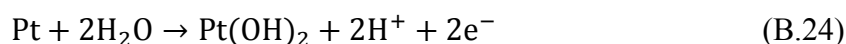
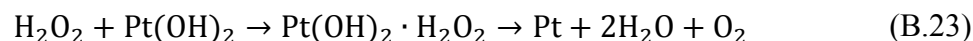
As a consequence, the improvement of electrode responses by activation procedure was here clearly demonstrated. A flow-induced removal of adsorbed species (e.g.,  $\text{PO}_4^{3-}$ ,  $\text{Cl}^-$ ), or residues (e.g.,  $\text{O}_2$ ,  $\text{H}^+$ ) on electrode surface probably operates along with a selective activation of Pt sites [229,230]. In comparison to bare Pt, current enhancement at Pt-black electrodes was moderate due to their initial high catalytic active surface. Furthermore, the stability in current response depends on Pt sites inhibition during the oxidation processes. As Pt/Pt-black electrodes provided more catalytic sites, electrodes remain fully activated during  $\text{H}_2\text{O}_2$  and  $\text{NO}_2^-$  detections.

### 2.1.2. Oxidation mechanisms of H<sub>2</sub>O<sub>2</sub> and NO<sub>2</sub><sup>-</sup>

#### Oxidation mechanisms at platinum surface

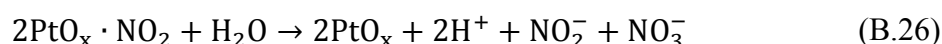
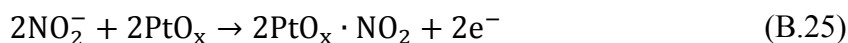
The mechanisms involved in H<sub>2</sub>O<sub>2</sub> and NO<sub>2</sub><sup>-</sup> oxidations on Pt electrodes have been extensively investigated [228,230-235]. Even both mechanisms differ greatly, their voltammograms were similar in shape. As previously noted for H<sub>2</sub>O<sub>2</sub>, a drop of current was also observed for NO<sub>2</sub><sup>-</sup> at high overpotentials leading to peak-shape waves (Figure B-15B).

In case of H<sub>2</sub>O<sub>2</sub>, the mechanism involves oxidation through electrochemically generated Pt(OH)<sub>2</sub> surface sites [229-233]:



This is a fast process. However, the reaction rate is inhibited by competitive adsorption of diverse species on the active sites as well as by further oxidation of these sites into PtO, PtO<sub>2</sub>.

In case of NO<sub>2</sub><sup>-</sup>, an overall oxidation into nitrates occurs through the homogeneous disproportionation of nitrogen dioxide [234,235]:



The kinetics of latter process is not very fast and even slows down with the formation of oxide layers on platinum surface.

Hence on bare Pt electrode, the decrease of current in case of H<sub>2</sub>O<sub>2</sub> can be explained by a decrease density of surface binding sites; whereas for NO<sub>2</sub><sup>-</sup> it can be attributed to reaction inhibition associated to lower kinetics on oxide layer. Conversely, on Pt/Pt-black electrodes, 0.1 mM H<sub>2</sub>O<sub>2</sub> and 0.1 mM NO<sub>2</sub><sup>-</sup> oxidations seem to be controlled by mass transport as the oxidation waves displayed current plateaus (Figure B-14A). High density of activated Pt sites possibly prevents inhibition effect and facilitates electron transfer.



### Oxidation mechanisms validation based on mass transport regimes

To evaluate the mass transport conditions at Pt-black electrodes, limiting currents were plotted as a function of the flow velocity. They were then compared to predictions issued from numerical simulations for steady-state regimes considering all hydrodynamic and geometrical parameters involved during experimental detection (Figure B-18). Note that the apparent active surface was estimated with a factor of 1.3 for Pt-black deposit as compared to bare Pt microband.

The range of flow rates investigated corresponded to laminar flows. They encompassed all the regimes starting from the thin layer regime (i.e., at flow velocities lower than  $0.15 \mu\text{Lmin}^{-1}$ ) to the Levich regime (i.e., at flow velocities higher than  $4.5 \mu\text{Lmin}^{-1}$ ) passing through an intermediate regime[214].

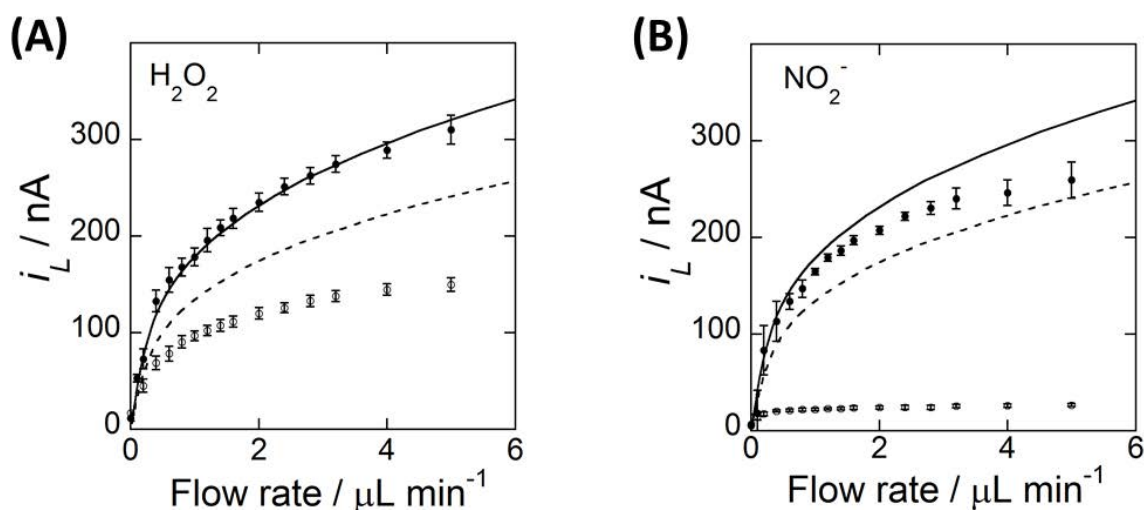


Figure B-18: Comparison between theoretical and experimental limiting currents as a function of the flow rate. (A) Detection of  $0.1 \text{ mM H}_2\text{O}_2$  at Pt-black ( $E = 0.45 \text{ V/REF}$ ) and bare Pt electrodes ( $E = 0.6 \text{ V/REF}$ ). (B) Detection of  $0.1 \text{ mM NO}_2^-$  at Pt-black ( $E = 0.85 \text{ V/REF}$ ) and Pt electrodes ( $E = 0.9 \text{ V/REF}$ ). In (A, B), experimental currents at Pt-black ( $\bullet$ ) and bare Pt electrodes ( $\circ$ ) are comparing with theoretical currents (solid curve for Pt-black with apparent active surface factor of 1.3, dashed curve for bare Pt) simulated with  $D_{\text{H}_2\text{O}_2} = D_{\text{NO}_2^-} = 1.5 \times 10^{-5} \text{ cm}^2 \text{ s}^{-1}$ .

For  $\text{H}_2\text{O}_2$ , a very good agreement was obtained between theoretical and experimental data on Pt/Pt-black electrodes (Figure B-18A); evidencing that over the wide range of flow velocities investigated, oxidation of  $\text{H}_2\text{O}_2$  was fully controlled by mass transport. This was not the case on bare Pt electrodes where no match could be observed with theoretical predictions whatever the flow rate velocities (currents still increased with flow rate, showing partial mass transport traits, but more likely being limited by a decreasing apparent active

surface). These results were consistent with previously introduced oxidation mechanism of  $\text{H}_2\text{O}_2$ , demonstrating again that the density of active sites on Pt-black deposits were sufficiently large enough for the reaction to be fully controlled by mass transport over the whole apparent active surface area. In this case, passive adsorptions of species and formation of inactive Pt sites did not hinder the overall activity.

For  $\text{NO}_2^-$ , the data on bare Pt electrodes was independent of flow rate and deviated seriously from theory (Figure B-18B), showing relative kinetic control of oxidation mechanism versus mass transport. In comparison, current at Pt/Pt-black electrodes were much higher and deviated much less from theory. Even if kinetic is locally inhibited by formation of surface oxides,  $\text{NO}_2^-$  oxidation on Pt/Pt-black electrodes was still efficient due to greater number of active sites at the nanometric scale and higher porosity of Pt-black deposits.

### 2.1.3. Calibration curve and electrode sensitivity

Calibration curves were established by injecting  $\text{H}_2\text{O}_2$  and  $\text{NO}_2^-$  samples respectively over a wide range of concentrations (Figure B-19A, -19B), and current responses were recorded both on Pt/Pt-black and bare Pt electrodes.

Data displayed linear relationships below the millimolar range with almost five decades linearity (Figure B-19C to F) when background currents were subtracted (average values before and after injection). The decrease in current observed above 1 mM was attributed to the saturation of oxygen and hydrogen peroxide on Pt sites [236,237]. Sensitivities were respectively  $6.02 \text{ A M}^{-1}\text{cm}^{-2}$  for  $\text{H}_2\text{O}_2$  and  $5.54 \text{ A M}^{-1}\text{cm}^{-2}$  for  $\text{NO}_2^-$ . Accordingly, these values were higher on Pt/Pt-black electrodes by a factor of 2.03 for  $\text{H}_2\text{O}_2$  and 8.84 for  $\text{NO}_2^-$  when compared to bare Pt electrodes. The limits of detection (LOD) were estimated from slope of calibration curve and three times the standard deviation (from at least 10 parallel tests at low sample concentration: 10 nM  $\text{H}_2\text{O}_2$  and 20 nM  $\text{NO}_2^-$ ). This led respectively to LOD of 7 nM  $\text{H}_2\text{O}_2$  and 12 nM  $\text{NO}_2^-$ . These results belong to the highest performances reported for stable ROS/RNS detection in microfluidic channel [80].

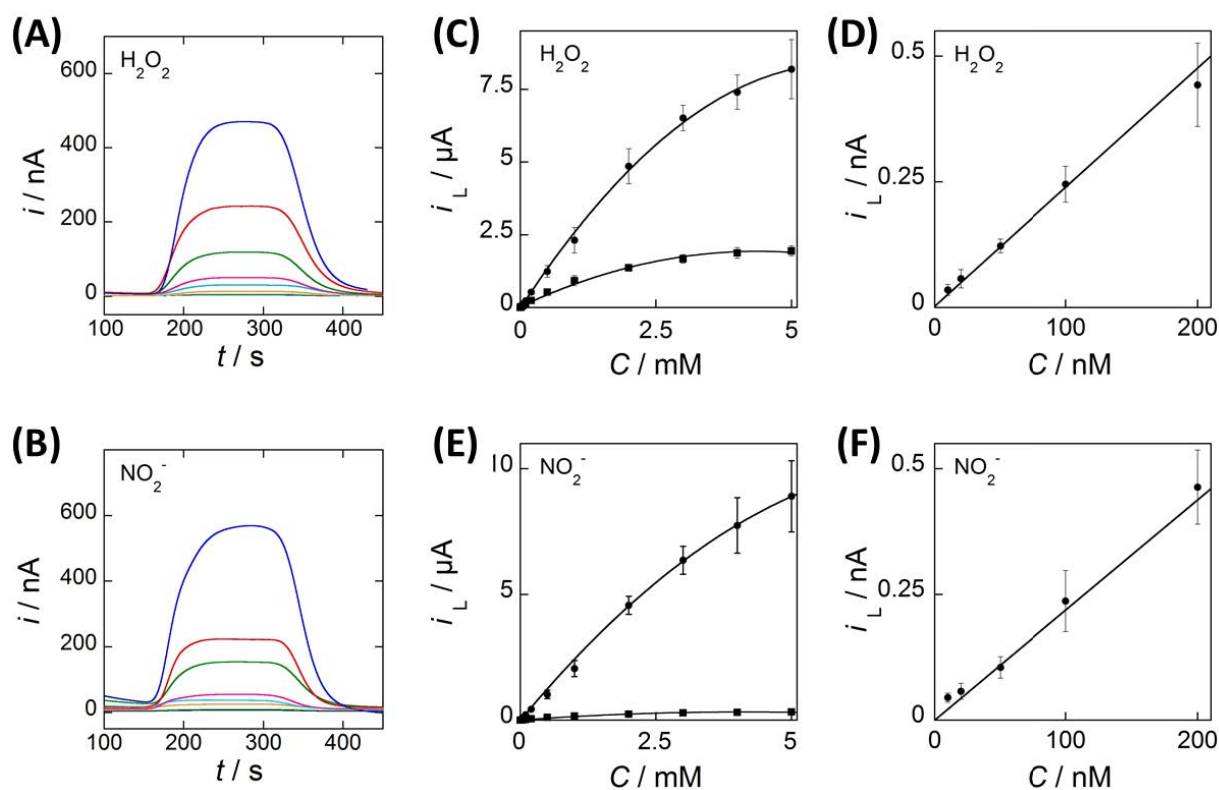


Figure B-19: Calibration curves obtained at Pt-black and bare Pt electrodes. (A, B) Examples of 5  $\mu\text{L}$  sample injections of various concentrations detected by Pt-black electrode, from top (0.2 mM) to bottom (1  $\mu\text{M}$ ). (C, D) Calibration curves for  $\text{H}_2\text{O}_2$  detection,  $E = 0.45 \text{ V/REF}$  on Pt/Pt-black electrodes ( $\bullet$ ), or  $E = 0.6 \text{ V/REF}$  on bare Pt electrodes ( $\blacksquare$ ). (E, F) Calibration curves for  $\text{NO}_2^-$  detection,  $E = 0.85 \text{ V/REF}$  on Pt/Pt-black electrodes ( $\bullet$ ), or  $E = 0.9 \text{ V/REF}$  on bare Pt electrodes ( $\blacksquare$ ). (D) and (F) are selected data from (C) and (E) respectively, showing current responses at very low concentrations. The slopes of calibration curves are respectively  $2.41 \times 10^{-3} \text{ A}^{-1} \text{ M}^{-1}$  for  $\text{H}_2\text{O}_2$  and  $2.22 \times 10^{-3} \text{ A}^{-1} \text{ M}^{-1}$  for  $\text{NO}_2^-$ .

## 2.2. *In vitro* detection of two unstable candidates: ONOO<sup>-</sup> and NO<sup>•</sup>

### 2.2.1. Detection of ONOO<sup>-</sup>

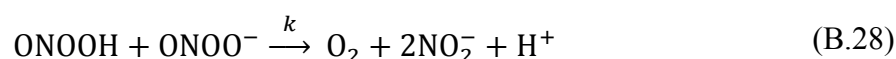
#### Natural decomposition

Since ONOO<sup>-</sup> naturally decomposes with time and pH, we had to take into account its chemical stability during electrochemical investigation. The evaluation of the kinetics was thus a necessary step before assessing the electrochemical performances of Pt/Pt-black electrodes.

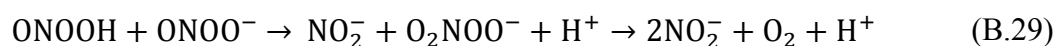
The pKa of peroxynitrous acid (ONOOH) is about 6.8 [238-240], thus both acid and anion forms are present at physiological pH. However, the acid is unstable and undergoes very fast isomerization to nitrate:



At higher pH, a decomposition pathway prevails with the production of dioxygen and nitrite:



This reaction proceeds via the formation of peroxynitric acid as intermediate during the following sequence [241]:



However, in most cases of interest here, the overall decay of ONOO<sup>-</sup> is first order and decreases upon increasing pH [242]. At physiological pH, the decomposition is more complicated and the half-life time is estimated about 1 s. This makes the ONOO<sup>-</sup> detection particularly challenging for the analysis of its content in biological samples. Its electrochemical oxidation is a one-electron reaction, whatever the pH[109]:



ONOO<sup>-</sup> is sufficiently stable in alkaline conditions (*cis*-conformation where the negative charge is localized over the entire molecule) with an extended life time (e.g., 5 hours in 0.3 M NaOH at 25°C) [240,241,243]. We then performed electrochemical experiments at pH 11.1 for practical reasons. Note that data obtained at this pH will be also valid for lower pH since the electrochemical reaction (B.30) and variation of diffusion coefficient are expected to be pH independent. Higher pH was also avoided to prevent degradation of Pt-black deposits.

### Current responses at Pt/Pt-black electrodes

Measurements were realized using bare Pt and Pt/Pt-black microband electrodes fabricated according to the procedure described before. Figure B-20 shows voltammograms obtained in case of continuous flowing solutions of 0.1 mM ONOO<sup>-</sup> (pH = 11.1) at both electrodes.

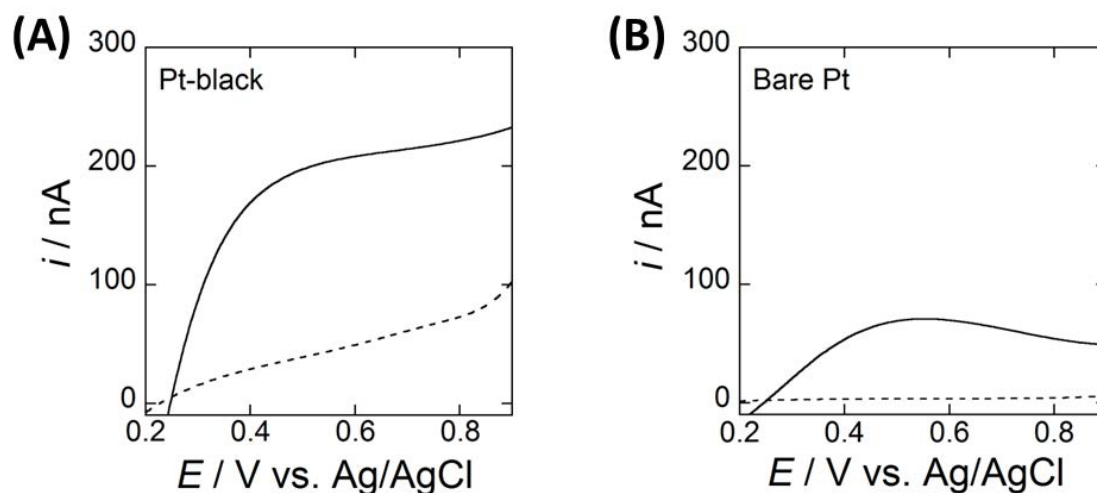


Figure B-20: Voltammograms in continuous flowing solutions of 0.1 mM ONOO<sup>-</sup> at (A) Pt-black and (B) bare Pt electrodes in pH 11.1 PBS. Background current responses in dashed curves; scan rate is 10 mV s<sup>-1</sup>.

In each case ONOO<sup>-</sup> started to be oxidized at potentials higher than 0.2 V/REF. At Pt-black electrodes a steady-state mass transport regime was reached above 0.45 V/REF as evidenced by a limiting current (or current plateau) at high potentials. In contrast, a peak-shaped voltammogram was observed under the same conditions at bare Pt electrodes of the same surface areas with current intensities two times lower.

Similarly as the results from H<sub>2</sub>O<sub>2</sub> and NO<sub>2</sub><sup>-</sup>, oxidation of ONOO<sup>-</sup> on bare Pt was not fully controlled by convective mass transport. It was probably altered by a more complex pathway involving other limiting steps due in part to some competitive poisoning of Pt surface.

Activation of electrodes prior to detection led to a noticeable increase of current at bare Pt electrodes (Figure B-21B). In this case, a flow-removal of residues adsorbed on Pt surface as well as a selective activation of Pt sites led to an enhancement of the electrochemical oxidation. However, intensities reached after activation still remained lower

than those recorded at Pt-black electrodes (Figure B-21A). Note also that the electrode stability was not satisfactory since current responses decreased with time from one to the other (Figure B-21D), demonstrating further that surface poisoning was persistent. On the contrary, currents recorded at Pt-black electrodes were more stable and no significant change was observed of current level before and after activation (Figure B-21A).

Such electrode treatment led to more reproducible results with long-term performances as it was confirmed in the case of repetitive injections of  $\text{ONOO}^-$  (Figure B-21C). From an electroanalytical point of view,  $\text{ONOO}^-$  detection was by far more efficient on optimized Pt-black electrodes than on bare Pt electrodes.

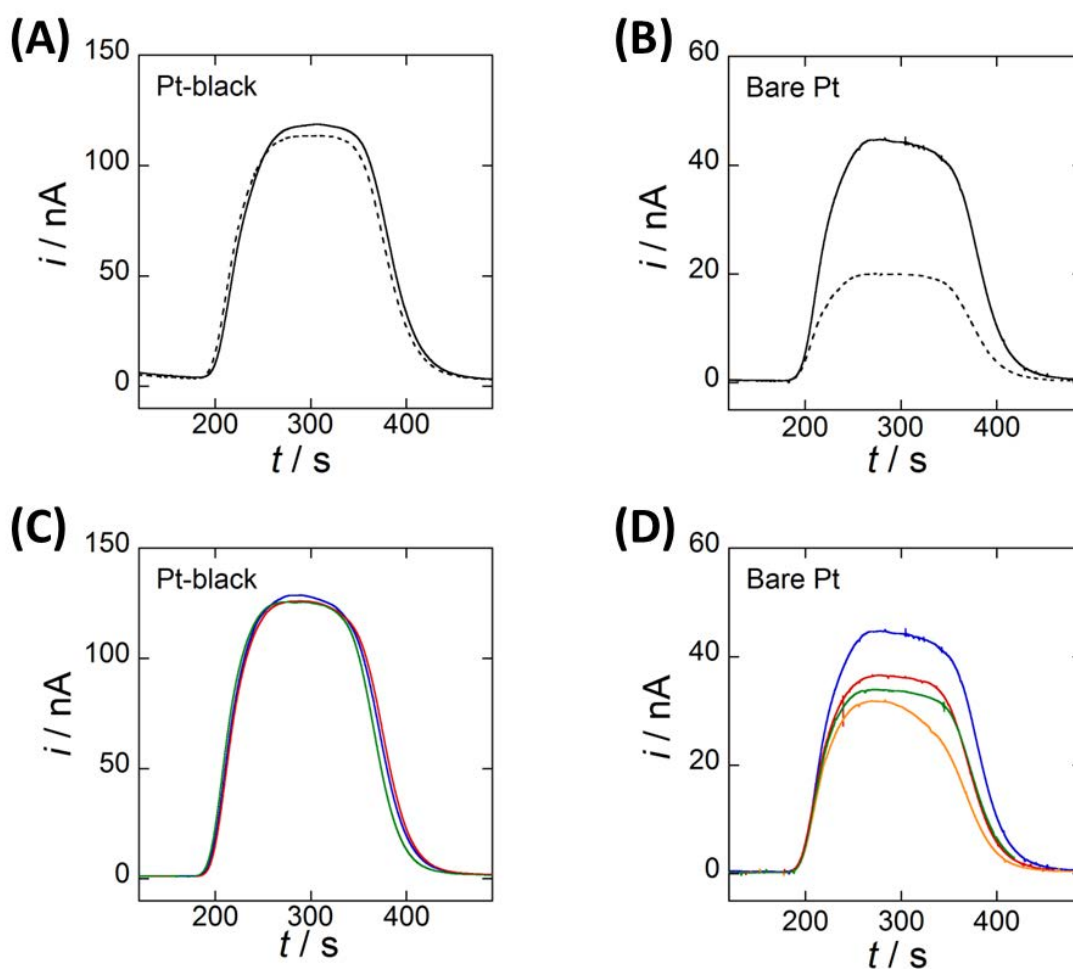


Figure B-21: (A, B) Current responses of  $5 \mu\text{L}$   $0.1 \text{ mM}$   $\text{ONOO}^-$  microinjections before (dashed curve) and after activation (solid curve) at (A) Pt-black and (B) bare Pt electrodes. (C, D) From top to bottom, current responses of repetitive microinjections of  $0.1 \text{ mM}$   $\text{ONOO}^-$  at (C) Pt-black and (D) bare Pt electrodes. In all cases,  $\text{pH} = 11.1$ ,  $E = 0.45 \text{ V/REF}$  and  $t$  refers to time after solution preparation.

### Investigation of decomposition kinetic parameters

These first results were confirmed by investigating kinetics of  $\text{ONOO}^-$  decomposition at lower pHs. Electrochemical measurements were achieved at Pt-black electrodes and compared to those obtained under the same conditions from UV-Vis spectra (Figure B-22).

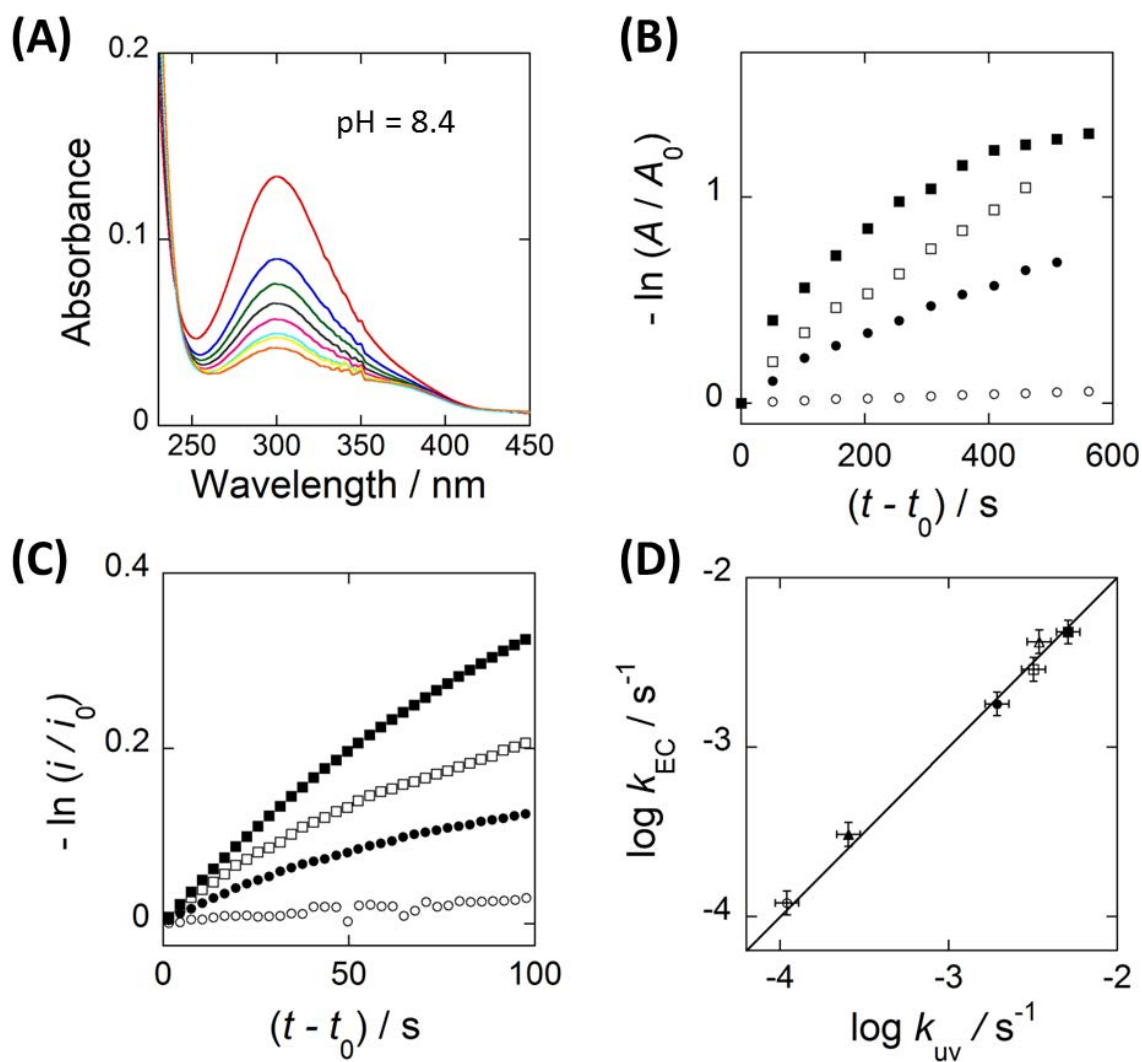


Figure B-22:  $\text{ONOO}^-$  decomposition investigation at different pHs. (A) Repetitive UV-Vis spectra of 0.1 mM  $\text{ONOO}^-$  solution at pH 8.4, starts from 20 s after solution preparation, with 51 s intervals between each curve. Absorbance decreases with time. (B) Variations of UV-Vis peak intensities at several pHs of 0.1 mM  $\text{ONOO}^-$  solutions.  $\lambda = 302$  nm and  $t_0 = 40$  s. (C) Current intensities monitored at Pt-black electrodes in 0.1 mM  $\text{ONOO}^-$  continuous flowing solutions at several pHs.  $E = 0.45$  V/REF and  $t_0 = 130$  s. (D) Comparison between kinetic constants evaluated from electrochemical detection ( $k_{\text{EC}}$ ) and UV-Vis spectra analysis ( $k_{\text{UV}}$ ) at times lower than 200 s after solution preparation. In (B to D), pH = 11.1 ( $\circ$ ), 10.8 ( $\blacktriangle$ ), 10.2 ( $\bullet$ ), 9.4 ( $\square$ ), 8.9 ( $\triangle$ ) and 8.4 ( $\blacksquare$ ).  $t_0$  refers the time duration between solution preparation and beginning of experiments, is recorded for kinetic studies.

In both cases  $\text{ONOO}^-$  decomposition was found to be first order over a range of 200 s after solutions preparation (Figure B-22B and -22C). At higher times, the kinetic profile was more complex as significant deviations from linear logarithmic plots occurred when pH tends to 8.4. This trend was consistent with other conclusions proposed under similar conditions [238].

Evaluation of the kinetic constant  $k$  (Equation (B.28)) from both types of measurements led to very consistent results (Figure B-22D). Accordingly,  $k$  increased by almost two orders of magnitude from  $10^{-4}$  to  $10^{-2.5} \text{ s}^{-1}$  when pH decreased from 11.1 to 8.4. All these data were in very good agreement with other values reported in literature [109,238,240,243]. These results again demonstrated the feasibility and reliability of  $\text{ONOO}^-$  detection at Pt-black electrodes.

#### Calibration curve and electrode sensitivity

Calibration curve was thus established from injections of different  $\text{ONOO}^-$  solutions at pH 11.1 (Figure B-23A). For that purpose, a wide range of concentrations was investigated after correcting them by taking into account the species decomposition at this pH.  $\text{ONOO}^-$  concentrations were estimated after the time delay separating the measurements from the solution preparation. Values on current plateau were also subtracted from residual currents monitored in absence of  $\text{ONOO}^-$ .

As a result, calibration curve displayed linear relationship with four decades linearity and a sensitivity of  $2.64 \text{ A M}^{-1}\text{cm}^{-2}$  (Figure B-23C). Conversely, linearity was no longer observed at concentration below 100 nM (Figure B-23D). The LOD assessed from calibration slope and three times standard deviation from repetitive measurements in nanomolar concentrations range was 40 nM. This limit agreed with data reported elsewhere [102,243,244]. However, using this procedure LOD was probably underestimated since signal reached at 50 nM was still far larger than noise (Figure B-23B).



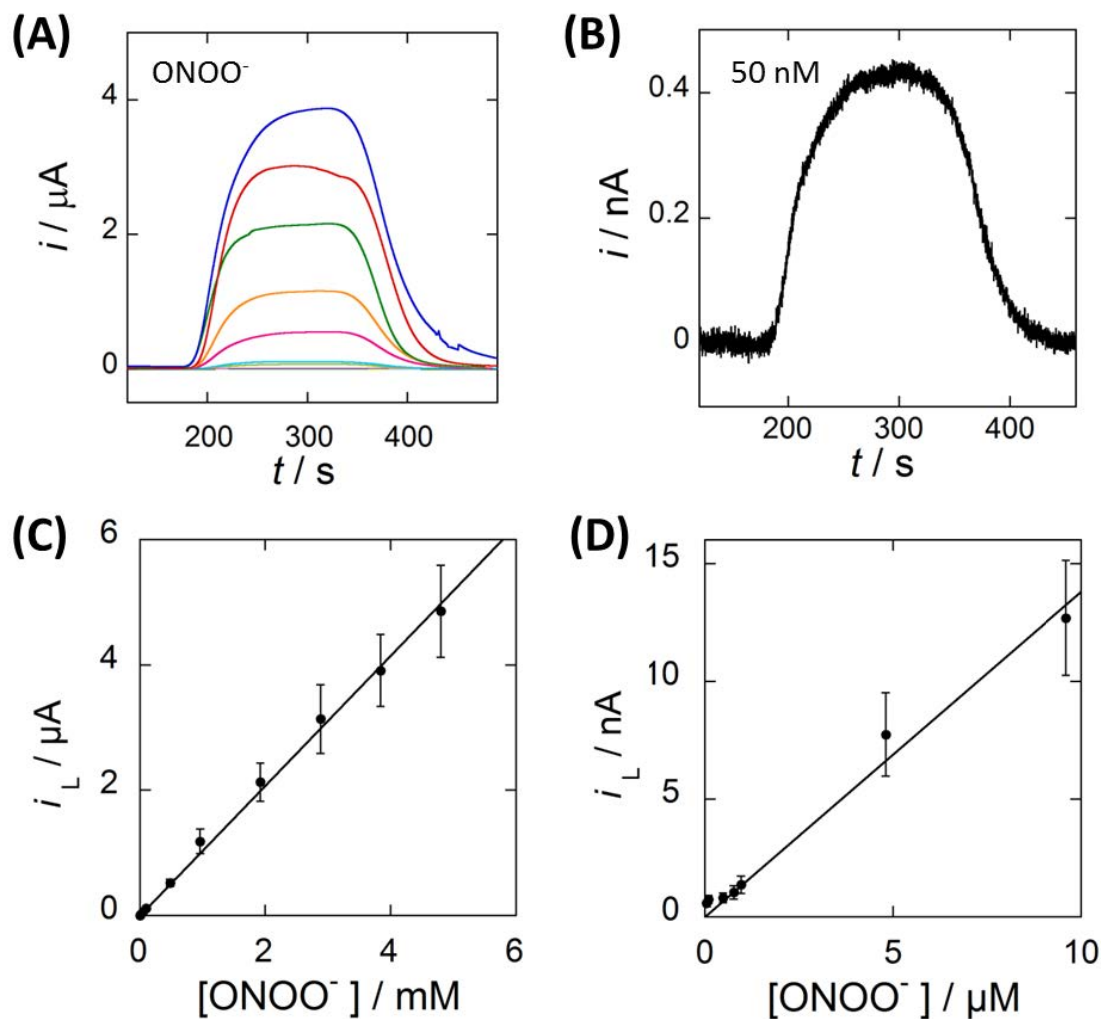


Figure B-23: (A) Current responses at Pt/Pt-black electrodes of ONOO<sup>-</sup> microinjections (5  $\mu\text{L}$ ) with various concentrations. From top to bottom: 4, 3, 2, 1, 0.5 and 0.1 mM, 50, 10, 5, 1, 0.5, and 0.1  $\mu\text{M}$ . (B) Current responses of 50 nM ONOO<sup>-</sup> microinjection. (C to D) Calibration curves of ONOO<sup>-</sup> detection at Pt-black electrodes. Currents monitored at 300 s after solution preparation and concentrations evaluated with decay rate  $k = 1.2 \times 10^{-4} \text{ s}^{-1}$ . Linear curve fit with slope equal to  $1.04 \times 10^{-3} \text{ A M}^{-1}$ . In (A to D),  $\text{pH} = 11.1$  and  $E = 0.45 \text{ V/REF}$ .  $t$  refers to time elapsed after solution preparation.

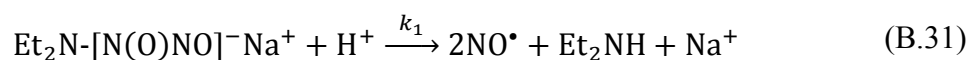
The calibration curve allowed also the diffusion coefficient of ONOO<sup>-</sup> to be estimated. According to theoretical steady-state currents predicted under this hydrodynamic regime at microchannel electrode (Equation (B.12)), it gave  $D_{\text{ONOO}^-} = (1.4 \pm 0.2) \times 10^{-5} \text{ cm}^2 \text{ s}^{-1}$ . This value is close to those usually considered for RNS in similar conditions [245-248].

### 2.2.2. Detection of NO<sup>•</sup>

#### NO<sup>•</sup> released from DEA-NONOate

The performances of NO<sup>•</sup> detection were evaluated using dynamic NO<sup>•</sup> concentrations generated through the decomposition of DEA-NONOate (NO<sup>•</sup> donor molecule) solutions. Preliminary studies evidenced that the decomposition rate depended strongly on the concentration of DEA-NONOate and pH. Therefore, NO<sup>•</sup> generation rates were carefully investigated through kinetic evaluations performed under the conditions in this study.

DEA-NONOate solutions chemically decompose into NO<sup>•</sup> when dissolved with aqueous solutions at physiological pH, according to the following process [249]:

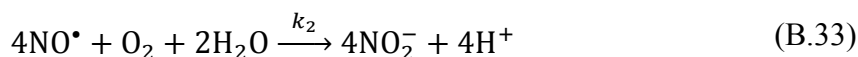


with a rate law of NO<sup>•</sup> formation given by:

$$V_1 = k_1[\text{Et}_2\text{N}-[\text{N}(\text{O})\text{NO}]^-] \quad (\text{B.32})$$

where  $k_1 = 7.22 \times 10^{-4} \text{ s}^{-1}$  at 22 °C at pH 7.4 [250].

However, NO<sup>•</sup> concentration results not only from the fast DEA-NONOate decomposition (Equation (B.31)) but also from a competition reaction between NO<sup>•</sup> and oxygen [251]:



which obeys a second order rate law given by:

$$V_2 = 4k_2[\text{NO}^\bullet]^2[\text{O}_2] \quad (\text{B.34})$$

where  $k_2 = (2.3 \pm 0.6) \times 10^6 \text{ M}^{-2} \text{ s}^{-1}$  at 20 – 25 °C [251-257].

Since the efficiency of NO<sup>•</sup> release is about 75% in Equation (B.31), 1.5 mole of NO<sup>•</sup> is generated per mole of DEA-NONOate [257]. Therefore, the kinetic profile of NO<sup>•</sup> release follows the balance between  $V_1$  and  $V_2$ :

$$\frac{d[\text{NO}^\bullet]}{dt} = 1.5 k_1 \exp(-k_1 t) [\text{Et}_2\text{N}-[\text{N}(\text{O})\text{NO}]^-]_0 - 4k_2[\text{NO}^\bullet]^2[\text{O}_2] \quad (\text{B.35})$$

where  $[\text{Et}_2\text{N}-[\text{N}(\text{O})\text{NO}]^-]_0$  is the initial concentration of DEA-NONOate.

Because  $V_1$  is much larger than  $V_2$ ,  $\text{NO}^\bullet$  concentration increases fast at very short times, reaches a maximum and then decays slowly [11]. Note that the corresponding half-life time of DEA-NONOate is 16 min at 22 °C in aerobic phosphate buffer at physiological pH [250]. To ensure that the time-course and concentration level of produced  $\text{NO}^\bullet$  were enough to complete adequate detections, we first performed measurements not later than 20 min (i.e., 1200 s) after the solution preparation.

### Current responses of $\text{NO}^\bullet$ at Pt/Pt-black electrodes

Electrochemical oxidation of  $\text{NO}^\bullet$  is a one-electron process according to:



Figure B-24A shows the successive voltammograms obtained under these conditions at Pt/Pt-black electrode from 270 to 770 s after solution preparation. However, extracting the electrochemical oxidation current for  $\text{NO}^\bullet$  required a correction from background current. So, voltammograms recorded after complete  $\text{NO}^\bullet$  decomposition were subtracted from the initial responses (Figure B-24B). This was a necessary step since  $\text{NO}^\bullet$  reaction with oxygen (Equation (B.33)) produces  $\text{NO}_2^-$  that accumulate and started to oxidize at slightly higher potentials [216]. It is also known that  $\text{NO}^\bullet$  donor like DEA-NONOate generates potential interfering species issued from own  $\text{NO}^\bullet$  reactivity or other decomposition products that might obstruct direct identification of  $\text{NO}^\bullet$  signals [249].

After background subtraction a wave was obtained with a maximum at  $E = 0.62 \text{ V/REF}$  (Figure B-24B) in contrast to a plateau expected under steady-state regime of mass transport. This electrochemical behavior could be related to the progressive generation of interfering products (mostly due to  $\text{NO}_2^-$ ) during the potential scan, as it was also confirmed latter by series of corrected voltammograms monitored as a function of time (Figure B-24C). Nevertheless, in comparison to bare Pt electrodes (Figure B-24B), corrected voltammograms displayed current magnitude almost 350 times larger at Pt-black deposits.

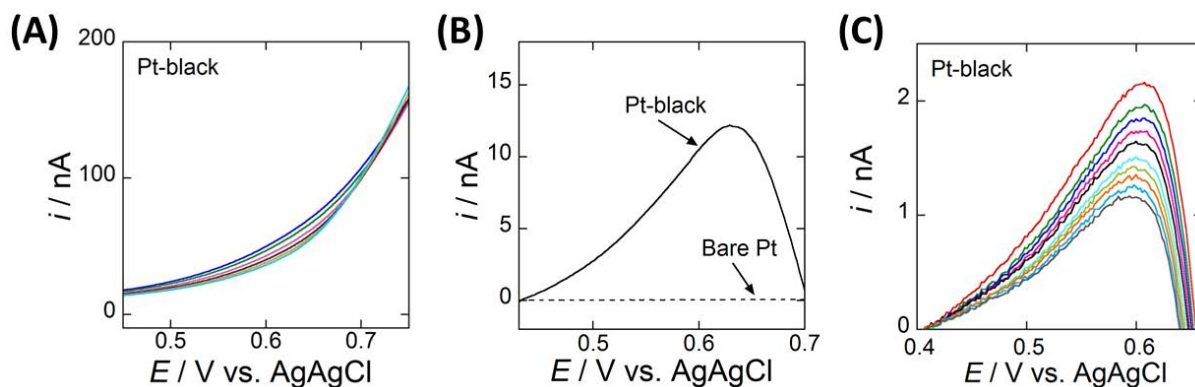


Figure B-24: (A) Successive voltammograms in a continuous DEA-NONOate flowing solution at Pt-black electrode, from 270 s (top) to 770 s (bottom) after solution preparation. (B) Background-corrected voltammograms at Pt-black (solid curve) and bare Pt electrodes (dashed curve), with initial responses of 270 s after solution preparation. (C) Background-corrected voltammograms at Pt-black electrode, with initial responses from 230 s (top) to 730 s (bottom) after solution preparation. In (A, B) 0.5 mM DEA-NONOate solution, pH = 7.4. In (C) 0.1 mM DEA-NONOate solution, pH = 7.4. Scan rate is  $10 \text{ mV s}^{-1}$ .

### Evaluation of *in vitro* NO<sup>•</sup> concentration during donor decomposition

In order to verify that the time-course and concentration level of produced NO<sup>•</sup> were adequately monitored, the kinetic profile of NO<sup>•</sup> was analyzed from series of UV-Vis spectra monitored under the same conditions since their variations tracked the rate of DEA-NONOate decomposition only (Figure B-25A). In this case, an average value of  $k_1$  could be determined at  $\lambda = 250 \text{ nm}$  with  $k_1 = (7.8 \pm 0.5) \times 10^{-4} \text{ s}^{-1}$  (Figure B-25B). By introducing this value in Equation (B.35),  $k_2$  was evaluated from the best fit of a series of chronoamperometric curves monitored at 0.62 V/REF at several DEA-NONOate concentrations.

For that purpose, diffusion coefficient of NO<sup>•</sup> was considered equal to  $1.5 \times 10^{-5} \text{ cm}^2 \text{ s}^{-1}$  [216] and currents were estimated on the basis of theoretical predictions accounting for the local hydrodynamic regime (Equation (B.12)).

A good agreement was observed between experimental and calculated currents for all initial DEA-NONOate concentrations only for  $k_2[\text{O}_2] = 5.5 \times 10^2 \text{ M}^{-1} \text{ s}^{-1}$  (Figure B-25). Since O<sub>2</sub> solubility at room temperature was about 0.25 mM, this gave  $k_2 = (2.2 \pm 0.4) \times 10^6 \text{ M}^{-2} \text{ s}^{-1}$ . All these results were thus perfectly consistent with values of  $k_1$  and  $k_2$  reported in the literature [250-257]. With these kinetic constant values, time-dependent concentration of NO<sup>•</sup> could be predicted whatever the donor concentration during its decomposition, providing important basis for quantitative analysis.

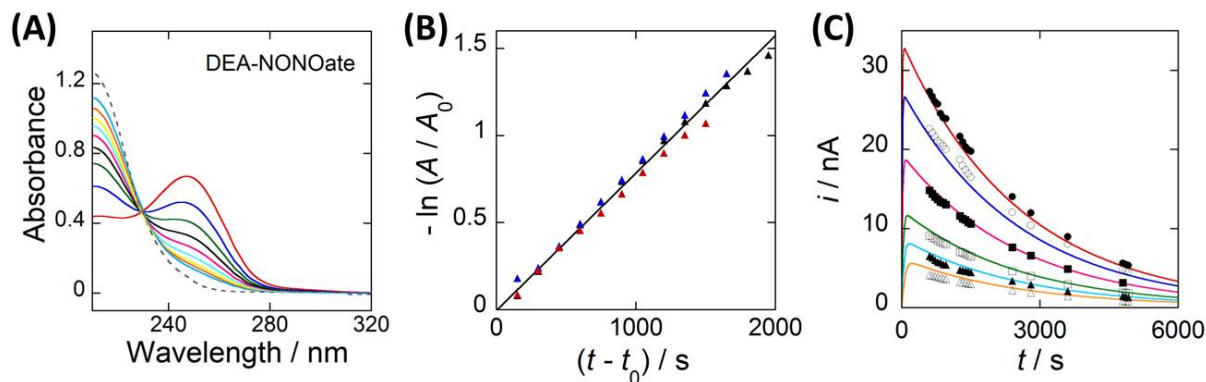


Figure B-25: (A) UV-Vis spectra of 0.1 mM DEA-NONOate, from 120 s (top) with 300 s intervals between each solid curve, until 9000 s (dashed curve) after solution preparation. Absorbance decreases with time. (B) Analysis of UV-Vis peak intensities for three series of measurements in 0.1 mM DEA-NONOate solutions at pH = 7.4.  $\lambda = 250$  nm,  $t_0 = 40$  s refers to the time to start measurements after solution preparation. Linear curve fitted with slope equal to  $k_1 = 7.8 \times 10^{-4} \text{ s}^{-1}$ . (C) Theoretical (solid curves) and experimental (symbols) chronoamperometric currents at Pt-black electrodes for various concentrations of DEA-NONOate flowing solutions. From top to bottom: 1.5 (●), 1 (○), 0.5 (■), 0.2 (□), 0.1 (▲) and 0.05 mM (Δ). Curves fit with  $k_1 = 7.8 \times 10^{-4} \text{ s}^{-1}$ ,  $k_2[\text{O}_2] = 5.5 \times 10^2 \text{ M}^{-1} \text{ s}^{-1}$  and  $i/[\text{NO}^*] = 1.13 \times 10^{-3} \text{ A M}^{-1}$ .

### Calibration curve and electrode sensitivity

On the basis of these kinetic determinations, a calibration curve was established over a submillimolar concentration range by evaluating  $\text{NO}^*$  concentrations at the time of each chronoamperometric measurement.

Accordingly, a linear variation was obtained over two decades (Figure B-26), showing that  $\text{NO}^*$  detection on Pt-black electrodes was very reliable over this concentration range. Note that the upper limit was constrained by the initial concentration of DEA-NONOate that could be used experimentally. The electrode sensing limitation was believed in a larger range since no deviation was observed at the highest experimental concentrations (i.e., 22  $\mu\text{M}$  of  $\text{NO}^*$  in Figure B-26A). Note also that the linear curves reported in these figures did not represent the result of curve fits but were the theoretical line predicted from previous determined values of  $k_1$  and  $k_2$ . These results confirmed again a good consistence among fitness of  $k_1$ ,  $k_2$  values over various concentrations, well-controlled convective mass transport, as well as species diffusion coefficient; indicating Pt-black deposits would be suitable and effective for  $\text{NO}^*$  monitoring.

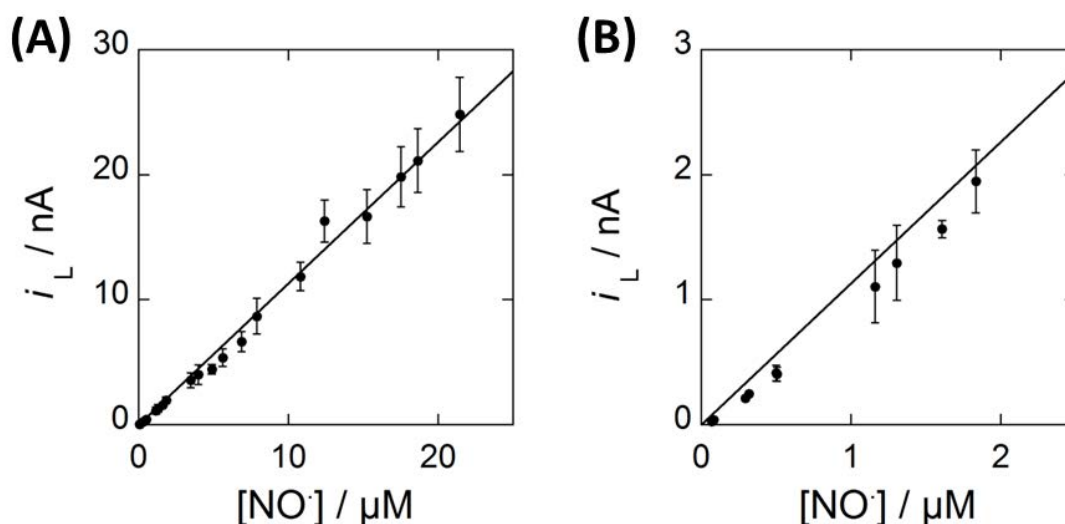


Figure B-26: (A) Calibration curve of  $\text{NO}^\bullet$  detection at Pt-black electrodes established from DEA-NONOate flowing solutions ranging from 1500 to 0.1  $\mu\text{M}$ , at pH 7.4. Corrected currents monitored at 850 and 1200 s after solution preparation. Linear curve with slope equal to  $1.13 \times 10^{-3} \text{ A M}^{-1}$ .  $E = 0.62 \text{ V/REF}$ . (B) is one magnified zone of (A) that refers particularly to the detection at low concentrations.

The LOD resulting from repetitive measurements at low  $\text{NO}^\bullet$  concentrations (i.e., close to 50 nM) was about 30 nM. This limit was similar to those already reported under various conditions with different geometries and electrode dimensions [52-54,82,202,212,256,258,259]. However, the sensitivity reached here with  $2.87 \text{ A M}^{-1} \text{ cm}^{-2}$  was higher by one order of magnitude than previously reported ones.

### 2.3. *In vitro* detection of samples mixture

#### Mixture of two stable species hydrogen peroxide and nitrite

Current responses after several injections of  $\text{H}_2\text{O}_2$  and  $\text{NO}_2^-$  mixture solutions (pH = 7.4) are reported in Figure B-27. Since current plateaus were observed at Pt/Pt-black electrodes, additivity between currents at the two detection potentials should apply.

Figure B-27A, -27B demonstrate that currents monitored of mixtures at the potential of 0.85 V/REF well corresponded to the sum of the individual current responses of  $\text{H}_2\text{O}_2$  ( $E = 0.45 \text{ V/REF}$ ) and  $\text{NO}_2^-$  ( $E = 0.85 \text{ V/REF}$ ) from separated injections. This was confirmed whatever the concentration ratio between  $\text{H}_2\text{O}_2$  and  $\text{NO}_2^-$ . Reciprocally, no interference of the  $\text{NO}_2^-$  was noticed on  $\text{H}_2\text{O}_2$  detection within the accuracy of measurements (Figure B-27C).

These properties were not observed at bare Pt electrodes since no current plateau could be achieved for  $\text{H}_2\text{O}_2$  detection and serious inhibition was observed at the oxidation potential of  $\text{NO}_2^-$  (Figure B-27D). This again evidenced that Pt/Pt-black electrodes are more stable and reliable even for detection of mixtures of  $\text{H}_2\text{O}_2$  and  $\text{NO}_2^-$ .

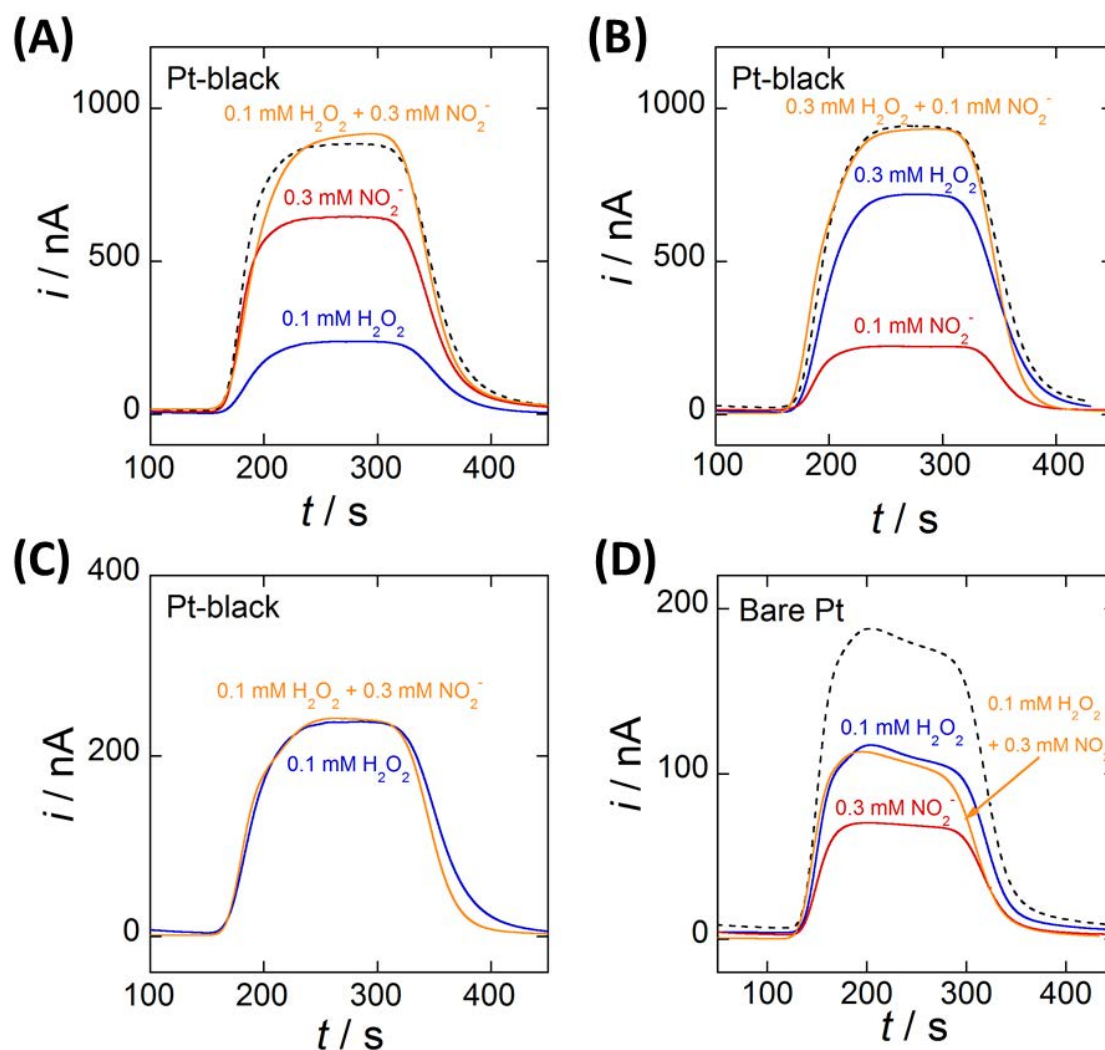


Figure B-27: Current responses monitored for 5  $\mu\text{L}$  separate injections of  $\text{H}_2\text{O}_2$  or  $\text{NO}_2^-$  solution and for their mixtures. (A, B) Experimental currents at Pt-black electrodes (solid curve) and corresponding sum of individual currents (dashed curve).  $\text{H}_2\text{O}_2$  detection ( $E = 0.45$  V/REF),  $\text{NO}_2^-$  detection ( $E = 0.85$  V/REF), mixture detection ( $E = 0.85$  V/REF). (C)  $\text{H}_2\text{O}_2$  detection at  $E = 0.45$  V/REF in presence or absence of  $\text{NO}_2^-$  at Pt-black electrodes. (D) The same tests as (A) but at bare Pt electrodes, with  $\text{H}_2\text{O}_2$  detection ( $E = 0.6$  V/REF),  $\text{NO}_2^-$  detection ( $E = 0.9$  V/REF), and mixture detection ( $E = 0.9$  V/REF).

Mixture of hydrogen peroxide, peroxyxynitrite, nitric oxide, and nitrite

As already known, oxidation of  $\text{ONOO}^-$  at the Pt-black electrode occurs at potentials close to  $\text{H}_2\text{O}_2$  oxidation[216]. A similar situation may apply to  $\text{NO}^\bullet$  oxidation in the presence of  $\text{NO}_2^-$  [11]. In order to be able to perform quantitative analysis of ROS and RNS mixtures at Pt-black electrodes, preliminary tests were performed to ensure (i) that no interferences or competitive reactions occurred during simultaneous oxidations and (ii) that the relative contributions of one species to the global response could be easily recovered at every detection potential.

The choice of an optimal detection potential for one species corresponded to a compromise between reaching a limiting current (i.e., a current plateau) and minimizing the influence of the other ROS/RNS on each individual current response. In the case of simultaneous detections of two species, it was convenient to select a potential related to significant contributions of the species involved.

Voltammetric profiles of  $\text{H}_2\text{O}_2$ ,  $\text{NO}^\bullet$  and  $\text{NO}_2^-$  were thus established separately at pH 7.4 under identical conditions. They are reported and compared in Figure B-28A.  $\text{ONOO}^-$  profile was previously recorded at pH 11.1 owing to its chemical stability. It was checked that its electrochemical oxidation (Equation (B.30)) was pH independent for conditions approaching physiological ones (data not shown).



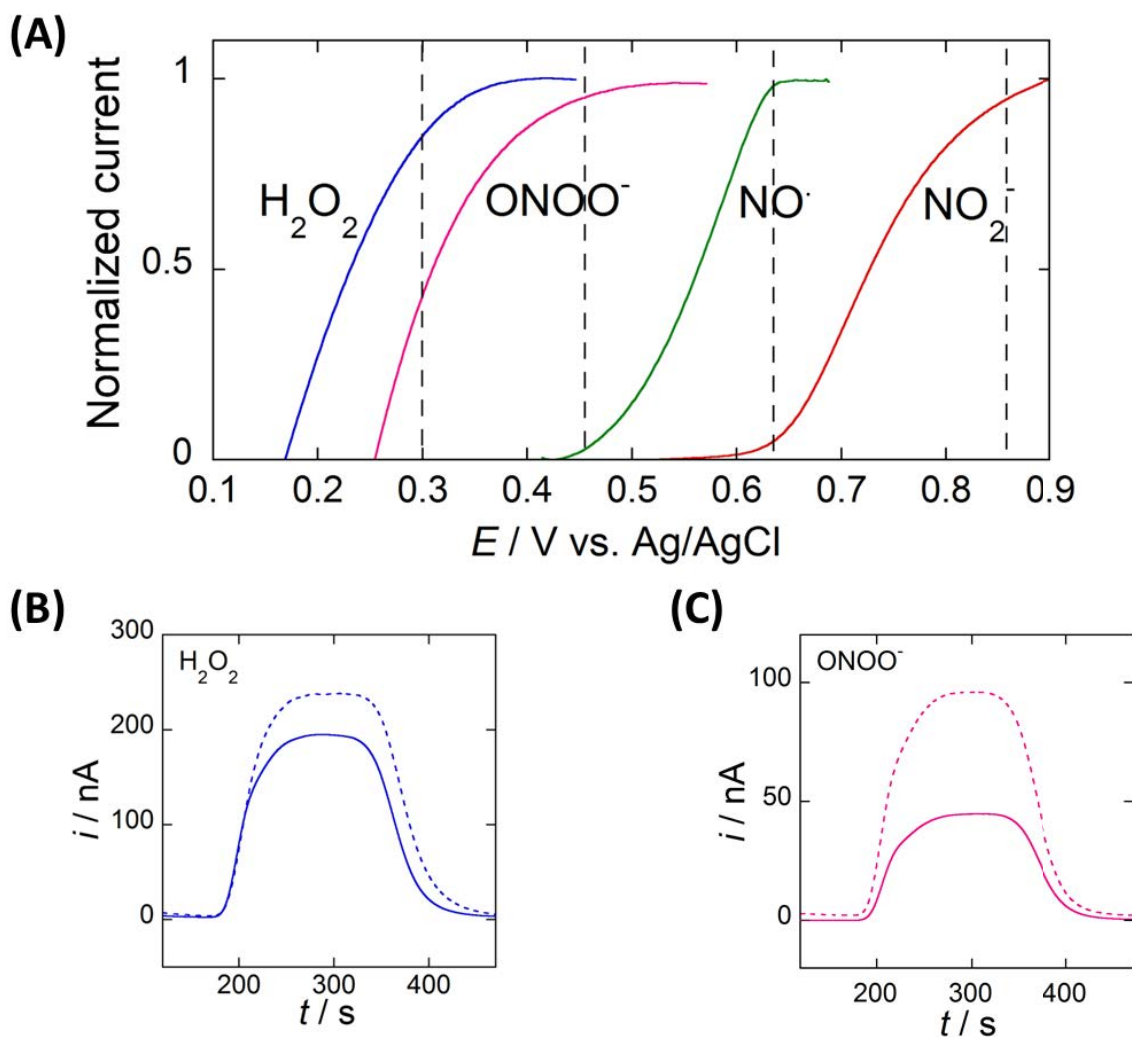


Figure B-28: (A) Normalized steady-state voltammograms obtained at Pt-black electrodes from separate flowing solutions of  $H_2O_2$ ,  $ONOO^-$ ,  $NO^\cdot$  and  $NO_2^-$ .  $pH = 7.4$  for all the species except for  $ONOO^-$  ( $pH = 11.1$ ). Dashed lines define the potentials in amperometry offering the best sensitivity and selectivity for the detection of each species. From left to right:  $E = 0.30, 0.45, 0.62, 0.85$  V/REF. (B) Current responses of  $0.1$  mM  $H_2O_2$  microinjections at  $pH = 7.4$ . (C) Current responses of  $0.1$  mM  $ONOO^-$  microinjections at  $pH = 11.1$ . In (B, C),  $E = 0.3$  V/REF (solid curve) and  $E = 0.45$  V/REF (dashed curve).

As observed, oxidation of  $H_2O_2$  overlapped strongly with  $ONOO^-$  while oxidation profiles of  $NO^\cdot$  and  $NO_2^-$  were well separated from the others. Accordingly, four optimal detection potentials were defined as reported by the vertical dashed lines in Figure B-28A.

Note that  $0.45$  V/REF were potentials selected previously both for  $H_2O_2$  and  $ONOO^-$  detections. In order to distinguish these two species, relative influences of  $H_2O_2$  and  $ONOO^-$  at  $0.3$  and  $0.45$  V/REF were then analyzed from the voltammetric profiles as well as from current responses obtained from a series of microinjections performed at these potentials (Figure B-28B, -28C).

Owing to these results, one had:

$$i_{0.30\text{ V}} = 0.85i_{\text{H}_2\text{O}_2} + 0.43i_{\text{ONOO}^-} \quad (\text{B.37})$$

$$i_{0.45\text{ V}} = i_{\text{H}_2\text{O}_2} + i_{\text{ONOO}^-} \quad (\text{B.38})$$

where  $i$  is the global current measured at each potential,  $i_{\text{H}_2\text{O}_2}$  and  $i_{\text{ONOO}^-}$  correspond to the individual limiting currents at plateau potential ( $E = 0.45\text{ V/REF}$ ).

These relations were also tested and validated experimentally by comparing current responses monitored with separate  $\text{H}_2\text{O}_2$  and  $\text{ONOO}^-$  solutions and mixtures of identical concentrations (Figure B-29A, -29B). These experiments were conducted at pH 8.4 (pH slightly higher than physiological conditions) in order to detect enough amount of  $\text{ONOO}^-$  (see decomposition kinetics in Figure B-22D). This pH value offered a good compromise for testing the performance of the electrochemical detections with synthetic mixtures since it deviates not too much from physiological condition and provides the necessary time delay between the solution preparation and measurements. These figures illustrate the perfect agreement obtained between currents in case of microinjections. The sum of individual currents matched the current measured for the corresponding mixture at each potential.

The same evaluation was extended to the two other species  $\text{NO}^\bullet$  and  $\text{NO}_2^-$  at 0.62 and 0.85 V/REF. On the basis of the voltammetric profiles reported in Figure B-28A, one obtained within the accuracy of the measurements:

$$i_{0.62\text{ V}} = i_{\text{H}_2\text{O}_2} + i_{\text{ONOO}^-} + i_{\text{NO}^\bullet} \quad (\text{B.39})$$

$$i_{0.85\text{ V}} = i_{\text{H}_2\text{O}_2} + i_{\text{ONOO}^-} + i_{\text{NO}^\bullet} + i_{\text{NO}_2^-} \quad (\text{B.40})$$

These relations were also confirmed by series of microinjections performed at these two potentials (Figure B-29C, -29D). Finally, the good agreement and additivity observed between data demonstrated that it was possible to evaluate the contributions of all the four species and therefore to assess the composition of unknown mixtures of  $\text{H}_2\text{O}_2$ ,  $\text{ONOO}^-$ ,  $\text{NO}^\bullet$  and  $\text{NO}_2^-$ . Indeed, provided that the mass transport regime in microchannel is well controlled and predicted [214,260,261], the determination of mixture composition from Equation (B.37) to (B.40) is straightforward. These results clearly suggested that no side reaction occurred during simultaneous oxidations of the four species. It gives the opportunity to detect, characterize and quantify small amounts of ROS/RNS cocktail released by populations of

living cells. Note that in such case, physiological pH should lead to correct results whenever ROS/RNS transport between the cells and the detecting electrodes is fast enough.

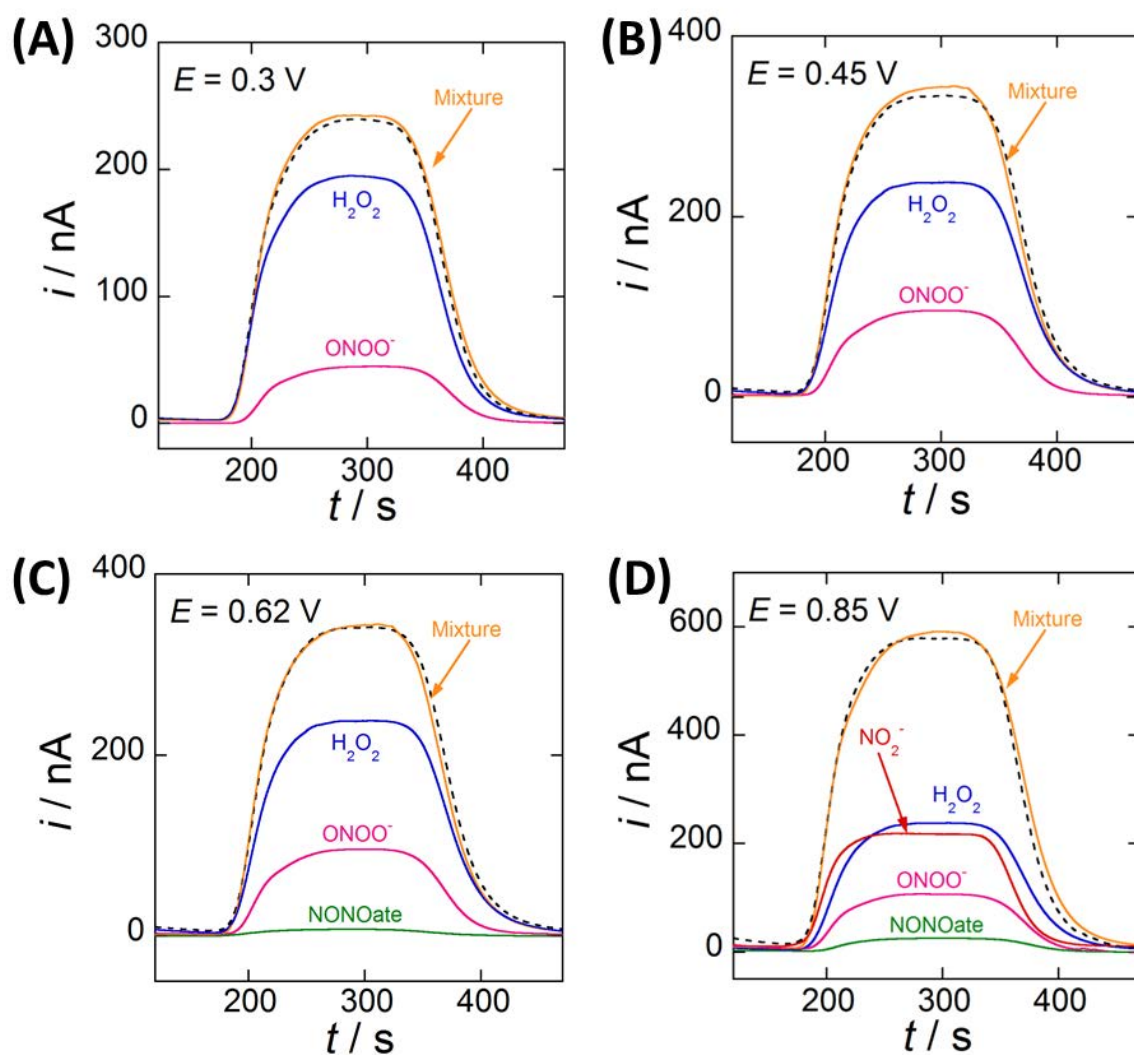


Figure B-29: Current responses at Pt/Pt-black electrodes (solid curve) as a function of the detection potential with microinjections of 0.1 mM separate solutions and mixtures of  $\text{H}_2\text{O}_2$ ,  $\text{ONOO}^-$ , DEA-NONOate and  $\text{NO}_2^-$  at  $\text{pH} = 8.4$ . Dashed curve refers sum of individual current responses obtained from separate solutions.

## 2.4. Conclusion of section 2

The optimized Pt/Pt-black microband electrodes showed satisfactory analytical performances in detecting four representative ROS/RNS (i.e., H<sub>2</sub>O<sub>2</sub>, ONOO<sup>-</sup>, NO<sup>•</sup>, and NO<sub>2</sub><sup>-</sup>) *in vitro*. Although mechanisms were fundamentally different, oxidation on Pt/Pt-black electrodes was found to be predominantly controlled by convective mass transport according to the device geometry and hydrodynamic velocity.

Owing to a larger number of active sites at nanometric level and higher porosity of Pt-black deposits, inhibition effects did not occur mostly leading to **effective** responses and long-term **stability** in contrast to bare Pt electrodes. Based on theoretical predictions of convective mass transport at microband electrodes, oxidation mechanisms as well as species-related kinetic parameters were investigated. The results matched well with data from literature, in particular with alternative spectroscopic measurements (i.e., UV-Vis). In all cases, Pt/Pt-black electrodes gave sensitive and reliable electrochemical responses (see Table B-1). **Individual components** as well as **mixtures** could be easily analyzed according to respective oxidation potentials. The detection limits down to several or tens of nanomolar well satisfy all the requirements for future monitoring of oxidative bursts from cells populations in microfluidics. All these results indicate that the optimized Pt/Pt-black electrodes offer high performances leading to promising bioanalytical applications for monitoring trace amount of ROS/RNS.

Table B-1: Analytical characteristics of four key ROS/RNS on Pt/Pt-black microband electrodes ( $w = 197 \mu\text{m}$ ) inside microchannel ( $L = 200 \mu\text{m}$ ,  $h = 20 \mu\text{m}$ ) under convective mass transport control (flow rate =  $2 \mu\text{L min}^{-1}$ ).

	Oxidation potential (V vs. Ag/AgCl)		Sensitivity (A M <sup>-1</sup> cm <sup>-2</sup> )	LOD (nM)	Linear range
H <sub>2</sub> O <sub>2</sub>	0.45	0.3 (85%)	6.02	7	10 nM – 2.5 mM
ONOO <sup>-</sup>		0.3 (43%)	2.64	40	50 nM – 5.0 mM
NO <sup>•</sup>	0.62		2.87	30	50 nM – 22 μM (limited by donor)
NO <sub>2</sub> <sup>-</sup>	0.85		5.54	12	20 nM – 3.0 mM

### 3. Conclusion of Part B

In contrast to bare Pt electrodes, Pt/Pt-black microband electrodes allowed enhanced electrochemical performances and long-term stability towards the four crucial ROS/RNS ( $\text{H}_2\text{O}_2$ ,  $\text{ONOO}^-$ ,  $\text{NO}^\bullet$ , and  $\text{NO}_2^-$ ). These benefits are due to the large number of active sites on electrode surface that facilitates electron transfer and prevents inhibition effects. The plating process was optimized in order to reach the highest signal-to-noise ratio while keeping compatibility of the deposit thickness with microfluidic devices. In parallel, activation of electrodes gave reproducible results, making these electrodes easily reusable.

High reliability and sensitivity of measurements were achieved under laminar flow inside microfluidic channel, allowing the species oxidation mechanisms (for  $\text{H}_2\text{O}_2$  and  $\text{NO}_2^-$ ) and the decomposition kinetic parameters (for  $\text{ONOO}^-$  and  $\text{NO}^\bullet$ ) to be fully investigated according to the steady-state mass transport regimes in experimental conditions. Furthermore, detections were successfully performed in case of the mixture of the four species. Sample compositions can be evaluated at selected detection potentials. These results validate the possibility of simultaneous electrochemical detections of ROS and RNS in microfluidic devices using Pt/Pt-black electrodes. Thus highly effective **electroanalytical sensor** for interpreting **oxidative bursts** from living cells can be expected. One must underline that temporal resolution below the second-time-scale can be achieved at channel microelectrodes owing to flexibility of device geometry and flow velocity control.

*PART C: Monitoring of cellular oxidative stress by Pt/Pt-black electrodes-integrated microsystems*



## **PART C: Monitoring of cellular oxidative stress by Pt/Pt-black electrodes-integrated microsystems**

In this part, Pt/Pt-black electrodes-integrated microdevices are developed to monitor ROS/RNS release from living cells. The four key compounds (i.e.,  $\text{H}_2\text{O}_2$ ,  $\text{ONOO}^-$ ,  $\text{NO}^\bullet$  and  $\text{NO}_2^-$ ) can be selectively detected at the four optimal potentials determined in Part B. Owing to the biocompatibility of PDMS-glass microchip and easy integration of microband electrodes, cell culture, stimulation, and detection are performed in the small “all-in-one” device. Specifically, due to advanced photolithographic patterning and flexible arrangement of microstructures, cellular oxidative bursts are fully investigated under different configurations. Microband electrodes are positioned either directly beneath a few living cells, or downstream a large cells population to achieve non-invasive measurements. In both cases, simultaneous detection of multiple compounds during oxidative stress is expected in a high-throughput manner. To provide comparison, responses from isolated single cells to the same biochemical stimulus are also monitored at platinized carbon-fiber microelectrodes, by adopting the synaptic configuration previously reported as a standard detection method in many studies of our group [75,76,79,109,117-119,133,220].

### **1. Investigation of oxidative stress in laboratory**

#### **1.1. Cell models**

Many aerobic cells, such as skin fibroblasts [75], phagocytes [262], vascular smooth muscle cells [263], endothelial cells [264] and lymphocytes [265], correspond to cell models of interest and are used in laboratory to investigate oxidative bursts. However, the burst amplitude obviously depends on individual cell line and can be dramatically different as it is essentially a function of cell's metabolic activity.



Macrophage, a crucial phagocyte in immune system, is famous for its self-survival phagocytosis behavior that primarily protects host integrity against hazardous foreign particles. The macrophage incorporates a specific arsenal of enzymes (i.e., NADPH oxidases and NO synthases) aimed at readily producing large amounts of ROS and RNS [118,200,220], plus its easy maintenance and biosafety, greatly fulfilling the prerequisites for *ex vivo* measurements. As an example [265], the burst generated by activated murine Raw 264.7 macrophages was about 13 times larger in amplitude than that from murine T lymphocytes (Figure C-1). Even the bigger B lymphocytes provided responses much smaller than macrophages (similar to those of T lymphocytes), again demonstrating the favored mass oxidative production from macrophages was a result of specific metabolic activity rather than simply caused by cell's surface area.

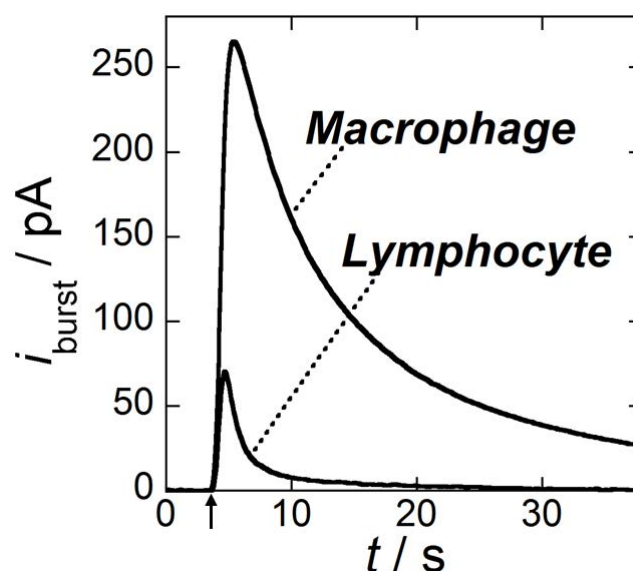


Figure C-1: Comparison of oxidative bursts detected after physical stress on a murine T lymphocyte or a murine macrophage Raw 264.7. Curves are the means of measurements (50 lymphocytes and 80 macrophages) detected at platinized carbon-fiber microelectrodes by amperometry at 0.65 V vs. SSCE. The black arrow on the x-axis represents the time when cells are activated [265].

This immortalized cell line (Raw 264.7 macrophages) was previously studied in a set of works in our laboratory [118,119,133,220] over different stimulation modes (see below). For the sake of consecutive effort, they are still adopted in the following *ex vivo* experiments conducted inside the Pt/Pt-black microband electrodes-integrated devices.

## 1.2. Cell stimulations

According to the characteristics of a particular cell line, different stimulating methods are performed to initiate ROS/RNS generation. In the case of macrophages, membrane-bound NADPH oxidase (phagocytic isoform of NOX2) is reported to be primarily responsible for ROS generation, while both inducible and constitutive isoforms of NO synthase (iNOS and eNOS) have been found to provoke RNS release. Therefore, stimulus that has effects on one or more enzymatic pools can be imposed to initiate extracellular or/and intracellular oxidative bursts. Generally, stimulation in the laboratory is carried out either through physical penetration [75,76,109,117,118] or by locally delivery of biochemical agents [119,133,200,220]. In each case, enzymatic activity possesses particular mechanisms and leads to specific response features; some examples are introduced in the following context.

### 1.2.1. Mechanical penetration

At single-cell level, oxidative stress is usually provoked by penetrating the tiny tip of a glass microcapillary across cell plasma membrane. This mechanical penetration creates transitory microhole on the lipid bilayer (through which ions such as  $K^+$ ,  $Na^+$ ,  $Ca^{2+}$  and  $Cl^-$  can diffuse) and induces depolarization of the membrane, exhibiting certain similarity with the process caused by invading micro-organisms [118]. The entry of ions, in particular of calcium ions, allows activation of a group of calcium-dependent enzymes (i.e., NADPH oxidase and constitutive NO synthase enzymes in macrophages) and subsequently leads to mass generation of ROS/RNS.

Such a stress is achieved by rapidly pricking cell membrane along the “z” direction (Figure C-2A), controlled by micromanipulator under microscope. After penetrating, capillary is retracted immediately and the cellular responses are directly monitored by amperometry (Figure C-2B).

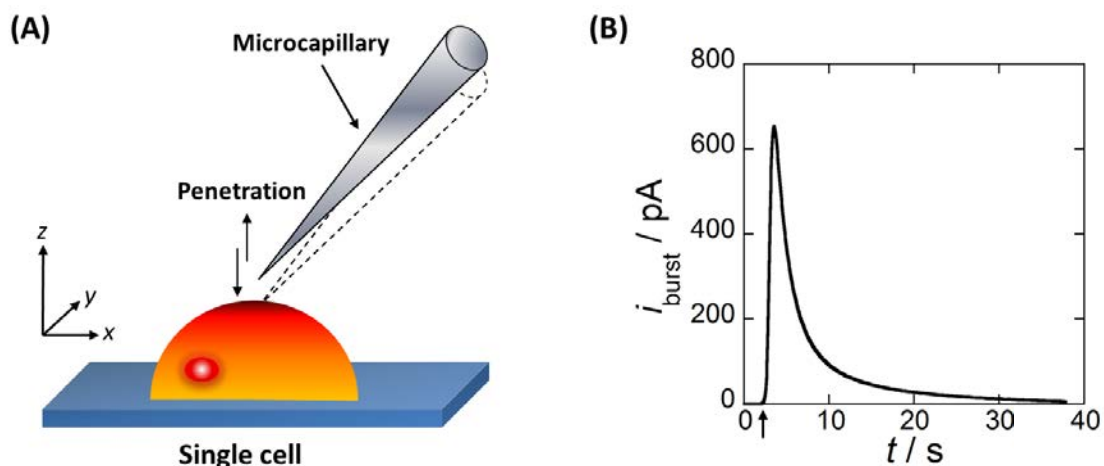


Figure C-2: (A) Schematic representation of mechanical puncturing across cell membrane by a microcapillary. (B) Typical amperometric responses after this physical stimulation, black arrow indicates the time when microcapillary penetrates cell membrane. Detection engaged at constant potential of 0.85 V vs. SSCE with the whole event duration around 40 s [118].

Indeed, the sudden depolarization has been adopted to induce oxidative bursts in different types of cells besides macrophages. Though current intensities vary a lot (from tens to several hundreds of picoamperes, corresponding to cell metabolic activity), the current-time curves are following the similar trend, which is a very fast increase of current at beginning, reaching a maximum after about one second and then undergoes a slow decrease until back to the baseline level after tens of seconds (Figure C-2B) [5,75,118]. Characteristics and kinetics of burst fluxes can be deduced from this spike-shaped signal (from maximum oxidation current, electrical charge and the peak's half-width duration).

This physical stimulation represents an excellent technique for rapid and efficient activation of oxidative stress in laboratory conditions. However, either the highly experience-demanding manipulation or necessity of repetitive experiments on large numbers of single cells for statistic purpose substantially prevents its flexible and extensive application.

### 1.2.2. Biochemical stimulation

On the other side, oxidative stress of macrophages could also be aroused by delivering specific biochemical agents to cells surroundings (Figure C-3). These activators promote phosphorylation of enzyme subunits (e.g., phorbol esters [133,266-268]), interact with cell membrane receptors (e.g., endotoxins and cytokines [220,269,270]), or affect calcium channels (e.g., calcium agonist [5,200,271]), subsequently activating specific enzymatic pools and leading to production of ROS/RNS. Unlike mechanical penetration, biochemical drugs are present within the solution and can initiate oxidative stress simultaneously from a group of cells. Signal collection is conducted at any selected cells via adjusting arrangement of target cells and detection sensors. Over this stimulation, a much moderate and durative oxidative release is expected as compared to the condition under physical stress.

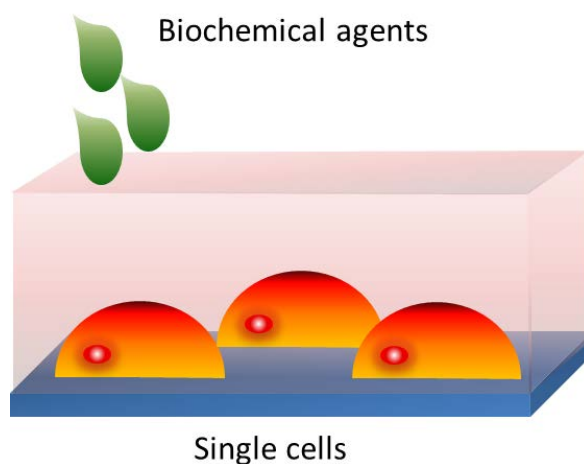


Figure C-3: Illustration of biochemical stimulation by immersing cells in biochemical agents.

#### Immune factors

The combination of cytokine interferon- $\gamma$  and bacterial-derived endotoxin lipopolysaccharide (IFN- $\gamma$ /LPS) is a typical biochemical stimulus for macrophages [133,220]. This immunological activator provokes expression of inducible NO synthase (iNOS) as mimicking an *in vivo* inflammation process. Unlike the situation of mechanical penetration, a pre-activation time of 18 to 24 hours was reported [220] for first transcribing gene of these inducible enzymes into their final active states and then provoking the oxidative stress.

The typical ensuing amperometric response of a single immunostimulated Raw 264.7 macrophage (Figure C-4) presented a main broad (lasted c.a. 1 h) but weak peak (current

intensity lower than 1 picoampere), featuring a continuous release of oxidative species; while several concomitant sharp spikes (insets in Figure C-4) were considered due to the cellular events of fluxes emission related with endosomes or exocytosis of phagosomes [220,272]. Higher production of  $\text{NO}^\bullet$ , together with the derived nitrating candidates  $\text{ONOO}^-$  and  $\text{NO}_2^-$  mainly constituted bursts cocktail whereas no significant  $\text{H}_2\text{O}_2$  was measured.

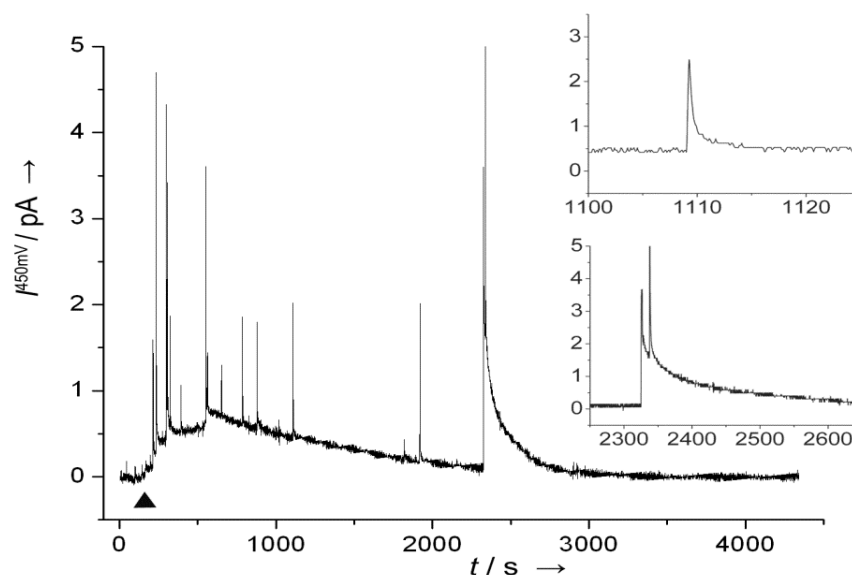


Figure C-4: Typical amperometric responses from a single IFN- $\gamma$ /LPS-stimulated macrophage, measured at 0.45 V vs. SSCE after 19.5 hours stimulation. The black triangle indicates the time at which microelectrode is placed just above the cell. Insets show representative zooms of two amperometric spikes [220].

Additional production of  $\text{H}_2\text{O}_2$  can be expected when the pre-immunoactivated macrophages are monitored in the presence of phorbol ester: phorbol 12-myristate 13-acetate (PMA) [133], since it is known to activate phagocytic NADPH oxidase. Results showed the endogenous  $\text{NO}^\bullet$  production rate remained unchanged following PMA addition, while that of  $\text{O}_2^-$  was doubled.

Except for the mentioned biochemical agents, thrombin platelet-derived growth factor (PDGF), tumour necrosis factor- $\alpha$  (TNF- $\alpha$ ), interleukin-1 (IL-1) and angiotensin II [273-275] are also well known to initiate oxidative stress from a variety of cell lines.

As compared to the situation under direct physical stress, mechanisms herein relay on recognition of stimuli by membrane receptors, and genetic expression of enzyme assembling, inevitably prolonging stimulation time. Moreover, the immunostimulated cells produce primarily intracellular superoxide and nitric oxide radicals that in turn activate multiple intracellular signaling pathways and probably trigger irreversible alteration of cell's metabolism. Therefore, this type of stimulation is usually adopted for investigation of inflammatory situation.

### Calcium agonists

Cytosolic free calcium ion concentration is an important intracellular messenger system. In resting cells, this concentration is kept very low (c.a. 100 nM) by calcium pumps. In response to specific stimulus, calcium pumps are impacted and calcium concentration rises to micromolar levels, resulting in the activation of corresponded cellular processes.

Calcium ionophore A23187 enables a fast, efficient, and reproducible activation of oxidative bursts [200]. This type of agent directly interacts with calcium channels on cell membrane, leading to a local variation of cytosolic calcium state as well as membrane polarity. Consequently, the calcium-dependent enzyme groups (e.g., NADPH oxidases and constitutive NO synthases) are provoked similarly as the situation under physical modification of cell-membrane polarity. On the other hand, just like the case of immune-activator, calcium ionophore A23187 is freely delivered to the buffer solution and then a group of cells are activated instead of one-by-one stimulation. The current response detected from a single macrophage over A23187 stimulation is shown in Figure C-5. An immediate release of electroactive species was observed while the whole process lasted more than ten minutes with a moderate current (several picoamperes). Thus from an experimental point of view, working with calcium agonists such as A23187 corresponds to a compromise between the sudden mechanical depolarization and immune activation, in terms of duration, signal intensity and biological relevance. This kind of activator is thus applied in the following experiments to explore oxidative stress either at single-cell or cells population level.

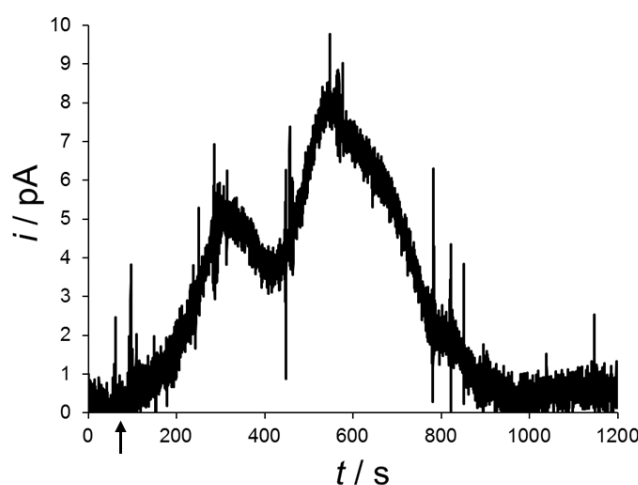


*Figure C-5: Responses of a single macrophage after the microinjection of calcium ionophore. Detection made by amperometry at 0.85 V vs. SSCE at nearby synaptic microelectrode. Black arrow at x-axis indicates the time when A23187 stimulation starts [200].*

### 1.3. Conclusion of section 1

Murine **Raw 264.7 macrophages** serve ideal laboratory models for studying cellular oxidative stress, owing primarily to their robustness and abundant enzymes that are able to generate a large amount of ROS/RNS. They have been previously chosen in our laboratory to establish the basic interpretation of oxidative bursts at single-cell level; and for the sake of conformity, they will be used as well in the following experiments.

In this work, macrophages will be stimulated by **calcium ionophore A23187**, because this activator assumes a fast, ubiquitous and reproducible stimulation, bypassing either the sharp and repetitious manipulations (in case of mechanical penetration) or the long recognition and transcription process (in case of immunostimulation).

## 2. Detection of oxidative bursts from cells populations on basal microband electrode

### 2.1. Experimental conditions

#### 2.1.1. Microdevice configuration

As mentioned in the introduction part, our group has explored extensively the oxidative stress at single-cell level by using the synaptic microelectrode configuration. This setup finds its excellent sensitivity and efficiency through minimizing the distance between microelectrode surface and that of the emitting cell (c.a. 1  $\mu\text{m}$ ). The adequate local concentration of ROS/RNS (micro- to millimolar) ensures reliable electrochemical responses from an analytical point of view, while the fast response of the electrode facilitates high temporal resolution. As a consequence, the key ROS/RNS ( $\text{H}_2\text{O}_2$ ,  $\text{ONOO}^-$ ,  $\text{NO}^\bullet$  and  $\text{NO}_2^-$ ) generated by single cells have been kinetically and quantitatively interpreted under this configuration.

Inspired by this approach, we considered hereafter a PDMS-glass reversibly-bonded microdevice in which electrochemical sensors were placed just beneath emitting cells to collect immediately the species released (called as “basal configuration” in this text). As illustrated in Figure C-6, this device comprised four uncovered chambers ( $d = 0.6$  cm). Each chamber independently comprised three microband electrodes (i.e., one Pt/Pt-black WE,  $w = 197$   $\mu\text{m}$ ; one Ag/AgCl REF,  $w = 150$   $\mu\text{m}$ ; and one Pt CE,  $w = 150$   $\mu\text{m}$ ) at the exposed glass surface. The working electrodes were platinized by black platinum ( $J = -8$   $\text{mA cm}^{-2}$ ;  $Q = -240$   $\text{mC cm}^{-2}$ ) to increase the electrode sensitivity, stability and selectivity towards ROS/RNS; and reference electrodes were made by oxidizing Ag microband to Ag/AgCl in 5 mM  $\text{FeCl}_3$  solution to support potential applied in each chamber. The fabrication details can be found in Appendix III.2 of “Multi-sensor for *ex vivo* basal detection”.

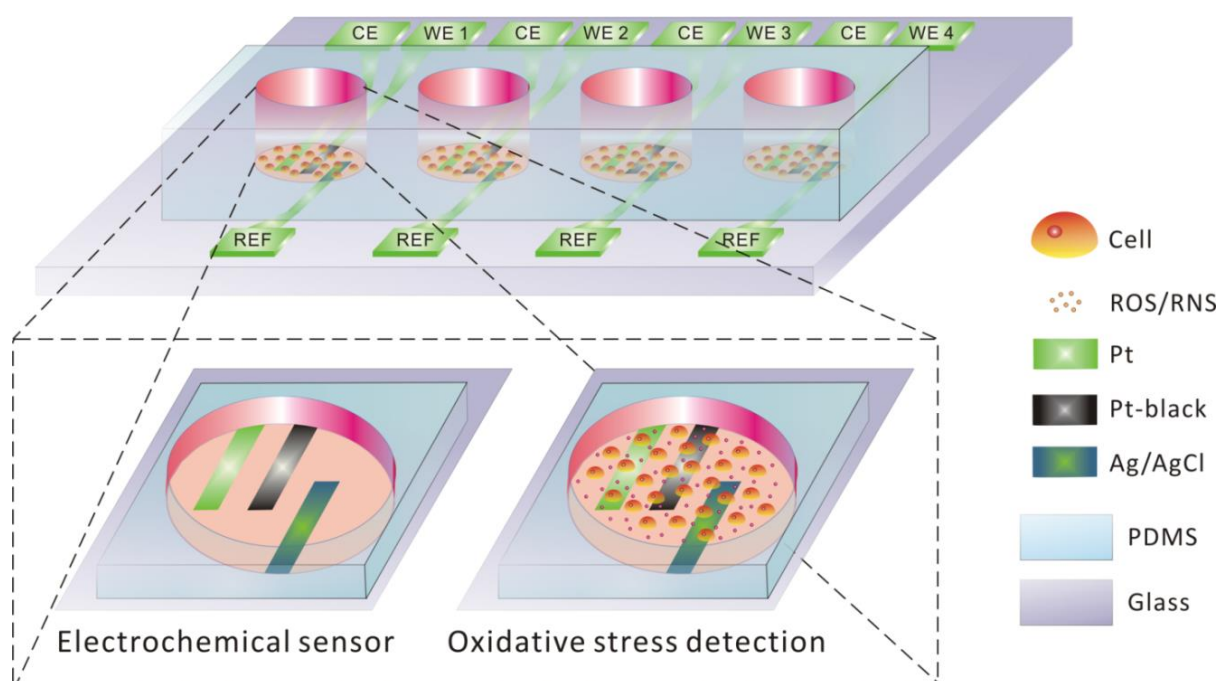


Figure C-6: Schematic illustration of 4-chamber contained PDMS-glass microdevice (top figure); and magnified views of microband CE, WE and REF within each chamber, before (bottom left figure) or during cells population basal detection (bottom right figure).

Murine Raw 264.7 macrophages were preliminary confined within each chamber where calcium ionophore (A23187) was thus introduced to initiate mass generation of ROS/RNS. The species released by adherent living cells were then detected simultaneously by the basal WE in each of the four chambers. Each WE was individually biased at one selected potential (i.e., 0.30, 0.45, 0.62 or 0.85 V vs. Ag/AgCl) according to *in vitro* voltammetric studies of  $\text{H}_2\text{O}_2$ ,  $\text{ONOO}^-$ ,  $\text{NO}^\bullet$  and  $\text{NO}_2^-$  (results in Part B). This gave the possibility to delineate the four compounds after performing parallel measurements from only one experiment.



Accordingly, this microsystem was expected to offer a multi-sensor that could efficiently detect multiple analytes simultaneously from cells populations with the aim of getting rapid insights about average cells behaviors.

Measurements were then conducted at the platform of microscope inside a Faraday cage to minimize the environmental noise. To better evaluate this basal configuration and discrepancies that could emerge from comparison with single-cell measurements, macrophages were primarily isolated and studied using synaptic microelectrodes configuration under similar conditions of cell maturation and stimulation.

### 2.1.2. Cells viability and density

Murine Raw 264.7 macrophages were harvested from one culture flask, resuspended in each chamber and cultured for 12 to 24 h inside a 37°C, 5.5% CO<sub>2</sub> incubator (cells preparation see Appendix III.3). Then growth medium was replaced by Locke's buffer (150 µL in each well, pH = 7.4 containing 2.5 mM of calcium ions) just before electrochemical studies. This process allowed cells to reach a good attachment and viability on glass substrate (Figure C-7A). The number of adherent cells at working electrode surface was estimated from the average density (i.e.,  $(1.2 \pm 0.2) \times 10^5$  cells cm<sup>-2</sup>) derived from at least 10 independent loading manipulations (one example is shown in Figure C-7B). Accordingly it gave an average collection of 1200 cells detected by each microband WE ( $w = 197$  µm,  $l = 5$  mm). The following amperometric signal was thus considered and analyzed as global responses by this cells population.

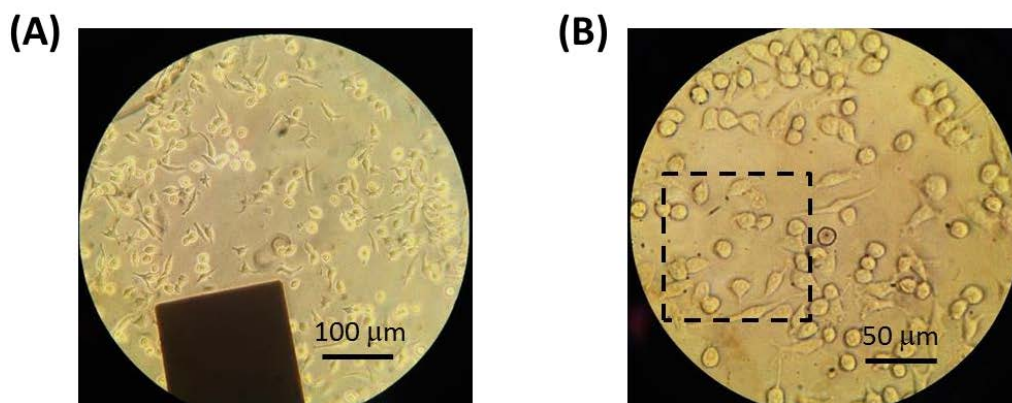


Figure C-7: (A) Macrophages immobilized at glass substrate after 18 hours culture. (B) One example of cells density estimation made by counting the number of vital cells within black pane (100 µm×100 µm). Scale bar is 100 µm in (A), and 50 µm in (B).

## 2.2. Qualitative detection of ROS and RNS production

### 2.2.1. Characteristics of amperometric responses

In order to ultimately transpose experimental conditions and to appropriately monitor a group of living cells, the release of ROS/RNS was first followed at the single-cell level by well-defined synaptic microelectrode configuration.

Isolated single cells were sparsely deposited at the bottom of a petri dish (Appendix III.3) and activated by injecting 40  $\mu\text{L}$  of a calcium ionophore A23187 stock solution (1 mM), with a micropipette, into its close environment (to obtain 10  $\mu\text{M}$  final concentration within 4 mL buffer).

The oxidative release was collected by a platinized (30  $\mu\text{C}$  deposit of black platinum) carbon-fiber microelectrode, which was positioned 1 – 2  $\mu\text{m}$  above the membrane of an isolated cell with the sensing surface covering whole cell-emitting region. Note that in this case, four optimal potentials correspond to 0.30, 0.45, 0.65, and 0.85 V vs. SSCE, and combination of relations were derived from previously reported works at platinized carbon-fiber electrode (see Appendix III.2 of “Pt-black coated carbon-fiber microelectrode”). Slight differences as compared to microband electrodes might result from the variations of Pt-black deposits in geometry, morphology and quantity on different substrates.

In this artificial synaptic configuration, electrochemical detection was performed at the cell apex as described in Appendix III.4. Distinct from the current responses over control experiment (without A23187 stimulation), a signal higher in amplitude and duration was observed from an activated macrophage (Figure C-8A). As compared to oxidative bursts initiated after direct physical stress (Figure C-2B), the current responses with A23187 also displayed an immediate increase after stimulation, indicating a sudden activation of enzymatic pools; whereas the maximum current intensity (a few picoamperes) reached about 5 minutes after stimulation, and the entire release lasted around 10 minutes, demonstrating a much gentler process but longer duration of ROS/RNS production.

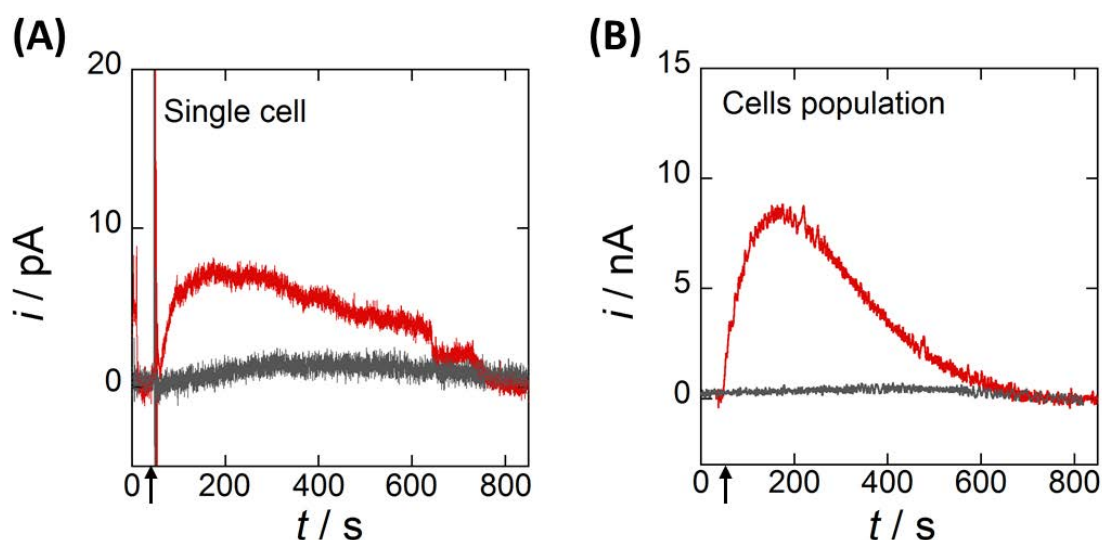


Figure C-8: Typical amperometric responses from (A) a single macrophage or (B) a group of 1200 macrophages over  $10\ \mu\text{M}$  A23187 stimulation. In each case, significant release of electroactive species was observed (red curve) as comparison to the control experiments performed at the same condition but without A23187 stimulation (grey curve). The particular responses of  $\text{ONOO}^-$  and  $\text{H}_2\text{O}_2$  from single macrophage were measured by platinized carbon-fiber microelectrode at  $0.45\ \text{V}$  vs. SSCE (according to Appendix III.2); while those resulted from cells population were detected by basal microband electrode at  $0.45\ \text{V}$  vs. Ag/AgCl (according to *in vitro* study in Part B). Black arrows at x-axis indicate the time when A23187 is injected to initiate oxidative stress.

The measurements of ROS and RNS production by a collection of c.a. 1200 cells were then performed on basal-integrated microband electrodes. As shown in Figure C-8B, under stimulation (injecting  $1.5\ \mu\text{L}$  of  $1\ \text{mM}$  stock solution into  $150\ \mu\text{L}$  buffer to form a final concentration of  $10\ \mu\text{M}$  A23187 in one chamber), the immediate current responses were evidenced under real-time monitoring. The release from cells population exhibited similarly long duration and peak-shaped features but much larger current intensity than the responses from a single cell. Currents increased within a few minutes to reach a maximum value of several nanoamperes, were constant for a while and then slowly decreased to the baseline level within 10 minutes after the initial stimulation. These responses were not observed in control experiments performed without involving any activation. All the results demonstrated an effective stimulation of cells population by delivering calcium ionophore and a fine and temporal collection of oxidative production at basal Pt/Pt-black microband electrodes. The quality of these results obtained from parallel measurements may thus lead to relevant statistical informations about a group of cells.

## 2.2.2. Cells variations and successive releases

### Cells variations

The current-time responses displayed variability between different cells populations, yet this was much less significant than that observed from single cells. Figure C-9B presents oxidative bursts released from four individual batches of Raw 264.7 macrophages. Very analogical signals were obtained, featured in common not only the shape (fast increase of currents until reaching summit at 3 to 4 minutes and then slowly decrease to baseline level around 10 minutes after stimulation) but also the highly reproducible current intensity (c.a. 22 nA at peak point). On the other side, in the cases of single-cell release, despite the conserved overall trend, differences were addressed strongly on signal shape and slightly on current intensity (Figure C-9A), indicating quite variable behaviors among individual cells. Accordingly, we assume that monitoring of cells population is preferred to illustrate average behaviors during cellular oxidative stress while single-cell measurement is carried out when particular emphasis is placed on cell variability.

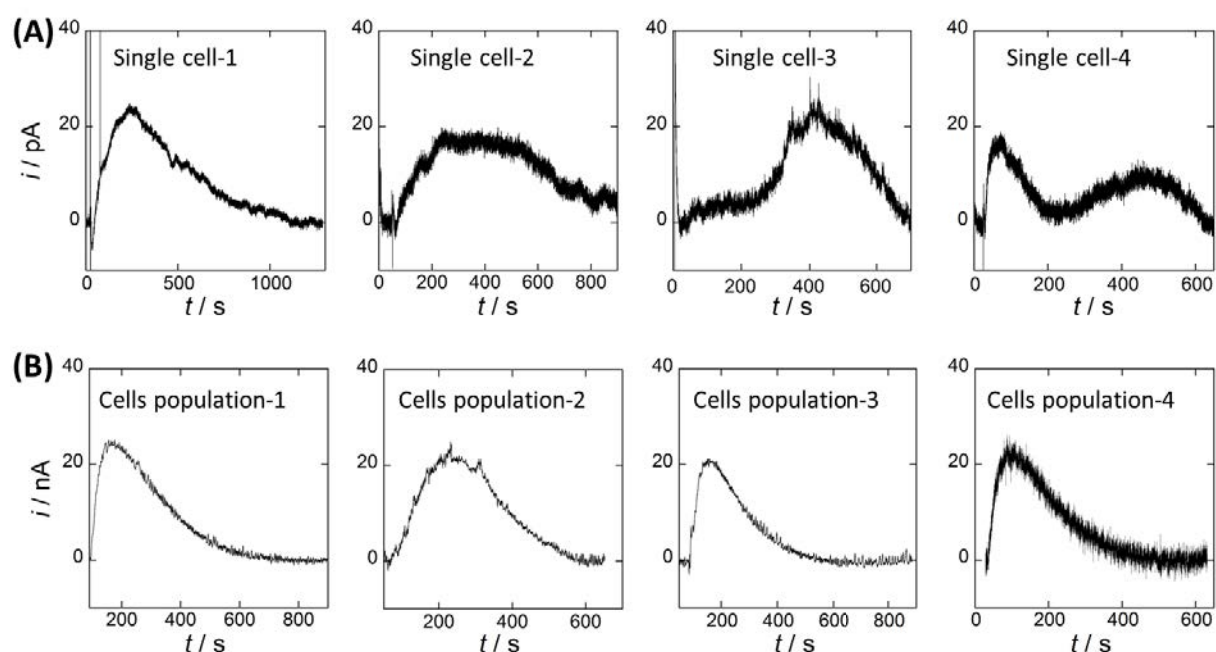


Figure C-9: (A) Variable oxidative release from individual single cells; amperometric responses recorded at 0.85 V vs. SSCE. (B) Variable oxidative release from different batches of c.a. 1200 cells; amperometric responses recorded at 0.85 V vs. Ag/AgCl.

### Successive oxidative releases

After response to a first stimulation returned to the baseline, re-injection of stimuli (10  $\mu\text{M}$  A23187) was performed in both sets of experiments (i.e., single-cell synaptic detection and basal detection of cells population). Successive releases of ROS and RNS were detected by amperometry (Figure C-10A, -10C), and the charges corresponded to the sequential stimulations are also demonstrated (Figure C-10B, -10D).

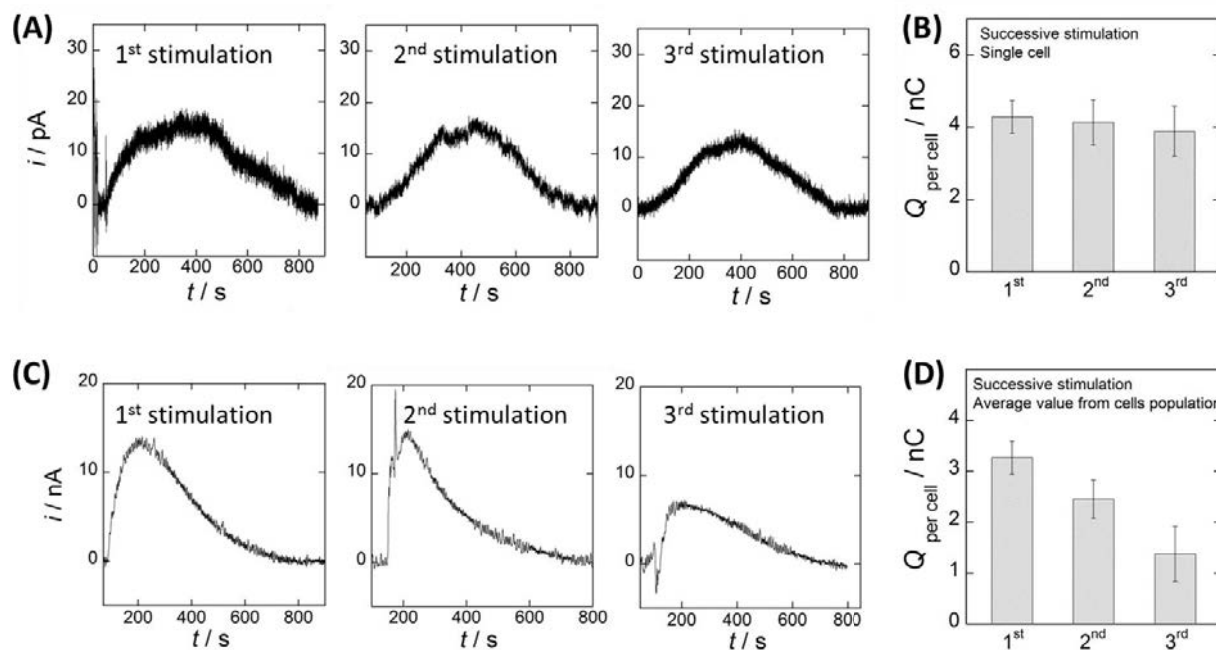


Figure C-10: Current responses over successive 10  $\mu\text{M}$  A23187 stimulation detected from (A) isolated single cells by synaptic microelectrode and from (C) cells population by basal microband electrode. Integrated charge amounts per cell with mean value and error bars are individually illustrated in (B) for single cells ( $n \geq 5$ ), and (D) for cells populations ( $n \geq 3$ ). Between sequential stimulations, 10 minutes intervals in culture medium were conserved to rest and recover the activated cells. The isolated single cells were detected at 0.65 V vs. SSCE while cells populations were measured at 0.62 V vs. Ag/AgCl. Under these conditions, oxidative compounds of  $\text{H}_2\text{O}_2$ , ONOO $\cdot$  and NO $\cdot$  were detected in both sets of experiments.

Clearly from these two sets of measurements, isolated macrophage monitored by microfiber ultramicroelectrodes displayed an excellent run-to-run reproducibility after many experiments, confirming firstly that no significant inhibition of platinum black sensing surface during long-term detection towards a variety of ROS and RNS, and secondly the non-invasive stimulation over A23187 which should interact only with the membrane calcium channels, not entailing any destructive process in macrophage cell (e.g., inflammatory situation).

In contrary, the average charge progressively withdrew when cells were detected by basal microband electrodes. That might be resulted from the enhanced interaction between neighboring cells since they were closely distributed in population. Another possibility, which is more likely to take place under basal configuration, is from the blasting of cells during electrochemical study. The latter influence could be due to the fact that cells were firmly adherent on the surface of working electrode, and some hazardous side products (e.g.,  $\text{OH}^\bullet$ ,  $\text{NO}^+$ ,  $\text{ONOO}^\bullet$ ) could be constrained just around the emitting cells; or even directly due to the prolonged contact between electrode and living cells which probably disturbed cells behaviors and electrode activity. However, the productions of ROS and RNS followed the first two stimulations were still of analytical importance according to their eligible amplitudes.

### 2.2.3. Cells detachment and chip reuse

Reuse of this device was feasible after detaching the macrophages within culture chambers. This was achieved by removing reversibly-bonded PDMS cover and then rinsing glass substrate surface with 70% ethanol alcohol under strong airstream. When the surface was thoroughly clean (Figure C-11A), cells were again found adherent and successfully grow at glass substrate. An eligible response of oxidative production was subsequently observed on the reused device. However, if the surface was not cleaned up (leaving some residues from prior group of cells; Figure C-11B), the new collection of living cells were not in good shape/viability even after a long-time recovering in growth medium. Consequently, the amperometric response displayed random features instead of a normal and integral signal. The minute/unstable fluxes and immethodical noise could not be characterized or quantified since the amperometric currents were likely affected by abnormal cell metabolism or by electrode surface contamination of adherent biological residues.

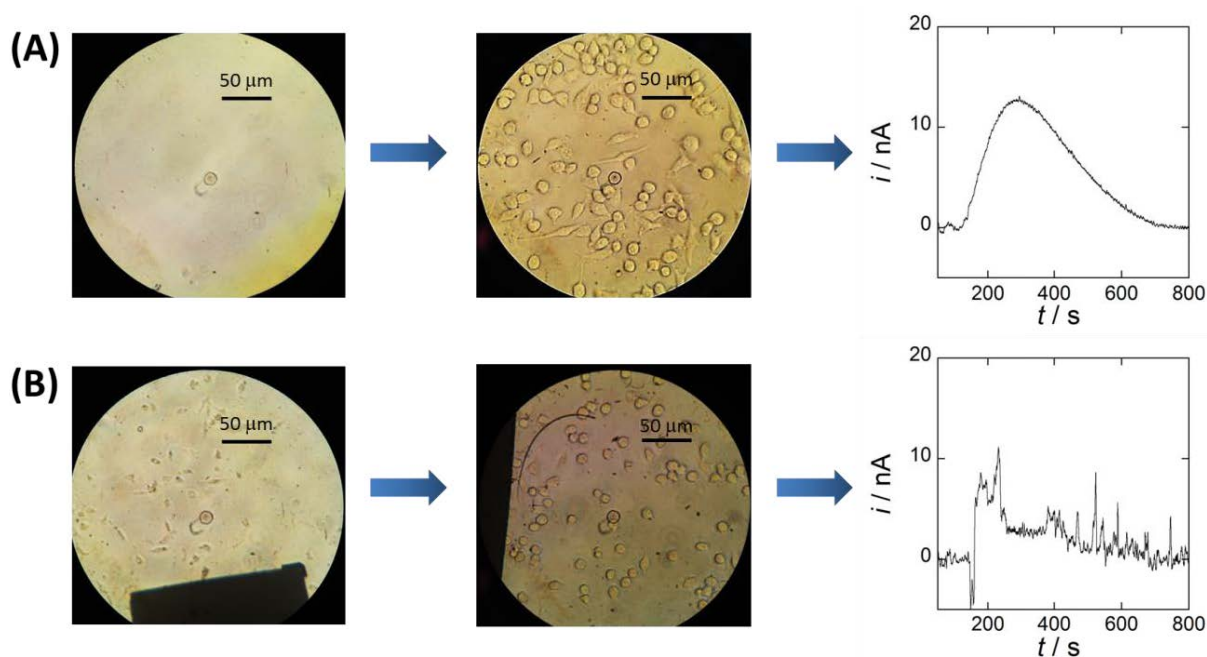


Figure C-11: Microscopic photos of Raw 264.7 macrophages cultured (A) in a reused device with thoroughly clean substrate, and (B) in a reused device with biological residues not thoroughly removed after former experiment. In each case, the amperometric responses of oxidative stress from the reloaded cells populations were detected at 0.62 V vs. Ag/AgCl.

## 2.3. Quantification of ROS and RNS production

### 2.3.1. Evaluation of fluxes and quantities of ROS and RNS production

According to the kinetic pathways concerning ROS/RNS generation and derivation under biological conditions, we consider  $\text{H}_2\text{O}_2$ ,  $\text{ONOO}^-$ ,  $\text{NO}^\bullet$  and  $\text{NO}_2^-$  as the predominant candidates to interpret the chemical nature of cellular oxidative stress in electrochemical detections. The amperometric measurements were then performed simultaneously at 0.30, 0.45, 0.62, and 0.85 V vs. Ag/AgCl at each microband WE by using the multi-channel potentiostat (experimental setup and process can be seen in Appendix III.4). Representative amperograms derived from the 4-chamber measurements are shown in Figure C-12. The response amplitude is clearly increasing with potential, demonstrating more electroactive species are detected at higher potentials; though the release kinetics (current-time course) is similar in each condition.



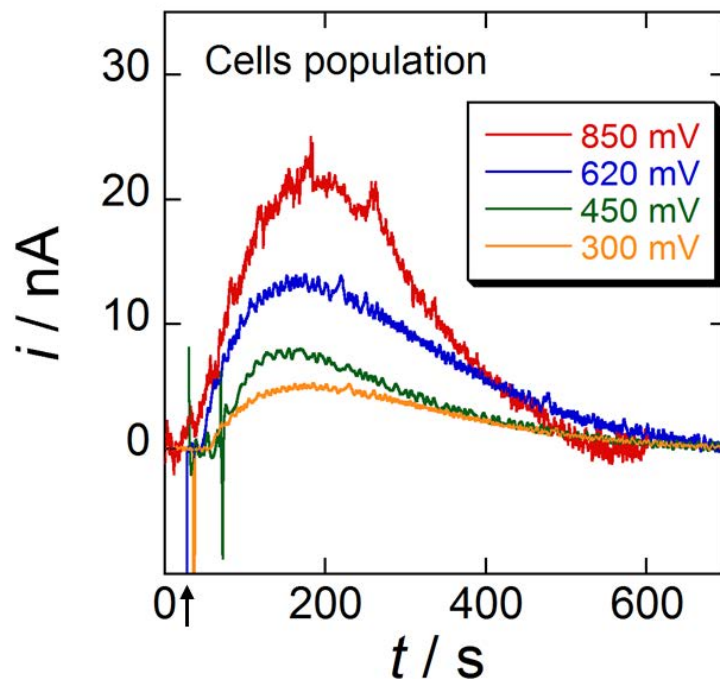


Figure C-12: Simultaneous amperometric responses from cells populations (c.a. 1200 cells) over  $10 \mu\text{M}$  A23187 stimulation. Four curves were respectively recorded at 0.30, 0.45, 0.62 and 0.85 V vs. Ag/AgCl. Black arrow at x-axis indicates the time when A23187 is injected to initiate oxidative stress.

According to results of ROS/RNS ( $\text{H}_2\text{O}_2$ ,  $\text{ONOO}^-$ ,  $\text{NO}^\bullet$  and  $\text{NO}_2^-$ ) detection from *in vitro* measurements (Equations (B.37) to (B.40)), the responses of each component could be specifically solved as linear combinations of the detected current at individual potentials:

$$i_{\text{NO}_2^-} = i_{0.85 \text{ V}} - i_{0.62 \text{ V}} \quad (\text{C.1})$$

$$i_{\text{NO}^\bullet} = i_{0.62 \text{ V}} - i_{0.45 \text{ V}} \quad (\text{C.2})$$

$$i_{\text{ONOO}^-} = 2.02 i_{0.45 \text{ V}} - 2.38 i_{0.30 \text{ V}} \quad (\text{C.3})$$

$$i_{\text{H}_2\text{O}_2} = 2.38 i_{0.30 \text{ V}} - 1.02 i_{0.45 \text{ V}} \quad (\text{C.4})$$

Therefore, both kinetic (species temporal fluxes) and quantitative results (species total amounts) can be deduced from the overall peak-shaped signals.

Emission fluxes of each compound  $j$  ( $\Phi_j$ ) by c.a. 1200 cells can be calculated from their respective current intensities under Faraday's law:

$$\Phi_j = \frac{i_j}{n_j F} \quad (\text{C.5})$$



where  $n_j$  is the number of electrons transferred in oxidation of one molecule ( $n_j = 1$  for  $\text{ONOO}^-$  and  $\text{NO}^\bullet$ ;  $n_j = 2$  for  $\text{H}_2\text{O}_2$  and  $\text{NO}_2^-$ );  $F$  is the Faraday's constant,  $96485 \text{ C mol}^{-1}$ . Therefore, the current detected can be converted into flux of species. For example, at the maximum release around 200 s after stimulation, from a batch of 1200 cells the following fluxes were deduced:  $\Phi_{\text{H}_2\text{O}_2} = 32 \pm 6 \text{ fmol/s}$ ,  $\Phi_{\text{ONOO}^-} = 41 \pm 7 \text{ fmol/s}$ ,  $\Phi_{\text{NO}^\bullet} = 70 \pm 10 \text{ fmol/s}$ , and  $\Phi_{\text{NO}_2^-} = 40 \pm 4 \text{ fmol/s}$ .

Stable ratio of individual species fluxes during entire oxidative stress was observed (Figure C-13B), implying a simultaneous and constant release fraction of all the involved components. Despite less collection of short-lived species (in particular for  $\text{ONOO}^-$ ) was detected as compared to single-cell detection under synaptic configuration (Figure C-13A); the basal detection configuration still exhibited the high reliability and reproducibility.

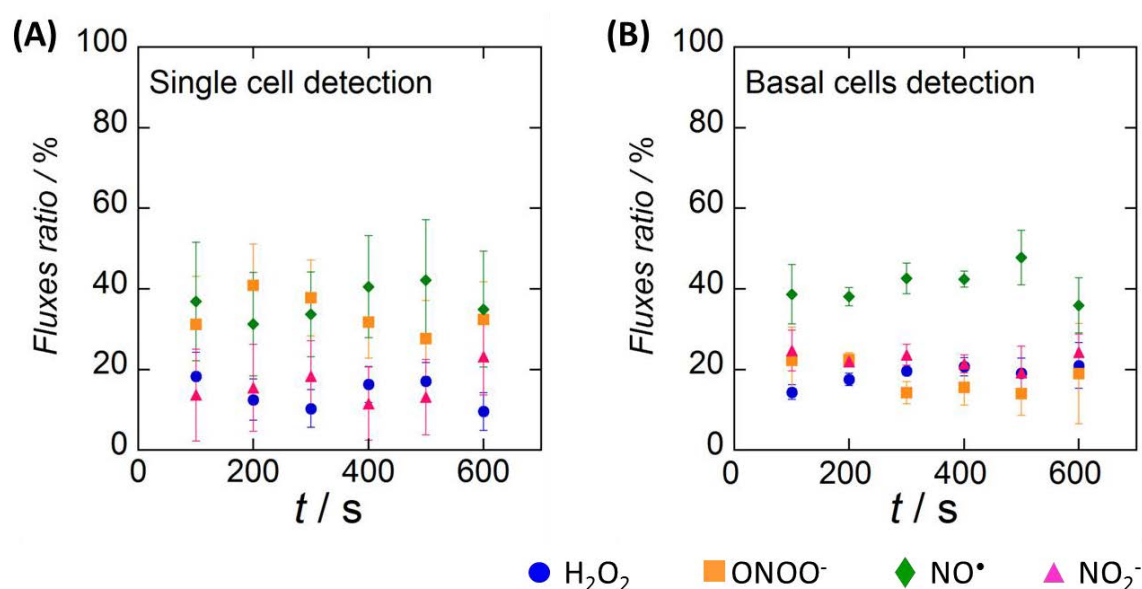


Figure C-13: The variation of fluxes ratio of the four oxidative species with time. (A) Species fluxes from single cells detected under synaptic configuration (20 – 30 experiments for each species). (B) Species fluxes from cells population detected under basal configuration (5 simultaneous experiments overall).

On the other side, the effective quantities of each species ( $N_j$ ) was deduced from integrating the overall charge of individual components during the entire oxidative stress:

$$N_j = \frac{\int_{t_i}^{t_i+\Delta t} i_j dt}{n_j F} \quad (\text{C.6})$$

where  $t_i$  is the time when oxidative emission is initiated (i.e., current responses start to increase), and  $\Delta t$  is the oxidative event interval (i.e., time during which the responses are

subtracted from baseline). Indeed, the linear combination of Equations (C.1) to (C.4) can also apply to the charges detected at each potential. According to the basal detection (pink columns in Figure C-14), A23187 activated Raw 264.7 macrophages secreted the following average quantities per cell:  $N_{\text{H}_2\text{O}_2} = 6.2 \pm 1.2$  fmol,  $N_{\text{ONOO}^-} = 4.8 \pm 2.4$  fmol,  $N_{\text{NO}^\bullet} = 12.6 \pm 3.4$  fmol, and  $N_{\text{NO}_2^-} = 7.0 \pm 2.8$  fmol.

These results are also compared with data obtained from single-cell measurements (the same cell line of Raw 264.7, blue columns in Figure C-14). The production of the two chemically stable species  $\text{H}_2\text{O}_2$  and  $\text{NO}_2^-$  was consistent whereas that of  $\text{NO}^\bullet$  and  $\text{ONOO}^-$  was slightly lower, but still close to the statistical errors. This difference might result from possible interactions between cells due to their close distribution, or from the basal configuration which may lead to lower collection efficiency of apex releases.

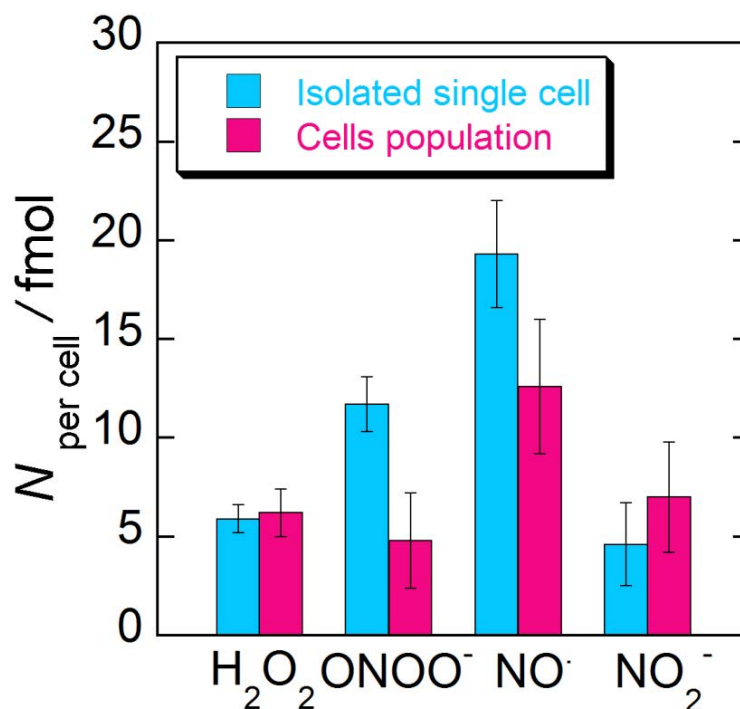


Figure C-14: Comparison of average release of  $\text{H}_2\text{O}_2$ ,  $\text{ONOO}^-$ ,  $\text{NO}^\bullet$  and  $\text{NO}_2^-$  per cell from single-cell detection (blue columns) and from cells population basal detection (pink columns) over  $10 \mu\text{M}$  A23187. Data for single-cell release was obtained after performing 20 – 30 experiments at each potential ( $n > 100$  experiments overall); while only 5 measurements were conducted for cells population, and in each measurement, four interested potentials were simultaneously applied.

However, statistical results from single-cell detection were only relevant after performing more than 100 individual experiments (20 – 30 tests at each selected potential); whereas the corresponding results of cells population detection were obtained only after combination of 5 experiments. This observation makes thus this basal detection mode highly

avored for highly demanding biological studies where various experimental conditions and parameters might be investigated (such as to evaluate drug effects). Indeed, the standard errors in latter case were strictly related to the variations between different batches of cells, since each data already represented the average behaviors of 1200 cells. Moreover, the fact that the stable fluxes composition and the similar level of species amounts detected from single-cell measurements or cells population assays justifies a posteriori of the present configuration of basal detection.

### 2.3.2. Evaluation of primary production of $O_2^-$ and $NO^\bullet$

One assumption for the release of oxidative species by macrophages, just like in the case of exocytosis, is that they are originally stocked inside cells and passively set free after activation. If so, the liberated ROS/RNS should fleet to the nearby microelectrodes in much less than one second according to their fast diffusion in aqueous medium ( $D \sim 10^{-5} \text{ cm}^2 \text{ s}^{-1}$ ). However, the duration of integral release (c.a. 10 minutes) observed in present work, whatever on single cells or cells population, makes this assumption impossible. The lipophilic property of most candidates (e.g.,  $NO^\bullet$ ,  $H_2O_2$ , and  $ONOO^-$  via its protonated form  $ONOOH$ ) further conflicts the preexistence of reservoirs of those compounds. Taking into account the previous studies in our group about oxidative stress on different types of cells, including macrophages[118,200], the mass generation of ROS/RNS is certainly due to activities of specific enzymes rather than the storage-and-liberation process as occurs in vesicular exocytosis.

Note that the four detected ROS/RNS are indeed derived from two primary reactive species (i.e.,  $NO^\bullet$  and  $O_2^-$ ) that are well-known to be generated from particular enzymatic sources. As demonstrated in the background part,  $NO^\bullet$  is synthesized from oxidation of L-arginine at the presence of NOS dimers. The presence of two NOS isoforms, namely endothelial NOS (eNOS) and inducible NOS (iNOS), have been previously evidenced in Raw 264.7 macrophage [276-278]. However, each has distinct activation pathway. The eNOS exhibits constitutive enzymatic activity for a fast and intense  $NO^\bullet$  generation; while the main  $NO^\bullet$  source characterized in macrophages is iNOS but a long-term delay before  $NO^\bullet$  production is necessary for genetic expression [133,220]. In our condition, macrophages were not pretreated with immunoactive factors but stimulated by calcium ionophores which are

supposed to directly interact with calcium channels. Accordingly, the  $\text{NO}^\bullet$  production should arise from the eNOS rather than iNOS since the former isoform is strongly activated by entry of calcium whereas the latter one is substantially insensitive to calcium concentration alteration. Moreover, the immediate release of ROS/RNS observed in our experiments also caters to a constitutive enzymatic pathway.

The primary source of  $\text{O}_2^{\bullet-}$  in aerobic cells is usually credited to mitochondrial respiratory chain. However its slow kinetics and minute production cannot explain the fast and intense bursts observed in present experiments. NOS enzymes are also suspected to produce  $\text{O}_2^{\bullet-}$  as well as the follow-up species when they follow cytosolic depletion of L-arginine. They function, similarly as oxidase, only in monomer form [279,280]. But this situation is unlikely in the present work since macrophages were cultured prior to electrochemical studies in a classical medium containing adequate arginine (0.4 mM). It neither seems possible that in each experiment, the monomer- and dimer-formed enzymatic sites always existed in constant proportion and gave rise to reproducible production of ROS and RNS. In addition, the simultaneous detection of  $\text{H}_2\text{O}_2$ ,  $\text{ONOO}^-$  and  $\text{NO}^\bullet$  strongly indicates a distinguished location of  $\text{NO}^\bullet$  and  $\text{O}_2^{\bullet-}$  enzymatic sources in the cell, because only such a situation may provide enough time for a portion of the  $\text{O}_2^{\bullet-}$  molecules to disproportionate into  $\text{H}_2\text{O}_2$  ( $k \sim 10^9 \text{ M}^{-1} \text{ s}^{-1}$ ) before they react with  $\text{NO}^\bullet$  to form  $\text{ONOO}^-$  ( $k \sim 10^{10} \text{ M}^{-1} \text{ s}^{-1}$ ). The alternative and more reasonable hypothesis for a distinct source of  $\text{O}_2^{\bullet-}$  during oxidative stress is thus addressed on the plasma membrane-bounded NADPH oxidase, which is abundant in phagocytes such as macrophages. These enzymes seem more likely to offer massive extracellular production of  $\text{O}_2^{\bullet-}$  through assembling of enzymatic units over activation of calcium channels by A23187. Some previous studies in our group [79,118,265] also supported this pathway and reported the quenching of ROS generation from both fibroblasts and macrophages by involving NADPH oxidase inhibitors.

As a consequence, the interaction of calcium ionophore with membrane calcium channels might simultaneously activate two types of enzymatic systems, namely constitutive NOS sites (located in the cytosol side and anchored to the cell membrane) which generate  $\text{NO}^\bullet$ , and transmembrane NADPH oxidase sites that generate  $\text{O}_2^{\bullet-}$ .

The original production of  $O_2^{\bullet-}$  and  $NO^{\bullet}$  can be established from the four detected species. Indeed, 1 molecule of detected  $H_2O_2$  results from disproportionation of 2 molecules of  $O_2^{\bullet-}$  (Equation (A.2));  $ONOO^-$  is formed by fast coupling of  $NO^{\bullet}$  and  $O_2^{\bullet-}$ , 1 molecule in each resource (Equation (A.9));  $NO_2^-$  is generated by spontaneous decomposition of  $ONOO^-$  (Equation (A.10)) and thus follows the same contribution as  $ONOO^-$  (i.e., 1 molecule of  $NO_2^-$  comes from 1  $NO^{\bullet}$  and 1  $O_2^{\bullet-}$ ); and excess  $NO^{\bullet}$  freely diffuses to the microelectrode surface without serious reaction with  $O_2$  over this short response time. These stoichiometries enabled the reconstruction of the original release of  $O_2^{\bullet-}$  and  $NO^{\bullet}$  according to the following equations:

$$(N_{O_2^{\bullet-}})^{prod} = 2(N_{H_2O_2})^{mes} + (N_{ONOO^-})^{mes} + (N_{NO_2^-})^{mes} \quad (C.7)$$

$$(N_{NO^{\bullet}})^{prod} = (N_{NO^{\bullet}})^{mes} + (N_{ONOO^-})^{mes} + (N_{NO_2^-})^{mes} \quad (C.8)$$

After reconstruction, our data show that primary production of  $O_2^{\bullet-}$  and  $NO^{\bullet}$  was quantified respectively around 25 fmol and 27 fmol per macrophage under A23187 stimulation in basal detection. The similar quantities of two original active species and the constant production kinetics of all detected components suggested that the two types of enzymatic systems operate in tandem, possibly coupled, in order to provide a defined and stable composition between ROS and RNS during the whole burst.

Note that some other oxidative species such as  $OH^{\bullet}$  are too short-lived, or like  $NO_3^-$  not electroactive under our experimental conditions to be treated as significant components of amperometric response, although their formation cannot be excluded. Indeed,  $NO_3^-$  may be evolved from first-order decomposition of  $ONOO^-$  ( $k = 0.2 \text{ s}^{-1}$ ; via the acid form of  $ONOOH$ , Equation (A.11)). However its amount is assumed not of great importance since the  $ONOO^-$  generated from emitting cells diffuse really fast to the adherent basal electrodes. Even when the contribution of  $NO_3^-$  is not negligible, owing to the fact that it is derived from equivalent  $NO^{\bullet}$  and  $O_2^{\bullet-}$  source, the overall ratio between each primary species is independent of  $NO_3^-$ . Therefore, the detected responses at least represent a minimal value of oxidative contents. By using the basal electrodes which direct contact emitting cells, the calculated quantities should reflect closely the substantial release during oxidative stress.

## 2.4. Conclusion of section 2

By placing electrochemical sensor in the vicinity of activated macrophages, the trace emission of oxidative species was finely characterized considering kinetic and quantitative criteria. A rapid response was observed from Raw 264.7 macrophages under A23187 stimulation, indicating an immediate activation of calcium-dependent enzymes (NADPH oxidase and constitutive NO synthase), as in the situation induced by physical membrane depolarization. However, in the present work, moderate and durative signals implied much gentler enzymatic process.

The single-cell release was detected by synaptic microelectrode. This configuration provided great collection efficiency with high temporal resolution, but inevitably needed repetitive and tedious experiments at any selected experimental condition to obtain statistical meaningful result. We thus reported a PDMS-glass microdevice to detect oxidative bursts from **cells population** (c.a. 1200 cells) by **basally-localized Pt/Pt-black microband** electrodes. In comparison to apical detection, similar releasing kinetics was measured, indicating also a **real-time** monitoring under basal configuration. Results from only **few** experiments directly satisfied **statistical** criteria. Moreover, multiple microband electrodes were easily patterned on the same glass substrate and were individually biased at selected potentials, giving access to **simultaneous** evaluation of the four key ROS/RNS (i.e.,  $\text{H}_2\text{O}_2$ ,  $\text{ONOO}^-$ ,  $\text{NO}^\bullet$  and  $\text{NO}_2^-$ ). Although this basal configuration may lose some apical production, the direct contact between electrodes and cells may affect cells behaviors or/and the sensor's analytical performance over the electrochemical detections. The observation of stable release and the globally similar species quantity than under synaptic configuration justifies the reliability of the present basal configuration.

### 3. Detection of oxidative bursts from cells population on downstream microband electrodes

#### 3.1. Experimental conditions

##### 3.1.1. Microdevice configuration

In order to bypass the disturbance from direct contact of working electrodes with living cells [100,281], we have designed another configuration of PDMS-glass hybrid microchip which successfully separates the cells culture chamber and electrochemical detection region. The major purpose here is to perform non-invasive detection; however, the increasing distance from the point of generation may trigger new difficulty, since some short-lived species such as  $\text{ONOO}^-$  and  $\text{NO}^\bullet$  decay rapidly (half-life in range of seconds) during the transport. In our case, flowing solution could be conveniently applied to shorten the delivery time and consequently improve the detection efficiency. As described in Figure C-15, this device comprised upstream one microchamber ( $l = 1 \text{ cm}$ ,  $w = 0.5 \text{ cm}$ ,  $h = 50 \mu\text{m}$ ) to immobilize living cells, and four downstream microchannels ( $l = 0.5 \text{ cm}$ ,  $w = 200 \mu\text{m}$ ,  $h = 20 \mu\text{m}$ ) where electrochemical measurements were performed in parallel.

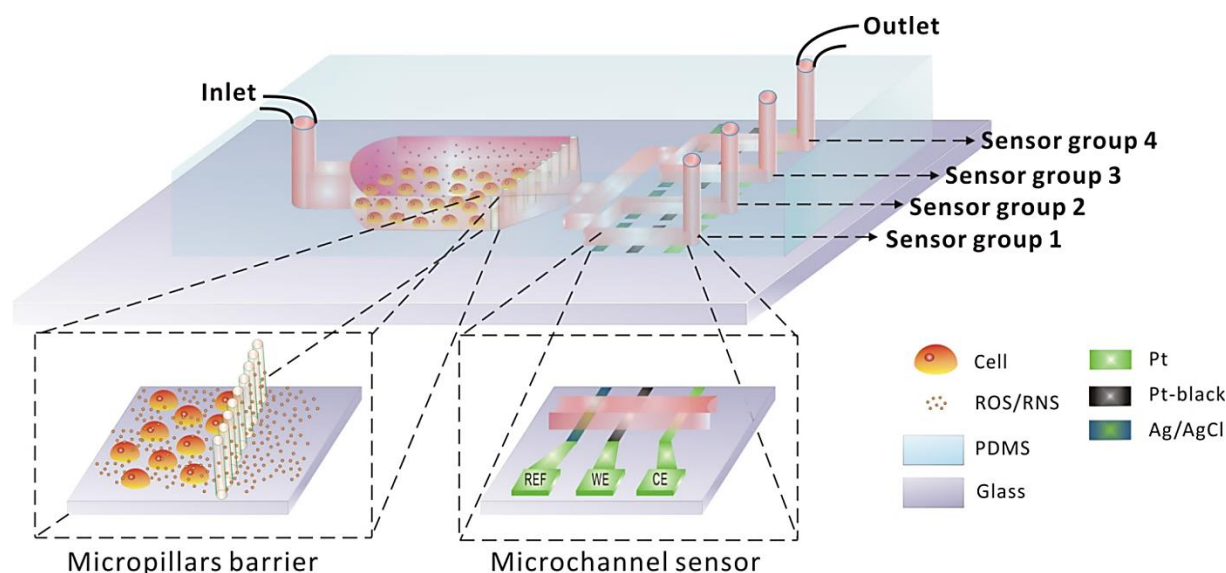


Figure C-15: Schematic illustration of 4-channel integrated PDMS-glass microdevice for downstream detection of oxidative bursts from cells population (top figure). Magnified views describe micropillars barrier that separates cell culture and detection (bottom left figure), and demonstration of one sensor group consisted of microband REF, WE and CE sequentially located beneath each downstream detection channel (bottom right figure).

This PDMS-glass microdevice provides a universal platform to investigate multiple electroactive messengers released from a large population of living cells without any invasion from electrodes. The controllable flow improves similarity with *in vivo* circulatory system and enables flexible investigation at different time durations. Thus both kinetic and quantitative information can be expected by manipulating flowing solution. The simultaneous characterizations and quantification of ROS/RNS can be conveniently accomplished at four parallel downstream sensors, allowing a fast and fine understanding of average cells behaviors.

The detection channels were positioned c.a. 2 mm after the culture chamber. Beneath each channel, microbands of one home-made Ag/AgCl REF ( $w = 200 \mu\text{m}$ ), one Pt/Pt-black WE ( $w = 197 \mu\text{m}$ ) and one Pt CE ( $w = 300 \mu\text{m}$ ) were respectively addressed at the entry, middle and end position. The working electrodes were platinized ( $J = -8 \text{ mA cm}^{-2}$ ;  $Q = -240 \text{ mC cm}^{-2}$ ) to increase sensitivity and selectivity towards ROS/RNS; and reference electrodes were made by oxidizing Ag microbands to Ag/AgCl in 5 mM FeCl<sub>3</sub> solution to support potential applied in each detection channel. Note that at the interface part between microchamber and microchannels, an array of micropillars ( $d = 50 \mu\text{m}$ , with interval gap of 10  $\mu\text{m}$ ) were incorporated to prevent cells from moving into the detection zone. The details of device constitution and fabrication are demonstrated in Appendix III.2 of “Multi-sensor for *ex vivo* downstream detection”.

All the manipulations in this microdevice (e.g., cell loading, culture, stimulation and detection) were carried out via aqueous fluids driven by a syringe pump. Murine Raw 264.7 macrophages were confined within the forward chamber; whereas the released products were branched into the following channels, and electrochemical responses were recorded when the sample solution passed through microsensors. The four working electrodes were individually assigned at 0.30, 0.45, 0.62 or 0.85 V vs. Ag/AgCl in accordance with previous study (see Part B).

We thus performed electrochemical detection either in non-stop flowing mode (Figure C-16A, -16B) or in 10-min stop mode (Figure C-16C, -16D).



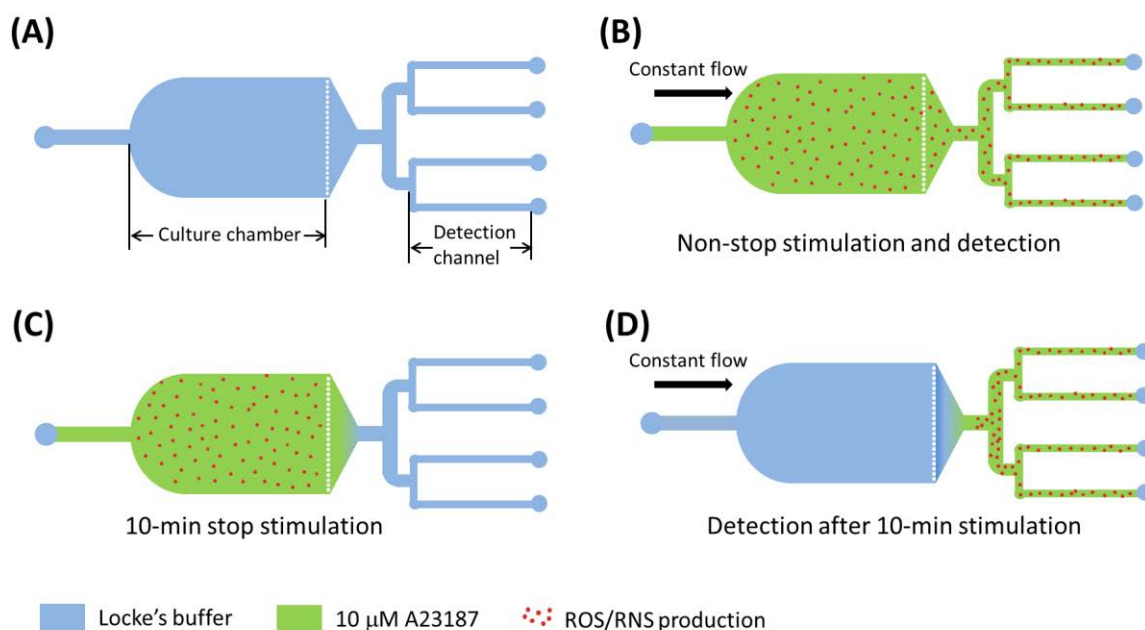


Figure C-16: Detection procedures in non-stop or 10-min stop mode. (A) Before stimulation, microdevice is fulfilled with Locke's buffer. (B) In non-stop mode, stimulus ( $10 \mu\text{M}$  A23187) is delivered into microchip at constant flow rate, and ROS/RNS emission from immobilized cells is continuously pumping to downstream sensors. (C) In 10-min stop mode, agent flow is stopped after injecting stimulus into microchamber part, cells are activated in static solution for c.a. 10 min, and (D) then ROS/RNS-accumulated sample solution is pumped to downstream sensors at constant flow rate.

### 3.1.2. Cells manipulation inside microdevice

#### Cells seeding and adhesion

Concentrated cell suspension was collected and resuspended into the microdevice by using the same protocol as described in the former basal studies with minor modifications. Before seeding cells, entire device was UV-sterilized and treated by fibronectin ( $50 \mu\text{g mL}^{-1}$ ) for 20 minutes. Then, cell suspension solution was directly driven into the microdevice by external syringe pump. After being rested for 1 h under zero flow condition in incubator, macrophages showed much favored attachment on the fibronectin-coated surface (implied by the stretching “arms” as shown in Figure C-17A) than on a pristine glass surface (Figure C-17B). This biocompatible modification, by using intermediate proteins, is a crucial step for in-situ cell study inside microfluidic system, since that ensures fast and robust cell adhesion before nutrients depletion within the small microenvironment and thus assists the following perfusion culture.

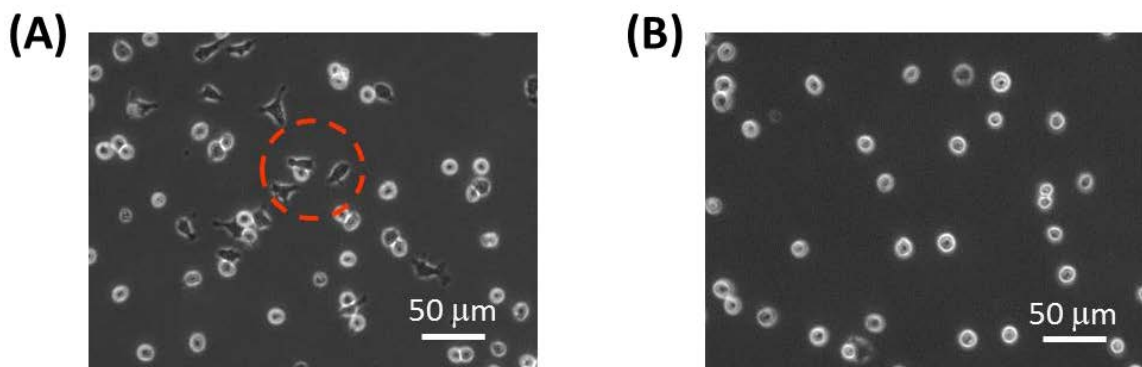


Figure C-17: Optical images demonstrate cell attachment on a glass substrate (A) with or (B) without fibronectin coating. Scale bar is 50  $\mu\text{m}$  in each image.

### Perfusion culture

As illustrated in the background part, cell maintenance inside a small culture room needs constant nutrition replenishment and wastes removal. Therefore, in this work, Dulbecco's modified eagle medium (DMEM)-based growth medium was continuously pumped into the microdevice after macrophages became adherent on the coated substrate (see Appendix III.3). However, the ensuing hydrodynamic shear stress is often an inherent limiting factor due to its detrimental effects on cells at high levels ( $> 15 \text{ dyn cm}^{-2}$ ) [170,282].

For a microfluidic 2D system, parabolic flow profile yields a simple estimate of shear stress at the surface [170]:

$$\text{shear stress} = \frac{6\mu u_{av}}{h^2 w} \quad (\text{C.9})$$

where the shear stress is presented in  $\text{dyn cm}^{-2}$  (1  $\text{dyn cm}^{-2}$  equals to  $0.1 \text{ kg m}^{-1}\text{s}^{-2}$ ),  $\mu$  is viscosity ( $\text{kg m}^{-1}\text{s}^{-1}$ ),  $u_{av}$  is average flow rate in culture chamber,  $h$  is chamber height, and  $w$  is the chamber width. Thus the shear stress is possible to be mitigated by tuning fluid velocity for a given device. In the present work, a perfusion rate of  $4.0 \mu\text{L min}^{-1}$  ( $u_{av} = 0.027 \text{ cm s}^{-1}$  inside microchamber) was applied during long-term cell culture; it correspondingly gave a shear stress of  $0.25 \text{ dyn cm}^{-2}$  when incorporating chamber dimension ( $h = 50 \mu\text{m}$ ,  $w = 5 \text{ mm}$ ) and viscosity of DMEM medium ( $7.8 \times 10^{-4} \text{ kg m}^{-1}\text{s}^{-1}$ ) [283].

This perfusion rate is sufficient to provide effective medium transport while the shear stress is of orders of magnitude below the level at which adverse effects might be introduced to cause cell injury.

After 24 h of perfusion culture, macrophages displayed good morphology and brightness (Figure C-18A) which indicated satisfying viability; and accordingly the good biological behaviors in following experiments could be expected. On the contrary, without continuous replacement of culture medium, adherent cells would suffer from fast nutrients depletion and local accumulation of toxic metabolites, resulting in ineffective growing, rounding up and even apoptosis (Figure C-18B).

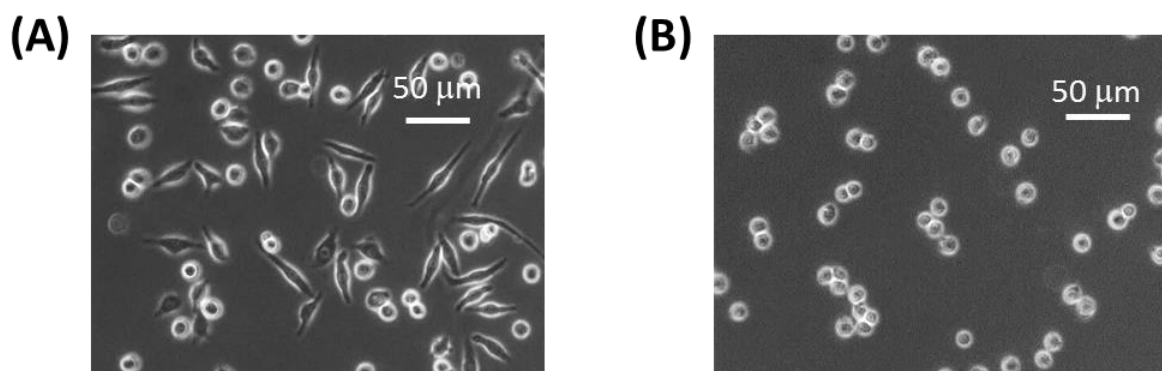


Figure C-18: Culture of macrophages for 24 h (A) with or (B) without continuous perfusion of growth medium. Scale bar is 50  $\mu\text{m}$  in each image.

Moreover, for adherent macrophages, the continuous flow of media accurately mimics the natural transport within microvascular network, thus providing more biologically meaningful conditions for *ex vivo* cellular assay.

By performing consecutive and stable media perfusion, long-term cell culture was achieved. Cells were able to continuously grow, proliferate, and even reach confluence all over the culture chamber (Figure C-19).

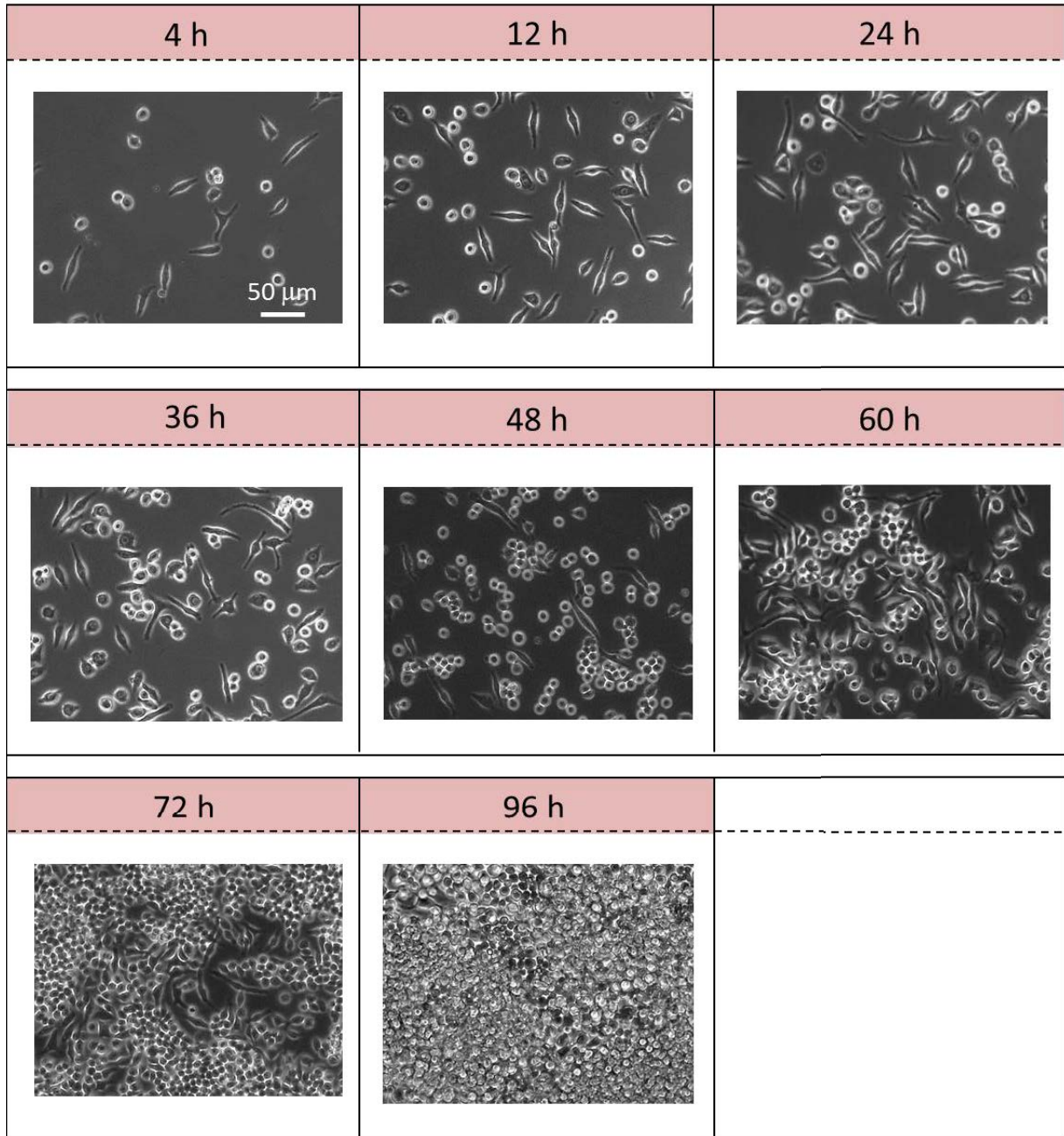


Figure C-19: Optical images illustrate long-term culture of Raw 264.7 macrophages inside microchamber for 4, 12, 24, 36, 48, 60, 72 and 96 h with continuous medium perfusion. Scale bar is 50  $\mu\text{m}$  for each image.

### Cells distribution and density

Electrochemical study of oxidative stress released by macrophages population was performed after 12 to 24 h continuous culture. According to Figure C-19 and Figure C-20, during this time period, cells population displays adequately homogeneous distribution and suitable density to not only support sufficient ROS/RNS production but also allow estimation of the number of objective macrophages. Before 12 h (e.g., image of 4 h culture in Figure C-19), cells distribution is not homogeneous enough to offer an accurate estimation of the overall number. Furthermore, the sparse cells density might lead to a low concentration of oxidative species and thus an undistinguished signal from the analytical point of view. On the other side, when culturing too long time (e.g., images of 48 – 96 h culture in Figure C-19), cells are tending to aggregate, and thus prevent precise calculation of emitting cells responsible for detected responses.

The number of macrophages was estimated by taking into account the chamber dimension and average cells density derived from at least 20 parallel experiments of seeding and culturing Raw 264.7 cells. Figure C-20 shows three individual examples from different cell batches after 12 to 24 h culture. Macrophages of good shape and brightness within marked zone (Figure C-20B, -20C and -20D) were counted. After calculation, an average density of  $(0.7 \pm 0.2) \times 10^5$  cells  $\text{cm}^{-2}$  was obtained, and correspondingly c.a.  $3.5 \times 10^4$  cells were expected within one microchamber to be responsible for ROS/RNS generation over A23187 stimulation. A primary quantitative assessment of oxidative release from a large collection of cells is achieved on this mathematic basis of cell density estimations.

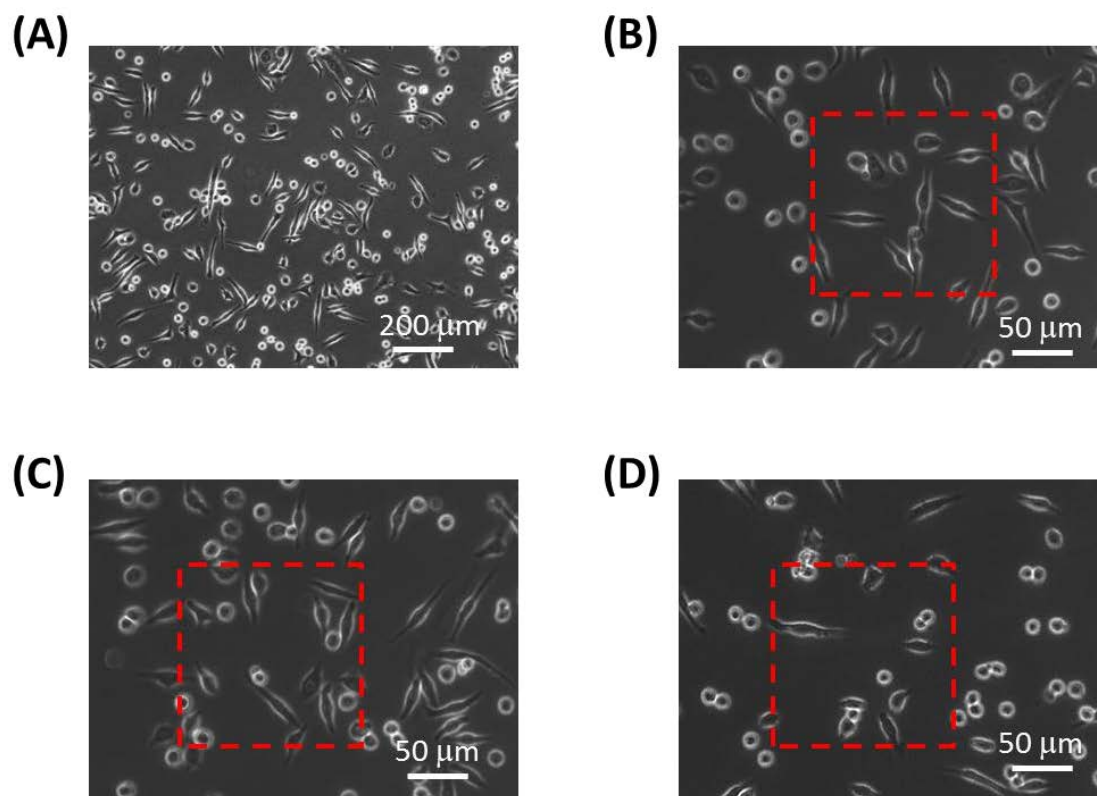


Figure C-20: Optical images of Raw 264.7 macrophages under perfusion culture for 12 to 24 h inside enveloped microchamber. (A) Image shows the uniform coverage of cells at the substrate surface. (B to D) Illustrations of cells density after the same seeding and culturing process for three individual cell batches; the calculation of density was made by counting the number of vital cells within red pane ( $150 \mu\text{m} \times 150 \mu\text{m}$ ). Scale bar is  $200 \mu\text{m}$  in (A), and  $50 \mu\text{m}$  in the other three images.

### Pillars effect

Since the microdevice is entirely connected, cells suspension is not naturally confined to the chamber domain. Micropillars ( $d = 50 \mu\text{m}$ ) were thus incorporated at the interface between chamber and channels parts to separate cell culture and detection. The gap distance between micropillars ( $10 \mu\text{m}$ ) was designed in agreement with the size of macrophages and thus acted as cells barrier during the whole *ex vivo* experiments. Macrophages were effectively confined to the upstream chamber as shown in Figure C-21A, offering the chance to engage electrochemical detection at downstream-located microband electrodes without the latent interference from the direct attachment between emitting cells and working electrodes. As comparison, the device without micropillars (Figure C-21B) was unable to stop cells from entering the downstream detection part. In addition, in absence of this pillars-barrier,

macrophages were usually observed to aggregate at the entry of detection channel since both width and height drastically decreased behind the interface zone (Figure C-21C).

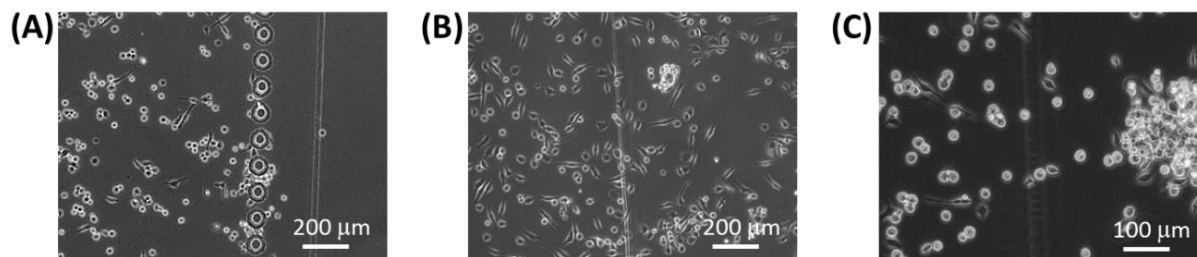


Figure C-21: Cell culture inside microchamber (A) with or (B) without micropillars array. Cells were effectively confined within chamber part when micropillars were involved. (C) Aggregation of cells at the entry of detection part when no pillars barrier was applied. Scale bar is 200  $\mu\text{m}$  in each of (A) and (B), and is 100  $\mu\text{m}$  in (C).

### Cells detachment and chip reuse

This irreversibly integrated microdevice is also reusable after biological measurements. Cells detachment was achieved by continuously rinsing microchamber with 0.05% trypsin-EDTA (ethylenediaminetetraacetic acid) solution. As shown in Figure C-22A, after c.a. 5 minutes rinse ( $4 \mu\text{L min}^{-1}$ ), a clean substrate was found again and the new collection of macrophages similarly exhibited great adhesion and viability in the reused chip. Cells could not be effectively removed by rinsing only with 70% ethanol; ubiquitous biological residues and unfavorable culture of newly seeded macrophages were observed (Figure C-22B). As compared to the basal detection system, it is possible that cells are more firmly attached to fibronectin-coated surface in present work, and accordingly are more difficult to remove. In addition, strong force is unfeasible during cells detachment in this enveloped chip since that may lead to leakage of the device or destruction of the vulnerable pillars-barrier structure. Thus, the more efficient cells dissociation agent of trypsin-EDTA was adopted in this platform due to its high digestive strength.



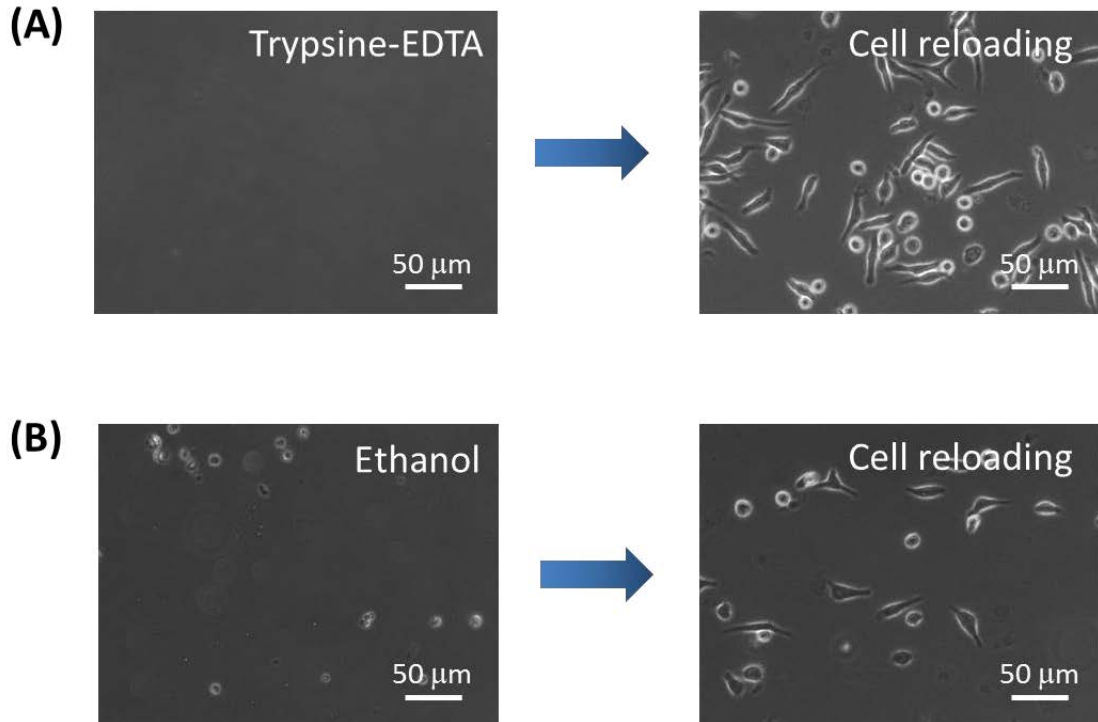


Figure C-22: Optical images of RAW 264.7 macrophages culture in a reused microdevice after detaching cells by rinsing microchamber with (A) 0.05% trypsin-EDTA, or (B) 70% ethanol. Before seeding the new collection of cells, the reused chip was sterilized by UV light and modified again with fibronectin to promote cells adhesion. Scar bar is 50  $\mu\text{m}$  in each graph.



### 3.2. Detection of ROS and RNS production

#### 3.2.1. Detection reproducibility between parallel electrodes

Cell-free microdevice was filled with 0.1 mM  $\text{H}_2\text{O}_2$  solution beforehand to check the parallelism of Pt/Pt-black sensors independently localized under each microchannel. The overall flow rate of sample solution was set at  $8 \mu\text{L min}^{-1}$ , corresponded to  $2 \mu\text{L min}^{-1}$  in each channel. Therefore, electrochemical responses were assumed to follow the same convective mass transport as reported in Part B. The simultaneous voltammograms obtained from four respective WEs are shown in Figure C-23, demonstrating fairly high reproducibility. We thus supposed that in this multi-sensor device, sample solution from upstream chamber was equally branched into each detection channel; stable potentials were supported by Ag/AgCl REFs at the entry of each channel; and the individual Pt/Pt-black WEs responded to electroactive analyte in a simultaneous and highly comparable manner. Therefore, oxidative bursts released from an upstream cells population are able to be decomposed in their particular contents during only one parallel measurement.

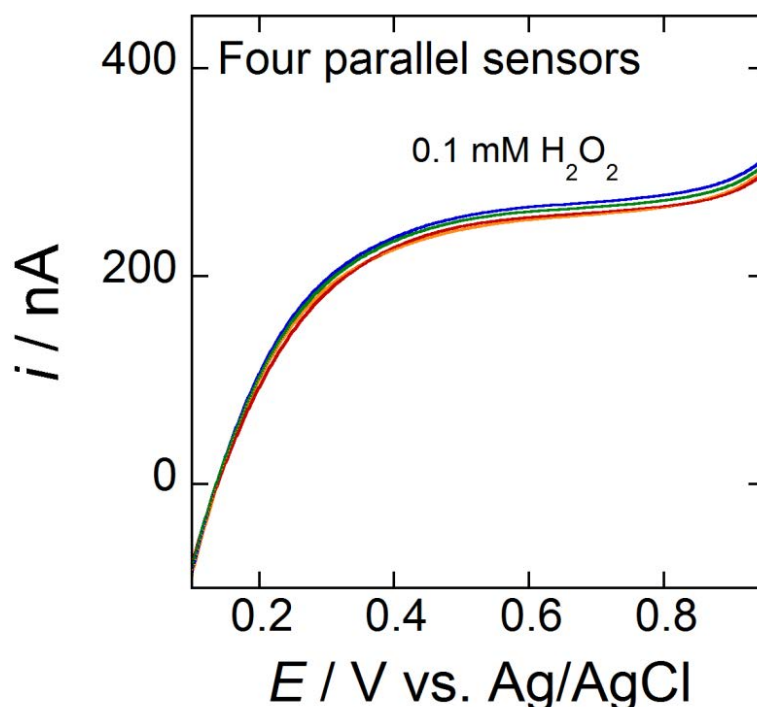


Figure C-23: Simultaneous voltammograms of 0.1 mM  $\text{H}_2\text{O}_2$  obtained from four respective Pt/Pt-black microband electrodes integrated individually to each downstream microchannel. Scan rate =  $10 \text{ mV s}^{-1}$ ; flow rate =  $2 \mu\text{L min}^{-1}$  in each channel.

### 3.2.2. Detection reliability after biocompatible coating

In the present work, to favor cell growth and proliferation, fibronectin layer was introduced into microdevice to promote biocompatibility of the bare glass substrate. However, unlike cells, this coating solution cannot be obstructed simply by pillars barrier and thus downstream sensors were also immersed in fibronectin during the treatment. A few studies [53,284-286] have reported that this agent caused a negative effect on electrochemical responses of redox probes. The similar observation was found in our multi-sensor system after being treated by fibronectin and perfused with medium for 24 h. A decrease of c.a. 25% in the intensity of oxidation response of  $H_2O_2$  compared with that detected by a fresh Pt/Pt-black microband electrode was revealed (Figure C-24). Although this influence was not extremely severe, it may lead to an underestimation of cells release in the following *ex vivo* experiments since quantification is based on the calibration curves established with fresh and activated Pt/Pt-black sensors.

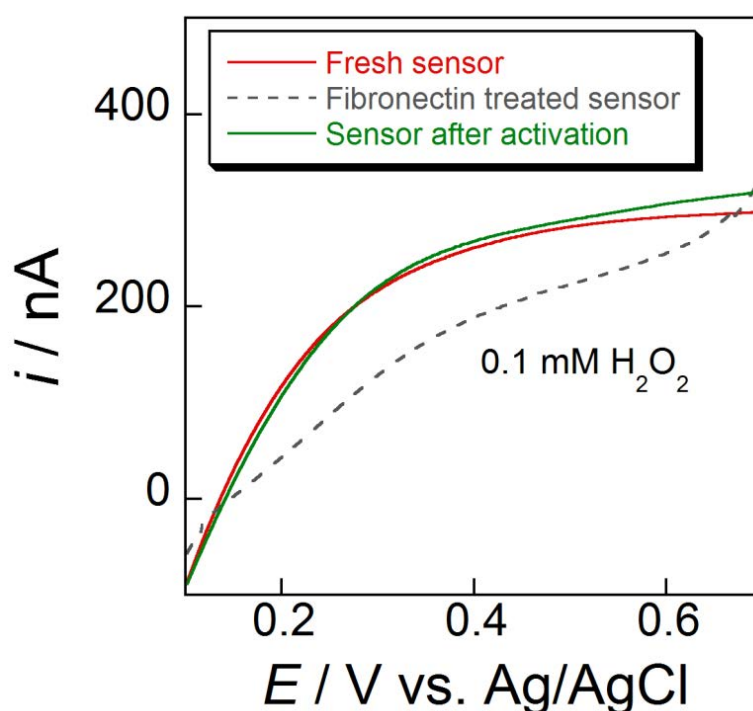


Figure C-24: Voltammograms of  $0.1 \text{ mM } H_2O_2$  at Pt/Pt-black microchannel sensor before (red curve) or after fibronectin treatment (dashed curve), and at the same degraded sensor after surface activation by potential pulses (green curve). Scan rate =  $10 \text{ mV s}^{-1}$ ; flow rate =  $2 \mu\text{L min}^{-1}$  in each channel.

To retrieve surface fouling of working electrodes, activation procedures previously adopted in the *in vitro* experiments, in terms of the alternative potential pulses (+ 0.2 V/REF, 1 s; -0.5 V/REF, 1 s; 30 cycles), was again applied. The voltammogram of 0.1 mM H<sub>2</sub>O<sub>2</sub> detected after activation of the degraded electrode is presented in Figure C-24. Clearly, electrode sensitivity was enhanced to reach the original level at which the steady-state current was found under control of convective mass transport. Accordingly, the calibration curves obtained in Part B are able to be quoted to estimate concentration of ROS and RNS detected on these activated sensors.

### 3.2.3. Detection during continuous flow

As the same to previous *ex vivo* experiments, culture medium within the device was replaced by Locke's buffer just before electrochemical study. Detection in this multi-sensor device was operated in continuous flowing solution (8  $\mu\text{L min}^{-1}$  in the overall device; 2  $\mu\text{L min}^{-1}$  in each channel). ROS/RNS production from the immobilized cells population was immediately delivered to the downstream electrodes (less than 1 s transition delay from the end of chamber) after introducing the flowing stimulation solution (10  $\mu\text{M}$  A23187). Details of experimental setup and manipulations are described in Appendix III.4.

The representative 4-channel amperometric responses are shown in Figure C-25. Signals featured similar shapes as the synaptic and basal detections, indicating as well the kinetic monitoring under this non-stop flowing mode. A fast increase of current represented an immediately release of ROS/RNS cocktail after stimulation, evidencing also the rapid activation of cells enzymatic systems by interacting calcium channels. After c.a. 10 minutes of continuous stimulation, the current responses became gradually undistinguishable from background level.

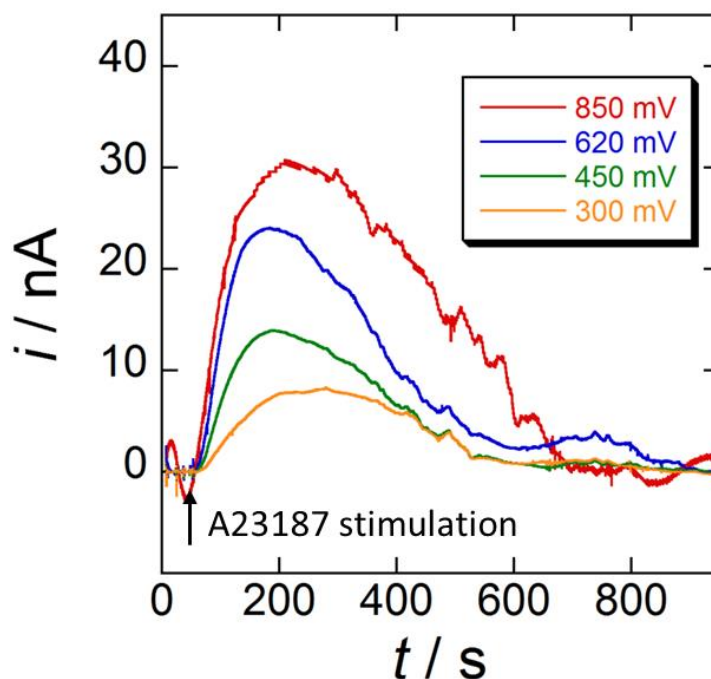


Figure C-25: Simultaneous amperometric responses from upstream cells population (c.a.  $3.5 \times 10^4$  cells) over  $10 \mu\text{M}$  A23187 stimulation. Four curves were respectively recorded at 0.30, 0.45, 0.62 and 0.85 V vs. Ag/AgCl. Black arrow at x-axis indicates the time when A23187 solution is pumped across the microchamber and ROS/RNS sample reaches immediately to the downstream sensors. Flow rate =  $2 \mu\text{L min}^{-1}$  in each channel.

The generated ROS and RNS were deduced from the combination of current detected at respective potentials (see Equation (C.1) to (C.4)). Instead of directly calculating the overall charge, the current intensity should be primarily converted into species concentration. This conversion is necessary because detected current in flowing solution results from species convective mass transport and reflects concentration rather than global quantity. The calculations were achieved by taking into account the slopes of calibration curves reported in Part B ( $S_{\text{H}_2\text{O}_2} = 2.41 \times 10^{-3} \text{ A M}^{-1}$ ;  $S_{\text{ONOO}^-} = 1.04 \times 10^{-3} \text{ A M}^{-1}$ ;  $S_{\text{NO}\cdot} = 1.13 \times 10^{-3} \text{ A M}^{-1}$ ;  $S_{\text{NO}_2^-} = 2.22 \times 10^{-3} \text{ A M}^{-1}$ ). Note that the observed currents (a few tens of nanoamperes) demonstrated that the local concentration of released species in this microfluidic environment was higher than the micromolar level, which led to an efficient detection according to the electrode performances reported in the previous work. The global production of each species ( $N_j$ ) can be deduced by the following equation:

$$N_j = \int [C_j] dV_{\text{plug}} = 4 \int_{t_s}^{t_s + \Delta t} \frac{i_j}{S_j} u_{\text{flow}} dt \quad (\text{C.10})$$

where  $[C_j]$  is the converted concentration of each species in sample solution;  $V_{\text{plug}}$  is the volume of ROS/RNS-containing sample solution that passes through detecting electrodes;  $i_j$  is

the current ascribed for each species;  $S_j$  is the calibration slope for each species;  $u_{\text{flow}}$  is the solution flow rate in each detection channel, equals to  $2 \mu\text{L min}^{-1}$  (a factor of 4 was introduced here since sample solution was branched into four parallel channels);  $t_s$  is the time when electrochemical responses started to increase (i.e., analyte solution just arrived at sensor surface), and  $\Delta t$  here refers to duration of sample passage.

As a result, the following average quantities per cell were obtained:  $5.1 \pm 0.8$  fmol  $\text{H}_2\text{O}_2$ ,  $6.3 \pm 1.8$  fmol  $\text{ONOO}^-$ ,  $7.8 \pm 1.7$  fmol  $\text{NO}^\bullet$  and  $6.7 \pm 1.1$  fmol  $\text{NO}_2^-$  (Figure C-26A). As for basal detection, lower quantities of  $\text{ONOO}^-$  and  $\text{NO}^\bullet$  were as well observed in this downstream configuration when compared to the values detected from single cells by synaptic microelectrode configuration. However, unlike basal mode, this result was not related to the attachment between cells and working electrodes, neither to the apical diffusion loss, but was more likely due to the sample transition delay from emitting cells to the downstream electrodes. Although this delay is less than 1 s under driven flow from the end of microchamber to the electrochemical sensor, the duration of solution passage over this chamber itself takes around 20 s. Therefore, an underestimation of content combination, especially for the unstable components  $\text{ONOO}^-$  and  $\text{NO}^\bullet$  was inevitable in our experimental conditions. Despite this deviation, the detected production of ROS/RNS (20 – 30 fmol per cell) as well as the peak-shaped amperometric responses were still of great significance to characterize and quantify oxidative bursts from the large cells population, particularly for the assessment of biological effects.

Moreover, stable release kinetics of individual species was observed during the entire process (Figure C-26B), again justified the constant and tandem composition of oxidative bursts and the reliability/reproducibility of the present microdevice.

As shown in Figure C-26A,  $\text{H}_2\text{O}_2$  and  $\text{NO}_2^-$  remained consistent with the isolated single-cell production, demonstrating effective collection of chemically stable components in this configuration. Particularly for  $\text{NO}_2^-$ , the slightly higher quantity might be partially explained by the spontaneous decomposition of  $\text{ONOO}^-$  and reaction of  $\text{NO}^\bullet$  with  $\text{O}_2$  (0.25 mM in aerobic solution) during the adequate time delay. Results that delineated oxidative bursts released on average by c.a.  $3.5 \times 10^4$  cells were obtained during one single measurement. Error bars in Figure C-26 (marked on the pink columns) described indeed the variations between five different batches of cells. For each measurement, simultaneous detections at four selected potentials were conducted in highly automated manner; and the detected compounds

were generated from the common cells population (not like in basal detection where species detected at each sensor were produced by respective group of cells), further promoting the parallelism of detection.

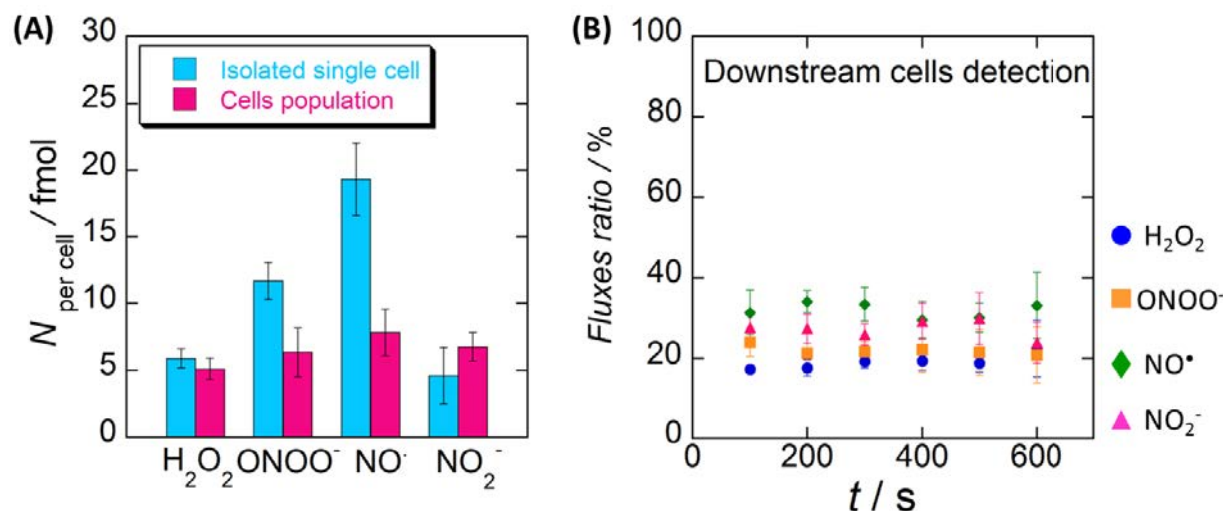


Figure C-26: (A) Comparison of average release of  $\text{H}_2\text{O}_2$ ,  $\text{ONOO}^-$ ,  $\text{NO}\cdot$  and  $\text{NO}_2^-$  per cell from single-cell detection (blue columns) and from cells population downstream detection (pink columns) over  $10\ \mu\text{M}$  A23187. Data for single-cell release was obtained after performing 20 to 30 experiments at each potential ( $n > 100$  experiments overall); while only 5 measurements were conducted for c.a.  $3.5 \times 10^4$  cells population, and in each measurement, four interested potentials were simultaneously applied. (B) The kinetic fluxes ratio of the four oxidative species released by cells population, detected under downstream configuration (5 simultaneous experiments overall).

Successive oxidative releases were monitored as well in the present microdevice. As shown in Figure C-27, highly reproducible and integral amperometric responses over three successive stimulations demonstrated the benefits of this configuration, namely no obvious perturbation of biological behavior of cells and redox performances of electrodes by avoiding direct contact between emitting cells and sensing probes.

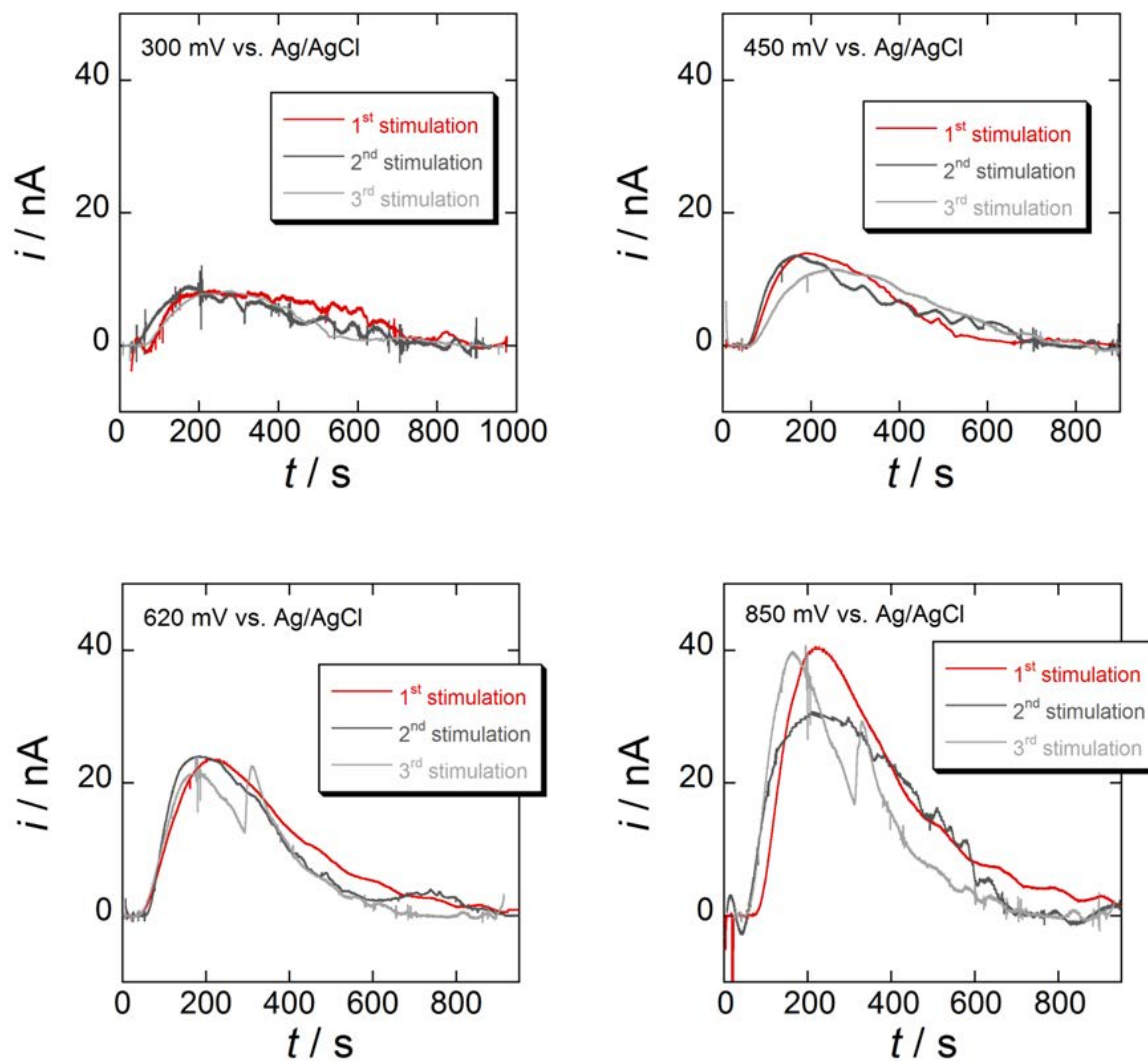


Figure C-27: Successive oxidative releases over  $10 \mu\text{M}$  A23187 from the same population of c.a.  $3.5 \times 10^4$  Raw 264.7 macrophages immobilized at upstream microchamber. Amperometric responses were recorded at 0.30, 0.45, 0.62 or 0.85 V vs. Ag/AgCl in each detection channel. Between sequential stimulations, 10 minutes intervals were conserved to rest the activated cells.

### 3.2.4. Detection after 10-min stop flow

From the former sets of experiments, we know that duration around 10 minutes is needed for the oxidative emission of macrophages over A23187 stimulation. Therefore, to obtain a highly concentrated ROS/RNS sample solution within microchamber, the stimulus ( $10 \mu\text{M}$  A23187) was locally delivered into the microchamber, followed by a 10-min static stimulation without any flow rate throughout the device (process and manipulations are described in Appendix III.4). Oxidative production was supposed to accumulate, with a slight diffusion under static solution, inside this small chamber. Then the buffer was pumped again ( $8 \mu\text{L min}^{-1}$ ) to push sample plug across downstream microchannels, and simultaneous electrochemical detections were conducted towards the homogeneous solution.

A typical experimental result is shown in Figure C-28A. Much higher faradic currents as compared to non-stop detection were evidenced; however, during a quite short passage time. This phenomenon indicated highly concentrated electroactive species were generated by cells population, and mainly confined to the small chamber. However, the difference from non-stop flowing detection is the dramatic decrease of signals observed for successive re-stimulation (Figure C-28B). An influence of normal cellular metabolism by accumulated local concentration of ROS/RNS within the microenvironment seemed likely to trigger the slacking down responses.

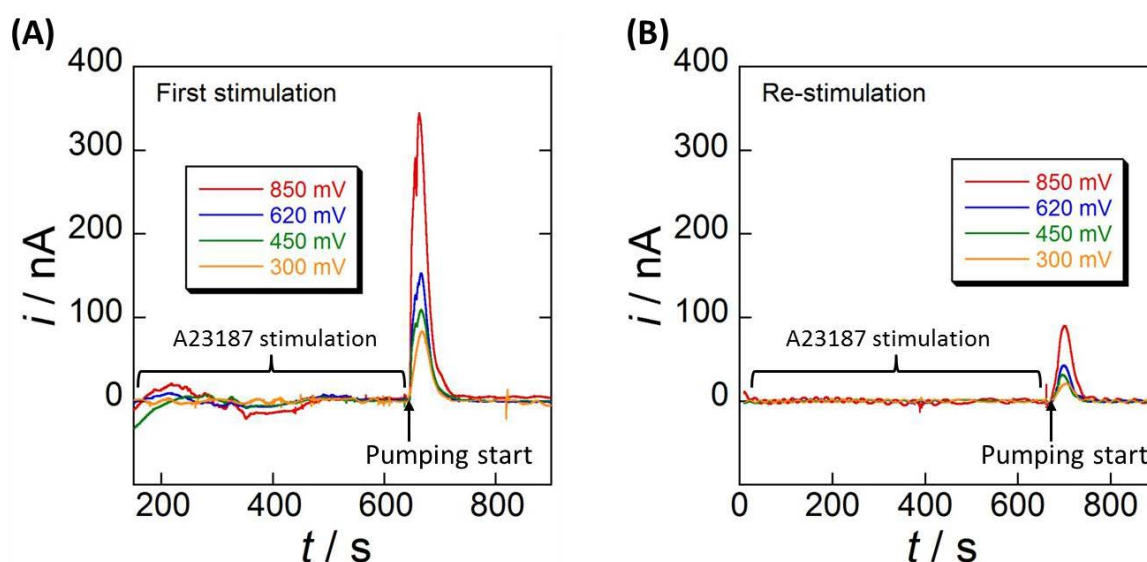


Figure C-28: Simultaneous amperometric responses detected at four independent downstream Pt/Pt-black microband electrodes, representing accumulated ROS/RNS released by a large population of c.a.  $3.5 \times 10^4$  cells inside microchamber after 10-min stimulation with static solution of  $10 \mu\text{M}$  A23187. Representative responses are demonstrated in (A) for the first stimulation, and (B) for the second stimulation. Electrodes respectively worked at 0.30, 0.45, 0.62 and 0.85 V vs. Ag/AgCl. The black arrows at x-axis indicate the time to start pumping sample solution pass through the downstream working electrodes. Flow rate =  $8 \mu\text{L min}^{-1}$  in the overall device.



After reconstructing current contribution for each species and converting this current to species concentration, the composition of accumulated oxidative production is interpreted in Figure C-29. As a result,  $4.1 \pm 0.9$  fmol  $\text{H}_2\text{O}_2$ ,  $10.2 \pm 1.2$  fmol  $\text{NO}_2^-$  was detected after 10-min stimulation in static solution. Signals of  $\text{ONOO}^-$  and  $\text{NO}^\bullet$  were not adequately obvious since the time delay was too long as compared to their short life time (few seconds). A part of these two highly active species may convert into the end products of  $\text{NO}_2^-$ , and that probably explains the higher  $\text{NO}_2^-$  signal as compared to previous measurements under shorter response time. Moreover, the gradually-accumulated ROS/RNS in cells' microenvironment might also affect their normal metabolism and then impact, more or less, the ensuing production. At this point, one cannot expect the information about any temporal variations of species releasing rates under 10-min stop mode; however, quantification of the stable candidates (e.g.,  $\text{H}_2\text{O}_2$  and  $\text{NO}_2^-$ ) and the evaluation of derivation/decomposition of unstable candidates over any certain period are still feasible. So, this downstream configuration offers a sensitive, highly-parallel, and also tunable platform to interpret multiple biological samples by manipulating flowing solution. Cells biologically-relevant effects can be flexibly investigated at any interested time point, with situation that mimics natural continuous perfusion or under static microenvironment.

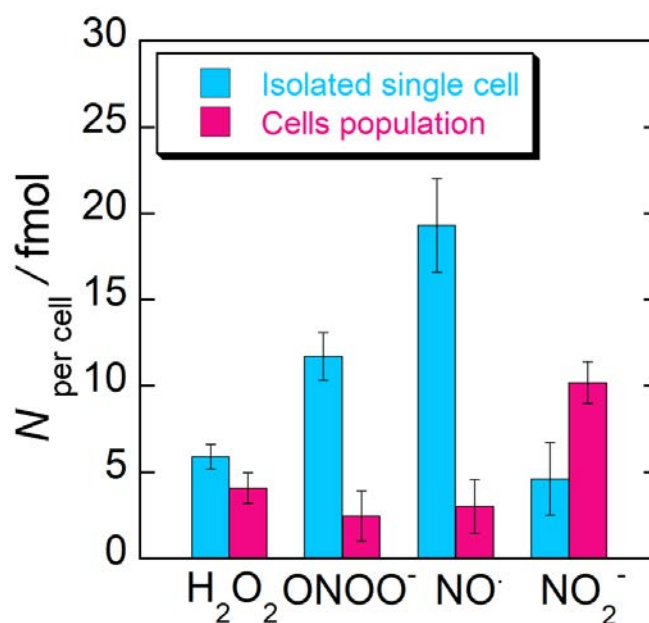


Figure C-29: Average release of  $\text{H}_2\text{O}_2$ ,  $\text{ONOO}^-$ ,  $\text{NO}^\bullet$  and  $\text{NO}_2^-$  per cell during oxidative bursts detected by downstream microelectrodes (pink columns) after 10-min static stimulation by  $10 \mu\text{M}$  A23187. Data for single-cell release (blue columns) was obtained after performing 20 to 30 experiments at each potential ( $n > 100$  experiments overall); while only 5 measurements were conducted for c.a.  $3.5 \times 10^4$  cells population, and in each measurement, four interested potentials were simultaneously applied.

### 3.3. Conclusion of section 3

In this section, we presented a PDMS-glass hybrid microfluidic chip consisted of **separated** microchamber for cell manipulation and microchannels for electrochemical detection. Fibronectin was coated on the glass substrate for biocompatibility purpose, facilitating fast immobilization of cells and long-term perfusion culture inside microsystem. Cells oxidative emission was equally branched into four downstream channels and simultaneously measured at four selected potentials by independently addressed working electrodes.

In the present work, oxidative compounds from a **large population of cells** (c.a.  $3.5 \times 10^4$  cells) were easily characterized at different time period after stimulation. Dynamic study of ROS/RNS was achieved under non-stop flow mode (1 s transport delay from the end of chamber to detecting sensors). Stable and simultaneous fluxes of individual species were observed, demonstrating the coupling activity of two enzymatic systems. And highly-reproducible responses over successive stimulations (10  $\mu$ M A23187) indicated **no perturbation** of cells normal metabolism in this flowing configuration. Measurements in 10-min stop mode displayed quite low contents of ONOO<sup>-</sup> and NO<sup>•</sup>, but much higher contents of the other two stable components especially for NO<sub>2</sub><sup>-</sup>. This might give a hint about decomposition of those unstable species and their partially conversion into the stable end products during this time delay. In addition, the drastic decrease of signal after re-stimulation possibly reflected negative influence of normal cellular metabolism in the presence of locally accumulated ROS/RNS. Under flowing conditions, the entire bioanalytical experiments were manipulated **automatically**. The current responses were enhanced by convective mass transport and accordingly the quantification of species was achieved after converting the detected current into species concentration. This conversion was based on previously established calibration curves of individual components under the same convective mass transport control. The reliability was further guaranteed after activating redox probes (electrochemical cleaning through alternative potential pulses) prior to the measurements. Highly **reproducible** results were obtained in this device, despite some underestimation of the two unstable components (ONOO<sup>-</sup> and NO<sup>•</sup>) were observed as compared to the highly-efficient synaptic single-cell measurements.

As a conclusion, this multi-sensor device offers a universal platform that enables highly effective and non-invasive detection of biological analytes released by a large population of cells. Statistical analyses of multiple compounds can be obtained by performing only few simultaneous measurements. Semi-kinetic and quantitative results are expected, particularly towards the stable products, in a **flexible** and **high-throughput** approach.

#### **4. Conclusion of Part C**

The oxidative bursts from Raw 264.7 macrophages under A23187 stimulation were investigated extensively by using a series of different experimental platforms.

Among which, the single-cell detection by **synaptic** microfiber electrode offered the best temporal resolution and collection efficiency to characterize the very origin of oxidative stress by A23187 activated macrophages, despite the expense of laborious work.

Detection of cells population (c.a. 1200 cells) by **basal** microband electrodes conveniently gave rise to the reproducible and statistical results in terms of both chemical composition and the real-time fluxes of cells releases, but might suffer from not only the loss of apex emission but also perturbation of cells normal behaviors.

Separating emitting cells and detecting sensors seemed a reasonable solution to bypass these defects. This **downstream** detection configuration inevitably led to longer transport time from the generating point to the electrochemical probes. However, flowing solution can shorten the delivery time and improve the detection efficiency. Furthermore, high biologically-relevant environment (as compared to perfusion transport within microvascular network) can be reproduced with microfluidic network, and toxic metabolites that might affect cells behaviors can be immediately removed from cells surroundings. The overall experiment including cell culture, stimulation and detection were automatically achieved with this device. The electrochemical responses also benefited from convective mass transport. By tuning the flowing mode (continuous and stop-flow modes), investigations could be carried out at different cellular event stages. Although underestimation of two highly-reactive components (i.e.,  $\text{ONOO}^-$  and  $\text{NO}^*$ ) were observed in this configuration in comparison to single-cell synaptic detection, the results were still relevant to enable a fine understanding of oxidative bursts from a large group of cells (c.a. 35000 cells).

The average productions of  $\text{H}_2\text{O}_2$ ,  $\text{ONOO}^-$ ,  $\text{NO}^\bullet$  and  $\text{NO}_2^-$  of Raw 264.7 macrophages over different situations are listed in following Table C-1 and compared in Figure C-30.

Table C-1: Reactive oxygen and nitrogen species released, on average, per Raw 264.7 macrophage over different stimulations and different experimental configurations.

Target	Detection mode		Stimulus	Production (fmol/cell)			
				$\text{H}_2\text{O}_2$	$\text{ONOO}^-$	$\text{NO}^\bullet$	$\text{NO}_2^-$
Single cell <sup>a</sup>	Synaptic sensor		Mechanical penetration [118]	5±1	9±1	14±2	6±1
			IFN- $\gamma$ /LPS [220]	0	7.5±0.9	8.9±1.9	4.0±1.3
			IFN- $\gamma$ /LPS/PMA [133]	4.2±0.9	9.1±1.9	6.0±1.2	5.6±0.4
			A23187	5.9±0.7	11.7±1.4	19.3±2.7	4.8±2.1
Cells population <sup>b</sup>	Basal sensor		A23187	6.2±1.2	4.8±2.4	12.6±3.4	7.0±2.8
	Downstream sensor	Non-stop		5.1±0.8	6.4±1.8	7.9±1.7	6.8±1.1
		10-min stop		4.1±0.9	2.5±1.4	3.0±1.5	10.2±1.2

(a: 20 to 30 individual experiments were performed at each potential; hundreds of experiments over four potentials. b: 5 simultaneous experiments were required for statistical results.)

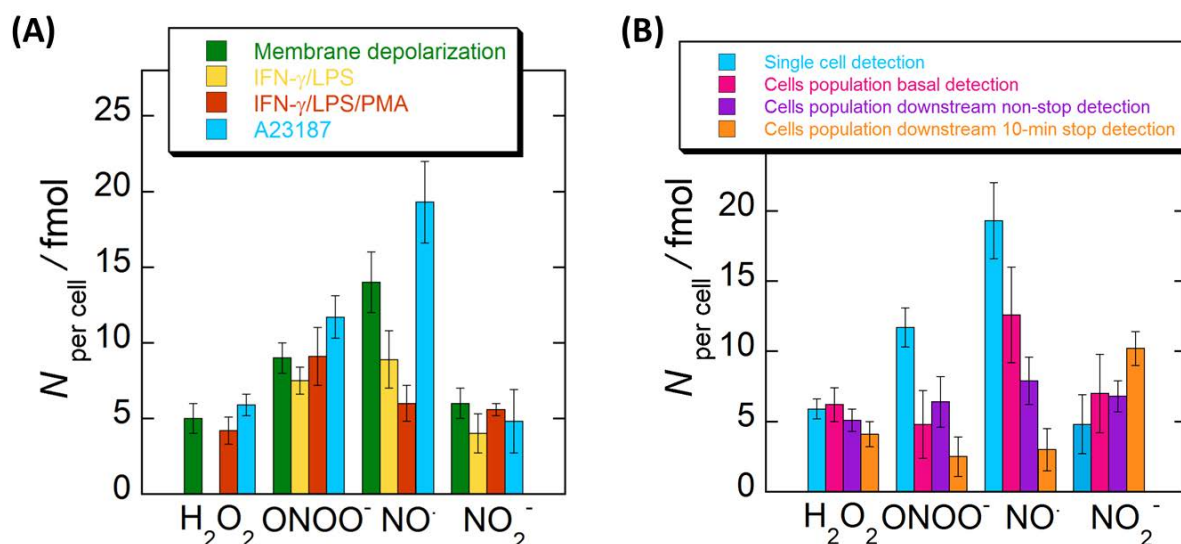


Figure C-30: Comparison of oxidative bursts released on average per cell, from (A) isolated single cells detected by synaptic microfiber electrodes over different stimuli (20 to 30 experiments in each column); or (B) under the same A23187 stimulation, but with different configurations, including synaptic detection of single-cell products (20 to 30 experiments in each column) and basal or downstream detection of cells population generation (5 experiments in each column, and one experiment simultaneously gave information about four respective species).

All the single-cell releases in Figure C-30A were evaluated under the same “artificial synapse” configuration. The comparable production of oxidative compounds over stimulation of membrane depolarization (green columns) and calcium ionophore A23187 (blue columns), together with the immediate response after stimulation (Figure C-2B, Figure C-8A), indicated constitutive enzymatic activities. While the absence of H<sub>2</sub>O<sub>2</sub> production (yellow columns), longer pre-activation process and much more durative but weaker release (Figure C-4) over exposition of immune factors IFN- $\gamma$ /LPS demonstrated a quite different stimulation pathway through inducible enzymatic pools.

In our series of experiments (over A23187 stimulation), all the working electrodes were platinized by Pt-black to guarantee high analytical performances; thus the respective results (Figure C-30B) reflected more the different features stemmed from each experimental configuration. A crucial point that has to be addressed is that a given microsystem and a given experimental configuration can be considered alone, i.e., its intrinsic ability to detect ROS/RNS in real-time, with accurate quantification and characterization at the very origin of cellular event. In this aspect, “artificial synapse” configuration offers the best choice. However, the analytical performance can also be viewed in the context of **biologically-relevant investigations**, such as evaluation of drug effects under varying experimental conditions and parameters. For our experimental condition, more than 100 parallel single-cell detections are needed to obtain reliable effect evaluation. Image to compare or modify a few experimental parameters, even thousands of operations are required, and are therefore too fastidious and time-consuming. In that way, a configuration that has some defects in detecting the real amounts of unstable components (i.e., ONOO<sup>-</sup> and NO<sup>•</sup>) is not necessarily to be discarded if it enables convenient evaluation of overall biological effects. Therefore, it has to be stated that the 4-channel downstream configuration, while sacrificing to some extent the real-time analysis, could remain an appropriate analytical tool to explore **cells average behaviors** in a non-invasive and highly-throughput manner. However, improvements are still possible such as further minimizing distance between emitting cells and sensing electrodes, or even adopting more integrated microfluidic structures to tackle the kinetic process and chemical nature of oxidative contents over any selected and precise number of cells.

## *General conclusion and perspectives*



## General conclusion and perspectives

As demonstrated in **Part A**, investigation of oxidative stress and ROS/RNS production is very important for understanding many complex physiological and pathological life processes. The present work took place in the context of developing functional microfluidic devices for high-throughput detection of multiple oxidative species released by living cells. The objective was to overcome practical difficulties resulting from single-cell electrochemical detections. Usually, this configuration requires a large amount of repetitive measurements under each experimental condition to obtain meaningful statistical results. Using microfluidic devices, cell culture, manipulation and simultaneous detections can be achieved through an automated and high-parallel procedure in order to get rapid insights about average cells behaviors.

Standard microfabrication technologies such as photolithography, lift-off and soft lithography were thus used to design several types of microfluidic devices according to different purposes. With flexible integration of thin-layer microband electrodes, both *in vitro* detections of synthetic solutions and *ex vivo* detections of oxidative burst emitted by living cells could be investigated.

The analytical performances of Pt/Pt-black microband electrodes towards four key ROS/RNS (i.e.,  $\text{H}_2\text{O}_2$ ,  $\text{ONOO}^-$ ,  $\text{NO}^\bullet$ , and  $\text{NO}_2^-$ ) were first studied in **Part B**. A constant-current plating process provided optimal Pt-black deposits with high signal-to-noise ratio of the electrode responses and compatible thickness for subsequent integration within microchannel. Owing to a larger number of active sites of Pt-black at the nanometric level, efficiency and long-term stability of electrochemical detections were observed in contrast to bare Pt. Oxidation mechanisms including decomposition kinetics were investigated based on theoretical predictions. Oxidation of species at Pt/Pt-black microband electrodes was mainly controlled by convective mass transport. Large linear concentration ranges and high sensitivities were obtained for all these species. High detection selectivity was achieved by choosing appropriate potentials. The good summation of individual species contributions at each potential allowed composition of sample mixtures to be easily determined.



Then in **Part C**, multiple Pt/Pt-black electrodes were integrated into elaborated microdevices to monitor cellular oxidative bursts. Owing to the flexible photolithographic patterning, releases of living cells were investigated under different configurations. Microband electrodes were placed either directly beneath a population of cells, or downstream the cells. The basally-localized electrodes provided high temporal resolution while the downstream probes led to non-disturbing and tunable investigations at different event stages. Despite the slightly lower collection efficiency of short-lived species ( $\text{ONOO}^-$  and  $\text{NO}^*$ ) achieved in both configurations, the stable release kinetics and the comparable quantity of detected species to synaptic configuration which justified the reliability of the present investigation. Highly reproducible and statistically relevant results were obtained within only few experiments.

Therefore, by integrating Pt/Pt-black microband electrodes into microfluidic devices, effective analysis towards cells populations is feasible. Kinetic and quantitative results can be achieved leading to high-throughput and high-parallel detections, in particular for chemically stable species.

When ability to detect cell releases in real-time and accuracy to interpret cellular events are required, “artificial synapse” configuration is the best choice. However, when analytical performances are considered in the context of efficient data collections, the microfluidic configurations become more attractive and competitive. A rapid and deep understanding of cells average behaviors can be provided for instance for drug screening. Preliminary *ex vivo* measurements were achieved within the present microdevices but these latter can still be optimized. On the one hand, decreasing further the distance between emitting cells and sensing electrodes, by adjusting device geometry or/and flow velocity, should lead to a better temporal resolution. On the other hand, incorporating electrodes on top of cells chamber could also mimic the synaptic configuration with higher collection efficiency and no disturbance of cells activities. Another possible improvement is microfluidic structures integrating traps of single cells, with ultramicroelectrodes array addressed close to each unit. The chemical nature and kinetic process of cells releases could be tackled over any selected and precise number of cells.

Thus, we believe that based on the high analytical performances of Pt-black thin-layer microelectrodes, sophisticated multi-sensor microfluidic devices can be developed. This prerequisite study paves the way to a very broad field of bioanalytical applications with flexible, label-free, low-cost, automated and high-throughput monitoring of cells behaviors.

# *Appendix*



## Appendix

### Appendix I. Electrochemical principles and microelectrodes

#### I.1. Electrochemical principles

Electrochemistry is a study of electrons' exchange in an oxidation-reduction process. As compared to normal redox reactions where the electron transfer is directly proceeding between molecules, electrochemistry deals with reactions which take place at interface between electrode and electrolyte. This separation facilitates understanding of the electron transfer mechanism and helps to unravel the essence of whole chemical process. Through the detected potential, charge, or current, electrochemical analysis gives various kinetic and thermodynamic information [287] for analytical purpose.

#### Electrochemical cell

A basic electrochemical system contains electrolyte and two conductive electrodes namely anode and cathode. At the anode, oxidation occurs and the species loss electrons towards electrode; whereas on cathode, equivalent electrons are transferred from electrode to another species leading to the following reactions:

- Anode reaction:  $Red_{(anode)} \rightarrow Ox_{(anode)} + ne^{-}$
- Cathode reaction:  $Ox_{(cathode)} + ne^{-} \rightarrow Red_{(cathode)}$

For each species, the electrode potential is determined by intrinsic properties as well as the surrounding compositions, leading to an inner driving force of this half-reaction. Under nonstandard condition, this potential could be described in terms of Nernst equation:

$$E = E^{\circ} - \frac{RT}{nF} \ln \frac{a_R}{a_O} \quad (\text{Appendix.1})$$

where  $E^\circ$  is the electrode potential in standard condition (solutes at unit activity  $a = 1$ , gases at pressure of 1 atm);  $R$  is gas constant, equals to  $8.314 \text{ J mol}^{-1} \text{ K}^{-1}$ ;  $T$  is absolute temperature in K;  $n$  is moles of electrons;  $F$  is Faraday's constant, equals to  $96485 \text{ C mol}^{-1}$ ;  $a_R$  and  $a_O$  respectively refer to the activities of chemical reagents in reduced and oxidized forms.

In most cases, people are interested in one half-reaction which happens around a working or indicator electrode; and in order to better focus on this study, a reference electrode with essentially constant composition is introduced to standardize the other half. Rather than the primary reference of standard hydrogen electrode (SHE), others namely saturated calomel electrode (SCE, potential of 0.241 V vs. SHE), sodium saturated calomel electrode (SSCE, potential of 0.236 V vs. SHE) and silver-silver chloride electrode (Ag/AgCl, potential of 0.197 V vs. SHE) are more convenient from an experimental standpoint (reference electrodes potentials in aqueous solutions at 25°C). Accordingly, with incorporation of a reference electrode, any potential change of the cell should be ascribed to the working electrode. When the potential is driven more negative, electrons energy on working electrode keeps raising, until high enough to transfer electrons into vacant molecule orbital of target species and generate a reduction current from electrode to solution (Figure Appendix-1A). On the contrary, if a more positive potential is imposed, electrons in occupied orbital find more favorable energy on electrode and accordingly lead to an oxidation current (Figure Appendix-1B).

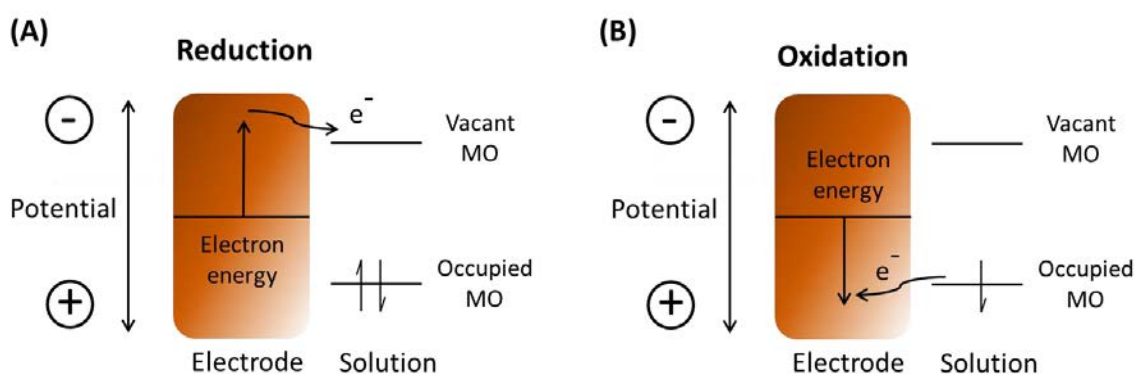


Figure Appendix-1: Illustration of (A) reduction and (B) oxidation processes of a target species at working electrode.

## Faradaic processes

When reaction takes place at an electrode surface, the amount of reacted substance is proportional to transferred electrons as described in the Faraday's first law:

$$m = \frac{QM}{nF} = \frac{it \cdot M}{nF} \quad (\text{Appendix.2})$$

where  $m$  is mass of reacted species;  $Q$  is the passed electric charge;  $M$  is molar mass of species;  $i$  is measured current; and  $t$  is the time.

However, sometimes due to unfavorable thermodynamic or kinetic factors, nonfaradaic process occurs. This process resembles a capacitor, with the whole array of charged species and oriented dipoles existing at metal-solution interface, establishing an electrical double layer [288] (Figure Appendix-2A). Although charge ( $q$ ) doesn't cross the interface, it could still exhibit a transient current (charging current) when potential, electrode area or composition changes, until the capacitance equation is balanced again:

$$q = AEC_d \quad (\text{Appendix.3})$$

where  $q$  is charge stored on surface;  $A$  is electrode surface area;  $E$  is applied potential;  $C_d$  is double-layer capacitance. Both faradaic and nonfaradaic processes contribute to current. Sometimes the impact of nonfaradaic current is neglected due to the very short duration; nevertheless, when potential is changing fast or at very low analyte concentration, the charging current can't be ignored since it is probably larger than the faradaic value.

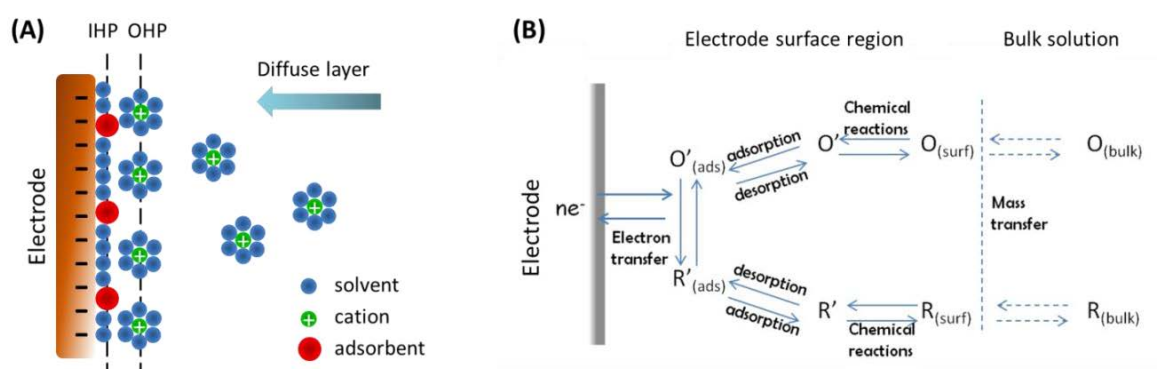


Figure Appendix-2: Illustrations of nonfaradaic and faradaic processes. (A) Proposed model of electrical double layer region: with inner Helmholtz plane (IHP) identified as electrical centers of specifically adsorbed ions; outer Helmholtz plane (OHP) defined as centers of nearest nonspecifically adsorbed solvated ions; and diffuse layer where these nonspecifically adsorbed ions are distributed due to thermal agitation. (B) Constitution of a general electrode reaction process, the reaction rate is related with multiple steps.

During the faradaic process, a heterogeneous reaction occurs at electrode-electrolyte interface; and the reaction rate is depending on not only usual kinetic variables, but also species mass transfer to electrode and myriad surface effects. For an overall electrode reaction, several processes affect the reaction rate as well as final current (Figure Appendix-2B) [289]:

- Mass transfer of species from bulk solution to electrode surface.
- Electron transfer between electrode and species at the interface.
- Relevant preceding or following chemical reactions.
- Adsorption, desorption, crystallization and other surface reactions.

The overall reaction rate is usually limited by one or more rate-determining steps with inherent sluggishness, and finally reaches a steady state where the rates of all steps are in consistent.

### Mass transfer model

In the simplest model, rates of all associated chemical reactions and kinetics of interfacial electron transfer are very rapid. The overall reaction rate ( $v_{rxn}$ ) is then governed by the mass transport rate ( $v_{mt}$ ) of electroactive species from bulk solution to the surface of electrode:

$$v_{rxn} = v_{mt} = \frac{i}{nFA} \quad (\text{Appendix.4})$$

Inside a solution, three modes of mass transfer contribute to the movement of species from one location to another:

- Migration under influence of electrical potential gradient.
- Diffusion under influence of concentration gradient.
- Convection caused by natural density gradient or extra force.

The migration effect could be reduced to negligible level by adding an inert supporting electrolyte (performing as ionic charge carriers); and that electrolyte, at the same time, leads to a lower solution resistance during measurements. Convection can be eliminated to a certain extent by preventing stirring and vibration. However, it is less likely to be completely avoided (in the form of natural convection). Sometimes for analytical purpose, the convection is even mechanically forced to enhance mass transport.

For the sake of simplicity, an approximate treatment of steady-state mass transfer has been considered. It is based on the following assumption: convection is only occurring beyond  $x = \delta$  ( $x$  is the distance from electrode surface,  $\delta$  is the thickness of stagnant layer). Therefore, the mass transfer flux at electrode surface can be written as following equation from Fick's first law when concentration gradient is assumed linear (Figure Appendix-3A):

$$v_{mt} = D \left[ \frac{\partial c}{\partial x} \right]_{x=0} = D [c^* - c_{(x=0)}] / \delta \quad (\text{Appendix.5})$$

where  $D$  is species diffusion coefficient;  $c_{(x=0)}$  refers to species concentration at electrode surface, which should be lower than  $c^*$  due to electrode consumption. When  $c_{(x=0)} = 0$ , the current under this situation is presented in limiting value ( $i_l$ ):

$$i_l = \frac{nFADc^*}{\delta} \quad (\text{Appendix.6})$$

Actually, the build-up of diffusion layer is a dynamic process. Diffusion layer grows with time (although this time period is short) until reaching the steady state confined by forced or natural convection (Figure Appendix-3B). The corresponding current can be deduced from time-dependent variation ( $i_t$ ) described by Fick's second law, and is described as Cottrell equation in case of planar electrode:

$$i_t = \frac{nFA\sqrt{D}c^*}{\sqrt{\pi t}} \quad (\text{Appendix.7})$$

Accordingly, the thickness of dynamic diffusion layer ( $\delta_t$ ) is quantified by species diffusion coefficient and experimental time:

$$\delta_t = \sqrt{\pi Dt} \quad (\text{Appendix.8})$$

Therefore, during this dynamic process, current decreases continuously with  $t^{-1/2}$ . However, with the presence of natural or forced convection, it finally approaches the limiting value under steady state (Figure Appendix-3C).



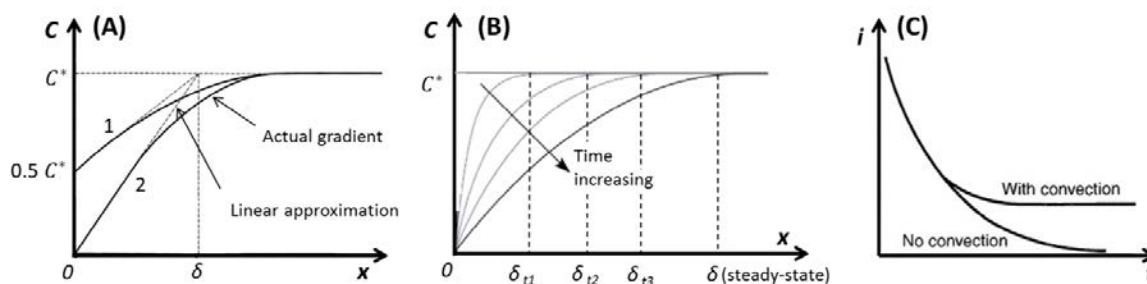


Figure Appendix-3: (A) Concentration profile (solid lines) and approximation of diffusion layer  $\delta$  as well as linear concentration gradient (dashed lines) when electrode is applied at different potentials: (1)  $c_{(x=0)}$  is about  $0.5c^*$ ; (2)  $c_{(x=0)} \approx 0$ . (B) Profile of diffusion layer growing with time until reaching steady state. (C) Mass transfer current decays with or without convection. [287]

These simplified anticipations facilitate understanding about mass transfer processes, offering primal basis to the rigorous description of current arising from diverse conditions (such as with electrodes in different shapes, under different convective conditions, and so on). Based on the convection-diffusion principles, many detection methods have been developed to investigate electrode reaction, either towards dynamic process or steady state. The concepts and operations for some popular techniques are presented in the following context.

## 1.2. General electrochemical techniques

In electrochemical analysis, many possible experimental designs have been conceived to correlate specific properties of species with digital signals. Despite the difference in instrumentation, all those techniques share several common features. According to which variables are under control, detection techniques can be generally classified as voltammetry (current is recorded while controlling potential), coulometry (transferred charge is measured under control of current or potential), and potentiometry (electrode potential is investigated under a condition of zero current) [290]. Most electrochemical measurements are conducted in an electrochemical cell consisting of three electrodes: a working electrode assigned for any change in overall cell potential; a reference electrode that provides a constant potential against which we measure the working electrode's potential; and a counter electrode that completes electronic circuit by reacting with the solvent or some other component of the solution matrix. Through manipulating potential or current with modern instruments, automated and flexible means to explore target species can be realized. Some primary methods (also applied in the present work) are introduced here to form a general view.

## Voltammetry

In voltammetry, a time-dependent potential is applied to the working electrode, and resulting current is plotted versus potential to establish a voltammogram. This voltammogram, as an electrochemical equivalent of a spectrum in spectroscopy, provides qualitative and quantitative information. Voltammetry is often the first experiment performed in an electrochemical study. The shape of a voltammogram is determined by several factors; besides the species intrinsic redox properties, how we measure the current and whether convection is included during mass transport are the most important ones. Two typical measurements are: “linear-sweep voltammetry (LSV)” where the potential is linearly scanned in either negative or positive direction (Figure Appendix-4A); and “cyclic voltammetry (CV)” which is conducted towards both directions by switching at a predetermined potential (Figure Appendix-5A) [291]. Single or multiple cycles can be operated depending on the requirements.

Since the faradaic current is balanced on Fick’s law and Nernst equation (in case of rapid electron transfer process), for a voltammogram, peak or plateau shape is commonly observed with respect to scan rate and diffusion process. In a static solution, peak current (Figure Appendix-4B) is frequently seen because diffusion layer keeps increasing during longer time. While under convection, current is more likely to reach a limiting value (Figure Appendix-4C) due to the fast establishment of steady state. Moreover, the standard-state potential of target reaction could be extracted where current is half of the limiting value; as this half-wave potential ( $E_{1/2}$ ) is not affected by concentrations, only related with thermodynamic property.

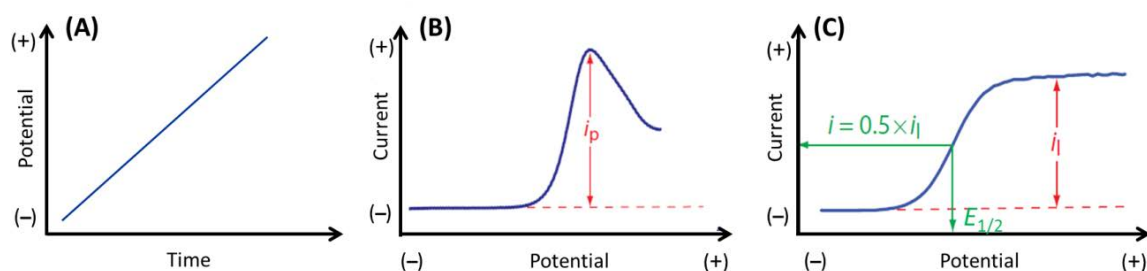


Figure Appendix-4: Illustrations of linear-sweep voltammetry. (A) Linear potential-excitation signal. (B) Resulting voltammogram in peak shape. (C) Resulting voltammogram in plateau shape with  $E_{1/2}$  referring potential at half limiting current. Dashed line here shows residual current.

At a normal planar electrode inside static solution, cyclic voltammetry is conducted under assumption of semi-infinite diffusion, and respective oxidation/reduction peak could be characterized by potential and current (Figure Appendix-5B). The peak current at 25°C is given by Randles-Sevcik equation:

$$i_p = (2.69 \times 10^5) n^{3/2} AD^{1/2} \nu^{1/2} c \quad (\text{Appendix.9})$$

where  $i_p$  is maximum current at peak;  $\nu$  is potential scan rate;  $c$  is the concentration of electroactive species at the electrode. This proportional relation between peak current and square root of scan rate is a crucial indication of a diffusion-controlled process under fast electron transfer. Furthermore, the diffusion coefficient of species can be estimated from intercept of  $\ln i_p$  vs.  $\nu$  plot, and that is also a meaningful application.

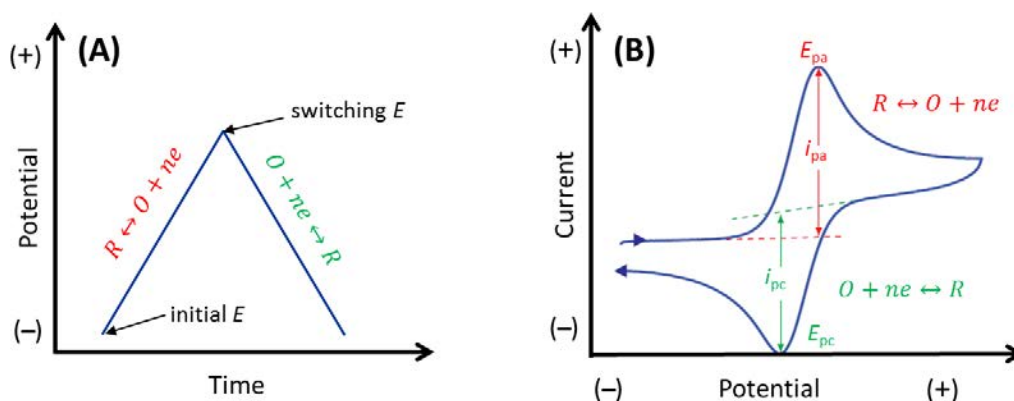


Figure Appendix-5: Illustrations of cyclic voltammetry. (A) One cycle of triangular potential-excitation signal showing the initial and switching potentials. (B) The resulting cyclic voltammogram showing measurement of peak currents and peak potentials.

For a well-behaved reversible system, the anodic and cathodic peaks exhibit equal currents:

$$|i_{pa}/i_{pc}| = 1 \quad (\text{Appendix.10})$$

Potentials of two peaks are stable under different scan rate, and the theoretical overpotential leads to a hysteresis between  $E_{pa}$  and  $E_{pc}$ :

$$|E_{pa} - E_{pc}| = \frac{59}{n} mV \quad (\text{Appendix.11})$$

In practical experiments, this difference could be slightly larger (70 to 100 mV for single electron transfer system). However, if the voltammogram has much larger potential separation or nonsymmetrical shape, electrode reaction is more likely irreversible. Such reversible peaks also provide thermodynamic information in terms of half-wave potential  $E_{1/2}$  (midway between these two peak potentials):

$$E^{\circ} = E_{1/2} = \frac{E_{pa} + E_{pc}}{2} \quad (\text{Appendix.12})$$

Voltammogram shows distinct advantages in exploring single or multi redox processes inside a common system. Diverse useful information could be obtained in a short time, including concentration, diffusion coefficient, reaction thermodynamics, adsorption processes, electron transfer kinetics and even following chemical reactions [292-294]. Combined with modern potentiostats which are capable of applying versatile time-dependent potential profiles, voltammetry has been used for analysis of a wide variety of analytes such as environmental and clinical samples.

### Chronoamperometry

In chronoamperometry, the potential value usually changes abruptly from one to another, and then keeps constant during a period (Figure Appendix-6A). The current variation is recorded as a function of time. For a semi-infinite system, typical interpretation of faradaic current is shown in (Figure Appendix-6B). As described in Cottrell equation, current generated from reduction or oxidation initially decays with  $t^{-1/2}$ , until a limiting current occurs when this layer remains constant under convection.

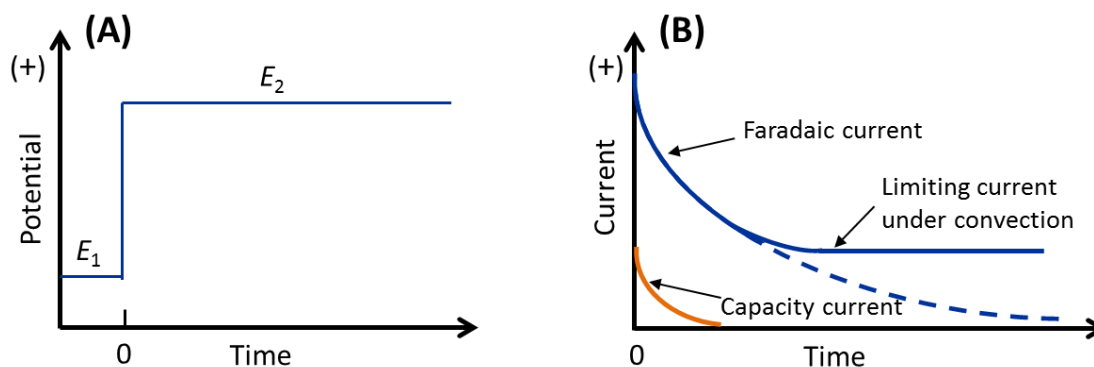


Figure Appendix-6: Illustrations of chronoamperometry. (A) Pulse-potential excitation signal. (B) Resulting current-time curve shows composition of charging current and faradaic current.

As with all pulsed techniques, chronoamperometry generates a high charging current that decays exponentially with time [291]. However, interference from capacity current can be eliminated within a fairly short time (Figure Appendix-6B). The steady-state current is more accurately presented and closely related with concentration. Thus the linear variation in current with different concentrations can offer a calibration curve and this makes chronoamperometry a widely-used quantification technique. Hydrodynamic conditions are

preferred in chronoamperometry, especially for some biological assays with low concentration of analyte; since convection further enhances mass transport and correspondingly improves the signal-to-noise ratio. In some cases, multiple potential pulses are applied in order to monitor several electroactive species.

### Chronopotentiometry

Chronopotentiometry, also called controlled-current coulometry [290], is based on a persistent electrolysis of analytes forced by one current pulse (Figure Appendix-7A). The total charge ( $Q$ ) during electrolysis is proportional to absolute amount of analytes, so as to be widely applied in electroplating [295] to produce a dense, uniform and adherent coating of metal or alloys on a conductive surface. At the moment when current is first applied, measured potential is abruptly changed, and then gradually varies as reactant concentration decreases; until those analytes are completely consumed at the working electrode, and potential rises sharply to initiate the next available reaction (Figure Appendix-7B) [296]. As compared to controlled-potential coulometry, this method allows charge calculation simply from the multiplication of current and time (Figure Appendix-7C); however, it is necessary to eliminate contribution of current from secondary reactions which might decrease the overall efficiency to less than 100%.

Rather than being kept constant, the current can also be changed with time linearly or reversely to evaluate specific electrochemical properties, such as the capacity and cycling stability of battery [297], or mechanism of multi-step redox reactions [298].

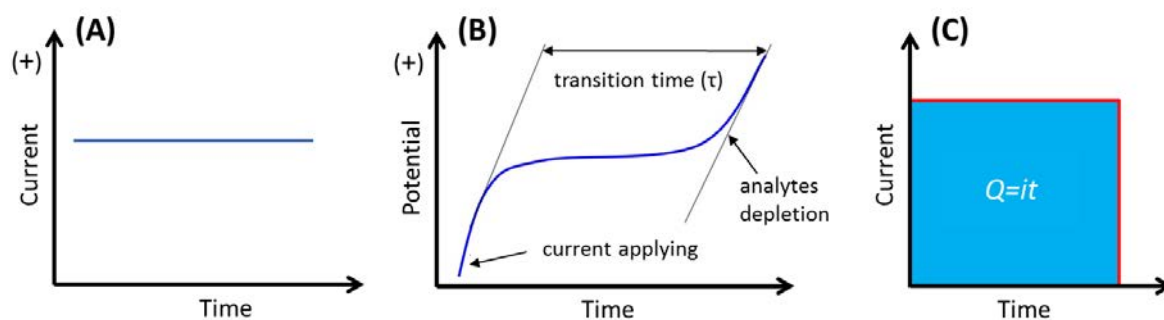


Figure Appendix-7: Illustrations for chronopotentiometry. (A) Constant current excitation signal. (B) Potential responses to applied current, showing transition process before secondary reactions. (C) Overall charge during this electrolysis process.

### Other techniques

Beside the methods mentioned above, techniques such as electrochemical impedance spectroscopy [299], pulse polarography [300], and stripping voltammetry [301] are also developed for matching different requirements. Depending on samples characteristics and interested information, specific electrochemical technique will be chosen in detection.

### **I.3. Microelectrodes and their electrochemical performances**

For a microelectrode, only one critical dimension is necessary to be confined to micro- or nanometers range; thus various shapes have been developed according to practical use [302]. Each type of microelectrode possesses peculiar features in mass transport while experiencing several essential rules in common [303]. Here some theoretical treatments of typical microelectrodes are introduced.

#### Several typical shapes of microelectrodes

- Spherical or hemispherical microelectrode

For an electrode of spherical shape, rather than the linear diffusion perpendicular to planar surface, a symmetrical spherical diffusion field (Figure Appendix-8) must be considered in solving Fick's laws [304]. The resulting diffusion current is written as:

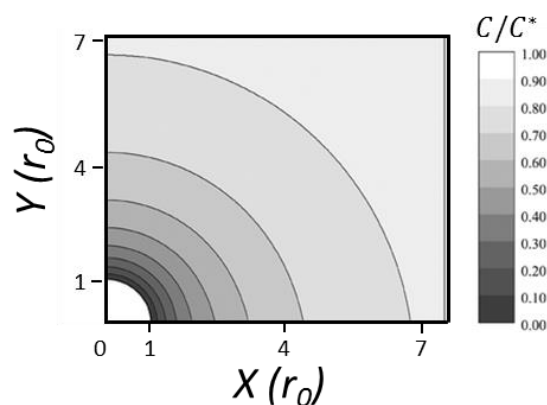


Figure Appendix-8: Simulated concentration profile at a spherical microelectrode [304].

$$i_t = \frac{nFA\sqrt{D}c^*}{\sqrt{\pi t}} + \frac{nFADc^*}{r_0} \quad (\text{Appendix.13})$$

where  $r_0$  is radius of the electrode.

The first term is identically Cottrell current of infinite planar diffusion; it dominates at short time when diffusion layer is smaller than  $r_0$ . Whereas the second term depicts steady-state current achieved later when diffusion layer grows larger than  $r_0$  (large radial diffusion

field compensates species depletion through drawing them from a continuous outer area). Timescale of each phase varies considerably with electrode size; and more precisely, the smaller the electrode, the shorter time it needs to reach steady state.

When it comes to a microspherical electrode, this steady state is attained fairly fast since diffusion layer only needs to grow several micrometers. Therefore, most relevant researches are based on steady-state current:

$$i_{ss} = \frac{nFADc^*}{r_0} \quad (\text{Appendix.14})$$

where  $A$  for spherical electrode is calculated by  $4\pi r_0^2$ ; and for hemispherical electrode is half of this value. During steady state, concentration profile near surface becomes independent of time (Figure Appendix-8), and is only linear with radial distance from electrode center ( $r$ ). Rather than an integral spherical microelectrode, hemispherical electrodes [305] made from electrodeposition of various metal materials on the surface of microdisk are more popular in practical use.

- Disk microelectrode

Microdisk electrodes are quite widely used in many applications [306,307]; however, more complex in theoretical view about diffusion behaviors. Asymmetrical growth towards two dimensions (radial and normal) leads to nonuniform distribution of current density at electrode surface (Figure Appendix-9), with largest value at the edge since it provides shortest travelling route for species from peripheral solution [308].

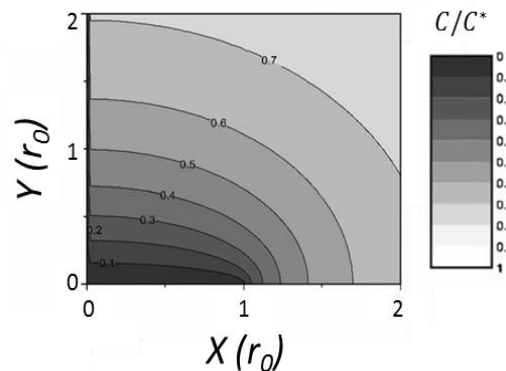


Figure Appendix-9: Simulated concentration profile at a disk microelectrode [308].

The current-time relationship has been presented as simple linear combination of planar and convergent terms, similarly as the result of spherical system:

$$i_t = \frac{nFA\sqrt{D}c^*}{\sqrt{\pi t}} + 4nFDc^*r_0 \quad (\text{Appendix.15})$$

where  $r_0$  is radius of disk. This relationship spans three regimes: once diffusion begins ( $\delta_t < r_0$ ), it remains purely planar character, showing Cottrell current; then as diffusion continues ( $\delta_t \approx r_0$ ), radial diffusion brings larger observed current than pure linear diffusion, manifesting

“edge effect” with nonuniform-distributed flux; finally at longer time when diffusion field grows much larger ( $\delta_t \gg r_0$ ), it resembles hemispherical case and current approaches a steady-state value:

$$i_{ss} = 4nFDc^*r_0 \quad (\text{Appendix.16})$$

This steady state at microdisk electrode can be established quite fast with a relatively large mass-transfer coefficient. For example, when  $D = 10^{-5} \text{ cm}^2 \text{ s}^{-1}$  (typical value for a molecule in aqueous solution), a 500 nm radius microdisk electrode deviates from planar diffusion field after 2.5  $\mu\text{s}$ , and establishes steady state after 25 ms. While for a 1 mm radius macroelectrode to reach exactly the same concentration profiles with respect to its radius, will take 250 s and 32 years respectively [308]. Nevertheless in a real system, diffusion layer, for a large disk electrode, is not infinitely growing and is usually limited by natural convection ( $\delta_{\text{conv}}$ ) [309]. These intrinsic benefits of microdisk electrodes allow investigation of steady state in a rather convenient, efficient and less risky manner. Nowadays, micro platinum disks with 5  $\mu\text{m}$  radius are already commercially available, and disks with radius less than 0.1  $\mu\text{m}$  have also been achieved under special processing.

- Cylindrical microelectrode

Cylindrical microelectrode is obtained by sealing thin metal wire or carbon fiber in tapered glass capillary [310]. It has only a single dimension of diffusion due to the simple geometry. Similarly, planar diffusion prevails at short times when diffusion length is smaller compared to curvature of electrode. Whereas in the long-time limit, mass transfer current is developed in terms of:

$$i_{qss} = \frac{2nFADc^*}{r_0 \ln \tau'} \quad (\text{Appendix.17})$$

where  $r_0$  is radius of cylindrical electrode. Here in the relationship contains a dimensionless parameter:  $\tau' = 4Dt/r_0^2$ , meaning that current still depends on time instead of a purely steady state. This is because cylindrical microelectrode usually has the length considerably exceeding micrometers range. Even so, time appears only as an inverse logarithmic function, and current indeed decays rather slowly during the long time. This case is usually called quasi-steady state.



- Band microelectrode

As analogy of the relationship between disk and hemisphere electrode, band electrode is a two-dimensional diffusion system behaving much like cylindrical case. Thus, according to the timescale of experiments, mass transport at microband electrode shifts from linear to radial diffusion, until approaches the limiting form:

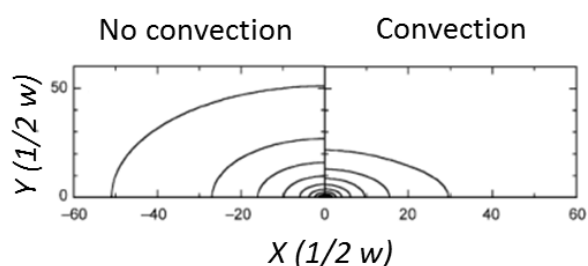


Figure Appendix-10: Simulated concentration profile at a band microelectrode with absence or presence of convection [309].

$$i_{qss} = \frac{2\pi nFADc^*}{w \ln(64Dt/w^2)} \quad (\text{Appendix.18})$$

where  $w$  is width of band electrode. Electrode surface area  $A$  could be much larger than a microdisk counterpart, since the length of band is not necessarily confined into micrometer level.

This system also grows into quasi-steady state, although diverging process differs with respect to electrode critical dimension. However, forced or natural convection is usually present, and the free diffusion is constrained to a certain thickness (from several to several-hundred micrometers against electrode surface, Figure Appendix-10) [309]. Consequently the mass transport current may reach a “truly” steady-state value in opposition to the quasi-steady-state regime. Indeed, these microband electrode are currently often used for their ease of fabrication and flexibility of integration in different working surroundings, including in open system [311], confined system [312], or in microfluidic channels [214,313].

As a conclusion, microelectrodes may differ in shapes and regimes, they own some common trends in electrochemical responses to abruptly applied potentials: transient planar diffusion, and then diverge to steady or quasi-steady state under enhanced mass transport. These characters, along with decreased resistance, high faradaic-to-charging current ratio, and simple instrumentation, make microelectrodes easily gives determination and speciation about nearby redox reactions (from well-established voltammograms or steady-state current), and accordingly favored in many elaborate investigations (e.g., exploration of rapid reaction mechanisms, unstable reactants, coupled homogeneous reactions, species with minute concentration or complicated kinetics, and imaging of redox centers present in thin sold films [220,314,315]).

### Microelectrode array (MEA)

The very small scale of microelectrode is the key to its special experimental utility, but it is as well a difficulty when thinking about the low current (usually in the range of nano-, pico-, or even femtoampere). To effectively magnify signal without losing characters of microelectrode, array forms are recently introduced in many researches [316-318].

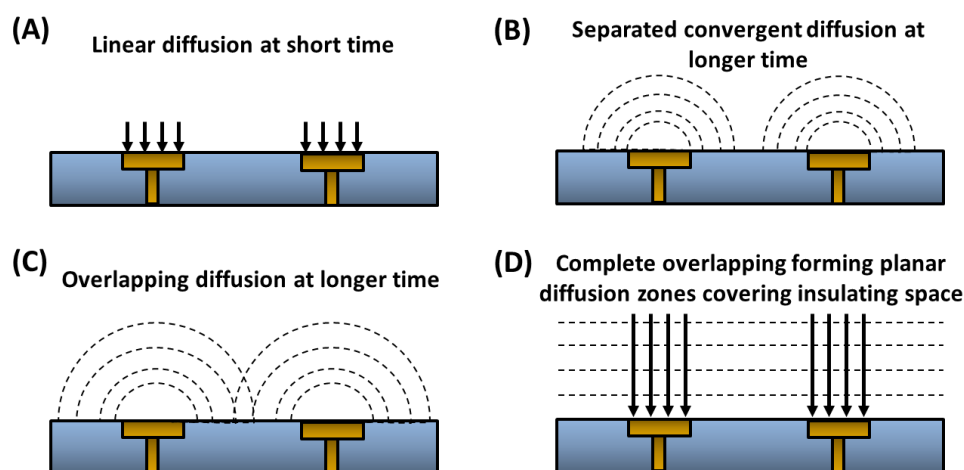


Figure Appendix-11: Schematic diagram of four categories of diffusion profile that may take place at MEA system.

MEA contains a large multitude of microelectrodes in well-organized order. They are normally placed in a common electric field, showing collective signal based on electrodes geometry and the overlaps of diffusion layer (typical cases in Figure Appendix-11). With specific critical dimensions and distance intervals, overall current measured could be: a simple summation of currents passing through individual electrodes (no overlap in case Figure Appendix-11A, -11B); smaller than the sum of currents when each electrodes work independently (partial overlap in Figure Appendix-11C); or as a macroelectrode response resulted from planar diffusion over the entire array (total overlap in Figure Appendix-11D) [319]. Even when signal is proportional to the area of whole array, the signal-to-noise ratio is greatly improved since noise is proportional only to the area of electrodes.

When individual microelectrode gives sufficiently large analytical signal (e.g., by introducing convective mass transport), each electrode could be modified towards one interested species. And the array systems are flexibly manipulated to engage simultaneous detection of multiple analytes or even to offer spatial resolution.

## **Appendix II. Microfluidic materials and microfabrication**

The fundamental driving force underlying avant-garde microfluidics is the balanced improvements in materials and fabrication to satisfy the requirements of different assays. Some key microfluidic materials and microfabrication technologies are given in the following context.

### **II.1. Materials**

Materials of microfluidic devices constantly play a primary role, not only due to large surface-to-volume ratios but also to the amplified effects coming from nature of materials. The development originated from glass and silicon, gradually shifted towards polymer substrates like PDMS, and hitherto a variety of interesting candidates have emerged, including hydrogels and paper-based materials [320].

There are several basic points that should be taken into account when choosing an appropriate material:

- Chemical and biological compatibility with working substances.
- Excellent electrical insulation, thermal conductivity and optical property.
- Accessibility of surface modifications to meet peculiar needs, such as for electrophoresis and protein immobilization.
- Convenient fabrication procedure, portability and rational expense.

#### **Inorganic materials**

Glass, quartz and silicon are the first generation materials used in microfluidic devices, exhibiting stable electroosmotic mobility, thermostability and solvent compatibility which spread their applications on electrophoresis, on-chip reactions, droplet formation and in-situ fabrication [321-323]. Micropatterns could be precisely transferred on silica and glass substrates by standard photolithography [324] or laser direct writing (for photosensitive glass) [325]. However, the fabrication process is normally quite burdensome with dangerous chemicals (e.g., hydrofluoric acid), and moreover, the final bonding needs high temperature, high pressure and super clean environment [320]. Besides, these materials are not gas

permeable, making them inconvenient for cell culture. All the limitations accelerated searching other substitutes that are inexpensive, easily fabricated and more compatible for biological purpose.

### Elastomers and plastics

Polymer materials are generally categorized into three classes: elastomers, thermosets and thermoplastics [320].

PDMS, the most popular elastomer in microfluidics, with low cost of microfabrication, gas permeability, and biocompatibility, is widely used in various bio-related researches [326,327]. Its siloxane backbones (Figure Appendix-12) allow convenient

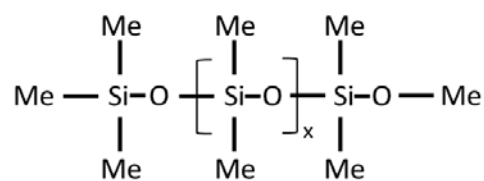


Figure Appendix-12: PDMS backbones.

bonding with glass, silicon or even another piece of PDMS (reversibly or irreversibly), solving the integration trials confront inorganic materials. The elasticity makes it possible to integrate small pumps/valves, giving access to highly-parallel manipulations. The drawback of PDMS, however, is addressed on incompatibility with organic solvents [328]. The inherent porous matrix with alkyl groups leads to absorption of small hydrophobic molecules and biomolecules such as proteins. This phenomenon could be circumvented by pretreatment of surface grafting.

SU-8 photoresist is a typical thermoset [329]. When heated or radiated, molecules cross link to form a rigid network, remaining stable shape before decomposition, even at high temperature. This feature benefits fabrication of true 3D structure, but on the other side thwarts high-density integration based on diaphragm valves. Furthermore, concerning the high cost, today SU-8 is commonly used to build stiff masters with microstructures for PDMS replicas fabrication.

Thermoplastic materials, such as polymethyl methacrylate (PMMA), polycarbonate (PC), polystyrene (PS), polyethylene terephthalate (PET) and polyvinylchloride (PVC), could be distinctly soften at glass transition temperature, and therefore become processable. The thermo-molding process is capable of producing chips at high rate and low cost, but requires metal or silicon template during high temperature processing. As compared to PDMS, poor gas permeability, hardship in bonding, and rigidity under room environment prevent them from being used in highly-integrated biocompatible systems. However, various surface modifications via dynamic coating or grafting [330] expand their utilization to some extent.

## Hydrogels

Hydrogels are highly porous materials derived from 3D networks of hydrophilic polymer chains that span in aqueous agent. Their aqueous nature and proper permeability of gas, small molecules and even bioparticles promote the prevailing applications in 3D cell culture [331]. According to different affinity, hydrogels are subdivided into animal-derived hydrogels (e.g., matrigel and collagen), plant-derived hydrogels (e.g., alginate and agarose), and synthesized hydrogels (e.g., polyethylene glycol (PEG) and polyacrylamide (PAAM)) [332]. All of them are capable of achieving cell adhesion and proliferation, naturally or after grafting functional groups. However, limited by the resolution in microfabrication (micrometer scale), they are mostly used for 3D cell culture in tissue engineering [333].

## Paper

Paper-based microfluidics [334] is burgeoning recently as an exponent of portable, low-cost, convenient and unsealed platform. The nature of cellulose paper (i.e., highly porous and excellent in wicking aqueous solutions) streamlines the utilization (automated capillary effects that allow sample manipulation without external power). In addition, fabrication of microchannel is also quite convenient, simply through generation of hydrophobic barriers with printing (e.g., wax printing [335] and inkjet printing [336]) or cutting methods. Benefited by convenience and cheap price, paper devices are very promising as commercial products for bioassays such as personalized medical care [337]; however, still with many challenges in front, such as better sensitivity and high-density integration.

The materials mentioned above are often combined to form a hybrid chip with extended functions. For example, soft components can be enclosed between hard layers, working as valves; porous materials can constitute a part of channel walls, permitting mass transfer of target compositions by diffusion while obstructing the bulk solution; glass substrates can be patterned with metal electrodes, and then incorporated with polymer-based microdevices for bioanalysis.

## II.2. Microfabrication techniques

To fabricate a microfluidic device, many techniques might be performed in sequence; sometimes to make multi-layer structures, processes are needed repeatedly. Several primary technologies are presented according to their functions (Figure Appendix-13), and specific details of those closely related to our work are introduced afterwards.

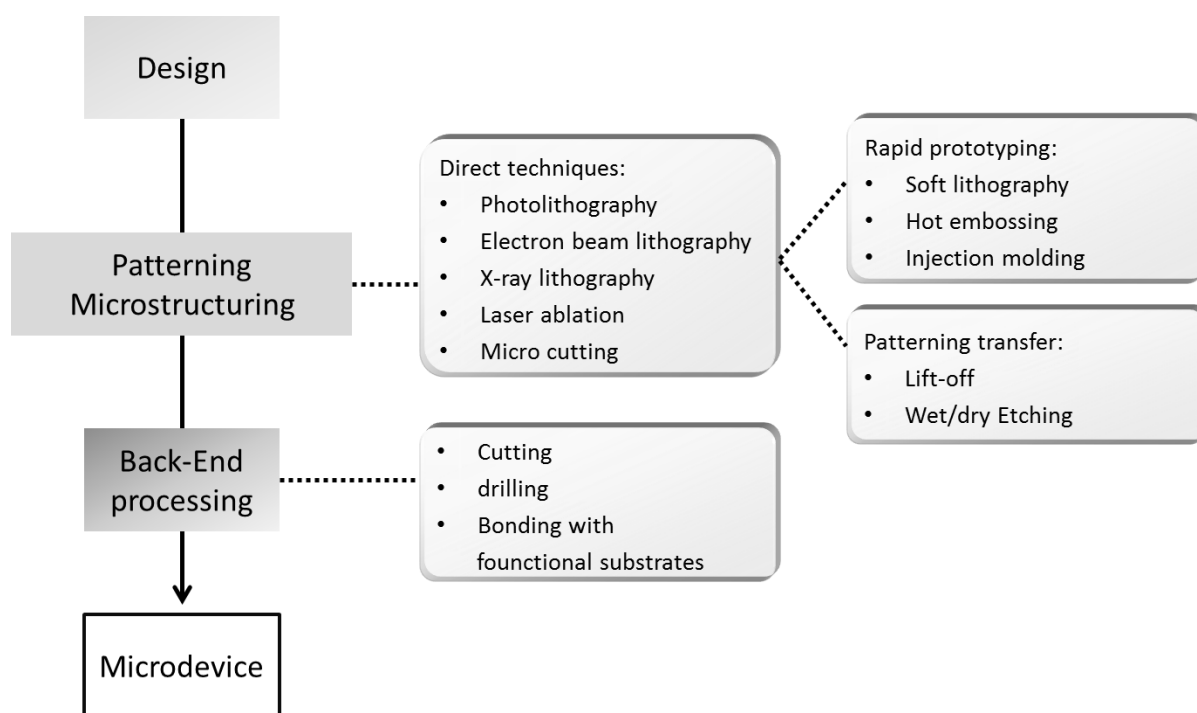


Figure Appendix-13: Process diagram of microfabrication technologies.

### Photolithography

Photolithography [338] is the most commonly used technology to define the original microstructures. It has many advantages like high resolution, convenience in transferring entire design at once, and feasibility of multi-layer structure. The basic principle is to generate patterns on resist-coated substrates (e.g., silicon and glass) through selective exposure to UV light source. A typical fabrication scheme is shown in Figure Appendix-14. The photoresist under transparent part of the predesigned mask becomes more (positive resist) or less (negative resist) soluble in a developing solution, therefore after development, the pattern on mask is precisely transferred onto the substrate.

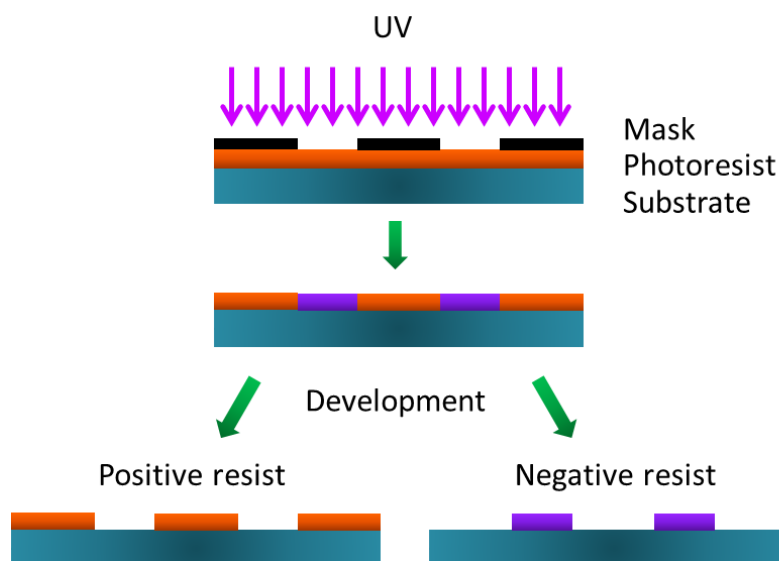


Figure Appendix-14: Schematic diagram of photolithography on positive (exposure part more soluble) or negative (exposure part less soluble) photoresist.

There are also some alternatives in defining microstructures, including electron beam lithography [339], X-ray lithography [340], laser ablation [341] and so on; each with particular protocol and characteristics. However, photolithography is illustrated here with details, since it predominately offers desirable masters for further manipulations (e.g., etching or polymer prototyping). The procedure of UV photolithography involves mask fabrication, wafer cleaning, photoresist preparing, spin coating, baking, alignment, exposure and development.

- **Masks:** A mask can be fabricated in different ways, mainly depending on the required resolution. The photo masks, made from quartz or glass covered by thin chromium layer, offers high resolution pattern (around 1  $\mu\text{m}$ ); while film masks, easily produced by digital printer with black inks, are suitable for features in bigger size (10  $\mu\text{m}$ ).

- **Wafer cleaning:** The substrates should be clean and dry prior to applying photoresist. The preparation of substrates normally starts with a solvent cleaning or a dilute acid rinse, and then followed by distilled water rinse.

- **Photoresist:** Photoresist is composed of epoxy resin, photoinitiator and solvent. When exposed to UV light, the physico-chemical properties of resists are altered and consequently change its solubility. For positive resist, exposed area is made soluble and easily removed inside liquid developer; for negative resist, on the contrary, exposed area is cured while the rest regions are removed.

Resists of SU-8 series [342] are quite widely used as negative resist to form thick image with vertical sidewalls (up to 2 mm in aspect ratio 20). Normally the higher resist's viscosity is, the easier it will be to acquire a thick film. These resists manifest great chemical and thermally stabilities after curing, and are best suited for permanent applications as masters.

Resists of AZ family [343-345] are able to serve thin films with good adhesion, high resolution, and high resistance to oxygen plasma etching. They are typically used to facilitate subsequent metal electroplating and lift-off process. Among which, AZ 5214E is specially favored owing to the capability of reversing images. When it acts as a positive resist, exposed part is removed; however, this part could be cross linked simply by applying an extra bake cycle. The unexposed part turns to be soluble after a flood exposure, leading to a negative image after development.

- Spin coating: This process is to generate uniform thickness of resist layer. Desired thickness could be obtained by selecting appropriate spin speed for specific photoresist (Table Appendix-1).

*Table Appendix-1: Spin speed vs. thickness for SU-8 2000 photoresists [346].*

Spin speed (rpm)		1000	2000	3000	4000
Thickness ( $\mu\text{m}$ ) of series photoresists	2005	8	6	5	4.5
	2010	20.5	13	10.5	9.5
	2015	38	21	16	13

- Soft bake: After spin coating, the resist film needs a soft baking to evaporate solvent and condense itself. It is usually performed on a level hot plate, initiated from a lower temperature to a higher one (e.g., from 65°C to 95°C) [342], allowing for better coating fidelity, reduced edge bead and better resist-to-substrate adhesion.

- UV exposure: Exposure is routinely performed under proper wavelength, such as i-line at 365 nm [347] is optimized as radiation source for SU-8 resist. The lamp power ( $\text{mW cm}^{-2}$ ) and delivered energy ( $\text{mJ cm}^{-2}$ ) strongly affect pattern transfer. Here is a reference table (Table Appendix-2) showing appropriate exposure conditions for different resists to acquire a good image without deformation, loss of sharpness or corners.

*Table Appendix-2: Exposure energy vs. thickness for SU-8 2000 photoresists [346].*

Thickness ( $\mu\text{m}$ )	0.5 – 2	3 – 5	6 – 15	16 – 25	26 – 40
Exposure energy ( $\text{mJ cm}^{-2}$ )	60 – 80	90 – 105	110 – 140	140 – 150	150 – 160



Aligning is frequently performed during exposure process. With the help of alignment targets (e.g., rectangles or cross marks), it is possible to generate well-defined multi-layer structures. According to different requirements, manipulations under contact, proximity or projection mode [348] are available.

- Post exposure bake: Following exposure, the exposed area of SU-8 film is selectively cross linked via post expose bake. Two-step baking is also preferred here to minimize stress, wafer bowing and resist cracking. Baking temperature and time should be modulated corresponding to specific resist and thickness.
- Development: Common solvent-based developers like ethyl lactate can dissolve not-polymerized portions, sometimes with help of strong agitation. After development, the substrate should be rinsed briefly with isopropyl alcohol, and then dried with air stream for future use.

### Soft lithography

Soft lithography [349] is a cost-effective and easily manipulated technology for pattern replication and rapid prototyping. It can be realized on many elastomeric materials such as PDMS to generate the flexible slide with excellent optical transparency, gas permeability, and biocompatibility. Additionally, the ease of fabrication, needlessness of clean room environment, and friendly integration, further expand its applications towards biomedical and clinical areas. However, most of current soft lithography processes still rely on modern photolithography at first to form the reusable master. And after that, thousands of “elastomeric replica” [350] could be easily produced by repeatedly casting mixture of prepolymer and curing agent on to the master, and then peeling off after solidification (scheme shown in Figure Appendix-15).

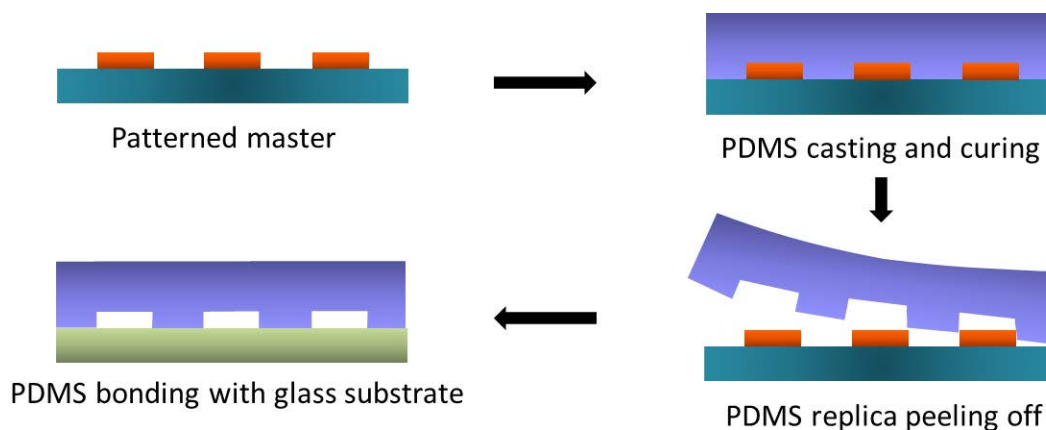


Figure Appendix-15: Scheme of soft lithography for generating PDMS replica.

Micro-contact printing and micromolding [351] are the two most important branches in soft lithography. The illustrations are depicted in Figure Appendix-16. Micro-contact printing, through contacting a soft polymer stamp to the substrate, easily and flexibly transfers target molecules pattern to forming microscale self-assembled monolayers (SAMs). While micromolding is a technique that uses an elastomer as the master for further molding, including replica molding, microtransfer molding ( $\mu$ TM), and micromolding in capillaries (MIMIC).

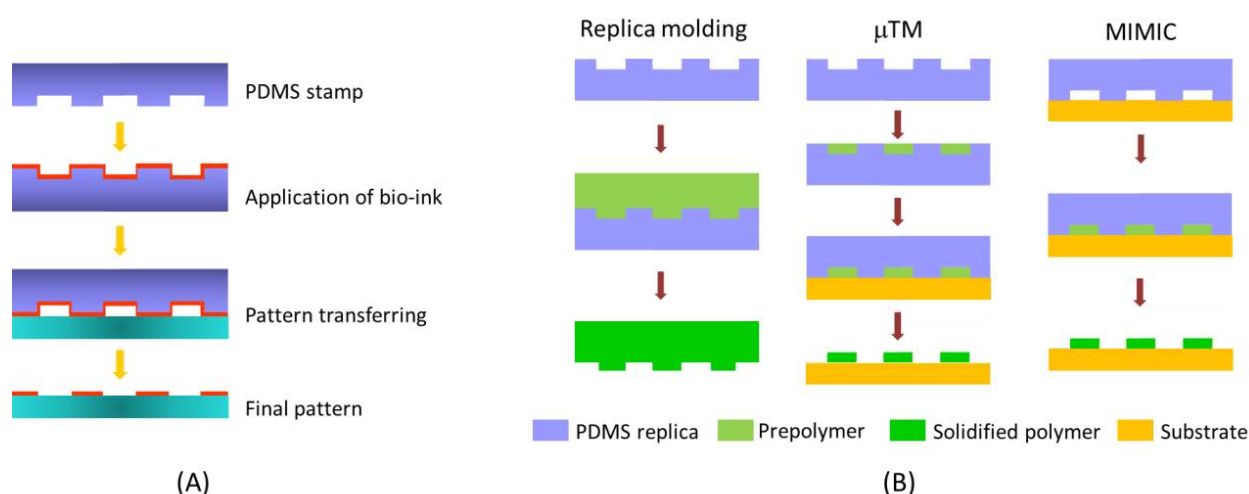
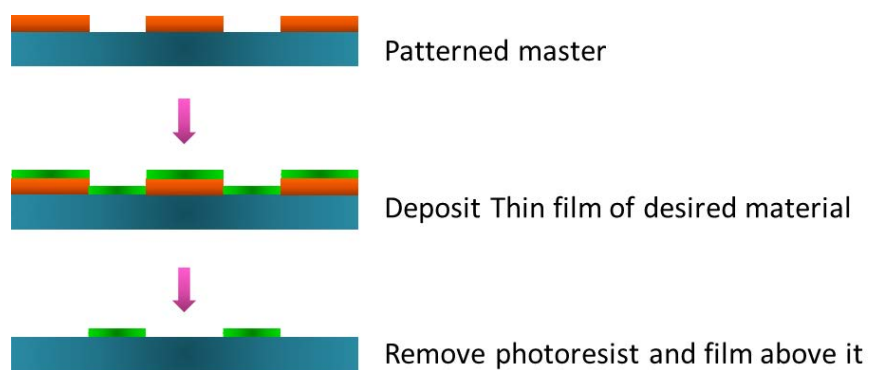


Figure Appendix-16: Schematic diagrams of (A) micro-contact printing to transfer biomaterial pattern, and (B) micromolding techniques with PDMS replica as a master.

### Lift-off

Lift-off is commonly used as an additive process to transfer a design (Figure Appendix-17). The target material is deposited on a substrate which is previously patterned by a sacrificial resist layer. After dissolution within a specific solution (e.g., acetone), the sacrificial layer is removed together with its upper film, only remaining the target material in the regions where it directly contacts the substrate. This mild transfer process is widely applied in fabrication of microelectrodes array as well as in some other cases where a direct etching process might have undesirable effects.



*Figure Appendix-17: Schematic diagram of pattern transfer through lift-off technology.*

Besides these mentioned techniques, wet or dry etching, hot embossing, injection molding and so on that continuously thrive the progress of microfluidics [349].

## Appendix III. Experimental section

### III.1. Solutions preparation

#### Solutions for *in vitro* experiments

- Phosphate-buffered saline (PBS buffer)

PBS buffer (10 mM Na<sub>2</sub>HPO<sub>4</sub>, 2.68 mM KCl and 140 mM NaCl; pH = 7.4) was used throughout the *in vitro* experiments. It was made by dissolving one PBS tablet (5g; Gibco) in 500 mL ultrapure water (resistivity of 18.2 MΩ cm at 25°C; Millipore).

- Pt-black plating solution

1 mL hydrogen hexachloroplatinate(IV) solution (8 wt.%; Sigma-Aldrich) and 1.6 mg lead(II) acetate trihydrate (99.8%; Sigma-Aldrich) were added into 6.36 mL PBS buffer to prepare Pt-black deposition solution. This stock solution was conserved in sealed, cool and lightproof condition.

- Ferrocenemethanol (FcMeOH)

FcMeOH (97%; Acros) was diluted to 0.5 mM with PBS buffer, used as model electroactive species to validate convective mass transport and to evaluate apparent active surface area of the microchannel electrodes.

- Hydrogen peroxide (H<sub>2</sub>O<sub>2</sub>) and nitrite (NO<sub>2</sub><sup>-</sup>)

A series of hydrogen peroxide and nitrite solutions (from 5 mM to 10 nM) were freshly prepared in PBS buffer from stock solutions (H<sub>2</sub>O<sub>2</sub>: 35 wt.%, Acros; NO<sub>2</sub><sup>-</sup>: 1 M solution made from 99% NaNO<sub>2</sub>, Sigma-Aldrich) before experiments.

- Peroxynitrite (ONOO<sup>-</sup>)

Peroxynitrite solutions (from 5 mM to 50 nM) were freshly prepared by diluting the alkaline stock solution (40 mM ONO<sub>2</sub>•Na stored at -80°C ; Cayman Chemicals) with a mixture of 10 mM PBS and 0.1 M NaOH (Acros) so as to reach the required pH between 11.1 and 8.4. This pH was systematically controlled with a pHmeter (Radiometer Analytical).

- Nitric oxide (NO<sup>\*</sup>)

Stock solution of 50 mM DEA-NONOate was initially prepared by dissolving 10 mg DEA-NONOate (Cayman Chemicals) in 0.96 mL 0.01M NaOH. Solid DEA-NONOate was previously stored under nitrogen at -80°C to avoid any serious decomposition. The prepared stock solution was conserved in an ice box for maximum 24 h before use. To initiate the release of NO<sup>\*</sup>, minute aliquots of stock solution were rapidly mixed with PBS buffer (pH = 7.4) to provide DEA-NONOate donor solutions with desired concentrations.

Since peroxyntirite and DEA-NONOate solutions decomposed with time, the duration  $t_0$  between solution preparation and beginning of experiments was recorded and reported systematically in kinetic studies (in Part B-2.2.).

#### Solutions for *ex vivo* experiments

- Locke's buffer

The Locke's solution was used as buffer throughout the *ex vivo* experiments. It was prepared with 5.6 mM glucose, 154 mM NaCl, 3.6 mM NaHCO<sub>3</sub>, 5.6 mM KCl, 15 mM Hepes, 1.2 mM MgCl<sub>2</sub>, and 2.5 mM CaCl<sub>2</sub> in pure water (pH 7.4). This buffer solution was stored at -20°C, thawed and filtered (Nylon membrane with pore size of 0.22 μm; Costar) before use.

- Culture medium

Growth and maintenance of Raw 264.7 macrophages were supported by Dulbecco's modified eagle medium (DMEM, containing 1 g L<sup>-1</sup> D-glucose and pyruvate; Gibco, USA) supplemented with 5% fetal bovine serum (FBS; Gibco) and 1% penicillin/streptomycin (Pen Strep; Gibco). This medium base was stored in sterile conical tubes (50 mL; Falcon) inside refrigerator (4°C); filtered (0.22 μm pore size; Costar) and pre-warmed to 37°C before use.

- Calcium ionophore A23187

The 1 mM calcium ionophore A23187 (Sigma-Aldrich) was prepared with Bioultra ethanol (Sigma-Aldrich), stored in sterile safe-lock tubes (1.5 mL; Eppendorf) at -20°C. During electrochemical studies, this solution was diluted to 10 μM concentration in Locke's buffer to initiate cellular oxidative stress.

- Fibronectin

Fibronectin (Sigma-Aldrich) was prepared with Locke's buffer to  $50 \mu\text{g mL}^{-1}$ , stored in sterile safe-lock tubes (1.5 mL; Eppendorf) at  $-20^\circ\text{C}$  and thawed before use.

### III.2. Sensors preparation

#### Pt-black coated carbon-fiber microelectrode

- Carbon-fiber microelectrode

Individual carbon fibers ( $d = 10 \mu\text{m}$ ; Thornel P-55S, Cytec) were aspirated into glass capillary tubing (O.D. = 1.2 mm, I.D. = 0.7 mm; GC-120F-10, Clark Electromedical Instruments). The capillary was pulled with a vertical micropuller (PB-7; Narishige), thinning at the center and eventually yielding two identical microelectrodes. Each microelectrode was back-filled with a drop of mercury, and an electrical contact was made by inserting a nichrome wire (Demand Products) from the open part of the capillary (Figure Appendix-18).

To minimize noise, the protruding carbon fiber was insulated by electrochemical deposition of poly(oxyphenylene) according to the literature procedure [352]. This deposition was carried out for 3 minutes in a solution of allylamine (0.4 M), 2-allylphenol (0.23 M), and 2-butoxyethanol (0.23 M) in 1:1 (v/v) water/methanol. A potential of +4.0 V was applied between microelectrode and a platinum wire counter electrode. Subsequently the microelectrode was washed in distilled water and the polymer was cured for 3 h at  $150^\circ\text{C}$  in order to reticulate and form an insulating shielding ( $1 \mu\text{m}$  thickness) on the carbon-fiber surface (see inset of Figure Appendix-18). All the chemicals described here were purchased from Sigma-Aldrich.

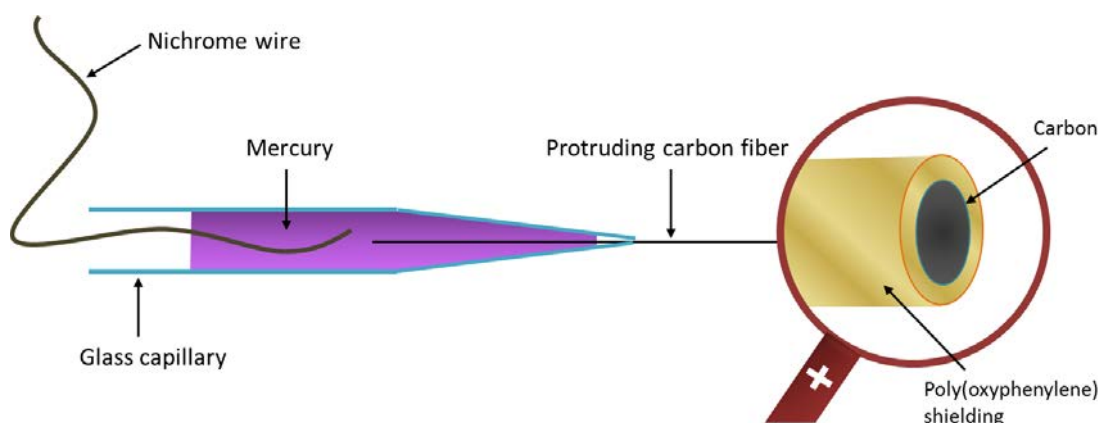


Figure Appendix-18: Structure illustration of carbon-fiber microelectrode, with the inset scheme demonstrating polymer insulated carbon tip.

- Platinization at carbon tip surface

The insulated fiber was cut to a suitable length (c.a. 0.6 cm) under a bifocal microscope (Stemi 2000; Zeiss), and the tip of the microelectrode was polished on a diamond particle whetstone microgrinder (EG-4; Narishige) at an angle of  $45^\circ$  for 6 min (polishing dish rotating at  $65 \text{ rev min}^{-1}$ ) to yield a clean, elliptical, and conductive surface. The polished carbon-fiber surface was platinized in Pt-black plating solution at  $-60 \text{ mV vs. SSCE}$ . The extent of platinization was controlled by monitoring the reductive current followed on a computer, and the process was interrupted a few seconds later when the electrical charge of the signal reached the desired value of  $30 \mu\text{C}$  (Figure Appendix-19) [11,118], which corresponded to the optimal activity of the electrode surface for the single cell oxidative stress detection. Platinized microelectrodes were stored in water at  $4^\circ\text{C}$  until use.

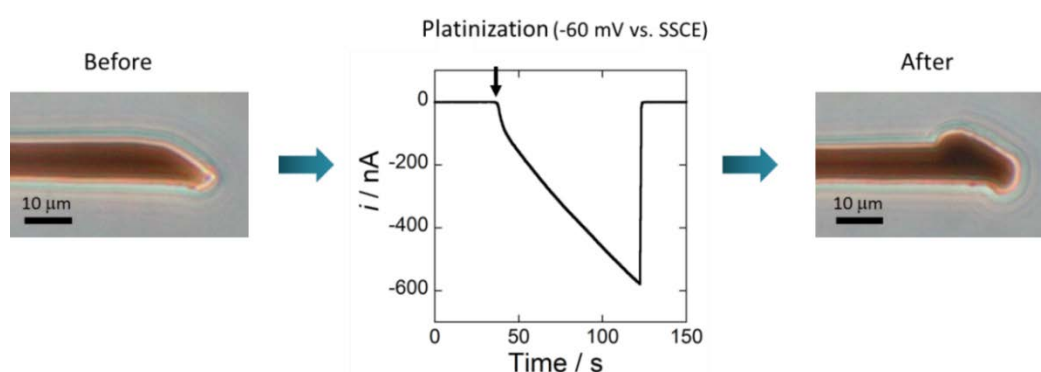


Figure Appendix-19: Platinization of carbon-fiber tip surface via electrodeposition. The middle graph shows evolution of the amperometric current following the reduction ( $E = -60 \text{ mV vs. SSCE}$ ) of Pt-black on microelectrode carbon surface. The deposition starts from the black arrow point and is pursued until reaching deposit charge of  $30 \mu\text{C}$ . Optical images describe one fiber tip before (left) and after (right) platinization. Scale bars are  $10 \mu\text{m}$  [11].

- Optimal potentials and quantitative basis of the four key ROS/RNS

The optimal detecting potentials of four key ROS/RNS (i.e., H<sub>2</sub>O<sub>2</sub>, ONOO<sup>-</sup>, NO<sup>•</sup> and NO<sub>2</sub><sup>-</sup>) on this platinized carbon-fiber microelectrode were previously determined by a series of *in vitro* and *ex vivo* studies [11,117-119,133,220,353]. Values corresponded to 0.30, 0.45, 0.65, and 0.85 V vs. SSCE were applied to perform the following single-cell oxidative stress detection. The responses of each component were also interpreted as linear combinations of the detected currents, serving the quantification basis:

$$i_{\text{NO}_2^-} = i_{0.85 \text{ V}} - i_{0.65 \text{ V}} \quad (\text{Appendix.19})$$

$$i_{\text{NO}^\bullet} = i_{0.65 \text{ V}} - i_{0.45 \text{ V}} \quad (\text{Appendix.20})$$

$$i_{\text{ONOO}^-} = 1.71 i_{0.45 \text{ V}} - 2.22 i_{0.30 \text{ V}} \quad (\text{Appendix.21})$$

$$i_{\text{H}_2\text{O}_2} = 2.22 i_{0.30 \text{ V}} - 0.71 i_{0.45 \text{ V}} \quad (\text{Appendix.22})$$

Slight differences (both in potential and mathematic relation) were observed as compared to the situation for platinized microband electrodes, which might result from the variations of Pt-black deposits (geometry, morphology, and quantity) on different substrates (i.e., carbon-disk vs. thin-layer platinum microband).

### **Pt/Pt-black microband electrodes-integrated devices**

The series of PDMS-glass microdevices used in this work were established for different experimental purposes. In general, the PDMS upper layer comprised microstructures while the glass substrate was patterned with microband electrodes. After bonding these two layers together, an integrated and portable electrochemical sensor was obtained. Although possessing similar fabrication procedures, each sensor featured particular design and parameters. The details are discussed in the following context.



### Microsensor for ROS/RNS *in vitro* detection

- Silicon master

Three parallel microchannels were designed for the *in vitro* detection sensor (Figure Appendix-20A). Photoresist SU-8 2015 (MicroChemicals), a negative resin, was applied to compose this model on silicon wafer; thus the structures were transferred from an inverse film mask (50800dpi; Selba). The generated microchannels were in rectangular section and a thickness value of 20  $\mu\text{m}$  was obtained (Figure Appendix-20B) according to the photolithographic parameters described in Table Appendix-3.

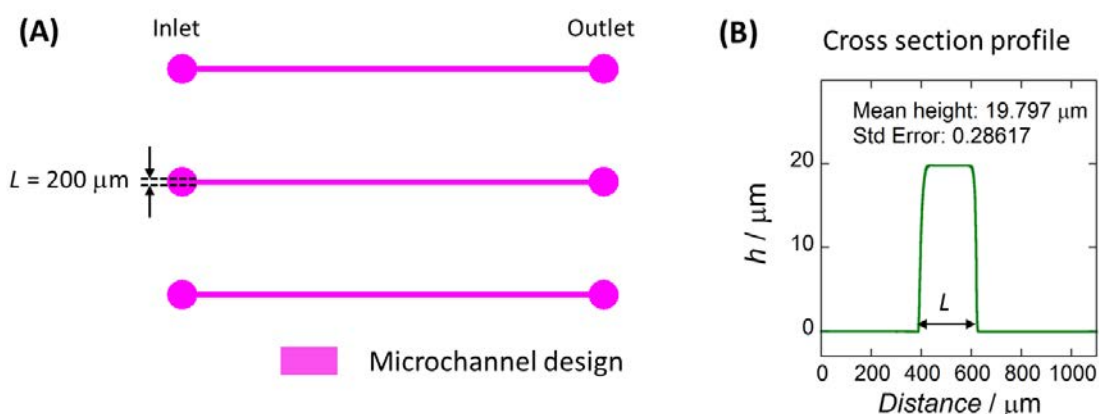


Figure Appendix-20: (A) Structure design for ROS/RNS *in vitro* sensor; with three parallel channels ( $L = 200 \mu\text{m}$ ) transferred to a silicon wafer. (B) Vertical section profile of the microchannel mold made by SU-8 2015 photoresist ( $h = 20 \mu\text{m}$ ).

Table Appendix-3: Photolithographic parameters for SU-8 2015 photoresist to form thin layer structure (20  $\mu\text{m}$  thickness).

Silicon wafer	$d = 4$ inch
Photoresist	SU-8 2015 (4 mL)
Spin-coating	500 rpm, 10 s; 2000 rpm, 30 s
Soft bake	65°C, 1 min; 95°C, 15 min
UV-exposure	9 s (13.4 $\text{mW cm}^{-2}$ )
Post bake	65°C, 1 min; 95°C, 3 min
Development	SU-8 developer, 2 – 3 min
Rinse	Isopropanol, water

The fabricated master was then treated by salinizing agent trimethylchlorosilane (TMCS; Sigma-Aldrich) for 2 min to prevent PDMS sticking, consequently prolonging the master's utilization time.

- PDMS replica

PDMS replica was made by casting a 10:1 mixture (polymer-to-curing agent ratio) of polydimethylsiloxane (PDMS, RTV-615; Momentive Performance Materials) onto the silicon master. After cured at 80°C for 1.5 h, the solidified PDMS replica was peeled off and injections/reservoirs were punched as necessary.

- Electrodes pattern on glass substrate

The glass substrate was patterned by several microband electrodes. The design is illustrated in Figure Appendix-21, composed of one REF ( $w = 500 \mu\text{m}$ , left), one CE ( $w = 500 \mu\text{m}$ , right) and several intermediate WEs ( $w = 197 \mu\text{m}$ ).

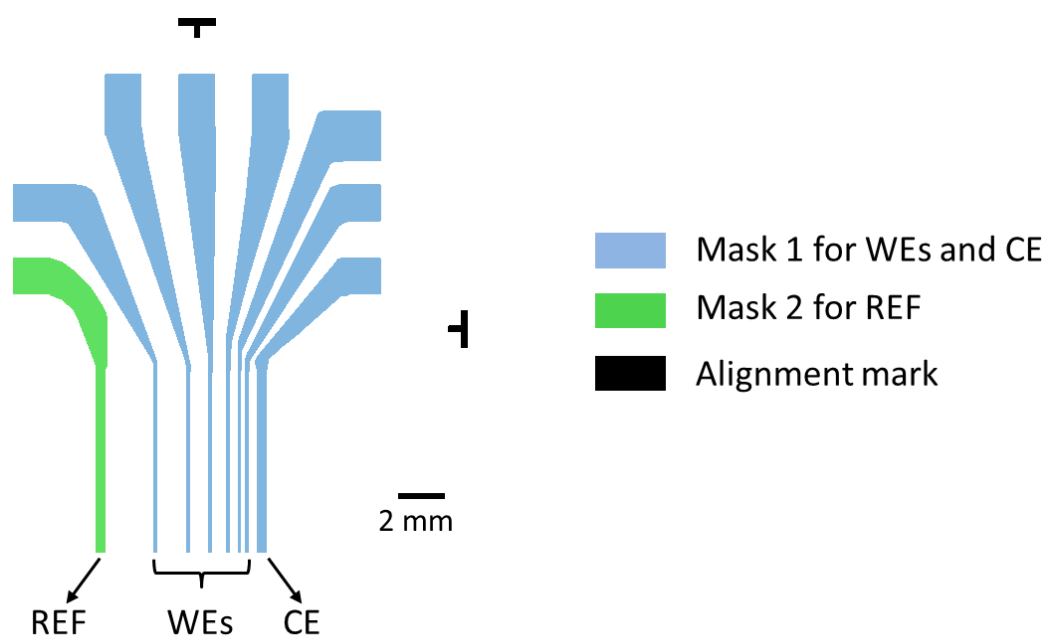


Figure Appendix-21: Design illustration of microelectrodes pattern for *in vitro* ROS/RNS detection. Mask 1 is designed for WEs and CE (Ti/Pt) while mask 2 is used for REF (Ti/Pt/Ag).

The patterns were transferred with AZ 5214 photoresist (MicroChemicals) after performing a two-step photolithography under high precision alignment (MJB4, SUSS MicroTec). The first mask generated thin-layer substrates of WEs and CE (Ti/Pt: 8/25 nm) while the second produced REF base (Ti/Pt/Ag: 8/25/50 nm). Ti was incorporated to enhance electrode adhesion with glass surface. Chromium photo masks ( $\mu$ PG101; Heidelberg Laser Mask Generator) were adopted here to facilitate accurate alignment. After photolithography, particular metal materials were homogeneously deposited by a sputtering coater (K675XD; Emitech). At last, the microband electrodes were shaped via lift-off process. Procedure and parameters are listed in Table Appendix-4.

*Table Appendix-4: Parameters of photolithography (for AZ 5214 resin), metallization, and lift-off procedures to generate thin-layer microband electrodes pattern on glass slide.*

Glass slide	76 × 26 mm
Cleaning	Acetone (ultrasonic 15 min), isopropanol, water
Photoresist	AZ 5214 (1 mL)
Spin-coating	1500 rpm, 5 s; 4000 rpm, 35 s
Soft bake	125°C , 1 min 45 s
UV-exposure	4 s (13.4 mW cm <sup>-2</sup> )
Post bake	125°C , 1 min 45 s
UV-exposure	15 s (13.4 mW cm <sup>-2</sup> )
Development	AZ 726 developer, 30 s
Rinse	Isopropanol, water
Metallization	Ti/Pt, 8/25 nm (WEs and CE); Ti/Pt/Ag, 8/25/50 nm ( REF)
Lift-off	Acetone, 20 min
Rinse	Isopropanol, water

Afterwards, these microelectrodes were connected with conductive wire (Wire Wrapping Wire; OK Industries) through conductive epoxy (A:B = 1:1, solidified at 40°C for 1 h; CircuitWorks). Some WEs were further platinized in Pt-black plating solution at a constant current density (-8 mA cm<sup>-2</sup>; 30 s). The home-made Ag/AgCl REF was fabricated by immersing Ti/Pt/Ag microbands in 5 mM FeCl<sub>3</sub> (Sigma-Aldrich) for 30 s.

- Device assembly

The PDMS replica was irreversibly bonded to the glass substrate via oxygen plasma (2 min, Harrick), offering a robust microdevice capable of driving flowing fluids. The microchannels were assembled perpendicular to microband electrodes (Figure Appendix-22). Thus effective electrode lengths were limited by microchannel width ( $L = 200 \mu\text{m}$ ) and the solution volume above these microbands was restricted by microchannel height ( $h = 20 \mu\text{m}$ ). Note that during electrochemical studies, only one WE was connected and only one channel was filled with solution, the others remaining empty. The integration of three independent microchannels and several parallel WEs was for the sake of utilization efficiency (in case of electrodes brokenness or channel leakage).

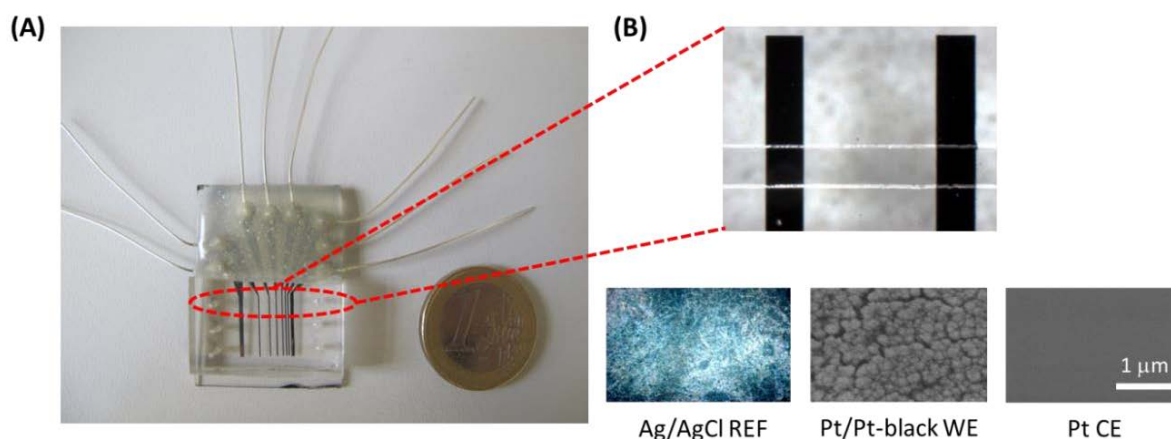


Figure Appendix-22: (A) Photo of PDMS-glass assembly for ROS/RNS *in vitro* detection. (B) Magnified optical image shows the perpendicular position of microband electrodes vs. microchannel (top figure); and the ones respectively demonstrate surface of Ag/AgCl REF, Pt/Pt-black WE and Pt CE (bottom figures; scar bar is  $1 \mu\text{m}$  in each one).

### Multi-sensor for *ex vivo* cells basal detection

- Silicon master and PDMS replica

In this case, a smooth and flattened PDMS slide was obtained from a bare silicon wafer. After curing the polymer mixture, PDMS replica was peeled off and punched with a circular steel indenter ( $d = 0.6 \text{ cm}$ ; Biopunch) to generate four parallel uncovered chambers which would serve cells confinement and detection.

- Electrodes pattern on glass substrate

Similarly as before, microband electrodes were patterned through two times of photolithography and lift-off processes. The design is shown in Figure Appendix-23, with the first mask generated Ti/Pt thin-layer WEs ( $w = 197 \mu\text{m}$ ) and CEs ( $w = 150 \mu\text{m}$ ) whereas the second mask produced Ti/Pt/Ag thin-layer REFs ( $w = 150 \mu\text{m}$ ). Every three electrodes (one CE, one WE and one REF) composed one sensor group; four independent groups were integrated in one device.

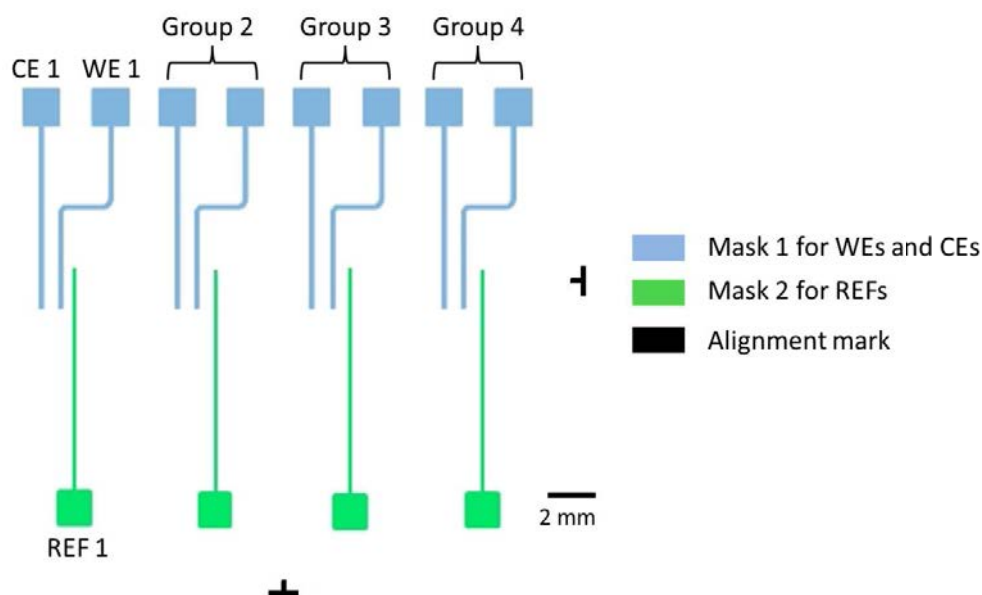


Figure Appendix-23: Design illustration of microelectrodes pattern for cells population basal detection. Mask 1 is designed for WEs and CEs (Ti/Pt) while mask 2 is used for REFs (Ti/Pt/Ag).

Materials and fabrication procedures were exactly the same as mentioned in Table Appendix-4. After obtaining the electrodes-patterned substrate, electrical connection was made, WEs were platinized with Pt-black, and REFs were converted to Ag/AgCl to support potentials throughout the electrochemical measurements.

- Device assembly

Here for the basal detection, no pressure-driven flow was involved. Therefore, PDMS slide was simply pressed against the glass surface to form a reversible assembly, allowing convenient cleaning and reuse of device.

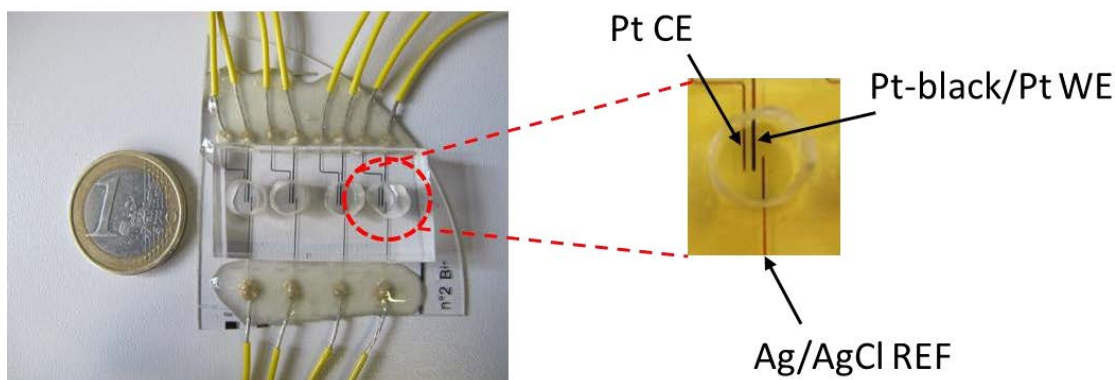


Figure Appendix-24: Photo of PDMS-glass assembly for cells basal detection. The device includes four parallel uncovered chambers which respectively confines three microband electrodes (one WE, one REF, and one CE in inset image) at the glass substrate.

As illustrated in Figure Appendix-24, each uncovered PDMS chamber confined one sensor group (i.e., one Pt/Pt-black WE, one Ag/AgCl REF, and one Pt CE). The effective electrodes lengths were around 5 mm, and the solution volume in each chamber was restricted of 150  $\mu$ L. During electrochemical studies, the four groups of sensor were simultaneously and independently worked at one selected potential.

#### Multi-sensor for *ex vivo* cells downstream detection

- Silicon master

A multi-layer microstructure was generated to enable separate cells culture and detection in one autonomous device. The global design is illustrated in Figure Appendix-25, the first mask features upstream microchamber ( $h = 50 \mu\text{m}$ ) which serves cells immobilization; while the second mask produces downstream microchannels ( $h = 20 \mu\text{m}$ ) that allows dynamic delivery of ROS/RNS production to electrochemical probes. Within the chamber mold, circle structures are incorporated either sparsely as support pillars ( $d = 100 \mu\text{m}$ ; see the left inset) to prevent subsidence of PDMS chamber; or densely in line at the end of chamber ( $d = 50 \mu\text{m}$  with intermediate gaps of  $10 \mu\text{m}$ ; see the middle inset) as a barrier to prevent cells from moving into the detection zone. Note that the channels part should be cautiously aligned to the chamber part (see the right inset). Otherwise a gap at the interface might lead to a failure of stream flowing.

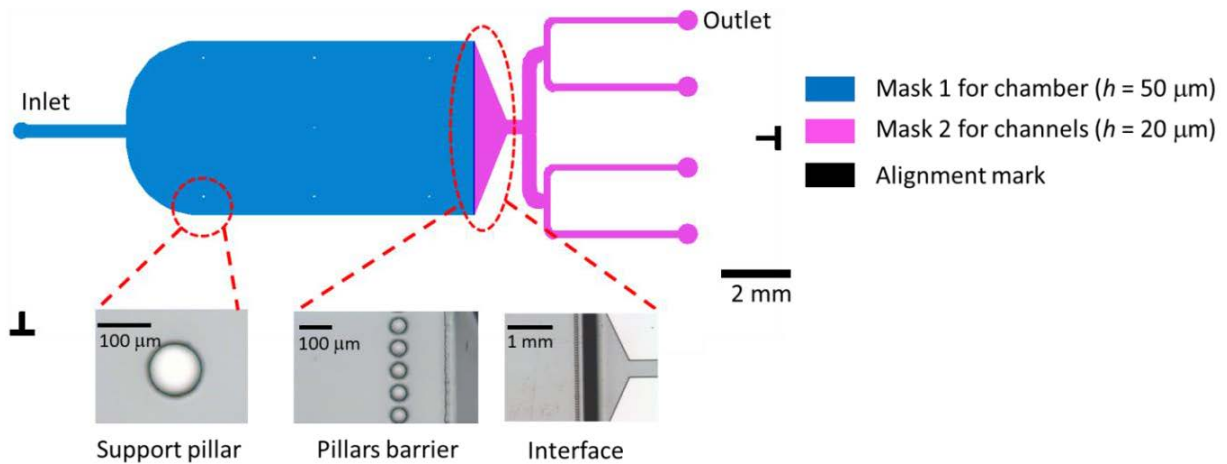


Figure Appendix-25: Design illustration of multi-layer structure for cells population downstream detection. One upstream microchamber and four downstream microchannels are incorporated. Insets represent, from left to right, the local images of support pillars, barrier pillars, and chamber-to-channels interface.

This compound structure was transferred to silicon wafer after two-step photolithography (Table Appendix-5). The mold of thicker chamber was constituted with SU-8 3050 while that of thinner channels was made by SU-8 2015. Both resins were negative thus inverse masks were sequentially adopted.

Table Appendix-5: Photolithographic parameters of SU-8 3050 photoresist to generate 50  $\mu\text{m}$  microchamber; and those of SU-8 2015 to produce 20  $\mu\text{m}$  microchannels.

Silicon wafer	$d = 4$ inch	
	Chamber part	Channel part
Photoresist	SU-8 3050 (4 mL)	SU-8 2015 (4 mL)
Spin-coating	500 rpm, 10 s; 3200 rpm, 30 s	500 rpm, 10 s; 2000 rpm, 30 s
Bake	65°C, 1 min; 95°C, 27 min	65°C, 1 min; 95°C, 15 min
UV-exposure	15 s (13.4 mW cm <sup>-2</sup> )	9 s (13.4 mW cm <sup>-2</sup> )
Bake	65°C, 1 min; 95°C, 3 min	65°C, 1 min; 95°C, 3 min
Develop	SU-8 developer, 3 – 4 min	SU-8 developer, 1 – 2 min
Rinse	Isopropanol, water	Isopropanol, water

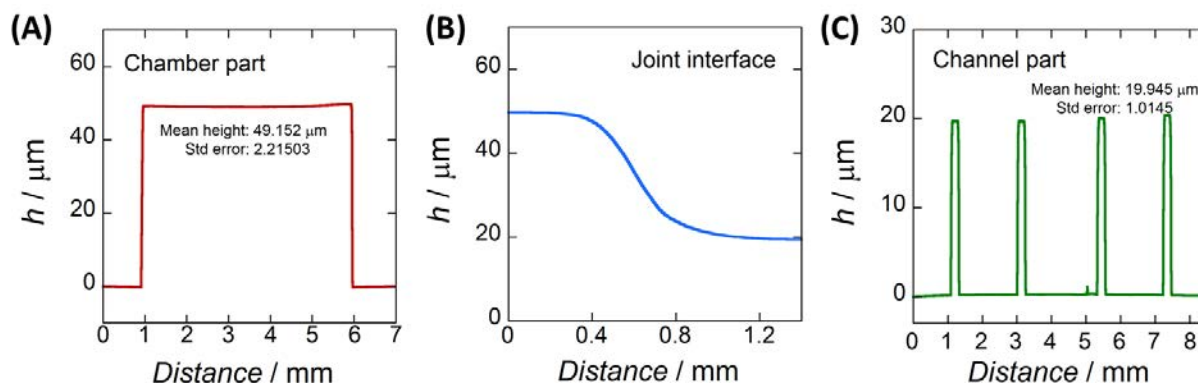


Figure Appendix-26: The vertical section profiles of (A) the microchamber mold made by SU-8 3050 photoresist ( $h = 50 \mu\text{m}$ ), (B) the joint interface between chamber and channels part, and (C) the microchannels mold made by SU-8 2015 photoresist ( $h = 20 \mu\text{m}$ ).

After fabrication, the whole master was baked at  $150^{\circ}\text{C}$  for half hour to smooth joint interface, and the condition of microstructures was checked under microscope. The vertical section profiles of chamber, channels and the interface in one ready-made master are illustrated in Figure Appendix-26. The desired thickness at each zone, as well as a smooth joint interface was observed.

- PDMS replica

Although this fabrication of multi-layer master was more complicated, once obtained, PDMS replicas were still simply got after casting and curing the polymer mixture.

- Electrodes pattern on glass substrate

The pattern of microband electrodes was fabricated according to the previously mentioned procedures (Table Appendix-4). However, the design is totally different and is shown in Figure Appendix-27.



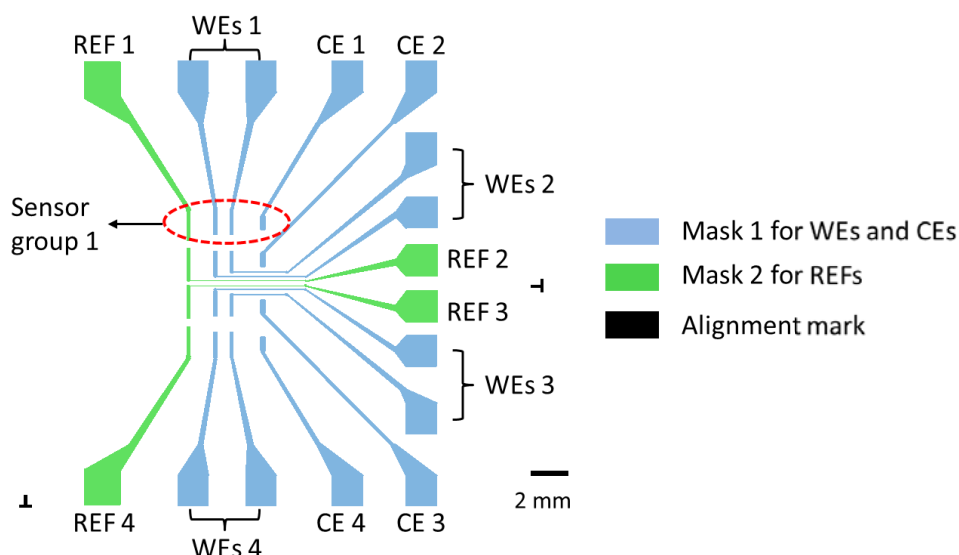


Figure Appendix-27: Design illustration of microelectrodes pattern for cells population downstream detection. Mask 1 is designed for WEs and CEs (Ti/Pt) while mask 2 is used for REFs (Ti/Pt/Ag).

The first mask generated Ti/Pt thin-layer WEs ( $w = 197 \mu\text{m}$ ) and CEs ( $w = 300 \mu\text{m}$ ) whereas the second mask produced Ti/Pt/Ag thin-layer REFs ( $w = 200 \mu\text{m}$ ). The electrodes in one row (e.g., red circle in Figure Appendix-27, REF + WE + CE) composed one sensor group; four independent groups were integrated in one device. After patterning, electrical connection was made, WEs were further platinized with Pt-black, and REFs were oxidized to Ag/AgCl to support potentials throughout all the measurements.

- Device assembly

The PDMS replica was irreversibly bonded to glass substrate (via oxygen plasma) for fluidic manipulations. The microband electrodes were assembled perpendicular to the microchannels, with the REF, WE, and CE respectively localized at the entry, middle, and end of each channel (schematic illustration in Figure Appendix-28A). The WEs were located about 4 mm (3.4 mm for WE 1, 4.3 mm for WE 1') after culture chamber, the effective length was limited by microchannel width ( $L = 200 \mu\text{m}$ ) and the volume of solution above these microbands was restricted by microchannel height ( $h = 20 \mu\text{m}$ ).

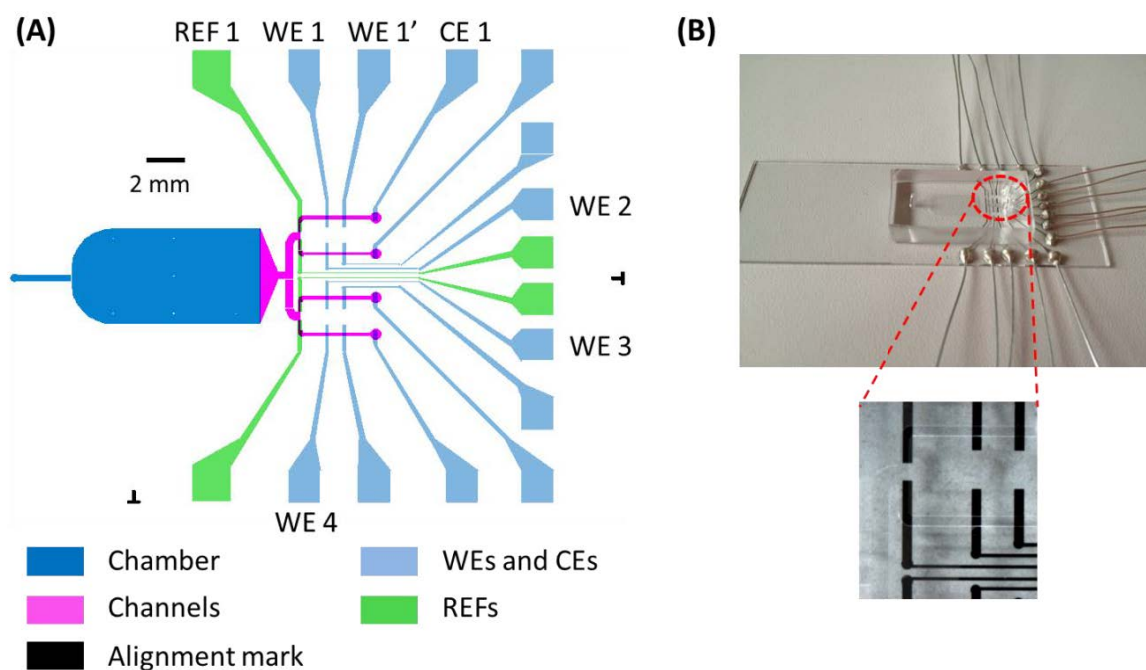


Figure Appendix-28: (A) Schematic illustration of integrated microdevice, showing the position of microband electrodes beneath microchannels. (B) Photo image of a substantial device for downstream cells detection; the inset is a magnified image showing the perpendicular location between WEs and corresponding microchannel.

A substantial assembly of microdevice is presented in Figure Appendix-28B. During electrochemical studies, solution was equally branched to these microchannels, and four aligned microchannel WEs (e.g., WE 1, WE 2, WE 3 and WE 4) simultaneously and independently worked at one constant potential. The design of two adjacent WEs (e.g., WE 1 and WE 1') in each channel was for utilization purpose and indeed only one WE per channel was connected during detection.

### III.3. Raw 264.7 macrophages preparation

#### Routine culture

- Cells passage and subculture

The macrophage-like Raw 264.7 cells (American Type Culture Collection, ATCC) were maintained in the DMEM-based medium in a 37°C incubator with a humidified atmosphere of 5% CO<sub>2</sub> (IGO150 CELLlife incubator; Jouan).

Subculture was conducted when the cells reached approximately 80% confluence (every 3 or 4 days; see Figure Appendix-29B). These confluent cells were rinsed with 7 mL sterile PBS, dislodged by 1 mL 0.05% Trypsin-EDTA (Gibco), suspended in 10 mL culture medium and then followed by a 1:10 dilution of cell suspension in fresh medium within a new culture flasks (75 cm<sup>2</sup>; Falcon; Figure Appendix-29A).

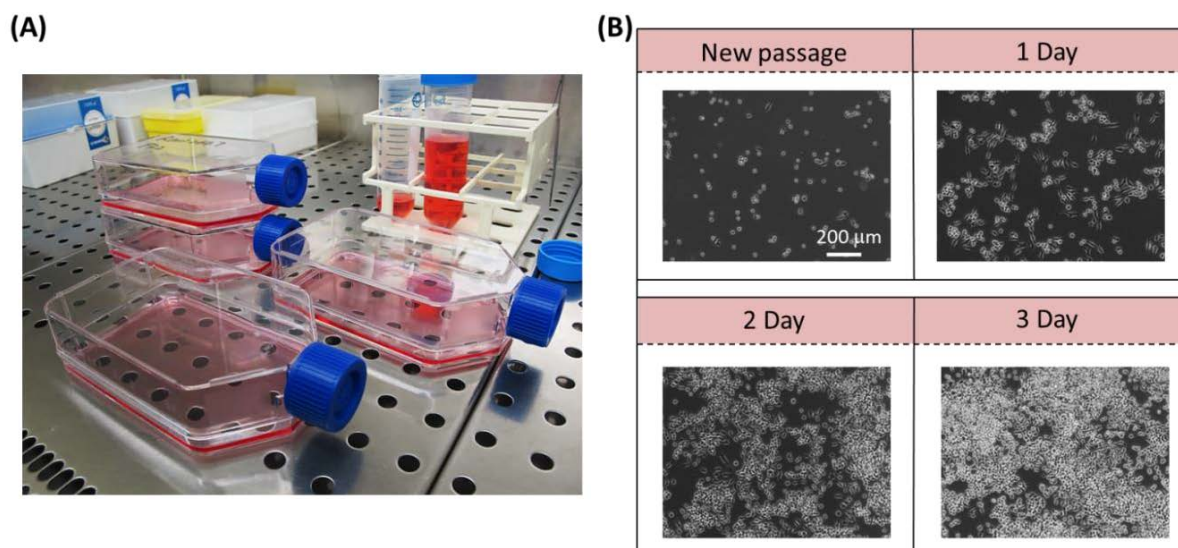


Figure Appendix-29: (A) Routine cells culture and passage in sterile flask. (B) Growth of Raw 264.7 macrophages in DEME-based medium after passage into a new flask.

- Cells freezing and thawing

Confluent cells monolayer was gently detached from the culture vessel, suspended, transferred into sterile safe-lock tubes (1.5 mL; Eppendorf) and were then centrifuged at 2000 rpm for 2 minutes (Biofuge 13; Heraeus Instruments). Supernatant was aseptically decanted without disturbing the cell pellet. Then the cell pellet was placed in sterile cryovial (2.0 mL; Fisher Scientific). 1mL of chilled freezing medium (composition: DMEM-based culture medium supplemented with 10% fetal calf serum (FCS) and 5% dimethyl sulfoxide (DMSO)) was added to each vial. These vials were sealed and stored in a -80°C refrigerator.

Before thawing the freezing cells, a water bath (Polystat 5; Bioblock Scientific) was warmed to 37°C. One cryovial was removed from the refrigerator and warmed as soon as possible. A new sterile flask (75 cm<sup>2</sup>) containing 12 – 15 mL fresh medium was prepared and the cells were gently dispensed into this flask. After incubation for 4 to 6 hours at 37°C, cells attachment was verified under an inverted microscope (Observer D1; Zeiss). The old medium was softly aspirated and then replaced by another 12 – 15 mL fresh medium. When cells showed satisfying viability, they could be maintained and subcultured as described above. Cultures were not maintained beyond three months. New freezing clusters were thawed at least two weeks prior to the end of the three-month culture period.

### Cells preparation for experiments

- Cells preparation: for single-cell analysis

Confluent Raw 264.7 macrophages in a 75 cm<sup>2</sup> flask were harvested and homogenized in 10 mL fresh medium (c.a. 10<sup>6</sup> cells mL<sup>-1</sup>). Two droplets (from disposable serological pipets; VWR) of this cell suspension were added to each petri dish ( $d = 3.5$  cm, Nunclon; filled with 3 mL medium, see Figure Appendix-30A) and followed by a 12 to 24 h culture inside incubator before electrochemical studies. Such a delay was necessary for the cells to adhere and recover at the dish surface. This very much diluted re-suspension led to isolated cells in quite sparse distribution, correspondingly facilitating accurate measurements of single-cell release without significant interference from neighboring cells.

- Cells preparation: for cells population basal analysis

Confluent Raw 264.7 macrophages were harvested from a 75 cm<sup>2</sup> flask, centrifugated at 1000 rpm for 5 min, and then homogenized in 2 mL fresh medium (c.a. 10<sup>7</sup> cells mL<sup>-1</sup>). 1.5 μL cell suspension was aspirated by a micropipette, and loaded into each uncovered PDMS-glass chamber ( $d = 6$  mm; four chambers in one device) which was previously filled with 150 μL warm medium (Figure Appendix-30B). The prepared microdevice was then placed inside CO<sub>2</sub> incubator for 12 – 24 h before electrochemical measurements.

- Cells preparation: for cells population downstream analysis

Confluent Raw 264.7 macrophages were harvested and homogenized as the same process in basal analysis. However, before seeding, this microdevice (composed of culture chamber and detection channels) was treated with  $50 \mu\text{g mL}^{-1}$  fibronectin for 20 min to promote fast and firm cells attachment. Then the cell suspension was extracted by a sterile luer-lok tip syringe (1 mL; BD) and immediately driven into the enveloped device by external syringe pump (Figure Appendix-30C). The connection between syringe and microchip was supported via Teflon tube (1.58 mm OD  $\times$  0.8 mm ID; Supelco). Each time during disconnecting or/and connecting, fresh medium was dripped to the connection part in order to prevent gas entry.

A gentle loading rate ( $2 \text{ mL min}^{-1}$ ) was applied in consideration of cells integrity. After pumping for 1.5 min, the microdevice was disconnected and placed inside incubator for c.a. 1 h. Cells were rested under zero flow condition during this period, and subsequently fresh medium was continuously pumped ( $4.0 \mu\text{L min}^{-1}$ ) to maintain constant nutrition replenishment and wastes removal. Electrochemical studies were performed after 12 to 24 h perfusion culture, when immobilized cells reached suitable density and viability.

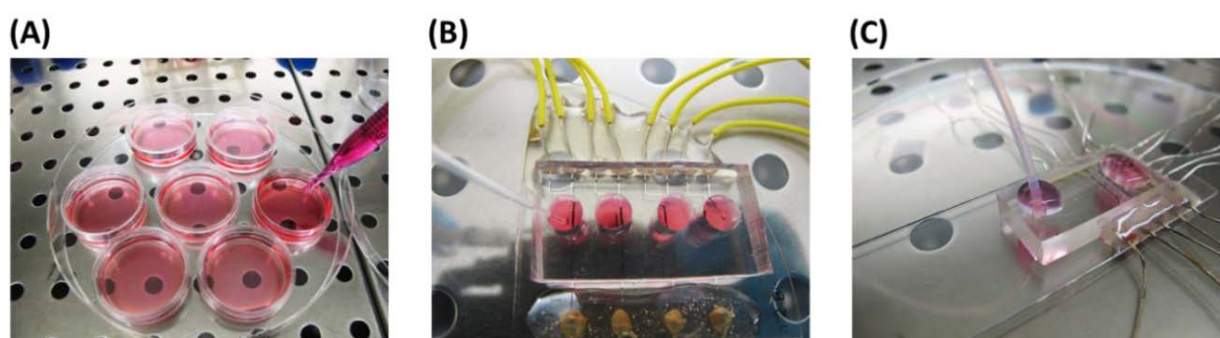


*Figure Appendix-30: Macrophages preparation for (A) single-cell detection in petri dish, (B) cells population basal detection in uncovered chambers, and (C) cells population downstream detection in sealed microfluidic device.*

Note that all the cells preparation processes were carried out under a biological safety cabinet (Delta 4; Euroflux), with all the instruments inside wiped by 70% ethanol beforehand. The commercial culture vessels were sterile and the home-made PDMS-glass microdevices were UV-sterilized for 20 min before cells introduction.

### III.4. Analytical measurements

#### In vitro ROS/RNS electrochemical detection

All *in vitro* electrochemical experiments inside microchannels were performed versus the Ag/AgCl REF at room temperature using a potentiostat (Autolab PGSTAT 30; Eco Chemie) controlled by GPES 4.9 software as shown in Figure Appendix-31. The flow was pressure-driven by syringe pump (Pump 11 Elite; Harvard Apparatus) at a constant average flow rate of  $2 \mu\text{L min}^{-1}$ , corresponding to a laminar flow regime in respect to the channel geometry. One exception was addressed in Part B-3.1.2, where a series of flow rate (0.1 to  $5 \mu\text{L min}^{-1}$ ) was applied to explore analytes oxidation mechanisms.

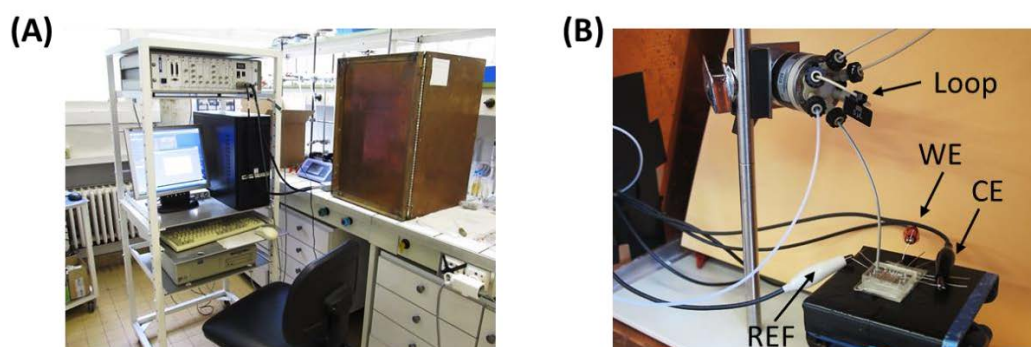


Figure Appendix-31: Experimental setup for ROS/RNS *in vitro* detection. (A) Electrochemical measurements were performed inside a Faraday cage, controlled by Autolab potentiostat. (B) Illustration of sample microinjection via a  $5 \mu\text{L}$  loop during measurements.

Before some electrochemical measurements, electrodes were activated by applying alternating potential pulses ( $+0.2 \text{ V/REF}$ , 1 s and  $-0.5 \text{ V/REF}$ , 1 s; 30 cycles) in flowing PBS. Analytes were introduced in microchannels in two ways, either as a continuous flow of solution or via microinjections of solution in a continuous PBS flow through a peek sample loop ( $5 \mu\text{L}$ ; Rheodyne). In the first case, voltammograms were recorded at a scan rate of  $10 \text{ mV s}^{-1}$ . In both cases, chronoamperometric measurements were performed under respective potentials in order to kinetically monitor current decay with time or to monitor steady-state current during the passage of specific analytes or mixtures above electrodes. The use of sample loop allowed an easy subtraction of the background current monitored before and after passage of sample plug.



Calibration curves were established from microinjections with various sample concentrations. Detection limits were calculated from independent tests (at least 10 tests) with samples in the nanomolar concentration range. For this evaluation, three times the standard deviation of the measurements and calibration slope were considered.

### Single-cell detection

The *ex vivo* experiments were performed at room temperature on the stage of inverted optical microscope (Observer-D1; Zeiss) inside a Faraday cage (Figure Appendix-32A). Just prior to the detection, culture medium was emptied from petri dish, replaced with 4 mL Locke's buffer after rinse. In the case of single-cell detection, a two-electrode setup (i.e., one SSCE reference electrode with one platinized (30  $\mu$ C Pt-black deposit) carbon-fiber working electrode; see Figure Appendix-32B) was adapted, since the detected current intensity was fairly small.

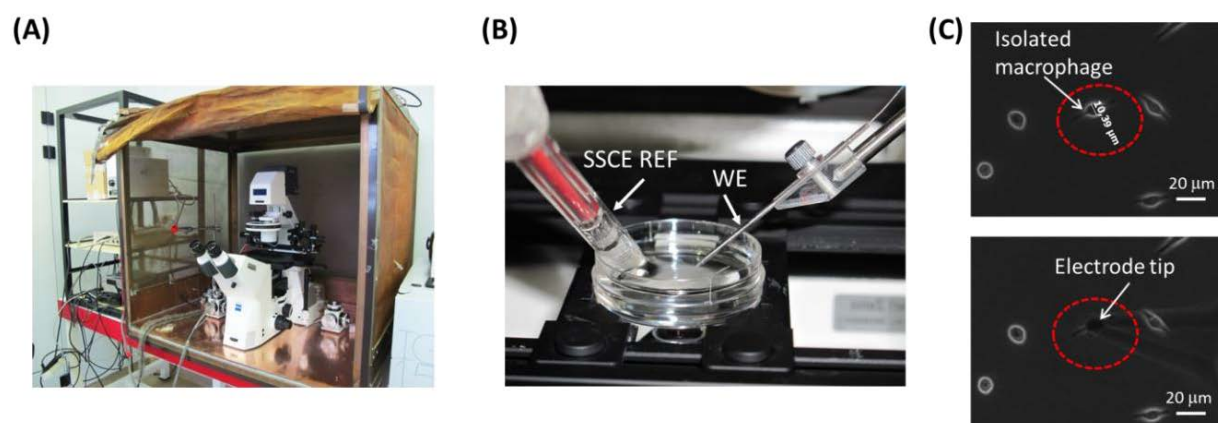


Figure Appendix-32: (A) Experiments performed at the platform of inverted microscope inside a Faraday cage. (B) Two-electrode configuration during single-cell monitoring. Position of working electrode was controlled by micromanipulator. (C) Optical images of isolated macrophages attached to petri dish (top image), and microelectrode placed above the target cell during measurement (bottom image).

Before detection, immobilized cells were checked under microscope and an isolated macrophage in good shape/brightness (Figure Appendix-32C, top image; captured by AxioVision imaging system) was selected as the detection target. The SSCE reference electrode was immersed in buffer solution without touching the bottom of petri dish. The platinized working electrode was primarily polarized in the upper buffer to obtain a stable current baseline, and then the fiber tip was precisely positioned by a three-axis micromanipulator (MHW-103; Narishige) at 1 – 2  $\mu$ m above this objective cell, with sensing surface covering the whole cell membrane (Figure Appendix-32C, bottom image).

40  $\mu\text{L}$  of A23187 (1 mM) was cautiously injected by a micropipette (Rainin manual Pipette) to the buffer solution (final concentration of 10  $\mu\text{M}$ ) to initiate cellular oxidative stress. Minute release of ROS/RNS from the single Raw 264.7 macrophage was detected in real time by amperometry (PRG-DEL Unite amperometric detector; Radiometer-Tacussel) at a constant potential. The time-course of amperometric current was monitored and stored on a computer (Latitude D600; Dell) through an analog-to-digital converter (Powerlab 4SP; ADInstruments) and its software interface (Chart version 4.2; ADInstruments). The decrease of the baseline current over the course of the measurement was fitted and subtracted by using the self-written exponential fit software (Gmef). Four selected potentials (0.30, 0.45, 0.65, and 0.85 V vs. SSCE [11,117-119,133,220,353]) were investigated, with at least 20 to 30 individual detections performed at each condition for statistical analysis.

### Cells population basal detection

Prior to experiments, the medium was aspirated from each uncovered chamber which was then rinsed and filled with Locke's buffer (150  $\mu\text{L}$ ). The morphology and density of immobilized cells were checked under microscope (Observer-D1; Zeiss); optical images were captured under 10 $\times$  or 20 $\times$  objective lens. Measurements were performed by using a multi-channel biopotentiostat (VSP-300; BioLogic; see Figure Appendix-33A) which could support four independent potentials at the same time. Each sensor group (Pt/Pt-black WE + Ag/AgCl REF + Pt CE confined in one chamber) was individually biased with one selected potential (Figure Appendix-33B). Before detection, the working electrodes were polarized for c.a. 1 minute at corresponding potential to stabilize background currents.

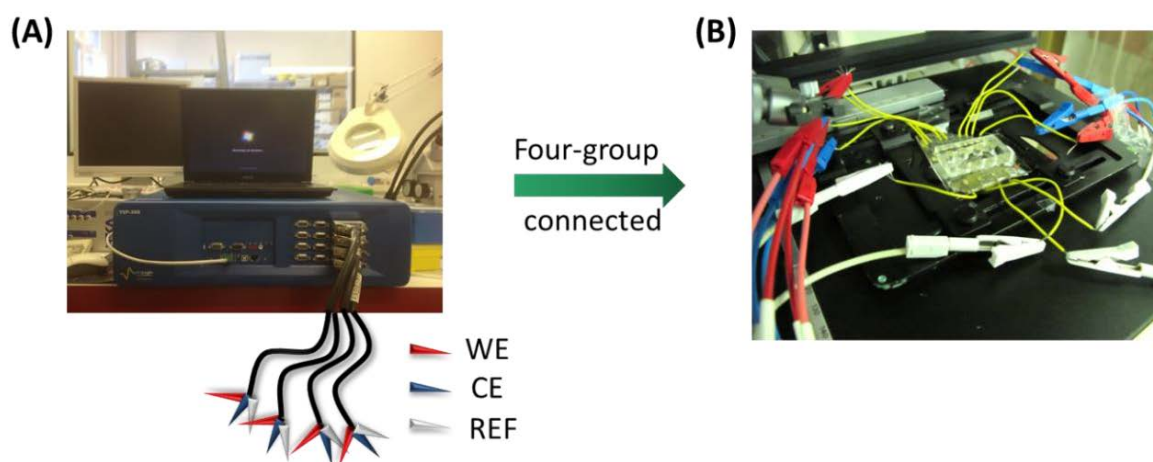


Figure Appendix-33: Experimental setup for cells population basal detection. (A) Multi-channel biopotentiostat which serves four independent potential outputs, with each output consisted of one WE (red tip), one CE (blue tip) and one REF (white tip). (B) Connections with the microdevice placed on the platform of inverted microscope inside a Faraday cage.



1.5  $\mu\text{L}$  A23187 stimulus (1 mM) was injected cautiously into each chamber (final concentration of 10  $\mu\text{M}$ ) and the real-time release of ROS/RNS from cells populations (c.a. 1200 macrophages above each working electrode) was detected simultaneously at 0.30, 0.45, 0.62, and 0.85 V vs. Ag/AgCl. These optimal potential values were chosen based on the *in vitro* voltammetric studies of the oxidation of independent solutions of  $\text{H}_2\text{O}_2$ ,  $\text{ONOO}^-$ ,  $\text{NO}^\bullet$  and  $\text{NO}_2^-$  reported on the same platinized microband electrodes in Part B. The time-courses of amperometric current were monitored and stored on a computer (Latitude E6410; Dell) through its software interface (EC-Lab V10.34; BioLogic). The decrease of the baseline current over the course of the measurement was fitted and subtracted by using the self-written program (Gmef). Three to five individual experiments were sufficient (when cells and sensors were both in good condition) for statistical analysis; each experiment simultaneously interpreted four key analytes released from c.a. 1200 cells.

#### Cells population downstream detection

In the downstream measurements, all the flow manipulations were driven by the syringe pump at a constant flow rate of 8  $\mu\text{L min}^{-1}$ , corresponding to a low shear stress of 0.5  $\text{dyn cm}^{-2}$  above immobilized cells in culture chamber and a tributary flow rate of 2  $\mu\text{L min}^{-1}$  in each downstream detection channel (four parallel channels behind one common culture chamber). This guaranteed the same hydrodynamic condition and calibration basis above microchannel working electrodes as reported in the *in vitro* studies (Part B).

Prior to experiments, the culture medium was replaced by pumping Locke's buffer into the microdevice. The morphology and density of immobilized macrophages were checked under microscope; and optical images were obtained with 10 $\times$  or 20 $\times$  objective lens. Measurements were conducted also by the multi-channel biopotentiostat (Figure Appendix-34). In each channel, the sequentially-localized Ag/AgCl REF, Pt/Pt-black WE and Pt CE were connected with one output system and applied with one particular constant potential (0.30, 0.45, 0.62, or 0.85 V vs. Ag/AgCl). Before detection, the WEs were activated by alternative potential pulses (+ 0.2 V/REF, 1 s; -0.5 V/REF, 1 s; 30 cycles) to relieve surface bio-fouling, and were subsequently polarized for 1 minute at corresponding potential to stabilize background currents.

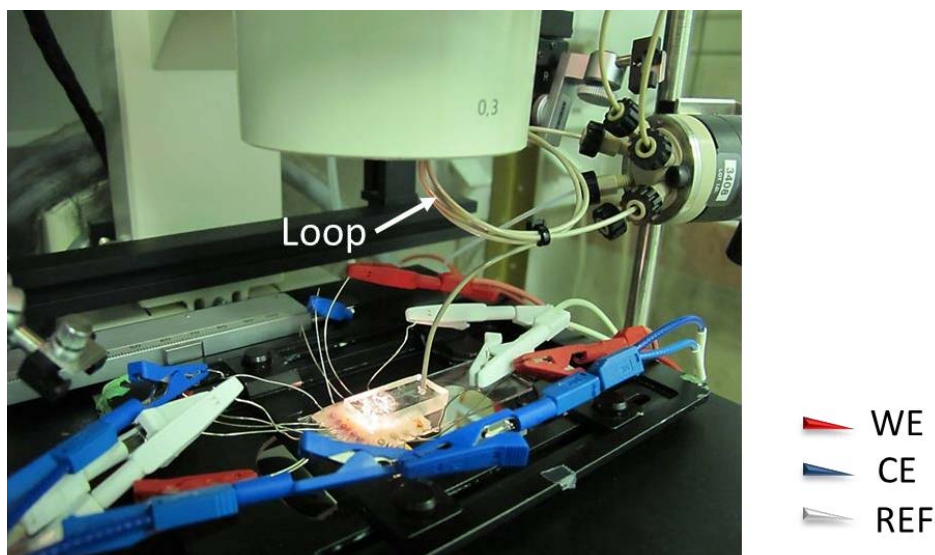


*Figure Appendix-34: Experimental setup for cells population downstream detection. The microchip was placed on the platform of inverted microscope inside a Faraday cage and was connected with multi-channel biopotentiostat which simultaneously supplied four individual outputting potentials. Flowing solution was controlled by syringe pump and the stimulus was delivered through a sample loop.*

The stimulating solution of 10  $\mu\text{M}$  A23187 (freshly prepared by adding appropriate aliquots of 1 mM A23187 stock solution into Locke's buffer) was introduced via microinjections in a continuous buffer flow through a peek sample loop (Rheodyne). For non-stop flow detection, a 100  $\mu\text{L}$  sample loop was adopted to supply adequate stimulus during the entire dynamic study of oxidative stress (c.a. 10 min). The semi real-time release of ROS/RNS from a large population of activated macrophages (c.a.  $3.5 \times 10^4$  cells) was simultaneously recorded at four independent microchannel sensors. On the other hand, for the 10-min stop flow detection, a small sample loop (5  $\mu\text{L}$ ) was used. The flow of stimulus was stopped after filling whole culture chamber (c.a. 2.5  $\mu\text{L}$  volume), and ROS/RNS emission was left accumulated around the cells-immobilized chamber. After 10-min stimulation, the static solution was pumped again at 8  $\mu\text{L min}^{-1}$ . The sample plug (ROS/RNS-containing) was branched to four parallel downstream channels and electrochemical responses were immediately detected during the sample passage.

The time-courses of amperometric current were monitored and stored on a computer (Latitude E6410; Dell) through its software interface (EC-Lab V10.34; BioLogic). The decrease of the baseline current over the course of the measurement was fitted and subtracted. Three to five individual experiments were sufficient (when cells and sensors were both in good condition) for statistical analysis; each experiment simultaneously interpreted four key analytes released from a large population of cells.

### Other analytical techniques

- Numerical simulations

The simulation formulation about species transport above the single microchannel band electrode is identical in the series of studies. The microchannel ( $w = 200 \mu\text{m}$  and  $h = 20 \mu\text{m}$ ) is considered to be filled continuously with a solution of electroactive species and electron transfers are supposed to be very fast. Thus the overall electrochemical reaction is controlled by mass transport under steady-state regime. Since the width of rectangular microchannel was much larger than its height, the diffusion and convection from mechanical transport reduced to a two-dimensional problem. Mass transport equation (Equation (B.6)) was solved numerically in 2D space at the steady-state regime using COMSOL Multiphysics 4.2 software in association with the classical boundary conditions mentioned in Part B-2.1.

The differential equation associated to the kinetic of  $\text{NO}^*$  release (Equation (B.35)) was also solved using COMSOL 4.2 software. A mathematical model based on least squares analysis of experimental kinetics was used to ensure optimal fit between experimental and calculated data. This model took into account predictions resulting from above simulations of mass transport regimes at channel microband electrodes.

- Ultraviolet-visible spectroscopy (UV-Vis)

Absorbance of peroxyxynitrite and DEA-NONOate solutions was performed at room temperature ( $22 \pm 1^\circ\text{C}$ ) using UV-Vis spectrophotometer (Lambda 45; Perkin Elmer). Absorbance was respectively monitored at  $\lambda = 302 \text{ nm}$  ( $\epsilon = 1670 \text{ M}^{-1} \text{ cm}^{-1}$ ) for peroxyxynitrite and  $\lambda = 250 \text{ nm}$ , ( $\epsilon = 6500 \text{ M}^{-1} \text{ cm}^{-1}$ ) for DEA-NONOate.



Figure Appendix-35: Lambda 45 UV-Vis system.

- Stylus profiler

The geometric dimensions (e.g., width and thickness) of: (i) microstructures such as microchannels or microchambers on silicon wafer, and (ii) Pt-black deposits on microband working electrodes were estimated by a Dektak XT stylus profiler (Bruker). Data was recorded and treated by Vision 64 software. A sub-nm resolution with high repeatability was possessed.



*Figure Appendix-36: The Bruker Dektak XT profilometer.*

- Scanning electron microscopy

The platinized Pt-black deposits were observed by SEM (S-800; Hitachi). All images were captured by using iXRF EDS2004 software and were subjected to particle analysis to determine average particles and clusters morphologies.



*Figure Appendix-37: Hitachi S-800 SEM.*



## *References*



## References

1. Bedard, K. and Krause, K.H., *Physiological Reviews*, **2007**. 87(1): p. 245-313.
2. Quinn, M.T., Ammons, M.C.B., and Deleo, F.R., *Clinical Science*, **2006**. 111(1): p. 1-20.
3. Vallance, P. and Leiper, J., *Nature Reviews Drug Discovery*, **2002**. 1(12): p. 939-950.
4. Bolisetty, S. and Jaimes, E.A., *International Journal of Molecular Sciences*, **2013**. 14(3): p. 6306-6344.
5. Amatore, C., Arbault, S., Guille, M., and Lemaitre, F., *Chemical Reviews*, **2008**. 108(7): p. 2585-2621.
6. Finaud, J., Lac, G., and Filaire, E., *Sports Medicine*, **2006**. 36(4): p. 327-358.
7. Hampton, M.B., Kettle, A.J., and Winterbourn, C.C., *Blood*, **1998**. 92(9): p. 3007-3017.
8. Lobachev, V.L. and Rudakov, E.S., *Uspekhi Khimii*, **2006**. 75(5): p. 422-444.
9. Pacher, P., Beckman, J.S., and Liaudet, L., *Physiological Reviews*, **2007**. 87(1): p. 315-424.
10. DeLeo, F.R., Allen, L.A.H., Apicella, M., and Nauseef, W.M., *Journal of Immunology*, **1999**. 163(12): p. 6732-6740.
11. Amatore, C., Arbault, S., Bouret, Y., Cauli, B., Guille, M., Rancillac, A., and Rossier, J., *Chemphyschem*, **2006**. 7(1): p. 181-187.
12. Rancillac, A., Rossier, J., Guille, M., Tong, X.K., Geoffroy, H., Amatore, C., Arbault, S., Hamel, E., and Cauli, B., *Journal of Neuroscience*, **2006**. 26(26): p. 6997-7006.
13. Furchgott, R.F., *Angewandte Chemie-International Edition*, **1999**. 38(13-14): p. 1870-1880.
14. Cifuentes, M.E. and Pagano, P.J., *Current Opinion in Nephrology and Hypertension*, **2006**. 15(2): p. 179-186.
15. Wood, J. and Garthwaite, J., *Neuropharmacology*, **1994**. 33(11): p. 1235-1244.
16. Eguchi, K., Nakanishi, S., Takagi, H., Taoufiq, Z., and Takahashi, T., *Neuron*, **2012**. 74(3): p. 517-529.
17. Wang, S. and Kasparov, S., *Faseb Journal*, **2005**. 19(5): p. A1679-A1679.
18. Valko, M., Leibfritz, D., Moncol, J., Cronin, M.T.D., Mazur, M., and Telser, J., *International Journal of Biochemistry & Cell Biology*, **2007**. 39(1): p. 44-84.
19. Thannickal, V.J. and Fanburg, B.L., *American Journal of Physiology-Lung Cellular and Molecular Physiology*, **2000**. 279(6): p. L1005-L1028.
20. Pycnogenol, <http://www.flavogard.com/Right%20side%20menu/cardiovascular.htm>.



21. Popolo, A., Autore, G., Pinto, A., and Marzocco, S., *Free Radical Research*, **2013**. 47(5): p. 346-356.
22. Del Hoyo, P., Garcia-Redondo, A., de Bustos, F., Molina, J.A., Sayed, Y., Alonso-Navarro, H., Caballero, L., Arenas, J., Agundez, J.A.G., and Jimenez-Jimenez, F.J., *Bmc Neurology*, **2010**. 10.
23. Cruz-Guilloty, F. and Perez, V.L., *Nature*, **2011**. 478(7367): p. 42-44.
24. Cheeseman, K.H. and Slater, T.F., *British Medical Bulletin*, **1993**. 49(3): p. 481-493.
25. David, E., Volk, *Citizendium*, **2009**.
26. Alvarez, B. and Radi, R., *Amino Acids*, **2003**. 25(3-4): p. 295-311.
27. Andrekopoulos, C., Zhang, H., Joseph, J., Kalivendi, S., and Kalyanaraman, B., *Biochemical Journal*, **2004**. 378: p. 435-447.
28. Szweda, P.A., Friguier, B., and Szweda, L.I., *Free Radical Biology and Medicine*, **2002**. 33(1): p. 29-36.
29. Hoeijmakers, J.H.J., *New England Journal of Medicine*, **2009**. 361(15): p. 1475-1485.
30. Winterbourn, C.C., *Biochimica et Biophysica Acta-General Subjects*, **2014**. 1840(2): p. 730-738.
31. Burns, J.M., Cooper, W.J., Ferry, J.L., King, D.W., DiMento, B.P., McNeill, K., Miller, C.J., Miller, W.L., Peake, B.M., Rusak, S.A., Rose, A.L., and Waite, T.D., *Aquatic Sciences*, **2012**. 74(4): p. 683-734.
32. Crow, J.P., *Nitric Oxide-Biology and Chemistry*, **1997**. 1(2): p. 145-157.
33. Gomes, A., Fernandes, E., and Lima, J.L.F.C., *Journal of Biochemical and Biophysical Methods*, **2005**. 65(2-3): p. 45-80.
34. Carvalho, H., Sellergren, A., Murray, L.C., and Pittman, R.N., *Faseb Journal*, **2006**. 20(4): p. A698-A698.
35. Cai, H., Dikalov, S., Griendling, K.K., and Harrison, D.G., *Methods Mol Med*, **2007**. 139: p. 293-311.
36. Setsukinai, K., Urano, Y., Kakinuma, K., Majima, H.J., and Nagano, T., *Journal of Biological Chemistry*, **2003**. 278(5): p. 3170-3175.
37. Mishina, N.M., Tyurin-Kuzmin, P.A., Markvicheva, K.N., Vorotnikov, A.V., Tkachuk, V.A., Laketa, V., Schultz, C., Lukyanov, S., and Belousov, V.V., *Antioxidants & Redox Signaling*, **2011**. 14(1): p. 1-7.
38. Shinohara, H., Wang, F., and Hossain, S.M., *Nat Protoc*, **2008**. 3(10): p. 1639-44.
39. Mesaros, S., Vankova, Z., Mesarosova, A., Tomcik, P., and Grunfeld, S., *Bioelectrochemistry and Bioenergetics*, **1998**. 46(1): p. 33-37.
40. Halliwell, B. and Whiteman, M., *Br J Pharmacol*, **2004**. 142(2): p. 231-55.

41. Hetrick, E.M. and Schoenfish, M.H., *Annual Review of Analytical Chemistry*, **2009**. 2: p. 409-433.
42. Kohno, M., *Journal of Clinical Biochemistry and Nutrition*, **2010**. 47(1): p. 1-11.
43. Petrucci, H.A., *General Chemistry: Chapter 7 Atomic Structure*, **1995-2002**. 7.29.
44. Chen, Y.R., *Methods Mol Biol*, **2008**. 477: p. 75-88.
45. Rodriguez-Rodriguez, R. and Simonsen, U., *Current Analytical Chemistry*, **2012**. 8(4): p. 485-494.
46. Bohle, D.S., Hansert, B., Paulson, S.C., and Smith, B.D., *Journal of the American Chemical Society*, **1994**. 116(16): p. 7423-7424.
47. Quinton, D., Griveau, S., and Bedioui, F., *Electrochemistry Communications*, **2010**. 12(10): p. 1446-1449.
48. Coneski, P.N. and Schoenfish, M.H., *Chemical Society Reviews*, **2012**. 41(10): p. 3753-3758.
49. Maria, H. and Magdalena, S., *New Perspectives in Biosensors Technology and Applications, Biomedical Engineering*. Edited by Pier Andrea Serra, **2011**: p. 343-372.
50. Kumar, S., Rhim, W.K., Lim, D.K., and Nam, J.M., *Acs Nano*, **2013**. 7(3): p. 2221-2230.
51. Dalle-Donne, I., Rossi, R., Colombo, R., Giustarini, D., and Milzani, A., *Clinical Chemistry*, **2006**. 52(4): p. 601-623.
52. Bedioui, F., Quinton, D., Griveau, S., and Nyokong, T., *Physical Chemistry Chemical Physics*, **2010**. 12(34): p. 9976-9988.
53. Griveau, S. and Bedioui, F., *Analytical and Bioanalytical Chemistry*, **2013**. 405(11): p. 3475-3488.
54. Privett, B.J., Shin, J.H., and Schoenfish, M.H., *Chemical Society Reviews*, **2010**. 39(6): p. 1925-1935.
55. McNeil, C.J., Greenough, K.R., Weeks, P.A., Self, C.H., and Cooper, J.M., *Free Radical Research Communications*, **1992**. 17(6): p. 399-406.
56. Mesaros, S., Vankova, Z., Grunfeld, S., Mesarosova, A., and Malinski, T., *Analytica Chimica Acta*, **1998**. 358(1): p. 27-33.
57. Privat, C., Stepien, O., David-Duflho, M., Brunet, A., Bedioui, F., Marche, P., Devynck, J., and Devynck, M.A., *Free Radical Biology and Medicine*, **1999**. 27(5-6): p. 554-559.
58. Campanella, L., Favero, G., Occhionero, E., and Tomassetti, M., *Analisis*, **1998**. 26(5): p. 223-228.
59. Green, M.J., Hill, H.A.O., Tew, D.G., and Walton, N.J., *Febs Letters*, **1984**. 170(1): p. 69-72.
60. Manning, P., McNeil, C.J., Cooper, J.M., and Hillhouse, E.W., *Free Radical Biology and Medicine*, **1998**. 24(7-8): p. 1304-1309.

61. Cooper, J.M., Thompson, G., and Mcneil, C.J., *Molecular Crystals and Liquid Crystals Science and Technology Section a-Molecular Crystals and Liquid Crystals*, **1993**. 234: p. 409-414.
62. Datta, H.K., Rathod, H., Manning, P., Turnbull, Y., and McNeil, C.J., *Journal of Endocrinology*, **1996**. 149(2): p. 269-275.
63. Descroix, S. and Bedioui, F., *Electroanalysis*, **2001**. 13(7): p. 524-528.
64. Song, M.I., Bier, F.F., and Scheller, F.W., *Bioelectrochemistry and Bioenergetics*, **1995**. 38(2): p. 419-422.
65. Meunier, A., *Méthodes analytiques pour la détection de phénomènes biologiques de sécrétion à l'échelle de la cellule unique*. Thèse de doctorat UPMC, **2011**: p. 166-167.
66. Chen, W., Cai, S., Ren, Q.Q., Wen, W., and Zhao, Y.D., *Analyst*, **2012**. 137(1): p. 49-58.
67. Peng, H.P., Liang, R.P., and Qiu, J.D., *Biosensors & Bioelectronics*, **2011**. 26(6): p. 3005-3011.
68. Wu, Y.H., Shen, Q.C., and Hu, S.S., *Analytica Chimica Acta*, **2006**. 558(1-2): p. 179-186.
69. Li, S.Q., Xia, J., Liu, C.Y., Cao, W., Hu, J.B., and Li, Q.L., *Journal of Electroanalytical Chemistry*, **2009**. 633(2): p. 273-278.
70. Wu, F.H., Xu, J.J., Tian, Y., Hu, Z.C., Wang, L.W., Xian, Y.Z., and Jin, L.T., *Biosensors & Bioelectronics*, **2008**. 24(2): p. 198-203.
71. Salimi, A., Miranzadeh, L., Hallaj, R., and Mamkhezri, H., *Electroanalysis*, **2008**. 20(16): p. 1760-1768.
72. Li, Z.F., Chen, J.H., Li, W., Chen, K., Nie, L.H., and Yao, S.Z., *Journal of Electroanalytical Chemistry*, **2007**. 603(1): p. 59-66.
73. Liu, S.Q., Xu, J.J., and Chen, H.Y., *Electrochemistry Communications*, **2002**. 4(5): p. 421-425.
74. Scandurra, G., Arena, A., Ciofi, C., and Saitta, G., *Sensors*, **2013**. 13(3): p. 3878-3888.
75. Arbault, S., Pantano, P., Jankowski, J.A., Vuillaume, M., and Amatore, C., *Analytical Chemistry*, **1995**. 67(19): p. 3382-3390.
76. Arbault, S., Pantano, P., Sojic, N., Amatore, C., BestBelpomme, M., Sarasin, A., and Vuillaume, M., *Carcinogenesis*, **1997**. 18(3): p. 569-574.
77. de Boer, J. and Hoeijmakers, J.H.J., *Carcinogenesis*, **2000**. 21(3): p. 453-460.
78. Ben-Amor, S., Devin, A., Rigoulet, M., Sojic, N., and Arbault, S., *Electroanalysis*, **2013**. 25(3): p. 656-663.
79. Amatore, C., Arbault, S., Bruce, D., de Oliveira, P., Erard, M., Sojic, N., and Vuillaume, M., *Analisis*, **2000**. 28(6): p. 506-517.
80. Qiang, L., Vaddiraju, S., Rusling, J.F., and Papadimitrakopoulos, F., *Biosensors and Bioelectronics*, **2010**. 26(2): p. 682-688.
81. Kicela, A. and Daniele, S., *Talanta*, **2006**. 68(5): p. 1632-1639.

82. Bedioui, F. and Villeneuve, N., *Electroanalysis*, **2003**. 15(1): p. 5-18.
83. Meulemans, A., *Neuroscience Letters*, **1993**. 157(1): p. 7-12.
84. Shibuki, K. and Okada, D., *Nature*, **1991**. 349(6307): p. 326-328.
85. Ferreira, N.R., Ledo, A., Frade, J.G., Gerhardt, G.A., Laranjinha, J., and Barbosa, R.M., *Analytica Chimica Acta*, **2005**. 535(1-2): p. 1-7.
86. Bedioui, F., Trevin, S., and Devynck, J., *Journal of Electroanalytical Chemistry*, **1994**. 377(1-2): p. 295-298.
87. Prakash, R., Srivastava, R.C., and Seth, P.K., *Polymer Bulletin*, **2001**. 46(6): p. 487-490.
88. Kitamura, Y., Uzawa, T., Oka, K., Komai, Y., Ogawa, H., Takizawa, N., Kobayashi, H., and Tanishita, K., *Analytical Chemistry*, **2000**. 72(13): p. 2957-2962.
89. Cooley, S. and Antal, M.J., *Journal of Analytical and Applied Pyrolysis*, **1988**. 14(2-3): p. 149-161.
90. Santos, R.M., Lourenco, C.F., Piedade, A.P., Andrews, R., Pomerleau, F., Huettl, P., Gerhardt, G.A., Laranjinha, J., and Barbosa, R.M., *Biosensors & Bioelectronics*, **2008**. 24(4): p. 704-709.
91. Pinsky, D.J., Patton, S., Mesaros, S., Brovkovich, V., Kubaszewski, E., Grunfeld, S., and Malinski, T., *Circulation Research*, **1997**. 81(3): p. 372-379.
92. Vilakazi, S.L. and Nyokong, T., *Journal of Electroanalytical Chemistry*, **2001**. 512(1-2): p. 56-63.
93. Diab, N. and Schuhmann, W., *Electrochimica Acta*, **2001**. 47(1-2): p. 265-273.
94. Isik, S., Oni, J., Rjabova, V., Neugebauer, S., and Schuhmann, W., *Microchimica Acta*, **2004**. 148(1-2): p. 59-64.
95. Pontie, M., Gobin, C., Pauporte, T., Bedioui, F., and Devynck, J., *Analytica Chimica Acta*, **2000**. 411(1-2): p. 175-185.
96. Pereira-Rodrigues, N., Albin, V., Koudelka-Hep, M., Auger, V., Pailleret, A., and Bedioui, F., *Electrochemistry Communications*, **2002**. 4(11): p. 922-927.
97. Wartelle, C., Rodrigues, N.P., Koudelka-Hep, M., and Bedioui, F., *Materials Science & Engineering C-Biomimetic and Supramolecular Systems*, **2006**. 26(2-3): p. 534-537.
98. Malinski, T. and Taha, Z., *Nature*, **1992**. 358(6388): p. 676-678.
99. Fabre, B., Burlet, S., Cespuglio, R., and Bidan, G., *Journal of Electroanalytical Chemistry*, **1997**. 426(1-2): p. 75-83.
100. Wartelle, C., Schuhmann, W., Blochl, A., and Bedioui, F., *Electrochimica Acta*, **2005**. 50(25-26): p. 4988-4994.
101. Park, S.S., Kim, J., and Lee, Y., *Analytical Chemistry*, **2012**. 84(3): p. 1792-1796.
102. Hulvey, M.K., Frankenfeld, C.N., and Lunte, S.M., *Analytical Chemistry*, **2010**. 82(5): p. 1608-1611.

103. Zakharova, E.A., Yurmazova, T.A., Nazarov, B.F., Wildgoose, G.G., and Compton, R.G., *New Journal of Chemistry*, **2007**. 31(3): p. 394-400.
104. Xue, J., Ying, X.Y., Chen, J.S., Xian, Y.H., Jin, L.T., and Jin, J., *Analytical Chemistry*, **2000**. 72(21): p. 5313-5321.
105. Peteu, S., Peiris, P., Gebremichael, E., and Bayachou, M., *Biosensors & Bioelectronics*, **2010**. 25(8): p. 1914-1921.
106. Cortes, J.S., Granados, S.G., Ordaz, A.A., Jimenez, J.A.L., Griveau, S., and Bedioui, F., *Electroanalysis*, **2007**. 19(1): p. 61-64.
107. Koh, W.C.A., Son, J.I., Choe, E.S., and Shim, Y.B., *Analytical Chemistry*, **2010**. 82(24): p. 10075-10082.
108. Wang, Y. and Chen, Z.Z., *Talanta*, **2010**. 82(2): p. 534-539.
109. Amatore, C., Arbault, S., Bruce, D., de Oliveira, P., Erard, M., and Vuillaume, M., *Chemistry-a European Journal*, **2001**. 7(19): p. 4171-4179.
110. Kozub, B.R., Rees, N.V., and Compton, R.G., *Sensors and Actuators B: Chemical*, **2010**. 143(2): p. 539-546.
111. Pietrzak, M. and Meyerhoff, M.E., *Analytical Chemistry*, **2009**. 81(9): p. 3637-3644.
112. Santos, W.J.R., Lima, P.R., Tanaka, A.A., Tanaka, S.M.C.N., and Kubota, L.T., *Food Chemistry*, **2009**. 113(4): p. 1206-1211.
113. Trofimova, N.S., Safronov, A.Y., and Ikeda, O., *Electrochimica Acta*, **2005**. 50(24): p. 4637-4644.
114. Armijo, F., Goya, M.C., Reina, M., Canales, M.J., Arévalo, M.C., and Aguirre, M.J., *Journal of Molecular Catalysis A: Chemical*, **2007**. 268(1-2): p. 148-154.
115. Ye, D.X., Luo, L.Q., Ding, Y.P., Chen, Q., and Liu, X., *Analyst*, **2011**. 136(21): p. 4563-4569.
116. Liu, T.S., Kang, T.F., Lu, L.P., Zhang, Y., and Cheng, S.Y., *Journal of Electroanalytical Chemistry*, **2009**. 632(1-2): p. 197-200.
117. Amatore, C., Arbault, S., Bruce, D., de Oliveira, P., Erard, M., and Vuillaume, M., *Faraday Discussions*, **2000**. 116: p. 319-333.
118. Amatore, C., Arbault, S., Bouton, C., Coffi, K., Drapier, J.C., Ghandour, H., and Tong, Y.H., *Chembiochem*, **2006**. 7(4): p. 653-661.
119. Amatore, C., Arbault, S., Jaouen, G., Koh, A.C.W., Leong, W.K., Top, S., Valleron, M.A., and Woo, C.H., *Chemmedchem*, **2010**. 5(2): p. 296-301.
120. Gardening Studio, **2013**, <http://gardeningstudio.com/animal-and-plant-cells/>.
121. Bery, M.N. and Grivell, M.B., *Bioelectrochemistry of Cells and Tissues*, **1995**: p. 134-158.
122. Lempka, S.F., Johnson, M.D., Moffitt, M.A., Otto, K.J., Kipke, D.R., and McIntyre, C.C., *Journal of Neural Engineering*, **2011**. 8(4).

123. Santhiago, M., Wydallis, J.B., Kubota, L.T., and Henry, C.S., *Analytical Chemistry*, **2013**. 85(10): p. 5233-5239.
124. Lin, S.P., Chen, J.J.J., Liao, J.D., and Tzeng, S.F., *Biomedical Microdevices*, **2008**. 10(1): p. 99-111.
125. Lavacchi, A., Bardi, U., Borri, C., Caporali, S., Fossati, A., and Perissi, I., *Journal of Applied Electrochemistry*, **2009**. 39(11): p. 2159-2163.
126. Wei, D., Bailey, M.J.A., Andrew, P., and Ryhanen, T., *Lab on a Chip*, **2009**. 9(15): p. 2123-2131.
127. Senthamarai, R. and Rajendran, L., *Electrochimica Acta*, **2008**. 53(10): p. 3566-3578.
128. Wu, W.Z., Huang, W.H., Wang, W., Wang, Z.L., Cheng, J.K., Xu, T., Zhang, R.Y., Chen, Y., and Liut, J., *Journal of the American Chemical Society*, **2005**. 127(25): p. 8914-8915.
129. Wang, W., Zhang, S.H., Li, L.M., Wang, Z.L., Cheng, J.K., and Huang, W.H., *Analytical and Bioanalytical Chemistry*, **2009**. 394(1): p. 17-32.
130. Wang, Y.X., Noel, J.M., Velmurugan, J., Nogala, W., Mirkin, M.V., Lu, C., Guille-Collignon, M., Lemaitre, F., and Amatore, C., *Proceedings of the National Academy of Sciences of the United States of America*, **2012**. 109(29): p. 11534-11539.
131. Wang, W., Xiong, Y., Du, F.Y., Huang, W.H., Wu, W.Z., Wang, Z.L., Cheng, J.K., Yang, Y.F., and Yang, Y.F., *Analyst*, **2007**. 132(6): p. 515-518.
132. Buckley, C., *UConn Today, Science&Health*, **2010**. University of Connecticut, <http://today.uconn.edu/blog/2010/07/understanding-balance-in-the-nervous-system/>.
133. Amatore, C., Arbault, S., and Koh, A.C.W., *Analytical Chemistry*, **2010**. 82(4): p. 1411-1419.
134. Lin, Y.Q., Trouillon, R., Svensson, M.I., Keighron, J.D., Cans, A.S., and Ewing, A.G., *Analytical Chemistry*, **2012**. 84(6): p. 2949-2954.
135. Hwang, S., LaFratta, C.N., Agarwal, V., Yu, X., Walt, D.R., and Sonkusale, S., *Ieee Sensors Journal*, **2009**. 9(5-6): p. 609-615.
136. Rajaraman, S., Choi, S.O., Shafer, R.H., Ross, J.D., Vukasinovic, J., Choi, Y., DeWeerth, S.P., Glezer, A., and Allen, M.G., *Journal of Micromechanics and Microengineering*, **2007**. 17(1): p. 163-171.
137. Hafez, I., Kisler, K., Berberian, K., Dernick, G., Valero, V., Yong, M.G., Craighead, H.G., and Lindau, M., *Proceedings of the National Academy of Sciences of the United States of America*, **2005**. 102(39): p. 13879-13884.
138. Samseya, J., Srinivasan, R., Chang, Y.T., Tsao, C.W., and Vasantha, V.S., *Analytica Chimica Acta*, **2013**. 793: p. 11-18.
139. Le, H.P., *Journal of Imaging Science and Technology*, **1998**. 42(1): p. 49-62.
140. Terry, S.C., Jerman, J.H., and Angell, J.B., *Ieee Transactions on Electron Devices*, **1979**. 26(12): p. 1880-1886.
141. Manz, A., Miyahara, Y., Miura, J., Watanabe, Y., Miyagi, H., and Sato, K., *Sensors and Actuators B-Chemical*, **1990**. 1(1-6): p. 249-255.

142. Deng, T., Wu, H.K., Brittain, S.T., and Whitesides, G.M., *Analytical Chemistry*, **2000**. 72(14): p. 3176-3180.
143. Boehm, D.A., Gottlieb, P.A., and Hua, S.Z., *Sensors and Actuators B-Chemical*, **2007**. 126(2): p. 508-514.
144. Mark, D., Haerberle, S., Roth, G., von Stetten, F., and Zengerle, R., *Chemical Society Reviews*, **2010**. 39(3): p. 1153-1182.
145. Linder, V., *Analyst*, **2007**. 132(12): p. 1186-1192.
146. Dittrich, P.S. and Manz, A., *Nature Reviews Drug Discovery*, **2006**. 5(3): p. 210-218.
147. Sun, J., Chen, P., Feng, X.J., Du, W., and Liu, B.F., *Biosensors & Bioelectronics*, **2011**. 26(8): p. 3413-3419.
148. Vannoy, C.H., Tavares, A.J., Noor, M.O., Uddayasankar, U., and Krull, U.J., *Sensors*, **2011**. 11(10): p. 9732-9763.
149. Xu, Z.Y., Gao, Y.H., Hao, Y.Y., Li, E.C., Wang, Y., Zhang, J.N., Wang, W.X., Gao, Z.C., and Wang, Q., *Biomaterials*, **2013**. 34(16): p. 4109-4117.
150. El Debs, B., Utharala, R., Balyasnikova, I.V., Griffiths, A.D., and Merten, C.A., *Proceedings of the National Academy of Sciences of the United States of America*, **2012**. 109(29): p. 11570-11575.
151. Gong, Z.C., Zhao, H., Zhang, T.H., Nie, F., Pathak, P., Cui, K.M., Wang, Z.Y., Wong, S., and Que, L., *Biomedical Microdevices*, **2011**. 13(1): p. 215-219.
152. Alrifaiy, A., Lindahl, O.A., and Ramser, K., *Polymers*, **2012**. 4(3): p. 1349-1398.
153. Chung, B.G., Lee, K.H., Khademhosseini, A., and Lee, S.H., *Lab on a Chip*, **2012**. 12(1): p. 45-59.
154. Liong, M., Hoang, A.N., Chung, J., Gural, N., Ford, C.B., Min, C., Shah, R.R., Ahmad, R., Fernandez-Suarez, M., Fortune, S.M., Toner, M., Lee, H., and Weissleder, R., *Nature Communications*, **2013**. 4.
155. Chikkaveeraiah, B.V., Bhirde, A.A., Morgan, N.Y., Eden, H.S., and Chen, X.Y., *Acs Nano*, **2012**. 6(8): p. 6546-6561.
156. Zhang, C. and van Noort, D., *Microfluidics: Technologies and Applications*, **2011**. 304: p. 295-321.
157. Sardesai, N.P., Kadimisetty, K., Faria, R., and Rusling, J.F., *Analytical and Bioanalytical Chemistry*, **2013**. 405(11): p. 3831-3838.
158. Mu, X., Zheng, W.F., Sun, J.S., Zhang, W., and Jiang, X.Y., *Small*, **2013**. 9(1): p. 9-21.
159. Pifferi, M., Bush, A., Montemurro, F., Pioggia, G., Piras, M., Tartarisco, G., Di Cicco, M., Chinellato, I., Cangiotti, A.M., and Boner, A.L., *European Respiratory Journal*, **2013**. 41(4): p. 960-965.
160. Athavale, M.A., Maitra, A., Patel, S., Bhate, V.R., and Toddywalla, V.S., *Indian Journal of Pharmacology*, **2013**. 45(4): p. 325-329.

161. Pompe, T., Keller, K., Mitdank, C., and Werner, C., *European Biophysics Journal with Biophysics Letters*, **2005**. 34(8): p. 1049-1056.
162. Murakami, T., *Analytica Chimica Acta*, **2000**. 415(1-2): p. 201-207.
163. Clemence, J.F., Ranieri, J.P., Aebischer, P., and Sigrist, H., *Bioconjugate Chemistry*, **1995**. 6(4): p. 411-417.
164. Kobayashi, J. and Rabinovitch, M., *Circulation*, **1993**. 88(4): p. 285-285.
165. Bettinger, C.J. and Borenstein, J.T., *Soft Matter*, **2010**. 6(20): p. 4999-5015.
166. Matthias, M. and Savas, T., *Current Opinion in Biotechnology*, **2014**. 25: p. 95-102.
167. Khademhosseini, A., Suh, K.Y., Jon, S., Eng, G., Yeh, J., Chen, G.J., and Langer, R., *Analytical Chemistry*, **2004**. 76(13): p. 3675-3681.
168. Solanki, A., Shah, S., Memoli, K.A., Park, S.Y., Hong, S., and Lee, K.B., *Small*, **2010**. 6(22): p. 2509-2513.
169. Yellow Tang Moodle, Available Images and Animations: Cell Unit, Extracellular matrix, [http://www.yellowtang.org/images/extracellular\\_matri\\_c\\_la\\_784.jpg](http://www.yellowtang.org/images/extracellular_matri_c_la_784.jpg).
170. Kim, L., Toh, Y.C., Voldman, J., and Yu, H., *Lab on a Chip*, **2007**. 7(6): p. 681-694.
171. Yeon, J.H. and Park, J.K., *Biochip Journal*, **2007**. 1(1): p. 17-27.
172. Wells, L. and Sheardown, H., *Investigative Ophthalmology & Visual Science*, **2005**. 46.
173. Hu, X.X., Shen, H., Yang, F., Bei, J.Z., and Wang, S.G., *Biomaterials*, **2008**. 29(21): p. 3128-3136.
174. Liu, B., Xu, F., Guo, M.Y., Chen, S.F., Wang, J., and Zhang, B., *Surface & Coatings Technology*, **2013**. 228: p. S568-S573.
175. Occhetta, P., Sadr, N., Piraino, F., Redaelli, A., Moretti, M., and Rasponi, M., *Biofabrication*, **2013**. 5(3).
176. Leclerc, E., Sakai, Y., and Fujii, T., *Biomedical Microdevices*, **2003**. 5(2): p. 109-114.
177. Schimek, K., Busek, M., Brincker, S., Groth, B., Hoffmann, S., Lauster, R., Lindner, G., Lorenz, A., Menzel, U., Sonntag, F., Walles, H., Marx, U., and Horland, R., *Lab on a Chip*, **2013**. 13(18): p. 3588-3598.
178. Hung, P.J., Lee, P.J., Sabounchi, P., Lin, R., and Lee, L.P., *Biotechnology and Bioengineering*, **2005**. 89(1): p. 1-8.
179. Meyvantsson, I. and Beebe, D.J., *Annual Review of Analytical Chemistry*, **2008**. 1: p. 423-449.
180. Hosmane, S., Yang, I.H., Ruffin, A., Thakor, N., and Venkatesan, A., *Lab on a Chip*, **2010**. 10(6): p. 741-747.
181. Yun, H., Kim, K., and Lee, W.G., *Biofabrication*, **2013**. 5(2).



182. Wu, T.H., Chen, Y., Park, S.Y., Hong, J., Teslaa, T., Zhong, J.F., Di Carlo, D., Teitell, M.A., and Chiou, P.Y., 2012 Ieee 25th International Conference on Micro Electro Mechanical Systems (Mems), **2012**.
183. Bambardekar, K., Dharmadhikari, A.K., Dharmadhikari, J.A., Mathur, D., and Sharma, S., Journal of Biomedical Optics, **2008**. 13(6).
184. Hoshino, K., Huang, Y.Y., Lane, N., Huebschman, M., Uhr, J.W., Frenkel, E.P., and Zhang, X.J., Lab on a Chip, **2011**. 11(20): p. 3449-3457.
185. Kang, J.H., Krause, S., Tobin, H., Mammoto, A., Kanapathipillai, M., and Ingber, D.E., Lab on a Chip, **2012**. 12(12): p. 2175-2181.
186. Gossett, D.R., Weaver, W.M., Mach, A.J., Hur, S.C., Tse, H.T.K., Lee, W., Amini, H., and Di Carlo, D., Analytical and Bioanalytical Chemistry, **2010**. 397(8): p. 3249-3267.
187. Aucoin, C.P., Nanne, E.E., and Leonard, E.F., Asaio Journal, **2009**. 55(5): p. 423-427.
188. Ji, H.M., Samper, V., Chen, Y., Heng, C.K., Lim, T.M., and Yobas, L., Biomedical Microdevices, **2008**. 10(2): p. 251-257.
189. Gu, S.Q., Zhang, Y.X., Zhu, Y., Du, W.B., Yao, B., and Fang, Q., Analytical Chemistry, **2011**. 83(19): p. 7570-7576.
190. Petersson, F., Aberg, L., Sward-Nilsson, A.M., and Laurell, T., Analytical Chemistry, **2007**. 79(14): p. 5117-5123.
191. Bose, S., Singh, R., Hanewich-Hollatz, M., Shen, C., Lee, C.H., Dorfman, D.M., Karp, J.M., and Karnik, R., Scientific Reports, **2013**. 3.
192. Tay, S., Hughey, J.J., Lee, T.K., Lipniacki, T., Quake, S.R., and Covert, M.W., Nature, **2010**. 466(7303): p. 267-U149.
193. Han, Q., Bagheri, N., Bradshaw, E.M., Hafler, D.A., Lauffenburger, D.A., and Love, J.C., Proceedings of the National Academy of Sciences of the United States of America, **2012**. 109(5): p. 1607-1612.
194. Zheng, W.F., Xie, Y.Y., Zhang, W., Wang, D., Ma, W.S., Wang, Z., and Jiang, X.Y., Integrative Biology, **2012**. 4(9): p. 1102-1111.
195. Vedel, S., Tay, S., Johnston, D.M., Bruus, H., and Quake, S.R., Proceedings of the National Academy of Sciences of the United States of America, **2013**. 110(1): p. 129-134.
196. Bao, X.R., Fraser, I.D., Wall, E.A., Quake, S.R., and Simon, M.I., Biophys J, **2010**. 99(8): p. 2414-22.
197. Spegel, C., Heiskanen, A., Acklid, J., Wolff, A., Taboryski, R., Emneus, J., and Ruzgas, T., Electroanalysis, **2007**. 19(2-3): p. 263-271.
198. Cui, H.F., Ye, J.S., Chen, Y., Chong, S.C., Liu, X., Lim, T.M., and Sheu, F.S., Sensors and Actuators B-Chemical, **2006**. 115(2): p. 634-641.
199. Asphahani, F., Wang, K., Thein, M., Veiseh, O., Yung, S., Xu, J.A., and Zhang, M.Q., Physical Biology, **2011**. 8(1).

200. Amatore, C., Arbault, S., Chen, Y., Crozatier, C., and Tapsoba, I., *Lab on a Chip*, **2007**. 7(2): p. 233-238.
201. Cui, H.F., Ye, J.S., Chen, Y., Chong, S.C., and Sheu, F.S., *Analytical Chemistry*, **2006**. 78(18): p. 6347-6355.
202. Quinton, D., Girard, A., Kim, L.T.T., Raimbault, V., Griscom, L., Razan, F., Griveau, S., and Bedioui, F., *Lab on a Chip*, **2011**. 11(7): p. 1342-1350.
203. Meunier, A., Jouannot, O., Fulcrand, R., Fanget, I., Bretou, M., Karatekin, E., Arbault, S., Guille, M., Darchen, F., Lemaitre, F., and Amatore, C., *Angewandte Chemie-International Edition*, **2011**. 50(22): p. 5081-5084.
204. Li, L.M., Wang, W., Zhang, S.H., Chen, S.J., Guo, S.S., Francais, O., Cheng, J.K., and Huang, W.H., *Analytical Chemistry*, **2011**. 83(24): p. 9524-9530.
205. Kane, B.J., Zinner, M.J., Yarmush, M.L., and Toner, M., *Analytical Chemistry*, **2006**. 78(13): p. 4291-4298.
206. Goto, M., Sato, K., Murakami, A., Tokeshi, M., and Kitamori, T., *Analytical Chemistry*, **2005**. 77(7): p. 2125-2131.
207. Ye, N.N., Qin, J.H., Shi, W.W., Liu, X., and Lin, B.C., *Lab on a Chip*, **2007**. 7(12): p. 1696-1704.
208. Rodrigues, N.P., Sakai, Y., and Fujii, T., *Sensors and Actuators B-Chemical*, **2008**. 132(2): p. 608-613.
209. Yin, H.B. and Marshall, D., *Current Opinion in Biotechnology*, **2012**. 23(1): p. 110-119.
210. Bennett, M.R. and Hasty, J., *Nature Reviews Genetics*, **2009**. 10(9): p. 628-638.
211. Di Carlo, D., Aghdam, N., and Lee, L.P., *Analytical Chemistry*, **2006**. 78(14): p. 4925-4930.
212. Cha, W., Tung, Y.C., Meyerhoff, M.E., and Takayama, S., *Analytical Chemistry*, **2010**. 82(8): p. 3300-3305.
213. Sullivan, S.P., Johns, M.L., Matthews, S.M., and Fisher, A.C., *Electrochemistry Communications*, **2005**. 7(12): p. 1323-1328.
214. Amatore, C., Da Mota, N., Sella, C., and Thouin, L., *Analytical Chemistry*, **2007**. 79(22): p. 8502-8510.
215. Amatore, C., Lemmer, C., Sella, C., and Thouin, L., *Analytical Chemistry*, **2011**. 83(11): p. 4170-4177.
216. Li, Y., Sella, C., Lemaitre, F., Guille-Collignon, M., Thouin, L., and Amatore, C., *Electroanalysis*, **2013**. 25(4): p. 895-902.
217. Ikariyama, Y., Yamauchi, S., Yukiashi, T., and Ushioda, H., *Journal of Electroanalytical Chemistry*, **1988**. 251(2): p. 267-274.
218. Casella, I.G. and Salvi, A.M., *Electroanalysis*, **1997**. 9(8): p. 596-301
219. Teshima, N., Genfa, Z., and Dasgupta, P.K., *Analytica Chimica Acta*, **2004**. 510(1): p. 9-13.

220. Amatore, C., Arbault, S., Bouton, C., Drapier, J.C., Ghandour, H., and Koh, A.C.W., *Chembiochem*, **2008**. 9(9): p. 1472-1480.
221. Ikariyama, Y., Yamauchi, S., Yukiashi, T., and Ushioda, H., *Journal of the Electrochemical Society*, **1989**. 136(3): p. 702-706.
222. Bartlett, P.N. and Esterle, T.F., *Journal of Electrochemistry*, **2012**. 18(5): p. 457-471.
223. Krishnamurthy, B. and Deepalochani, S., *International Journal of Electrochemical Science*, **2009**. 4(3): p. 386-395.
224. Bakos, I. and Horanyi, G., *Journal of Electroanalytical Chemistry*, **1995**. 397(1-2): p. 105-110.
225. Kim, C.S. and Oh, S.M., *Electrochimica Acta*, **1996**. 41(15): p. 2433-2439.
226. Borgmann, S., *Analytical and Bioanalytical Chemistry*, **2009**. 394(1): p. 95-105.
227. Breiter, M.W., *Electrochimica Acta*, **1966**. 11: p. 905-909.
228. Manica, D.P., Mitsumori, Y., and Ewing, A.G., *Analytical Chemistry*, **2003**. 75(17): p. 4572-4577.
229. Hall, S.B., Khudaish, E.A., and Hart, A.L., *Electrochimica Acta*, **2000**. 45(21): p. 3573-3579.
230. Hall, S.B., Khudaish, E.A., and Hart, A.L., *Electrochimica Acta*, **1999**. 44(25): p. 4573-4582.
231. Hall, S.B., Khudaish, E.A., and Hart, A.L., *Electrochimica Acta*, **1998**. 43(5-6): p. 579-588.
232. Hall, S.B., Khudaish, E.A., and Hart, A.L., *Electrochimica Acta*, **1998**. 43(14-15): p. 2015-2024.
233. Hall, S.B., Khudaish, E.A., and Hart, A.L., *Electrochimica Acta*, **1999**. 44(14): p. 2455-2462.
234. Piela, B., Piela, P., and Wrona, P.K., *Journal of The Electrochemical Society*, **2002**. 149(10): p. E357-E366.
235. Piela, B. and Wrona, P.K., *Journal of The Electrochemical Society*, **2002**. 149(2): p. E55-E63.
236. Gorton, L., *Analytica Chimica Acta*, **1985**. 178(2): p. 247-253.
237. Zhang, Y. and Wilson, G.S., *Journal of Electroanalytical Chemistry*, **1993**. 345(1-2): p. 253-271.
238. Kissner, R., Nauser, T., Bugnon, P., Lye, P.G., and Koppenol, W.H., *Chemical Research in Toxicology*, **1997**. 10(11): p. 1285-1292.
239. Koppenol, W.H., *Quimica Nova*, **1998**. 21(3): p. 326-331.
240. Luo, Y.J., Zhang, C.X., She, Y.B., Zhong, R.G., and Wei, P., *Reaction Kinetics Mechanisms and Catalysis*, **2010**. 101(2): p. 291-300.
241. Gupta, D., Harish, B., Kissner, R., and Koppenol, W.H., *Dalton Transactions*, **2009**(29): p. 5730.
242. Pfeiffer, S., Gorren, A.C.F., Schmidt, K., Werner, E.R., Hansert, B., Bohle, D.S., and Mayer, B., *Journal of Biological Chemistry*, **1997**. 272(6): p. 3465-3470.

243. Adegoke, O. and Nyokong, T., *Journal of Luminescence*, **2013**. 134: p. 448-455.
244. Chen, Z.J., Ren, W., Wright, Q.E., and Ai, H.W., *Journal of the American Chemical Society*, **2013**. 135(40): p. 14940-14943.
245. Bielski, B.H.J., Cabelli, D.E., Arudi, R.L., and Ross, A.B., *Journal of Physical and Chemical Reference Data*, **1985**. 14(4): p. 1041-1100.
246. Mikkelsen, R.B. and Wardman, P., *Oncogene*, **2003**. 22(37): p. 5734-5754.
247. Zacharia, I.G. and Deen, W.M., *Annals of Biomedical Engineering*, **2005**. 33(2): p. 214-222.
248. Liu, X.P. and Zweier, J.L., *Journal of Electroanalytical Chemistry*, **2013**. 688: p. 32-39.
249. Keefer, L.K., Nims, R.W., Davies, K.M., and Wink, D.A., *Nitric Oxide, Pt a - Sources and Detection of No; No Synthase*, **1996**. 268: p. 281-293.
250. Hrabie, J.A., Klose, J.R., Wink, D.A., and Keefer, L.K., *Journal of Organic Chemistry*, **1993**. 58(6): p. 1472-1476.
251. Pogrebnaya, V.L., Usov, A.P., Baranov, A.V., Nesterenko, A.I., and Bezyazychnyi, P.I., *Journal of Applied Chemistry of the Ussr*, **1975**. 48(5): p. 1004-1007.
252. Kharitonov, V.G., Sundquist, A.R., and Sharma, V.S., *Journal of Biological Chemistry*, **1994**. 269(8): p. 5881-5883.
253. Lewis, R.S. and Deen, W.M., *Chemical Research in Toxicology*, **1994**. 7(4): p. 568-574.
254. Pires, M., Rossi, M.J., and Ross, D.S., *International Journal of Chemical Kinetics*, **1994**. 26(12): p. 1207-1227.
255. Goldstein, S. and Czapski, G., *Journal of the American Chemical Society*, **1995**. 117(49): p. 12078-12084.
256. Cserey, A. and Gratzl, M., *Analytical Chemistry*, **2001**. 73(16): p. 3965-3974.
257. Griveau, S., Dumézy, C., Goldner, P., and Bedioui, F., *Electrochemistry Communications*, **2007**. 9(10): p. 2551-2556.
258. Hunter, R.A., Privett, B.J., Henley, W.H., Breed, E.R., Liang, Z., Mittal, R., Yoseph, B.P., McDunn, J.E., Burd, E.M., Coopersmith, C.M., Ramsey, J.M., and Schoenfisch, M.H., *Analytical Chemistry*, **2013**. 85(12): p. 6066-6072.
259. Davies, I.R. and Zhang, X.J., *Globins and Other Nitric Oxide-Reactive Proteins, Pt A*, **2008**. 436: p. 63-95.
260. Amatore, C., Da Mota, N., Sella, C., and Thouin, L., *Analytical Chemistry*, **2008**. 80(13): p. 4976-4985.
261. Amatore, C., Lemmer, C., Perrodin, P., Sella, C., and Thouin, L., *Electrochemistry Communications*, **2011**. 13(12): p. 1459-1461.
262. He, Y.Y., Huang, J.L., Block, M.L., Hong, J.S., and Chignell, C.F., *Journal of Investigative Dermatology*, **2005**. 125(3): p. 560-566.

263. Sung, H.J., Eskin, S.G., Sakurai, Y., Yee, A., Kataoka, N., and McIntire, L.V., *Annals of Biomedical Engineering*, **2005**. 33(11): p. 1546-1554.
264. Kirmizis, D., Papagianni, A., Dogrammatzi, F., Skoura, L., Belechri, A.M., Alexopoulos, E., Efstratiadis, G., and Memmos, D., *Journal of Atherosclerosis and Thrombosis*, **2010**. 17(12): p. 1256-1265.
265. Lachgar, A., Sojic, N., Arbault, S., Bruce, D., Sarasin, A., Amatore, C., Bizzini, B., Zagury, D., and Vuillaume, M., *Journal of Virology*, **1999**. 73(2): p. 1447-1452.
266. Arbault, S., Edeas, M., Legrand-Poels, S., Sojic, N., Amatore, C., Piette, J., Best-Belpomme, M., Lindenbaum, A., and Vuillaume, M., *Biomedicine & Pharmacotherapy*, **1997**. 51(10): p. 430-438.
267. Hortelano, S., Genaro, A.M., and Bosca, L., *Febs Letters*, **1993**. 320(2): p. 135-139.
268. DeCoursey, T.E., Cherny, V.V., Zhou, W., and Thomas, L.L., *Proceedings of the National Academy of Sciences of the United States of America*, **2000**. 97(12): p. 6885-6889.
269. Okada, M., Hasebe, N., Tashiro, N., Yamauchi, A., Kawabe, J., and Kikuchi, K., *Journal of Hypertension*, **2006**. 24: p. 393-393.
270. Wu, Y.Y., Cui, J., Bao, X.F., Chan, S.P., Young, D.O., Liu, D., and Shen, P.P., *International Journal of Molecular Medicine*, **2006**. 17(1): p. 141-150.
271. Michel, J.B., Feron, O., Sacks, D., and Michel, T., *Journal of Biological Chemistry*, **1997**. 272(25): p. 15583-15586.
272. Di, A., Krupa, B., Bindokas, V.P., Chen, Y.M., Brown, M.E., Palfrey, H.C., Naren, A.P., Kirk, K.L., and Nelson, D.J., *Nature Cell Biology*, **2002**. 4(4): p. 279-285.
273. Salabei, J.K., Cummins, T.D., Singh, M., Jones, S.P., Bhatnagar, A., and Hill, B.G., *Biochemical Journal*, **2013**. 451: p. 375-388.
274. Lin, X.Z., Zheng, W., Liu, J., Zhang, Y., Qin, H.H., Wu, H.C., Xue, B., Lu, Y., and Shen, P.P., *Antioxidants & Redox Signaling*, **2013**. 19(12): p. 1337-1355.
275. Lesniewski, L.A., Durrant, J.R., Connell, M.L., Henson, G.D., Black, A.D., Donato, A.J., and Seals, D.R., *American Journal of Physiology-Heart and Circulatory Physiology*, **2011**. 301(3): p. H1025-H1032.
276. Miles, P.R., Bowman, L., Rengasamy, A., and Huffman, L., *American Journal of Physiology-Lung Cellular and Molecular Physiology*, **1998**. 274(3): p. L360-L368.
277. deVera, M.E., Shapiro, R.A., Nussler, A.K., Mudgett, J.S., Simmons, R.L., Morris, S.M., Billiar, T.R., and Geller, D.A., *Proceedings of the National Academy of Sciences of the United States of America*, **1996**. 93(3): p. 1054-1059.
278. Connelly, L., Jacobs, A.T., Palacios-Callender, M., Moncada, S., and Hobbs, A.J., *Journal of Biological Chemistry*, **2003**. 278(29): p. 26480-26487.
279. Xia, Y. and Zweier, J.L., *Proceedings of the National Academy of Sciences of the United States of America*, **1997**. 94(13): p. 6954-6958.

280. Vasquez-Vivar, J., Kalyanaraman, B., Martasek, P., Hogg, N., Masters, B.S.S., Karoui, H., Tordo, P., and Pritchard, K.A., *Proceedings of the National Academy of Sciences of the United States of America*, **1998**. 95(16): p. 9220-9225.
281. Rodrigues, N.P., Bedioui, F., Deutsch, A., Zurgil, N., Afrimzon, E., Shafran, Y., and Deutsch, M., *Electrochemistry Communications*, **2006**. 8(2): p. 341-347.
282. Yeh, C.C., Chang, S.F., Huang, T.Y., Chang, H.I., Kuo, H.C., Wu, Y.C., Hsieh, C.H., Shi, C.S., and Chen, C.N., *Arthritis Research & Therapy*, **2013**. 15(2).
283. Bacabac, R.G., Smit, T.H., Cowin, S.C., Van Loon, J.J.W.A., Nieuwstadt, F.T.M., Heethaar, R., and Klein-Nulend, J., *Journal of Biomechanics*, **2005**. 38(1): p. 159-167.
284. Patel, B.A., Arundell, M., Quek, R.G.W., Harvey, S.L.R., Ellis, I.R., Florence, M.M., Cass, A.E.G., Schor, A.M., and O'Hare, D., *Analytical and Bioanalytical Chemistry*, **2008**. 390(5): p. 1379-1387.
285. Trouillon, R., Cheung, C., Patel, B.A., and O'Hare, D., *Biochimica Et Biophysica Acta-General Subjects*, **2010**. 1800(9): p. 929-936.
286. Meunier, A., Fulcrand, R., Darchen, F., Collignon, M.G., Lemaitre, F., and Amatore, C., *Biophysical Chemistry*, **2012**. 162: p. 14-21.
287. Allen, J.B. and Larry, R.F., "Electrochemical Methods: Fundamentals and Applications." John Wiley & Sons, Inc., **2001**: p. 1-43.
288. Chang, B.Y. and Park, S.M., *Annual Review of Analytical Chemistry*, Vol 3, **2010**. 3: p. 207-229.
289. Dennis, A., Mark, R., Jun, C., and Joselito, M.R., *Syntheses and Applications of Carbon Nanotubes and Their Composites*, *Nanotechnology and Nanomaterials*, Edited by Satoru Suzuki, **2013**. Chapter 22.
290. David, H., *Analytical Chemistry 2.0*, **2008**. Chapter 11: p. 667-781.
291. Pyun, S.I., Shin, H.C., Lee, J.W., and Go, J.Y., *Electrochemistry of Insertion Materials for Hydrogen and Lithium. Monographs in Electrochemistry.*, **2012**: p. 11-32.
292. Huang, S.B. and Wang, Z.J., *Applied Geochemistry*, **2003**. 18(8): p. 1215-1223.
293. Gil, M.L.A., Andreu, R., Calvente, J.J., and de Pablos, F., *Journal of the Electrochemical Society*, **2002**. 149(2): p. E45-E54.
294. Osteryoung, J., Talmor, D., Hermolin, J., and Kirowaeisner, E., *Journal of Physical Chemistry*, **1981**. 85(3): p. 285-289.
295. Helen, H.L. and Yinlun, H., *Encyclopedia of Chemical Processing*, **2006**: p. 1-10.
296. Li, G. and Miao, P., *Electrochemical Analysis of Proteins and Vells. Springer Briefs in Molecular Science.*, **2013**: p. 5-18.
297. Zhang, Y., Shin, H.C., Dong, J., and Liu, M., *Solid State Ionics*, **2004**. 171(1-2): p. 25-31.
298. Shin, H.C. and Liu, M.L., *Advanced Functional Materials*, **2005**. 15(4): p. 582-586.

299. Vidakovic-Koch, T., Mittal, V.K., Do, T.Q.N., Varnicic, M., and Sundmacher, K., *Electrochimica Acta*, **2013**. 110: p. 94-104.
300. Yilmaz, U.T. and Yazar, Z., *Food Analytical Methods*, **2012**. 5(1): p. 119-125.
301. Kurita, R., Nakamoto, K., Sato, Y., Kamata, T., Ueda, A., Kato, D., Hirono, S., and Niwa, O., *Analytical Sciences*, **2012**. 28(1): p. 13-20.
302. Amatore, C. and Fosset, B., *Analytical Chemistry*, **1996**. 68(24): p. 4377-4388.
303. Amatore, C., *Physical Electrochemistry: Principles, Methods and Applications*. Edited by Rubinstein, New York, **1995**. Chapter 4: p. 131-208.
304. Belding, S.R., Campbell, F.W., Dickinson, E.J.F., and Compton, R.G., *Physical Chemistry Chemical Physics*, **2010**. 12(37): p. 11208-11221.
305. Velmurugan, J., Noel, J.M., and Mirkin, M.V., *Chemical Science*, **2014**. 5(1): p. 189-194.
306. Jiang, J.H., Wang, X.Y., and Zhang, L., *Electroanalysis*, **2013**. 25(8): p. 2015-2020.
307. Kishi, A., Fukasawa, T., and Umeda, M., *Journal of Power Sources*, **2010**. 195(18): p. 5996-6000.
308. Rees, N.V. and Compton, R.G., *Chemical Communications*, **2010**. 46(24): p. 4238-4248.
309. Amatore, C., Pebay, C., Sella, C., and Thouin, L., *Chemphyschem*, **2012**. 13(6): p. 1562-1568.
310. Halouzka, V., Jakubec, P., Gregor, C., Jancik, D., Papadopoulos, K., Triantis, T., and Hrbac, J., *Chemical Engineering Journal*, **2010**. 165(3): p. 813-818.
311. Amatore, C., Fosset, B., Maness, K.M., and Wightman, R.M., *Analytical Chemistry*, **1993**. 65(17): p. 2311-2316.
312. Sekine, S., Nakanishi, S., Miyake, T., Nagamine, K., Kaji, H., and Nishizawa, M., *Langmuir*, **2010**. 26(13): p. 11526-11529.
313. Amatore, C., Belotti, M., Chen, Y., Roy, E., Sella, C., and Thouin, L., *Journal of Electroanalytical Chemistry*, **2004**. 573(2): p. 333-343.
314. Eswari, A. and Rajendran, L., *Journal of Electroanalytical Chemistry*, **2011**. 651(2): p. 173-184.
315. Sun, P., Laforge, F.O., and Mirkin, M.V., *Physical Chemistry Chemical Physics*, **2007**. 9(7): p. 802-823.
316. Wesche, M., Huske, M., Yakushenko, A., Bruggemann, D., Mayer, D., Offenhausser, A., and Wolfrum, B., *Nanotechnology*, **2012**. 23(49).
317. Amatore, C., Da Mota, N., Sella, C., and Thouin, L., *Analytical Chemistry*, **2010**. 82(6): p. 2434-2440.
318. Pebay, C., Sella, C., Thouin, L., and Amatore, C., *Analytical Chemistry*, **2013**. 85(24): p. 12062-12069.
319. Hood, S.J., Kampouris, D.K., Kadara, R.O., Jenkinson, N., del Campo, F.J., Munoz, F.X., and Banks, C.E., *Analyst*, **2009**. 134(11): p. 2301-2305.

320. Ren, K., Zhou, J., and Wu, H., *Acc Chem Res*, **2013**. 46(11): p. 2396-406.
321. Yen, B.K.H., Gunther, A., Schmidt, M.A., Jensen, K.F., and Bawendi, M.G., *Angewandte Chemie-International Edition*, **2005**. 44(34): p. 5447-5451.
322. Kenis, P.J.A., Ismagilov, R.F., Takayama, S., Whitesides, G.M., Li, S.L., and White, H.S., *Accounts of Chemical Research*, **2000**. 33(12): p. 841-847.
323. Marre, S. and Jensen, K.F., *Chemical Society Reviews*, **2010**. 39(3): p. 1183-1202.
324. Lin, C.H., Lee, G.B., Lin, Y.H., and Chang, G.L., *Journal of Micromechanics and Microengineering*, **2001**. 11(6): p. 726-732.
325. Sugioka, K. and Cheng, Y., *Lab on a Chip*, **2012**. 12(19): p. 3576-3589.
326. Zhu, Q.Y., Yang, W.X., Gao, Y.B., Yu, B.W., Qiu, L., Zhou, C., Jin, W., Jin, Q.H., and Mu, Y., *Chemical Journal of Chinese Universities-Chinese*, **2013**. 34(3): p. 545-550.
327. Ferry, M.S., Razinkov, I.A., and Hasty, J., *Methods in Enzymology, Vol 497: Synthetic Biology, Methods for Part/Device Characterization and Chassis Engineering, Pt A*, **2011**. 497: p. 295-372.
328. Mukhopadhyay, R., *Anal Chem*, **2007**. 79(9): p. 3248-53.
329. Jackman, R.J., Floyd, T.M., Ghodssi, R., Schmidt, M.A., and Jensen, K.F., *Journal of Micromechanics and Microengineering*, **2001**. 11(3): p. 263-269.
330. Tsao, C.W. and DeVoe, D.L., *Microfluidics and Nanofluidics*, **2009**. 6(1): p. 1-16.
331. Kosovskiy, M., *Genetic Engineering News*, **2005**. 25(13): p. 40+.
332. Tibbitt, M.W. and Anseth, K.S., *Biotechnology and Bioengineering*, **2009**. 103(4): p. 655-663.
333. Khademhosseini, A., *Abstracts of Papers of the American Chemical Society*, **2013**. 245.
334. Martinez, A.W., Phillips, S.T., Butte, M.J., and Whitesides, G.M., *Angewandte Chemie-International Edition*, **2007**. 46(8): p. 1318-1320.
335. Dungchai, W., Chailapakul, O., and Henry, C.S., *Analyst*, **2011**. 136(1): p. 77-82.
336. Maejima, K., Tomikawa, S., Suzuki, K., and Citterio, D., *Rsc Advances*, **2013**. 3(24): p. 9258-9263.
337. Martinez, A.W., Phillips, S.T., Carrilho, E., Thomas, S.W., Sindi, H., and Whitesides, G.M., *Analytical Chemistry*, **2008**. 80(10): p. 3699-3707.
338. Nam, Y., Kim, M., and Kim, T., *Journal of Micromechanics and Microengineering*, **2013**. 23(10).
339. Lee, B., Hong, J.M., Amos, N., Dumer, I., Litvinov, D., and Khizroev, S., *Journal of Nanoparticle Research*, **2013**. 15(6).
340. Heussler, S.P., Moser, H.O., and Kalaiselvi, S.M.P., *Microsystem Technologies-Micro-and Nanosystems-Information Storage and Processing Systems*, **2013**. 19(3): p. 335-341.



341. Abderrafi, K., Garcia-Calzada, R., Sanchez-Royo, J.F., Chirvony, V.S., Agouram, S., Abargues, R., Ibanez, R., and Martinez-Pastor, J.P., *Journal of Physics D-Applied Physics*, **2013**. 46(13).
342. MicroChem, NANO SU-8 Negative Tone Photoresist Formulations 50 and 100, MicroChem Corp, Newton, MA.
343. Livanos, A.C., Katzir, A., Shellan, J.B., and Yariv, A., *Applied Optics*, **1977**. 16(6): p. 1633-1635.
344. Gogolides, E., Baik, K.H., Yannakopoulou, K., Vandenhove, L., and Hatzakis, M., *Microelectronic Engineering*, **1994**. 23(1-4): p. 267-270.
345. O'Brien, J., Hughes, P.J., Brunet, M., O'Neill, B., Alderman, J., Lane, B., O'Riordan, A., and O'Driscoll, C., *Journal of Micromechanics and Microengineering*, **2001**. 11(4): p. 353-358.
346. MicroChem, SU-8 2000 Permanent Epoxy Negative Photoresist Processing Guidelines, MicroChem Corp, Newton, MA.
347. Gaudet, M., Camart, J.C., Buchailot, L., and Arscott, S., *Applied Physics Letters*, **2006**. 88(2).
348. Saez-Landete, J., Salcedo-Sanz, S., Cruz-Roldan, F., Amo-Lopez, P., and Blanco-Velasco, M., *Journal of Lightwave Technology*, **2008**. 26(9-12): p. 1702-1707.
349. Wu, J. and Gu, M., *Journal of Biomedical Optics*, **2011**. 16(8).
350. Hyun, J.K., Ahn, C., Kang, H., Kim, H.J., Park, J., Kim, K.H., Ahn, C.W., Kim, B.J., and Jeon, S., *Small*, **2013**. 9(3): p. 369-374.
351. Qin, D., Xia, Y.N., Rogers, J.A., Jackman, R.J., Zhao, X.M., and Whitesides, G.M., *Microsystem Technology in Chemistry and Life Science*, **1998**. 194: p. 1-20.
352. Kawagoe, K.T., Jankowski, J.A., and Wightman, R.M., *Analytical Chemistry*, **1991**. 63(15): p. 1589-1594.
353. Amatore, C., Arbault, S., and Erard, M., *Analytical Chemistry*, **2008**. 80(24): p. 9635-9641.

**Abstract:** With intrinsic benefits of electrochemistry and unprecedented progress in instrumentation, microelectrodes are playing prominent roles in the analysis of living cells behaviors. Nowadays, microfluidics also gains in popularity due to the feasibility of performing the entire bioanalytical experiment within an automated device. In this thesis, fabrication of Pt/Pt-black microband electrodes was thus optimized to detect ROS/RNS species during oxidative stress. They were integrated into PDMS-glass microdevices in order to analyze four key compounds (i.e.,  $\text{H}_2\text{O}_2$ ,  $\text{ONOO}^-$ ,  $\text{NO}^\bullet$ , and  $\text{NO}_2^-$ ) released from cells populations. High analytical performances were first evidenced according to the devices geometry and hydrodynamic conditions. The control of the electrochemical responses by mass transport was validated through comparison with theoretical predictions. Simultaneous detections of ROS/RNS release from macrophages were then carried out under two different configurations of microdevices. Reproducible and statistically relevant results were obtained within only few experiments. These microdevices allow for easy characterizations of average behaviors of cells populations. This study paves the way to a very broad field of bioanalytical applications integrating electrochemical detections for high-throughput monitoring of living cells.

**Keywords:** Oxidative stress, Microelectrode, Microfluidics, Amperometry, Platinum black

**Résumé:** Avec les avantages intrinsèques de l'électrochimie et les progrès sans précédent dans l'instrumentation, les microélectrodes jouent un rôle de premier plan dans l'analyse du comportement de cellules vivantes. Aujourd'hui, la microfluidique gagne également en popularité en raison de la possibilité d'effectuer l'ensemble de l'expérience de bioanalyse dans un dispositif automatisé. Dans cette thèse, la fabrication de microbandes Pt/noir-Pt a été optimisée pour détecter les espèces ROS/RNS durant le stress oxydant. Celles-ci ont été intégrées dans des microdispositifs en PDMS-verre afin d'analyser la libération de quatre composés clés (i.e.,  $\text{H}_2\text{O}_2$ ,  $\text{ONOO}^-$ ,  $\text{NO}^\bullet$ , et  $\text{NO}_2^-$ ) à partir de populations de cellules. Les performances analytiques ont été évaluées suivant la géométrie des dispositifs et les conditions hydrodynamiques. Le contrôle des réponses électrochimiques par le transport de masse a été validé par comparaison avec des prédictions théoriques. Des détections simultanées de ROS/RNS libérées par des macrophages ont ensuite été réalisées sous deux configurations différentes de dispositifs. Des résultats reproductibles et statistiquement pertinents ont été obtenus en seulement quelques expériences. Ces microdispositifs permettent de caractériser facilement le comportement moyen de populations de cellules. Cette étude préalable ouvre la voie à un très large champ d'applications bioanalytiques intégrant des détections électrochimiques à haut débit pour le suivi de cellules vivantes.

**Mots clés:** Stress oxydant, Microélectrode, Microfluidique, Ampérométrie, Noir de platine